LANCASTER UNIVERSITY

DOCTORAL THESIS

Superflow as a tool for studying superfluid ^{3}He

Author:
Asher Jennings

Supervisors:
Dr. Dmitry Zmeev
Prof. Rich Haley

*This thesis submitted for the fulfilment
of the degree of Doctor of Philosophy*

in the

Department of Physics
Faculty of Science and Technology

January 23, 2022

Abstract

Superflow as a tool for studying superfluid ^{3}He

by Asher Jennings

In this thesis, we use mechanical oscillators to induce fluid flow in the superfluid ^{3}He in order to investigate the properties of several superfluid phases. In particular, we investigate the B phase below temperatures of $230\,\mu$K and superfluid ^{3}He confined in an anisotropic aerogel.

Superfluid ^{3}He is a fermionic superfluid consisting of Cooper pairs. If the superfluid flows above a critical velocity called the Landau velocity, the Cooper pairs break and form into quasiparticles. When an oscillating object goes faster than the critical velocity, it experiences a large increase in the drag force on the object. In this work, we move a device in superfluid ^{3}He-B with constant velocity rather than oscillating it. We see only a small increase in damping for velocities above the critical velocity, instead of the large increase. After subtracting the results of thermally excited quasiparticles, we demonstrate that the small increase in damping is due to expelling quasiparticles occupying surface-bound-states on the wire surface. By monitoring the thermometer response to the movements, we measure the Kapitza resistance. We also observe the damping of wires oscillating in superfluid ^{3}He-B with a diameter approaching the coherence length. The damping is much smaller than expected from considering the collisions of thermally excited quasi-particles.

Lastly, we built a new device for exploring the superfluid phases of ^{3}He confined inside an anisotropic aerogel. The aerogel has $10\,$nm strands aligned parallel with a mean distance between the strands of $100\,$nm, close to the coherence length of the superfluid. The device can be moved and oscillated, inducing flow. By observing the resonance frequency and the damping of the device, one can measure the superfluid fraction and observe other phenomena in the superfluid. Sharp changes in the velocity of measurements below the aerogel transition temperature have been found using this technique.

Acknowledgements

Declaration

I declare that the work contained within this thesis is the author's own work and has not been submitted for the award of a higher degree at any other university. The work described is part of a collaborative effort of the Lancaster University Ultra-Low Temperature Physics group, however the majority of the analysis and data taking was performed by the author, except where otherwise noted.

I confirm that the total length of this thesis is 36365 words and does not exceed the 80000 word limit of a PhD thesis.

The following publications are published works of the author and others that contain work that has contributed to this thesis, correct as of the time of publication of this thesis:

- S. Autti, A. M. Guénault, A. Jennings, R. P. Haley, G. R. Pickett, R. Schanen, V. Tsepelin, J. Vonka, D. E. Zmeev, and A. A. Soldatov, "Effect of the boundary condition on the Kapitza resistance between superfluid ^{3}He-B and sintered metal", *Physical Review B* **102**, 064508 (2020).

- S. Autti, S. L. Ahlstrom, R. P. Haley, A. Jennings, G. R. Pickett, M. Poole, R. Schanen, A. A. Soldatov, V. Tsepelin, J. Vonka, T. Wilcox, A. J. Woods & D. E. Zmeev, "Fundamental dissipation due to bound fermions in the zero-temperature limit", *Nature Communications* **11**, 4742 (2020).

Asher Jennings

Contents

List of Figures

List of Abbreviations

2D	**2**-**D**imensional
3D	**3**-**D**imensional
AC	**A**lternating **C**urrent
BCS	**B**ardeen, **C**ooper and **S**chreiffer
BEC	**B**ose-**E**instein **C**ondensate
DAQ	**D**igital **A**cquisition
DC	**D**irect **C**urrent
EMF	**E**lectro**m**otive **F**orce
HWD	**H**eight times **W**idth over **D**rive
HQVs	**H**alf **Q**uantum **V**ortices
MEMS	**M**icro**e**lectro**m**echanical **S**ystem(s)
NEMS	**N**ano**e**lectro**m**echanical **S**ystem(s)
ICTa	**I**nner **C**ell **Ta**ntalum
NMR	**N**uclear **M**agnetic **R**esonance
OCTa	**O**uter **C**ell **Ta**ntalum
QTF(s)	**Q**uartz **T**uning **F**ork(s)
SEM	**S**canning **E**lectron **M**icroscope
VWR(s)	**V**ibrating **W**ire **R**esonator(s)

Chapter 1

Introduction

In the popular imagination, quantum physics is thought of as describing the realm of extremely small objects. In reality, there are macroscopic quantum systems that arise from quantum mechanics. Two such quantum systems are the quantum fluids superfluid helium-4 and superfluid helium-3 [1]. Whole bucketfuls of helium-4 can be described as following a single wave function, as the particles in the fluid condensate into the quantum ground state at low temperatures. Of the two, superfluid ^{3}He is the much more complex, as superfluidity requires ^{3}He atoms to form pairs called Cooper pairs [2]. It is fermionic, magnetic and has a triplet wave-function state which allows for the stabilisation of multiple superfluid phases. This leads to a rich and diverse range of phenomena. Whilst most closely related to unconventional superconductors, the fundamental physics in superfluid ^{3}He allows the quantum fluid to be used as a quantum analogue or simulator of many other systems. Moreover, superfluid ^{3}He is the purest system in the universe. The lack of impurities allow a much easier theoretical treatment of the superfluid. As a liquid, it is easy to introduce controlled impurities. A commonly used impurity is an aerogel: a sponge-like porous material made of 1 nm–10 nm sized solid strands with a small mean free path between the strands, usually 10 nm–100 nm in distance.

This work describes the design and undertaking of experiments in superfluid ^{3}He with the goal of investigating both bulk superfluid ^{3}He and ^{3}He confined to an aerogel. The main tool used to investigate the superfluid is a mechanically moving object that induces mass flow in the superfluid, known as superflow. In the bulk superfluid, we study superflow with velocities above the critical Landau velocity. For ^{3}He in aerogel, we use a nematic aerogel to introduce anisotropy into the system.

1.1 Faster than Landau Experiment

It was previously thought that superflow above the Landau velocity was impossible. The Landau velocity in superfluid ^{3}He-B at saturated vapour pressure is $v_\mathrm{L} = 27\,\mathrm{mm\,s^{-1}}$. A slightly lower critical velocity was found by experiments using moving objects to induce

flow [3, 4]. To explain the lower critical velocity, Lambert developed a model incorporating the local flow of the fluid around the object, which reduces the critical velocity from the Landau velocity by a factor depending on the geometry of the moving object [5].

A recent experiment demonstrated it is possible to move an object above the critical velocity and the Landau velocity without experiencing a large increase in the drag force on the object, as long as the velocity remains constant [6]. There is some small increase in damping, which was thought to be from expelling surface Andreev bound quasiparticles that exist on the surface of the object when immersed in superfluid ^{3}He-B. By introducing a direction dependence of the motion, we investigate the reasons for this peculiar behaviour and use superflow at velocities above v_L to investigate the dynamics of the surface states.

This works also presents a thermometric analysis of the experiments to measure the thermal boundary resistance, or Kapitza resistance, between copper plates covered with silver sinter and superfluid ^{3}He. The results of this analysis has an impact on the design of future nuclear demagnetisation stages and the aerogel experiments.

1.2 ^{3}He in a Nematic Aerogel

A new phase of superfluid ^{3}He was discovered in the nematic aerogel nafen, called the polar phase [7]. The phase was detected by nuclear magnetic resonance (NMR). Previous experiments in this phase have led to the stabilisation of half-quantum vortices (HQVs), also detected by NMR [8]. These vortices can be created by Kibble-Zureck mechanism or by the rotation of the superfluid. Another way to create vortices is to move an object inside the superfluid. In the case of this work, moving the aerogel itself.

Since measurements on the polar phase required NMR, the magnetic fields used were quite low. If the polar phase can be stabilised, another theoretically predicted phase should be present at high magnetic fields called the beta (β) phase [9]. This phase is undetectable by NMR, but can be detected by using superflow. The fraction of fluid inside the nematic aerogel that is superfluid abruptly changes when beta phase transitions to the polar phase. The superfluid fraction inside an aerogel can be measured by oscillating it [10, 11].

Much of the work presented in this thesis can be viewed with the main goal of searching for the β phase. A new mechanically oscillating device with an NMR coil attached was created and immersed in superfluid ^{3}He. Inside the NMR coil, the aerogel nafen-92 was inserted in which the polar phase can be stabilised. The NMR coil allows low field measurements to ensure the polar phase is present in the sample. At high fields, we can oscillate the device with the aim of measuring the superfluid fraction of the liquid ^{3}He confined within the aerogel. At low fields, the aim was also to detect HQVs created

by mechanical motion and possibly measure their dynamics using NMR. Whilst the experiment so far is ultimately inconclusive about the presence of the β phase, the data presented demonstrates some strange effects that are likely due to the aerogel.

1.3 Layout

Chapter 2 gives a brief introduction to helium and superfluids in general, before covering the necessary theoretical details of superfluid ^{3}He. At the end, continuous wave NMR as it pertains to ^{3}He is described.

Chapter 3 covers the devices used in the experimental cell, both theoretically and practically. It begins with a description of damped-driven mechanical resonance using the mass-spring model, and makes an analogy to electrical resonance. We then theoretically describe damping mechanisms in superfluid ^{3}He. Finally we discuss the design and operation of specific devices used in this work.

Chapter 4 gives details of other experimental apparatus and techniques used in this work. As the details of dilution refrigeration and nuclear demagnetisation is extensive in low temperature literature, only very brief descriptions of the cooling techniques used are given. The layout of the experimental cells are shown and the design of a helium purifier is discussed.

Chapter 5 presents the results of experiments where an object is moved faster than the Landau velocity. We explore the difference between moving the object in a constant direction and changing direction. We use these results to confirm the surface Andreev bound states as a mechanism for damping when moving at a constant velocity and elucidate the dynamics of bound states.

Chapter 6 describes the results of some thermometric experiments. It consists of two sections. First, the temperature response of the thermometers in time to the faster than Landau experiments is analysed to find the Kaptiza resistance of our sintered-nuclear refrigerant. The Kapitza resistance is compared when the sinter is plated with pure ^{3}He versus with 2 layers of solid ^{4}He. Second, we describe preliminary measurements of vibrating wire resonators with radii approaching the coherence length of the superfluid and discuss their applicability as thermometers.

Chapter 7 presents results of the new flopper device with an NMR coil and aerogel attached, termed the NMR-flopper. First, NMR measurements in a low magnetic field are presented. Then our efforts in search of the β phase using the mechanical properties of the device are shown.

Lastly, Chapter 8 summarises the thesis and gives some indications for future research that might be derived from this work.

Chapter 2

Liquid Helium

Without a sufficiently high pressure, both helium-3 and helium-4 remain liquid even at absolute zero [1, 2, 12, 13]. A simple argument demonstrating this phenomenon is that the zero point energy of the atoms is large. The zero point energy for ^{3}He or ^{4}He is given by

$$E_0 = \frac{3\hbar^2 \pi^2}{2m_{3,4} V_{3,4}^{\frac{2}{3}}},$$ (2.1)

where $\hbar$ is the reduced Planck's constant, $m_{3,4}$ is the mass of a ^{3}He or ^{4}He particle respectively and $V_{3,4}$ is the volume of the "box" the particle is confined in. As helium is such a light particle, it gives rise to a very large energy. Since the energy increases as the confining box decreases, the energy of solid helium is much higher than that of liquid helium, preventing solidification. In fact, the zero point energy is several times larger than that of the attractive van der Waal's force between two helium atoms. For helium-3, there is also an attractive force due to nuclear dipole interaction, but this is a small correction. Similarly, since the attractive forces between atoms are very small, when in the gaseous state both isotopes can be considered an ideal gas.

Instead of remaining a simple classical fluid, both isotopes undergo a phase transition into a so-called "superfluid" state. The superfluid state is a macroscopic quantum system described by a condensate, in which all the particles are governed by a single macroscopic wave function. Furthermore, the ^{4}He and ^{3}He superfluid phases are distinct from each other. ^{4}He atom has an even number of nucleons, and therefore an integer spin. The helium-4 atom is therefore bosonic and the superfluid state more akin to a Bose-Einstein Condensate (BEC) gas. ^{3}He atom has an odd number of nucleons, hence having half-integer spin in total and is fermionic. A fermionic system requires the fermions to form into pairs called Cooper pairs in order to condense into the superfluid state. The Cooper pairing process is also found to happen to electrons in superconductors, and as such ^{3}He is often considered a charge-less superconductor. These differences mean that the respective superfluid transitions in each isotope happen at much different temperature scales. The transition temperature for superfluid ^{4}He happens on the order of Kelvins,
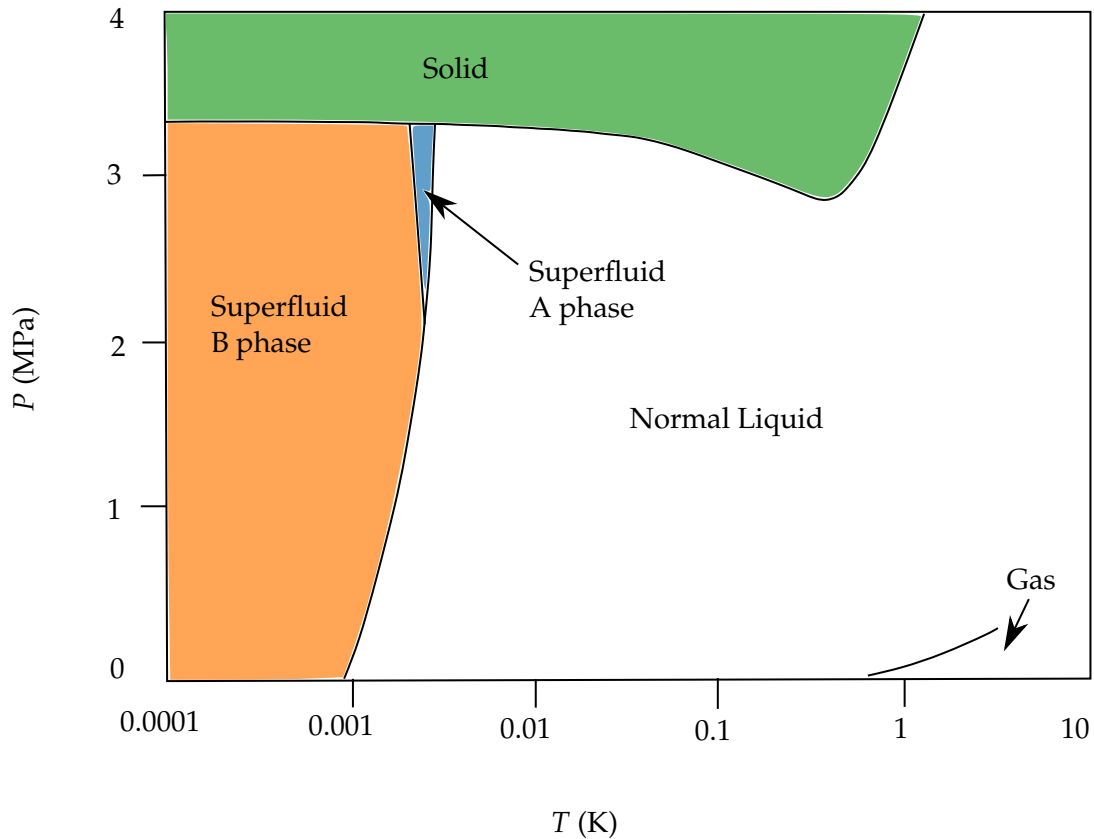
FIGURE 2.1: The phase diagram of helium at low temperatures and zero
magnetic field. Note the log scale on temperature axis [2].

with the transition temperature $T_\lambda = 2.17\,\text{K}$ at saturated vapour pressure. For ^3He the superfluid transition temperature T_c is on the order of millikelvins, with the zero-pressure transition temperature being 929 μK, shown by the phase diagram in Fig. 2.1.

The major difference between the fermionic superfluid state of ^3He and bosonic superfluid ^4He is that there are actually multiple superfluid phases, rather than the one. This comes from the magnetic properties of the Cooper pair formed. The ground state of the Cooper pair wave function in superfluid ^3He has orbital angular momentum $l = 1$ and spin $s = 1$.

2.1 Brief Introduction to Superfluids

Experimentally, the first signs of a phase transition are sharp discontinuities in the specific heat capacity [14] but the most immediately striking property of a superfluid is the ability to flow with zero viscosity [15, 16]. The superfluid can flow through extremely narrow

channels with no friction and even flow up walls as a thin film. In a normal liquid, the van der Waal's forces between the wall and liquid and the surface tension of the film comes into equilibrium with the viscous friction and gravity opposing the film. In a superfluid, the absence of viscosity means that film flow is nearly always possible [1]. Objects moving within a superfluid experience almost no drag force, as if in a mechanical vacuum. This behaviour exists as long as the object is moving below a certain critical velocity, known as the Landau velocity v_{L} [17, 18]. Similarly, a superconductor conducts with zero resistance as the electrons superflow. One can exploit this property to create supercurrents of fluid flow by rotating a vessel containing the superfluid.

Another common feature is extremely fast heat conduction [19, 20]. The heat transport is not done through convection but as a temperature-entropy wave known as second sound. Sound propagation in superfluids is complex, with possible sounds such as a third and fourth sound. In ^{3}He superfluid and normal liquid phases, a zeroth sound consisting of the oscillations of momentum distribution of quasiparticles near the Fermi energy also exists. Another common feature is the existence of quantised vortices.

Two Fluid Theory

At high temperatures, a superfluid can be modelled with the two-fluid theory [1, 17, 20]. According to the two-fluid model, the fluid behaves as a mixture of two interpenetrating fluids. It is important to keep in mind that this is only a model and there are not actually two separate liquids. One fluid is the "normal" fluid whilst the other is the superfluid, which increases in concentration as temperature T decreases which can be roughly measured by the density. Accordingly, the liquid does not immediately become entirely superfluid. The total density of the liquid is constant however the superfluid density ρ_{s} and normal fluid ρ_{n} varies with temperature. The total density is therefore

$$\rho_{\text{He}} = \rho_{\text{n}}(T) + \rho_{\text{s}}(T). \tag{2.2}$$

Many of the properties of the two fluids explain phenomena observed above. The normal fluid carries the entropy and viscosity of the total fluid. As the temperature decreases below the transition point, a sudden drop in normal fluid density and therefore viscosity occurs. The normal and superfluid densities as a function of temperature in superfluid ^{3}He-B are plotted in Fig. 2.2. Below about $0.3T_{\text{c}}$ in the B phase of superfluid ^{3}He, the normal fluid density is vanishingly small. Flow through narrow channels is flow of the superfluid component. The heat conduction is also explained by counterflow of the two-fluid components which move in anti-phase with each other, known as second sound. Since the normal fluid component carries both the temperature and entropy, this can be seen as an entropy wave.
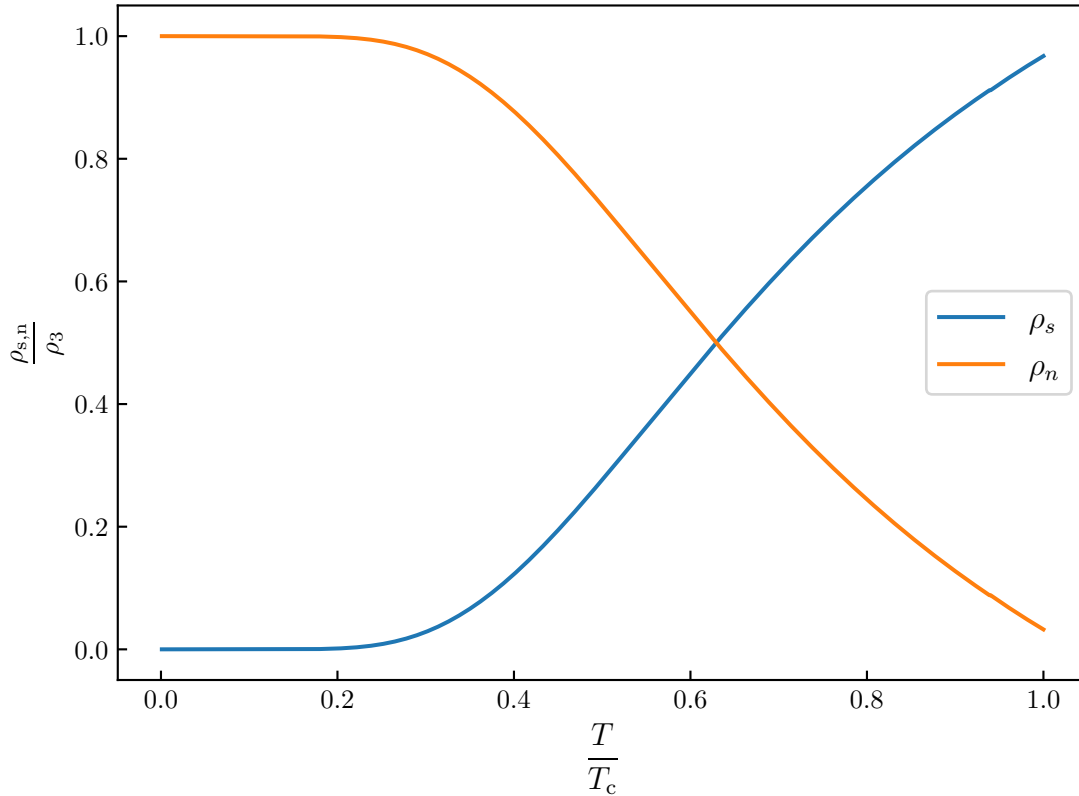
FIGURE 2.2: The normalised superfluid and normal fluid fractions of superfluid ^{3}He-B at all pressures as a function of the reduced temperature $\frac{T}{T_c}$ [13].

Quantum Turbulence

Consider a condensate described by the macroscopic wave function

$$\Psi = \sqrt{n_s}\, e^{i\Theta(\mathbf{r})}, \tag{2.3}$$

as found in superfluid ^{4}He [1]. Here, n_s is the superfluid number density, $\mathbf{r}$ is a position in space, and Θ is the phase. Comparing the classical momentum $\mathbf{p} = m_4\mathbf{v}$ and the momentum operator $\hat{p} = i\hbar\nabla$ we get an expression for the superfluid velocity

$$\mathbf{v}_s = \frac{\hbar}{m_4}\nabla\Theta(\mathbf{r}). \tag{2.4}$$

If we imagine the superfluid moving along a closed loop C around a region of non-superfluid, the circulation would be

$$\kappa = \oint_C \mathbf{v}_s \cdot d\mathbf{r}. \tag{2.5}$$
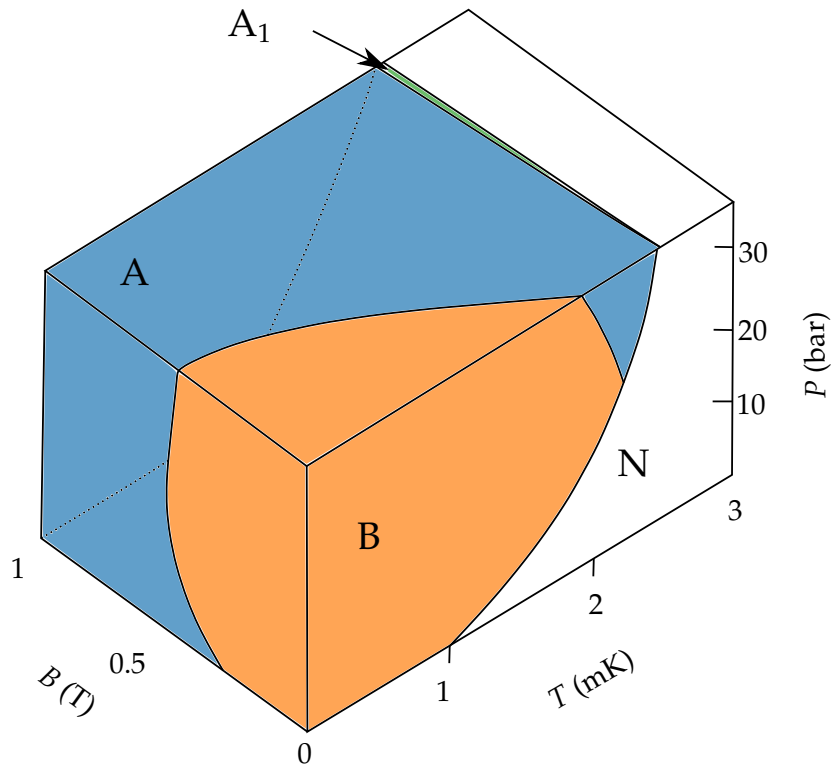
FIGURE 2.3: The phase diagram of liquid helium-3.

Only the phase varies with position, but it must be continuous and return back to the original value. It is therefore limited to being integer multiples of 2π. Thus the circulation is

$$\kappa = \Xi \frac{h}{m},\tag{2.6}$$

where Ξ is an integer. We can therefore say circulation is quantised in units of $\frac{h}{m_4}$. A similarly argument can be made for quantisation of vortices in the B phase of superfluid ^{3}He as it is isotropic. Instead of the helium-4 mass m_4, the mass of one Cooper pair $2m_3$ appears. For the A phase circulation does not have to be quantised at all. There also exists exotic possible configurations, such as double-core vortices in the A phase and half-quantum vortices in the polar phase.

2.2   Liquid Helium-3

2.2.1   Landau Fermi-Liquid

Since fermions cannot occupy the same state as another fermion, at temperature $T = 0$, fermions will fill increasing energy states up until the Fermi energy E_F [2, 13]. Fermions with mass m at E_F can be said to have Fermi momentum $\mathbf{p}_F$. The relationship between the two is given by

$$E_F = \frac{|\mathbf{p}_F|^2}{2m}. \tag{2.7}$$

At a finite temperature ($T > 0$), states close to E_F can be excited to a state above E_F, creating a "hole" in the now unoccupied state. The probability of a state being occupied excited above E_F is described by the Fermi-Dirac distribution

$$f(E, T) = \frac{1}{e^{(E - E_F)/k_B T} + 1}, \tag{2.8}$$

where k_B is the Boltzmann constant. The 3-D density of states for a symmetric free Fermi gas is

$$g(E) = \frac{(2m)^{\frac{3}{2}} \sqrt{E}}{2\pi^2 \hbar^3}, \tag{2.9}$$

and the number density of the system at zero temperature where all states are occupied only up to E_F is then

$$n = \frac{N}{V} = \int_0^{E_F} g(E) f(E, T = 0) dE = \frac{1}{2\pi^2} \left(\frac{2m E_F}{\hbar} \right)^{\frac{3}{2}}. \tag{2.10}$$

However, liquid ^{3}He is an interacting system and the excitations of one particle affects the others around it. The effects of the strongly interacting system can be resolved by treating the excitation as a virtual quasiparticle with spin-1/2 and effective mass of $m = m_3^*$. The quasiparticles are therefore still fermions and obey Fermi-Dirac statistics (as long as the states are well defined, which they are at low temperature). The effective mass is related to the mass of a single ^{3}He atom by

$$m_3^* = m_3 \left(1 + \frac{1}{3} F_1 \right). \tag{2.11}$$

The accepted mass of a helium atom is $m_3 = 5.008 \times 10^{-27}$ kg and the Fermi parameter F_1 is dependent on the pressure, ranging from 5.31 at 0 bar and 14.21 at 33 bar [2]. One can rearrange (2.10) to find E_F, and using the relation $T_F = k_B E_F$ find the Fermi temperature of liquid ^{3}He as $T_F = 4.9$ K.

2.2.2 Properties of Normal Fluid ^{3}He

Several properties of normal fluid ^{3}He can be derived from the Landau Fermi-liquid behaviour. The heat capacity of a Fermi gas at temperatures below the Fermi temperature is

$$C_{V,\text{FG}} = \frac{\pi^2}{2} \frac{n}{E_\text{F}} k_\text{B}^2 T, \tag{2.12}$$

and the susceptibility of a Fermi gas is a constant

$$\chi_\text{FG} = I(I+1)\mu_0 \mu_n^2 g_n^2 \frac{2n}{3E_\text{F}}. \tag{2.13}$$

$I = \frac{1}{2}$ is the nuclear spin, μ_0 is the vacuum permeability, μ_n the nuclear magnetic moment and g_n the so-called g-factor.

Once the Fermi-liquid corrections are fully taken into account the heat capacity is [13]

$$C_V = \frac{m_3^*}{m_3} C_{V,\text{FG}} \tag{2.14}$$

and the susceptibility is [13]

$$\chi_\text{N} = \frac{m_3^*}{m_3} \left(\frac{1}{1 + 0.25 G_0} \right) \chi_\text{FG}. \tag{2.15}$$

G_0 is experimentally determined to be -2.8, indicating the nuclear spins of ^{3}He tend to orient parallel as in paramagnetism.

Finally of interest is the viscosity. The viscosity of a Fermi gas can be found from Boltzmann's kinetic theory of gas, where the gas molecules have a velocity v and mean free path λ, with the overall gas density ρ. The viscosity of such a system is [13]

$$\eta = \frac{1}{3} \rho v \lambda. \tag{2.16}$$

One can replace the velocity v with the Fermi velocity v_F at low temperatures, and also use the mean scattering time $\tau = \frac{\lambda}{v_\text{F}}$. The mean scattering time for a fermionic system is proportional to T^{-2} for $T << T_\text{F}$. Hence the viscosity is proportional T^{-2}. This is in good agreement with experimental measurements [21].

Finally we have all the relevant temperature dependencies for low temperature normal fluid ^{3}He: $C_V \propto T$, χ_N is constant and $\eta \propto T^{-2}$.

2.2.3 Superfluid Phases

The movement of a magnetically polarised quasiparticle causes the quasiparticle fluid around it to be induced with the opposite polarisation. The oppositely polarised field

then attracts another quasiparticle. This coupling mechanism between quasiparticles leads to the overall lowering of energy in the system and is similar to the Cooper pairing mechanism found in superconductors and described by Bardeen Cooper and Schreiffer (BCS) [22]. Unlike in standard BCS theory the magnetic interaction favours quasiparticles with parallel spin and therefore the total spin s of the pair equals 1 [23, 24]. To preserve antisymmetry with respect to exchange of identical particles, the total orbital angular moment $l = 1$ also. This leads to the creation of spin-triplet wave function of spin combinations: $\uparrow\uparrow$, $\frac{1}{\sqrt{2}}(\uparrow\downarrow + \uparrow\downarrow)$, and $\downarrow\downarrow$. On the z axis these result in three spin state projections $s_z = (-1, 0, 1)$ and three angular momentum state projections $l_z = (-1, 0, 1)$, leading to a total of nine different complex combinations. These Cooper pairs are quasi-bosonic and can therefore undergo condensation [2, 13].

As a condensate, superfluid ^{3}He can be described by a macroscopic wave function. Unlike that of the ^{4}He wave function (2.3) it must reflect the triplet state and therefore can be written as

$$|\Psi(\mathbf{k})\rangle = \psi_{\uparrow\uparrow}(\hat{\mathbf{k}})\,|\uparrow\uparrow\rangle + \psi_{\downarrow\downarrow}(\hat{\mathbf{k}})\,|\downarrow\downarrow\rangle + \frac{1}{\sqrt{2}}(\psi_{\uparrow\downarrow}(\hat{\mathbf{k}})\,|\uparrow\downarrow\rangle + \psi_{\downarrow\uparrow}(\hat{\mathbf{k}})\,|\downarrow\uparrow\rangle), \qquad (2.17)$$

where ψ_{xx} are amplitudes of the spin projections and $\mathbf{k}$ is the Cooper pair momentum vector ($\hat{\mathbf{k}}$ indicating a unit vector).

The Cooper pairs formed in the superfluid state are bosonic and can occupy the same state, allowing for condensation (otherwise superfluidity would not occur), which reduces the overall energy. Since the Cooper pairs' binding energy reduces the quasiparticle energy below E_F, the quasiparticle dispersion curve shifts as shown in Figure 2.4. This binding energy creates an energy gap Δ in the quasiparticle dispersion curve similar to that found in the superconductor. The energy required to break a Cooper pair is therefore 2Δ. The energy of the Cooper pairs is a function of the energy gap and $\mathbf{k}$

$$E = \sqrt{\zeta^2 + |\Delta(\mathbf{k})|^2} \qquad (2.18)$$

where ζ is the excess kinetic energy $\frac{p^2 - p_\mathrm{F}^2}{2m_3^*}$.

2.2.4 Bulk Superfluid Phases of Superfluid ^{3}He

Order Parameter and d-vector

The order parameter $A_{\mu j}$ describes many of the physical properties of a particular superfluid state. It describes the probability to form a Cooper pair depending on its position in space, orientation of its orbital angular momentum denoted by the unit vector $\hat{\mathbf{l}}$ and
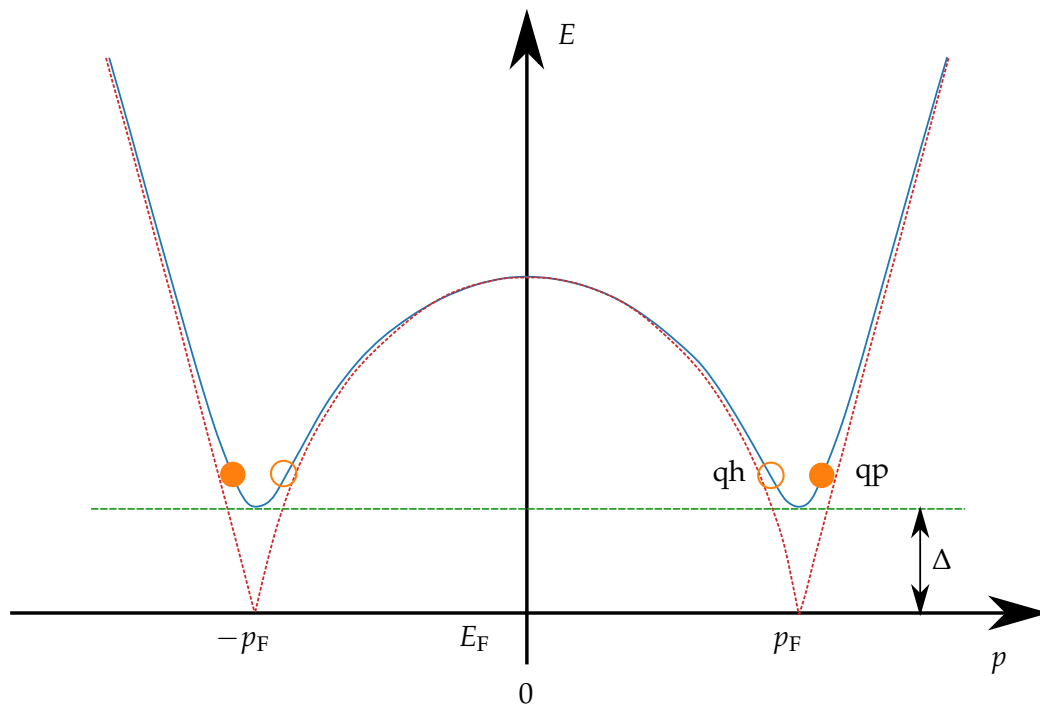
FIGURE 2.4: Quasiparticle (qp) and quasihole (qh) dispersion curve of superfluid ^{3}He when $\Delta \neq 0$ as is the case in ^{3}He-B, shown by the blue line. The red dashed line shows the dispersion curves of a Landau Fermi-liquid.
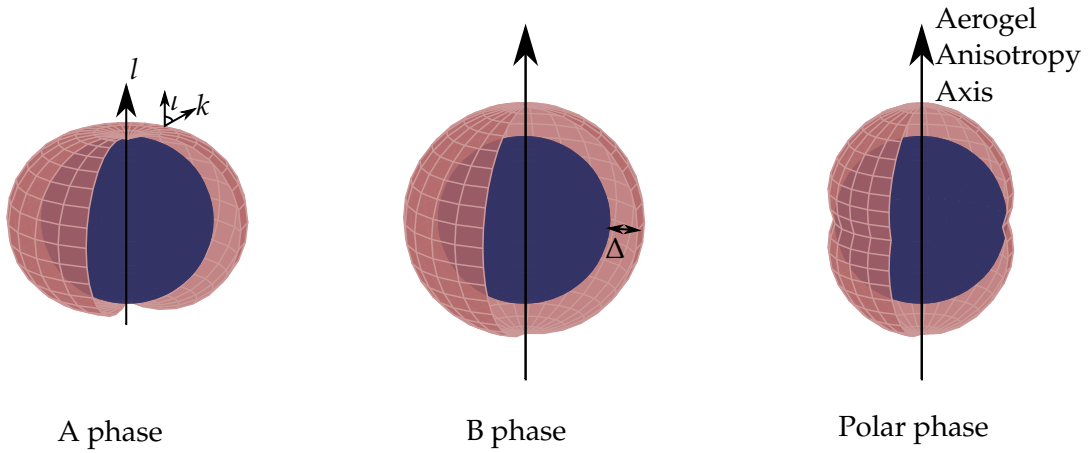
FIGURE 2.5: The energy gap around the Fermi surface of the various superfluid ^{3}He phases. The size of the energy gap is not to scale with the Fermi sphere.

orientation of its total spin. The μ and the j subscripts represent the spin and orbital momentum degrees of freedom, respectively. This probability is related to the gap energy.

It is common to use the unit vector $\hat{\mathbf{d}}$ to describe the spin state of the Cooper pair [2]. The physical meaning of $\hat{\mathbf{d}}$ vector is that it points in the direction of zero-total spin: $\mathbf{S} \cdot \mathbf{d} = 0$. Much of the properties of a superfluid ^{3}He phase can be described by the orientations of spin, orbital and Cooper pair momentum unit vectors, $\hat{\mathbf{d}}$, $\hat{\mathbf{l}}$ and $\hat{\mathbf{k}}$.

B Phase

The Balian-Werthamer-phase, BW-phase or B phase has a wave function with the same form as (2.17), with equal amplitudes and therefore equal populations of each type of Cooper pair. Since all states in the superfluid B phase are equally populous the state can be said to be isotropic. The general form of the order parameter is [2, 13]

$$A_{\mu j}^{\mathrm{B}} = \Delta_{\mathrm{B}} e^{i\Theta} R_{\mu j}(\hat{\mathbf{n}}_R, \iota).$$ (2.19)

$R_{\mu j}(\hat{\mathbf{n}}_R, \iota)$ are components of a rotation matrix $\mathbf{R}$ coupling spin and orbital angular momentum around an arbitrary axis $\hat{\mathbf{n}}_\mathbf{R}$ with an angle ι, shown to be 104° to minimise the dipole energy that arises from the dipole-dipole interaction of ^{3}He nuclei [25]. It follows from this that $\hat{\mathbf{d}}$ is parallel to $\hat{\mathbf{k}}$ and has no preferred direction, and that for the B phase the energy gap is also isotropic, shown in Fig. 2.5. The energy gap depends only on pressure, field and temperature. The energy gap at zero temperature, pressure and field in the weak coupling limit is

$$\Delta_B \left(T = 0 \right) = 1.76 k_B T_c. \tag{2.20}$$

The phase is represented by Θ, similar to the case of the ^{4}He wave function. The phase changes over distances larger than the coherence length [2]

$$\xi(T, P) = \frac{\xi_0(P)}{\sqrt{1 - \frac{T}{T_c}}}. \tag{2.21}$$

The value of ξ_0 ranges from 80 nm at 0 bar to 10 nm at 34 bar. At low temperatures and pressures it is roughy a constant $\xi(0, 0) \approx 80$ nm [26].

To break the Cooper pair and form quasiparticles, the states must be excited to an energy equal or above the energy gap. This is reflected in the changed dispersion curve shown in Fig. 2.4. The energy of the quasiparticles is now

$$E = \sqrt{\zeta^2 + |\Delta_B|^2} \tag{2.22}$$

Frictionless flow can occur with objects below a certain critical velocity known as the Landau velocity. At this velocity a dissipative process known as "pair-breaking" begins, in which normal ^{3}He quasiparticles are produced by the breaking of Cooper pairs. Hence the Landau velocity in ^{3}He is given by the dividing the energy required to break produce one quasiparticle with momentum equal to the Fermi momentum [6],

$$v_L = \frac{\Delta_B}{|\mathbf{p}_F|} \approx 27 \, \text{mm s}^{-1}. \tag{2.23}$$

In the low temperature limit (2.8) can be simplified to $f(E, T) = e^{-E/k_B T}$. The quasiparticle density number is given by $\int_{\Delta_B}^{\infty} g(E) f(E, T) \, dE$. In the low temperature limit only states near E_F are populated, hence the density of states $g(E) \approx g(E_F)$, which results in

$$N = g(E_F) k_B T \, e^{-\frac{\Delta_B}{k_B T}}. \tag{2.24}$$

The exponential temperature dependence means the density of quasiparticles is extremely small at low temperatures, giving rise to the so-called "ballistic regime" ($T \leq 0.3 T_c$). In this regime, the scattering length between quasiparticles becomes much larger than the dimensions of the cell (typically the smallest dimension is on the order of 1 cm). Quasiparticle-quasiparticle interactions can thus be neglected, and only interactions with surfaces in the cell are taken into account.

The relevance of (2.24) is apparent when calculating the heat capacity. The specific heat of the B phase is [13, 27]

$$C_B = \sqrt{2\pi} \, g(E_F) k_B \Delta_B \left(\frac{\Delta_B}{k_B T} \right)^{\frac{3}{2}} e^{-\frac{\Delta_B}{k_B T}}. \tag{2.25}$$

The magnetic susceptibility of the B phase is lower than that of both the A phase and normal phase, as the presence of $\frac{1}{\sqrt{2}}\left(\uparrow\downarrow + \uparrow\downarrow\right)$ pairs which have no *z*-projection of the spin ($s_z = 0$) reduces the overall magnetisation. At high magnetic fields, however, the relative population of these pairs becomes smaller. The gap is then distorted, from the spherically symmetric shape to an ovoid. This phase is sometimes known as B$_2$ phase but is simply referred to as the B phase in this work.

A Phase

The Anderson-Brinkman-Morell (ABM) or A phase has no pairs with spin compnent ($\mathbf{S} = 0$) and the wave function is [13]

$$|\Psi(\mathbf{k})\rangle = \psi_{\uparrow\uparrow}(\hat{\mathbf{k}})|\uparrow\uparrow\rangle + \psi_{\downarrow\downarrow}(\hat{\mathbf{k}})|\downarrow\downarrow\rangle. \tag{2.26}$$

The phase exists only at high temperatures and pressures in zero magnetic field but is much more apparent at higher magnetic fields. The order parameter for the A phase is [2, 13]

$$A_{\mu j}^{\mathrm{A}} = \Delta_{\mathrm{A}} e^{i\Theta} \mathbf{d}_{\mu} (\hat{\mathbf{m}}_j + i\hat{\mathbf{n}}_j), \tag{2.27}$$

where $\hat{\mathbf{m}}$ and $\hat{\mathbf{n}}$ are mutually orthogonal unit vectors in orbital space. These two unit vectors define the preferred direction in orbital space $\hat{\mathbf{l}}$ such that $\hat{\mathbf{l}} = \hat{\mathbf{m}} \times \hat{\mathbf{n}}$. The absolute value of the order parameter in ^{3}He is proportional to the energy gap. The gap parameter for the A phase Δ_{A} is dependent on the direction of quasiparticles' momentum and orbital angular momentum

$$\Delta_{\mathrm{A}} = \Delta(T)\sqrt{\frac{3}{2}}\sin\left(\hat{\mathbf{k}}\hat{\mathbf{l}}\right) \tag{2.28}$$

with $\Delta(T = 0) = 2.029 k_{\mathrm{B}} T_{\mathrm{c}}$. This results in a strongly anisotropic gap with nodes along $\hat{\mathbf{l}}$ where the gap is zero and superfluidity does not exist, illustrated in Fig. 2.5. Near T_{c}, the maximum energy gap can be written as

$$\Delta_{\mathrm{A}} \approx 3.42 k_{\mathrm{B}} T_{\mathrm{c}} \sqrt{1 - \frac{T}{T_C}}. \tag{2.29}$$

A consequence of the nodal points is that moving objects can always break pairs and therefore feel friction. ^{3}He-A can still be said to be superfluid as mass flow can take part without dissipation but moving objects will always experience a viscous force.

The magnetic susceptibility of the A phase depends strongly on the orientation of the magnetic field $\mathbf{B}$ to the vector $\hat{\mathbf{d}}$. When $\mathbf{B} \perp \hat{\mathbf{d}}$ the magnetic susceptibility equals the normal phase susceptibility given by (2.15).
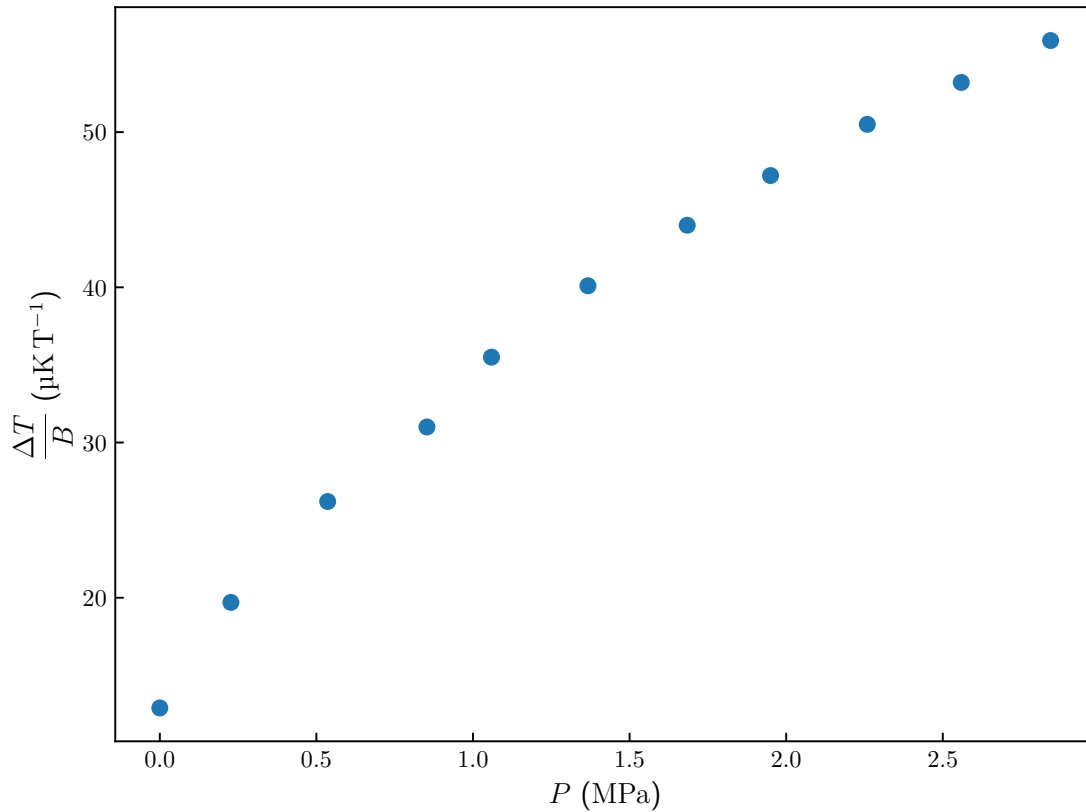
FIGURE 2.6: The temperature width of the A_1 phase per unit magnetic field as a function of pressure [12].

In a high magnetic field this phase also distorts, with different amplitudes of $\uparrow\uparrow$ and $\downarrow\downarrow$ pairs corresponding to a smaller relative population of the $\downarrow\downarrow$ pairs. The phase has similar properties as the pure A phase and as such will also be referred to as the A phase but is also known as the A_2 phase.

A_1 Phase

The A_1 phase only exists at high temperatures, pressures and in a magnetic field. It is characterised by having only one of the possible spin states, the $|\uparrow\uparrow\rangle$ state. Thus, the wave function is [2, 13]

$$|\Psi(\mathbf{k})\rangle = \psi_{\uparrow\uparrow}(\hat{\mathbf{k}})\,|\uparrow\uparrow\rangle\,. \tag{2.30}$$

The width of the A_1 phase is a function of pressure and is directly proportional to magnetic field. Fig. 2.6 shows the temperature width of the A_1 phase in units of $\mu\mathrm{K\,T}^{-1}$ as a function of pressure.

Textures

The alignment of the direction of the orbital angular momentum **l** over space is known as the "texture" in ^{3}He [2].

In ^{3}He-A the minimisation of the dipole-dipole interaction prefers the $\hat{\mathbf{d}}$ vector and orbital angular momentum $\hat{\mathbf{l}}$ to be parallel or anti-parallel. In addition to the dipole-dipole interaction, there are several other interactions that induce textural changes, such as the interaction with a magnetic field, walls, bending energy and the counterflow energy. In the A phase, there is a fixed condition that near a surface the superfluid must orient $\hat{\mathbf{l}}$ perpendicular to the surface.

Of particular interest to this work are the magnetic healing length and the orientation of $\hat{\mathbf{l}}$ by the superflow $\mathbf{v}_\mathrm{s}$ of ^{3}He-A. In a magnetic field, the free energy is lower when $\hat{\mathbf{d}} \perp \mathbf{B}$. The magnetic healing length in the A phase is [2]

$$\zeta^\mathrm{A}_\mathrm{mag} = \frac{B_\mathrm{A}}{B} \zeta_0 \tag{2.31}$$

with B_A an empirical constant. At fields about $10\,\mathrm{mT}$, the healing length is about $10^2 \zeta$, on the order of $1\,\mathrm{\mu m}$. The healing length can be used to find the field needed to overcome the dipole interaction by substituting $\zeta^\mathrm{A}_\mathrm{mag}$ with the dipole healing length, which in the Ginzburg-Landau regime is [2]

$$\zeta^\mathrm{A}_\mathrm{di} = \frac{1}{2} \sqrt{\lambda_\mathrm{di}} \cdot \zeta_0. \tag{2.32}$$

Here, $\lambda_\mathrm{di} \approx 5 \times 10^{-7}$ is a dimensionless parameter describing dipole coupling between atoms in ^{3}He [2]. The required magnetic field is typically on the order of a few milliteslas.

Superflow tends to orient as $\mathbf{v}_\mathrm{s} \parallel \hat{\mathbf{l}}$ with the change in energy per unit volume given by [13]

$$\frac{\Delta E_\mathrm{sf}}{V} = \frac{1}{2} \left(\rho_{\mathrm{s}\parallel} - \rho_{\mathrm{s}\perp} \right) (\hat{\mathbf{l}} \cdot \mathbf{v}_\mathrm{s}) \approx -10\,\mathrm{J\,m^{-3}} \times \left(1 - \frac{T}{T_\mathrm{c}} \right), \tag{2.33}$$

where the anisotropic superfluid density in the A phase is written as the components perpendicular and parallel to $\hat{\mathbf{l}}$, $\rho_{\mathrm{s}\perp}$ and $\rho_{\mathrm{s}\parallel}$ [2].

2.3 ^{3}He in Aerogels

There are some ways to drastically alter the relative stability of the potential phases of superfluid ^{3}He. One typical way is to confine the superfluid in extremely small slab geometries, creating a quasi 2D superfluid [28, 29]. The other is to introduce some impurities into the system such as aerogel. Aerogels consist of extremely small diameter particles
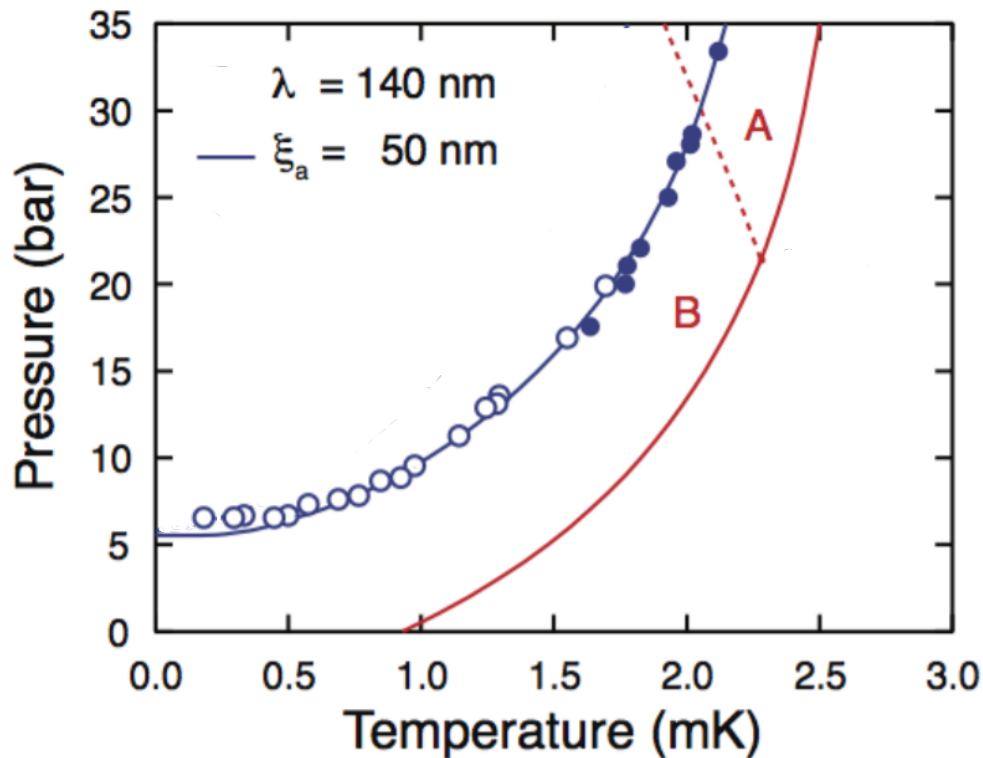
FIGURE 2.7: Pressure-temperature phase diagram of superfluid ^{3}He in an aerogel (blue) compared with the bulk phase diagram (red lines). Open circles indicate data from Cornell University [32] and closed circles indicate data from Northwestern University [33, 34]. The blue line is a theoretical fit with the mean free path for quasiparticle λ and silica particle-particle correlation length ξ_a. Figure taken from [30].

melded together into strands (typically on the order of 1–10 nm with an order of magnitude larger mean distance between strands (typically on the order of 100 nm [30]. Aerogels are thus typically extremely light and porous materials, usually with porosity above 95%. The aerogel strands can be arranged in a random or preferred direction. When arranged with a preferred direction, the aerogel is said to be anisotropic. The measure of anisotropy is typically to compare the mean free path between strands in a parallel and perpendicular direction. An aerogel that has all strands arranged almost completely parallel to each other is referred to as a "nematic" aerogel [7, 31]. Nafen is an example of a nematic aerogel.

2.3.1 Superfluid Transition Suppression

One of the primary effects on superfluidity of immersing an aerogel in liquid ^{3}He is a reduction in the superfluid transition temperatures [32–36]. Fig. 2.7 shows the pressure-temperature phase diagram of superfluid ^{3}He in a 98% porous silica aerogel at zero field. Furthermore, a reduced NMR frequency shift and a reduced superfluid fraction as compared with bulk ^{3}He for the same pressure has been found in these silica aerogel samples [30].

The superfluid suppression and the changed phase diagram of the superfluid effects of an aerogel strongly depends on the properties of the aerogel. Similarly, the properties of each phase can be changed by the aerogel.

To introduce anisotropy into an aerogel it is common to "stretch" the aerogel or compress it with strain. The introduction of a stretching anisotropy into an aerogel increased the stability of the A phase compared to the B phase at high pressures. The angular momentum $\hat{\mathbf{l}}$ can orient either perpendicular or parallel to the strain axis. The direction $\hat{\mathbf{l}}$ appears to prefer an orientation along the direction of the anisotropy. At higher temperatures, NMR experiments have shown that the A phase is stabilised with $\hat{\mathbf{l}}$ parallel to the strain axis but suddenly reorients to be perpendicular after crossing a lower temperature transition [30].

2.3.2 Phases in Nematic Aerogels

Polar Phase and Polar Distorted Phases

Recently, a phase not energetically favourable in bulk superfluid called the polar phase was stabilised in the nematic aerogel nafen by Dmitriev *et al.* [7]. In a low density (90 mg · cm^{-3}) sample they found three phases: the polar distorted B (PdB) phase, the polar distorted A (PdA) phase and the polar (P) phase. In high density nafen (243 mg · cm^{-3}) only the polar phase has been found. Fig. 2.8 shows the currently known *P-T* phase diagrams for superfluid ^{3}He in these nafen samples, known as nafen-90 and nafen-243 for their respective densities. In addition to immersing the nafen samples, the experimental cell and nafen samples had to be pre-plated with about 2.5 layers of solid ^{4}He for the phases to be stabilised. The solid ^{4}He plating increases the specularity of quasiparticle scattering conditions on the aerogel strands surface. Without first pre-plating the aerogel surface with approximately 2.5 monolayers of ^{4}He, the polar phase is not stabilised [31]. The formation of the polar and polar distorted phases is due to to the strong orientation of orbital momentum perpendicular to the walls of the strands, and therefore $\hat{\mathbf{m}}$ in the anisotropy direction.

The order parameter of the polar phase and polar distorted A phase is similar to the A phase order parameter in (2.27). The aerogel anisotropy forces the unit vector $\hat{\mathbf{m}}$ to be
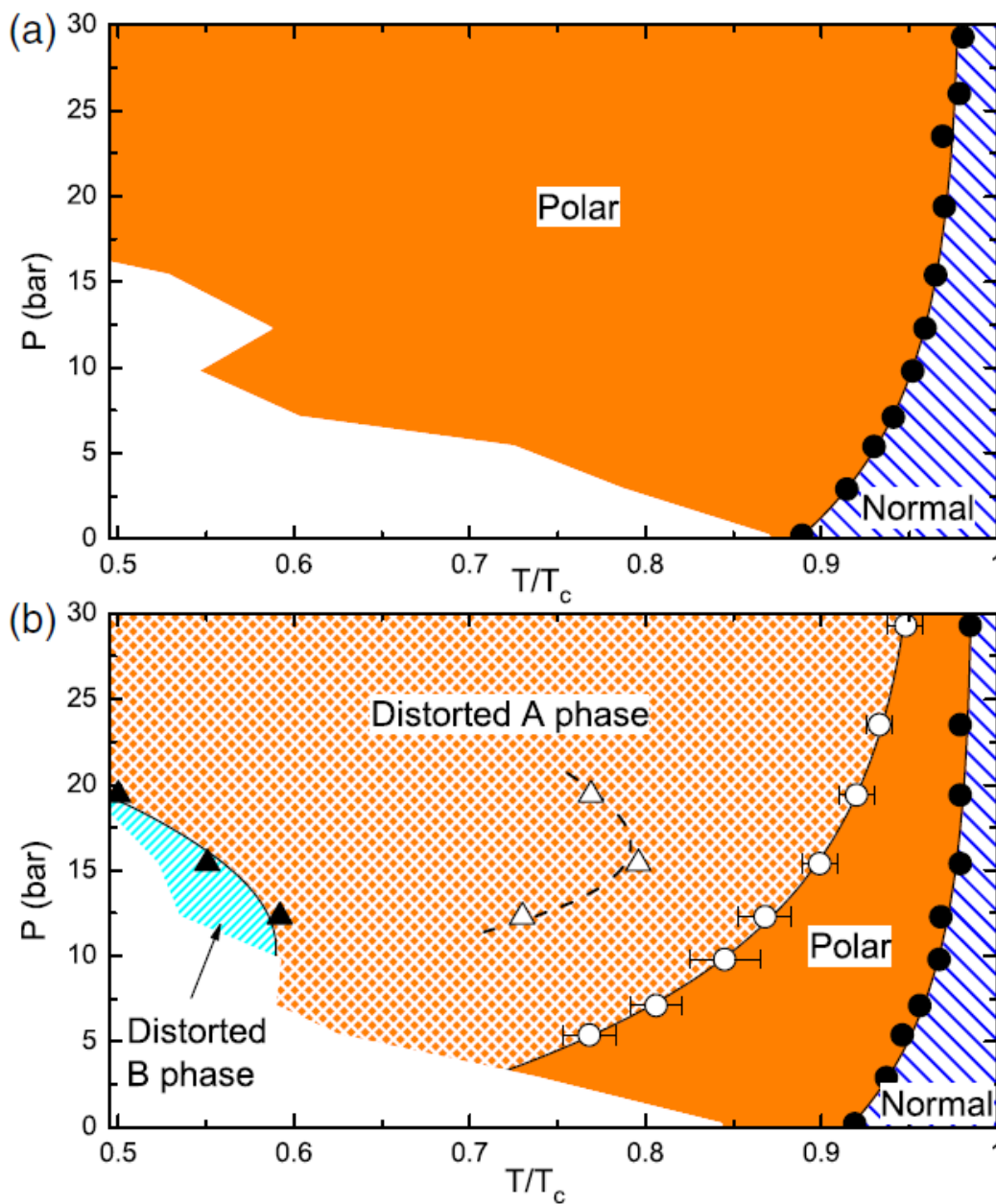
FIGURE 2.8: Phase diagrams of superfluid ^{3}He in the nematic aerogels (a) nafen-243 and (b) nafen-90 at low magnetic fields of $10\,\mathrm{mT}$–$37\,\mathrm{mT}$. In nafen-243 (a) only the polar phase is stabilised whilst in nafen-90 polar distorted A and B phases are apparent. Similar to silica aerogels, there is a suppression of T_c and the (polar-distorted) A phase is favoured at lower temperatures and pressures compared to bulk. Image taken from [7].

aligned with the axis of aerogel anisotropy. We can write the order parameter for all three in the general form

$$A_{\mu j}^{\mathrm{P}} = \Delta_{\mathrm{P}} e^{i\Theta} \hat{\mathbf{d}}_\mu (a\hat{\mathbf{m}}_j + ib\hat{\mathbf{n}}_j).$$

(2.34)

The constants a and b are constrained such that $a^2 + b^2 = 1$. For the A phase proper, $a = b$; for the polar distorted A phase $a^2 > b^2 > 0$; for the polar phase $a = 1$ and $b = 0$. All three phases are referred to as Equal Spin Pairing phases (ESP). The polar distorted A phase is still chiral as with the A phase with zero energy gap nodal points at $\pm \hat{\mathbf{l}}$. The polar phase is not chiral, however, and has zero energy gap along the entire plane normal to $\hat{\mathbf{m}}$ as shown in Fig. 2.5.

Beta Phase

The β phase is similar to the A_1 phase in that it consists of only the spin up Cooper pairs. The order parameter is given by [30, 31]

$$A_{uj}^{\beta} = \left(\frac{\Delta_1}{\sqrt{2}}(d_\mu + e_\mu) + \frac{\Delta_2}{\sqrt{2}}(d_\mu - e_\mu) \right) \hat{\mathbf{m}},$$

(2.35)

where $\hat{\mathbf{e}}$ is a unit vector in spin space perpendicular to $\hat{\mathbf{d}}$, $\Delta_{1,2}$ are the gap parameters and $\hat{\mathbf{m}}$ is again aligned with the anisotropy direction of the nafen strands. When $\Delta_2 = 0$ the state is purely the β phase, and when $\Delta_1 > \Delta_2 > 0$ the phase is distorted as there is a relatively smaller population of $\downarrow\downarrow$ Cooper pairs compared to $\uparrow\uparrow$ pairs, similar to the A_2 phase. This phase can be known as the P_2 phase. Through this work we will use the term polar phase to distinguish it from the pure β phase. When $\Delta_1 = \Delta_2$ the phase becomes the pure polar phase in (2.34).

The β phase shares many similar properties as the A_1 phase. It only exists in magnetic fields, and the temperature range of its existence increases as pressure and field increases. Surovtsev calculated a phase diagram for a nematic aerogel in high magnetic field shown in Fig. 2.9 [9]. One can expect the dependence on the temperature width of the β phase to have a very similar dependence on field and pressure as the A_1 phase given in Fig. 2.6. The temperature width of the pure β phase is linearly dependent on the magnetic field and is given by

$$\frac{\Delta T_\beta}{T_{\mathrm{ca}}} \approx 2\eta_a B$$

(2.36)

where T_{ca} is the superfluid transition in aerogel which we can take from Fig. 2.8 [7] and $\eta_a = 0.02\,\mathrm{T}^{-1}$ in silica aerogel [9]. For nafen-90 a $B = 0.5\,\mathrm{T}$ and $P = 0\,\mathrm{bar}$ this creates a splitting $\Delta T_\beta \approx 8\,\mu\mathrm{K}$, similar to the value from Fig. 2.6. Evidence for this phase following
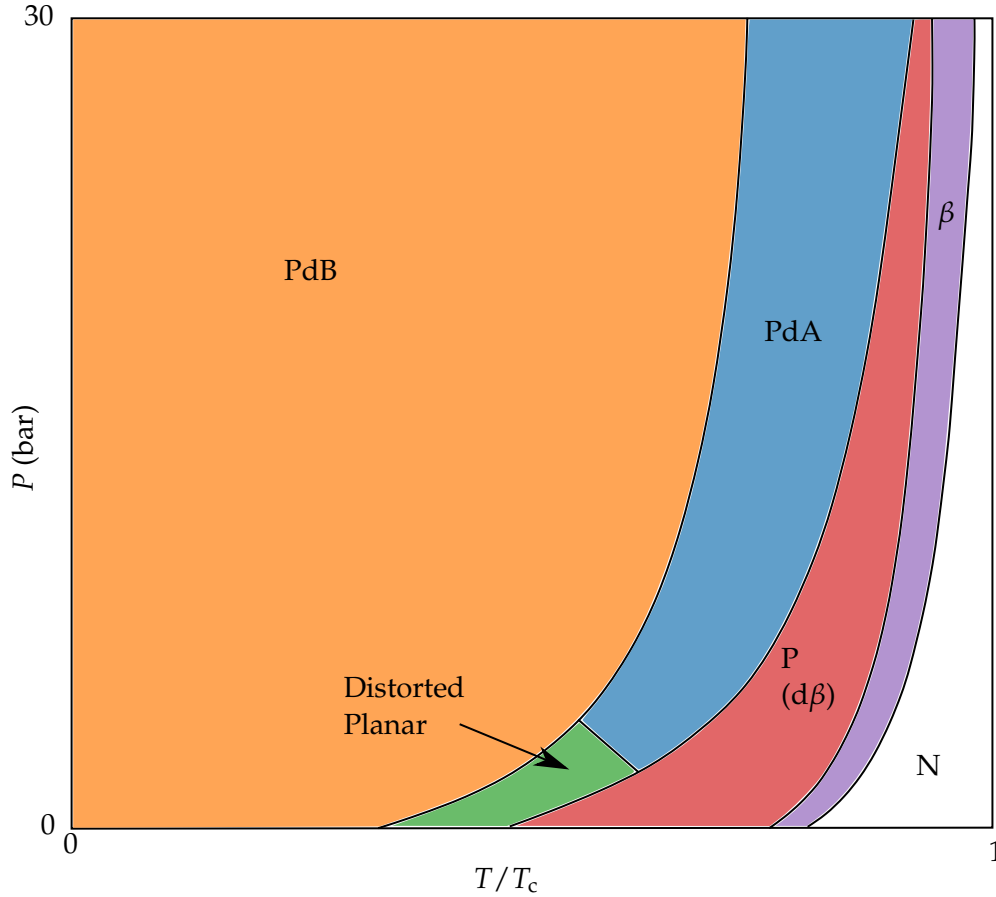
FIGURE 2.9: The pressure-temperature phase diagram of superfluid ^{3}He in nematic aerogel (nafen-90) at high magnetic field. "P" refers to polar phase P_2 when $\Delta_1 > \Delta_2 > 0$ in (2.35). Similarly, "β" is just the pure β phase where $\Delta_2 = 0$. "PdA" and "PdB" refer to polar-distorted A and B phases respectively. Image adapted from [9], where details of the calculations and about planar phase can be found.

this theoretical prediction has recently been found by Dmitriev *et al.*, using a vibrating wire with a nematic aerogel attached [11].

Furthermore, Surovtsev calculated several thermodynamic properties that can be used to identify the phase transitions [37]. The superfluid fraction depends on the direction of superflow, whether it is normal to the aerogel anisotropy axis ($\rho_{s\perp}$) or parallel ($\rho_{s\parallel}$). Fig. 2.10 shows the superfluid density for an orientation where the direction of motion for a moving aerogel sample is parallel to the direction of anisotropy. The β phase transition is more easily detectable by measuring the superfluid fraction in the case where superflow is parallel to the anisotropy.

Surovtsev also predicts a temperature dependent critical velocity [37]. In the aerogel state, the order parameter is degenerate over up-up and down-down pairs only for
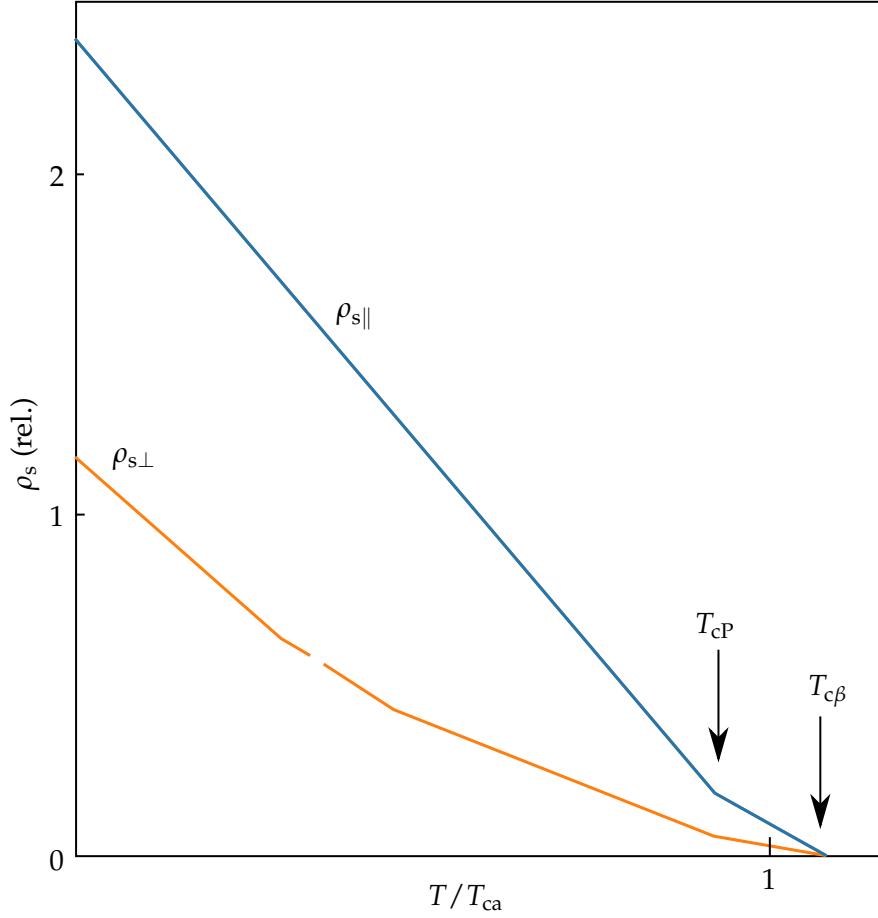
FIGURE 2.10: The calculated superfluid fraction for superflow in a directions parallel ($\rho_{\mathrm{s}\|}$) and perpendicular to ($\rho_{\mathrm{s}\perp}$) the aerogel anisotropy direction in the weak coupling limit. The superflow velocity is $v_s < v_d$. Image adapted from [37].

superflows with higher energy than the dipole energy. In the discussion of textures, we saw the minimisation of the dipole energy gives a preferred direction, which lifts the degeneracy. When the superfluid velocity is degenerate, the superfluid velocities of up-up and down-down pairs ($v_{\mathrm{s}}^{\uparrow}$ and $v_{\mathrm{s}}^{\downarrow}$) are independent. When the dipole energy is dominant, $v_{\mathrm{s}}^{\uparrow} = v_{\mathrm{s}}^{\downarrow}$ and the total superfluid density can be calculated. We can estimate this critical velocity by comparing the superfluid velocity to the dipole length:

$$v_{\mathrm{d}} > \frac{\hbar}{\xi_{\mathrm{di}} m_3} \sqrt{|\frac{\Delta_1}{\Delta_2}|} \approx 1\,\mathrm{mm\,s}^{-1}. \tag{2.37}$$

The approximate value of $1\,\mathrm{mm\,s}^{-1}$ comes from the dipole length $\xi_{\mathrm{di}} = 10\,\mu\mathrm{m}$ and the case where $\Delta_1 \sim \Delta_2$, far from the β transition [37]. At higher temperatures, it should be on the order of v_{L}.

2.4 Nuclear Magnetic Resonance

A ^{3}He nucleus possesses a magnetic moment and an angular momentum. Therefore, a common technique used to study superfluid ^{3}He is Nuclear Magnetic Resonance, more commonly known as NMR. When a ^{3}He nucleus is placed in an external magnetic field, the spin of the nucleus begins to precess around the magnetic field at a frequency known as the Larmor frequency [38]

$$f_L = \frac{\omega_L}{2\pi} = -\frac{\gamma_3}{2\pi} B_{ext} \tag{2.38}$$

determined by the external field and the gyromagnetic ratio γ_3. The sign of the gyromagnetic ratio indicates the direction of the precession. For ^{3}He

$$\frac{\gamma_3}{2\pi} = 32.434 \, \text{MHz} \, \text{T}^{-1} \tag{2.39}$$

For a general particle with spin and therefore a magnetic moment, the angle between the direction of the external field and the spin is a constant depending on the initial spin polarisation.

One can then perturb the precession of the spins by applying a second, weaker oscillating magnetic field that is orientated transverse to the constant main external field. The energy may be absorbed when the frequency of this signal is equal to Larmor frequency. In continuous wave NMR, this magnetic resonance seen around the Larmor frequency is Lorentzian-like [38]. The two components, absorption and dispersion, are defined by

$$\text{Absorption} = \frac{\chi}{2} \frac{\frac{1}{T_2}}{\frac{1}{T_2^2} + (\omega - \omega_L)^2}, \tag{2.40}$$

$$\text{Dispersion} = \frac{\chi}{2} \frac{(\omega - \omega_L)}{\frac{1}{T_2^2} + (\omega - \omega_L)^2}. \tag{2.41}$$

T_2 is the rate of decay of the transverse magnetisation. The integral of the absorption component can be used to measure the magnetic susceptibility χ whilst the width of the line shape is limited by T_2 such that $\Delta\omega = 2T_2$.

Continuous Wave NMR in superfluid ^{3}He

NMR is a powerful tool for investigating superfluid ^{3}He. Indeed, superfluidity in ^{3}He was first discovered experimentally using NMR. As ^{3}He enters from the normal phase into the A phase the NMR signal shifts from the Lorentzian frequency whilst retaining the same amplitude. Going from the A phase to the B phase the NMR signal suddenly returns to ω_L and the amplitude begins decreasing due to the lower magnetisation of the B phase.
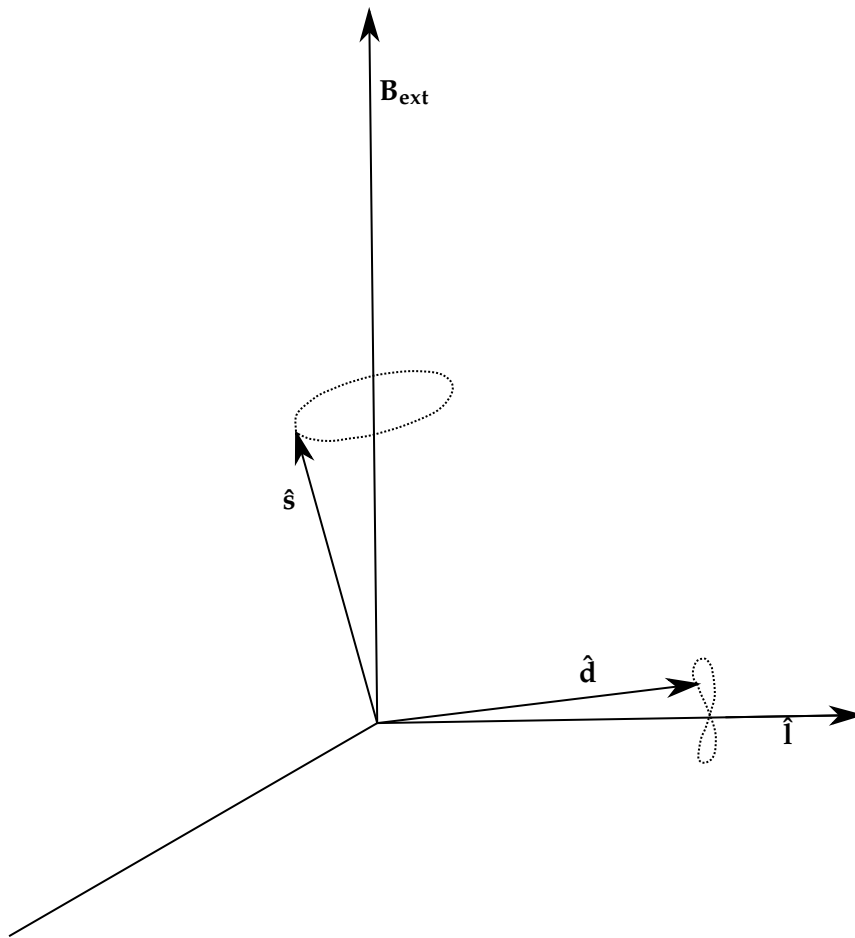
FIGURE 2.11: The precession of a spin in superfluid ^{3}He about an external magnetic field $\mathbf{B_{ext}}$ after a small RF pulse. $\hat{\mathbf{d}}$ is initially parallel to $\hat{\mathbf{l}}$ and perpendicular to the spin $\hat{\mathbf{s}}$. However, after the pulse the spin begins precessing at the Larmor frequency about $\mathbf{B_{ext}} = B\hat{\mathbf{z}}$, meaning $\hat{\mathbf{d}}$ precesses around $\hat{\mathbf{l}}$ at double the frequency in a figure-of-eight motion. This creates an additional "torque" that shifts the spin precession frequency away from the Larmor frequency.

The physical origin of the frequency shift is the dipole-dipole interaction. In superfluid ^{3}He-A the macroscopic dipole interaction causes the orbital momentum and $\hat{\mathbf{d}}$ to be parallel to each other. Furthermore, $\hat{\mathbf{l}}$ must be perpendicular to the external magnetic field $\mathbf{B_{ext}} = B_0\hat{\mathbf{z}}$. However, as $\hat{\mathbf{d}}$ is also perpendicular to the spin $\mathbf{s}$, when the oscillating RF field is applied and the spins begin precession the $\hat{\mathbf{d}}$ vector must also precess, creating an extra "torque" force (see Fig. 2.11). This torque increases the resonant frequency.

Using this idea, Legett derived the equations of motion for the spin system in superfluid ^{3}He [25]. The frequency of the NMR signal in the A phase (when the vectors $\hat{\mathbf{l}}$ and $\hat{\mathbf{d}}$ are "locked") is given by [39]

$$\omega_A^2 = \omega_L^2 + \Omega_A(T)^2, \tag{2.42}$$

where Ω_A is the longitudinal NMR resonance frequency. In the B phase a slightly more complicated picture arises. It depends on the local angle ϕ between the $\hat{\mathbf{n}}_R$ in (2.19) and the magnetic field. The frequency shift is then [39]

$$\omega_B \approx \omega_L + \frac{\Omega_B(T)^2}{2\omega_L} sin^2(\phi) \tag{2.43}$$

Again, Ω_B indicates the longitudinal NMR resonant frequency. Since ϕ depends on the local texture, when there is no dominant texture the B phase NMR peak can be seen as a sum of independent oscillator peaks. Since the magnetisation of ^{3}He-B is smaller than in the normal and A phases, according to (2.40) and (2.41) the peak will be smaller. The ratio of the frequency shifts is defined by [39]

$$\frac{\Omega_B^2}{\Omega_A^2} = \frac{5}{2}\frac{\chi_B}{\chi_A} \tag{2.44}$$

In the polar phase, the NMR frequency shift depends on the angle μ between the external magnetic field B and the aerogel anisotropy direction [7, 8, 39]

$$\omega_P \approx \omega_L + \frac{\Omega_P(T)^2}{2\omega_L}\cos^2(\mu). \tag{2.45}$$

NMR can be further used to probe defects such as quantum vortices or domain walls, as the local texture depends on the defects. One type of defect present in the polar phase but as yet unfound in the bulk phases are Half-Quantum Vortices (HQVs). Above a magnetic field of 3 mT, the magnetic energy is larger than the dipole energy. To minimise the magnetic energy, $\hat{\mathbf{d}}$ becomes orientated perpendicular to the field, as it does with the A phase. The unit vector $\hat{\mathbf{d}}$ can be orientated in any direction in the plane perpendicular to $\mathbf{B}$. The direction of $\hat{\mathbf{d}}$ in the plane can be described by an angle ν. When considering an ordinary single quantum vortex, for the wave function to be single valued the phase had to change by an integer multiple of 2π. In a HQV the phase changes only by π, but the spin angle ν also changes by π for the order parameter to remain single-valued [8]. HQVs therefore only carry a half quantum of mass circulation.

HQVs can be detected by a secondary satellite NMR peak with a negative frequency shift away from the main peak, shown in Fig. 2.12 [8]. The magnitude of the frequency of the satellite peak is

$$\omega_{\text{sat}} \approx \omega_L + \frac{\Omega_P(T)^2}{2\omega_L}\left(\cos^2(\mu) - \Lambda\sin^2(\mu)\right) \tag{2.46}$$

where $\Lambda \leq 1$.
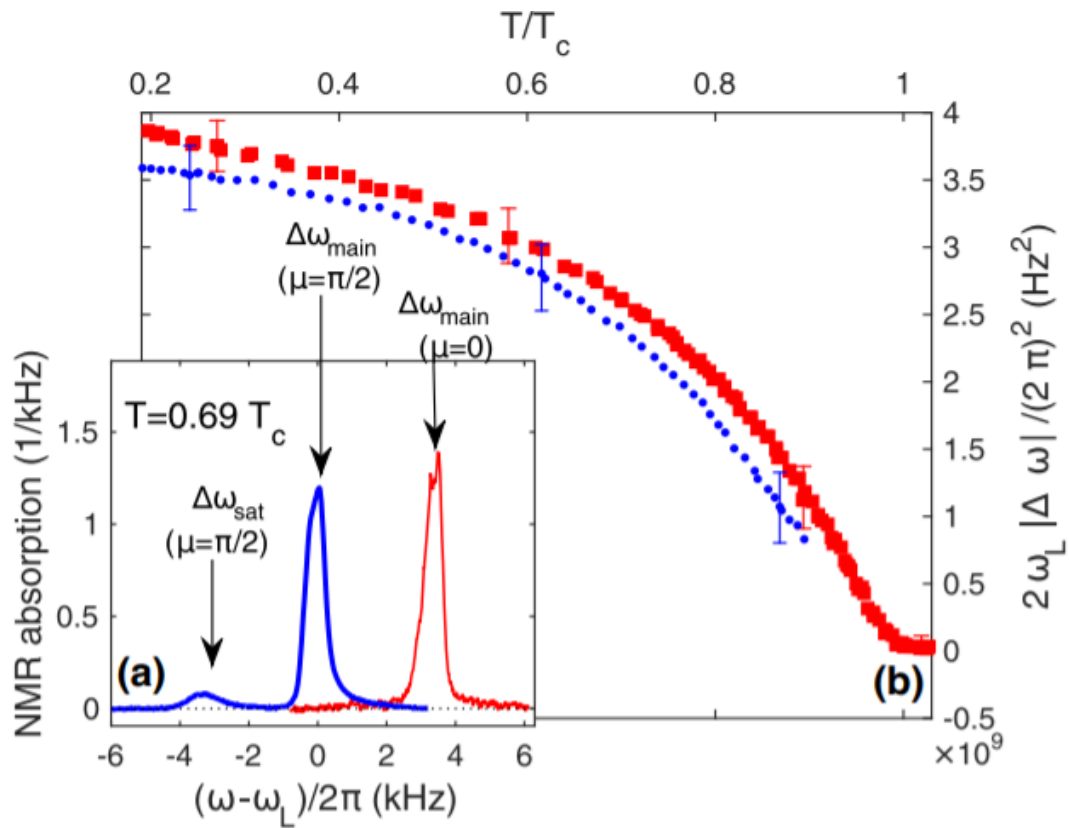
FIGURE 2.12: Observation of HQVs by continuous wave NMR with an external field of 12 mT. The aerogel sample used was nafen-243 with the superfluid pressurised to 7.1 bar. (a) Typical NMR sweeps at a given temperature for two different orientations of the angle μ. Here, the satellite peak corresponding to HQVs can be seen. (b) The temperature dependence of the magnitude of the frequency shifts. $\Delta\omega = \omega - \omega_L$. Figure taken from [8].

Chapter 3

Resonators

Probing a superfluid at extremely low temperatures provides a large challenge. The superfluid has weak mechanical interactions that only get weaker as the superfluid fraction increases. Probing a superfluid requires very sensitive devices that will still work at low temperatures. Additionally, helium is not a charged material, which makes using electronic techniques difficult.

However, there are some properties of liquid helium superfluids one can take advantage of that cannot easily be taken advantage of in cold atomic gas condensates or at all in the case of superconductors. NMR is one such tool [8, 40]; as are electron bubbles [41, 42] or frozen tracer particles [43–45] that can be injected into the liquid; and a container with a desired geometry can easily manipulate the superfluid. Work using confined geometry and thin films of fluids on surfaces to probe 2-D superfluidity is very common [46–48]. More recently, superfluid ^{3}He has been confined in extremely thin slabs with an observed change in order [28, 29]. Furthermore, these containers and geometries themselves can be manipulated to induce flows in the superfluid. Rotating cryostats [8, 49] are used to investigate quantum vorticity and more.

Most obviously, though, macroscopic objects can be immersed within liquid helium directly. Torsional oscillators [35, 50], vibrating wires [51, 52], vibrating grids [53], tuning forks [54–56], microplates [57, 58] and more have been used. Experiments at Lancaster in both superfluids ^{3}He and ^{4}He commonly use the effects of the superfluid on resonant modes of mechanical oscillators. Smaller mechanical oscillator devices have high mass and momentum sensitivity that are sensitive to superfluids and their excitations even at low temperatures where the normal fluid fraction is close to zero [59, 60]. Operation at ultra-low temperatures necessarily imposes restrictions on the parameters and construction of the oscillators: they must generate minimal amount of heat when operating. Typically, much less than a nanowatt. In this chapter, we describe such vibrating devices and the properties of resonance we exploit to probe superfluid ^{3}He.

3.1 Mechanical Oscillator Basics

3.1.1 Damped Driven Oscillator

The response of a damped, driven resonant mode of a three-dimensional mechanical oscillator can be modelled using the one-dimensional mass-spring approximation [54]. The equation of motion for a damped and periodically driven mass-spring system is

$$m\ddot{x} + \gamma\dot{x} + k_{\mathrm{e}}x = F_{\mathrm{drive}}e^{i\omega t}. \tag{3.1}$$

Here x is the displacement, γ is the damping, k_{e} is the effective spring constant, F_{drive} is the driving force, m is the (effective) mass, ω is the angular frequency of the periodic driving force, t is the time and the dot notation is used to show derivatives with respect to time. The natural angular resonant frequency of the oscillator is

$$\omega_0 = 2\pi f_0 = \sqrt{\frac{k_{\mathrm{e}}}{m}}. \tag{3.2}$$

f_0 is the natural resonant frequency. A steady state solution for equation (3.1) takes the form $x = x_0 e^{i(wt-\varphi)}$ where x_0 is a constant and φ is the phase. Substituting in this solution and rearranging for x_0 gives

$$x_0 e^{-i\varphi} = \frac{F_{\mathrm{drive}}}{m\omega_0^2 - m\omega^2 + i\gamma\omega}, \tag{3.3}$$

and for velocity

$$\dot{x}_0 e^{-i\varphi} = i\omega x_0 e^{-i\varphi} = \frac{i\omega F_{\mathrm{drive}}}{m\omega_0^2 - m\omega^2 + i\gamma\omega}. \tag{3.4}$$

Taking real and imaginary components of the velocity, we obtain

$$\Re(\dot{x}_0 e^{-i\varphi}) = \omega F_{\mathrm{drive}}\frac{\gamma\omega}{(m\omega_0^2 - m\omega^2)^2 + \gamma^2\omega^2}; \tag{3.5}$$

$$\Im(\dot{x}_0 e^{-i\varphi}) = \omega F_{\mathrm{drive}}\frac{m\omega_0^2 - m\omega^2}{(m\omega_0^2 - m\omega^2)^2 + \gamma^2\omega^2}. \tag{3.6}$$

The real and imaginary components are known as the absorption and dispersion components, respectively. The maximum velocity occurs at the frequency which fulfils the condition

$$m\omega = \sqrt{m^2\omega_0^2 - \frac{\gamma^2}{4}}. \tag{3.7}$$

For small damping ($\gamma \ll \omega_0$), this occurs at the natural resonance frequency, $\omega = \omega_0$. For $\gamma > 2\omega_0$, resonance does not occur and there is no maximum (see section 3.1.1). The maximum value for small damping is then

$$\frac{F_{\text{drive}}}{\gamma} = v_{\text{max}}. \tag{3.8}$$

In the small damping limit, the imaginary component has extrema corresponding to the two solutions of $\omega\gamma + m\omega_n^2 - m\omega^2 = 0$. These minima in the imaginary component occur when the real component is at half its maximum value. An example response is given in Fig. 3.1. The difference between the two extrema gives the width of the resonance. In the small damping limit this results in

$$\Delta\omega = 2\pi\Delta f = \frac{\gamma}{m}, \tag{3.9}$$

hence the width is directly related to the damping. The phase can also be found using identities as

$$\varphi = \arctan\left(\frac{\gamma\omega}{m\omega_0^2 - m\omega^2}\right). \tag{3.10}$$

At resonance the denominator equals zero and the phase is $\dfrac{\pi}{2}$.

Two other important characteristics are the quality factor or Q-factor

$$Q = \frac{\omega_0}{\Delta\omega} = \frac{f_0}{\Delta f}, \tag{3.11}$$

which is also the ratio of energy stored by the oscillator over the energy dissipated. The last important characteristic used is "Height times Width over Drive" (HWD) which is equivalent to

$$\text{HWD} = \frac{v_{\text{max}}\Delta f}{F_{\text{drive}}} = \frac{1}{2\pi m}. \tag{3.12}$$

We can see that HWD is constant for given parameters, and therefore can be used to recalculate the height, width, or drive when two of those parameters are known.

Damping Mechanisms

Energy loss in a real mechanical oscillator occurs through several mechanisms. Some of these mechanisms are intrinsic to the oscillator; some are extrinsic mechanisms are due to interactions with the surrounding media. The contributions of damping mechanisms to the total resonance width can simply be summed [61]

$$\Delta f = \Delta f_m + \Delta f_n + \Delta f_o \ldots \tag{3.13}$$
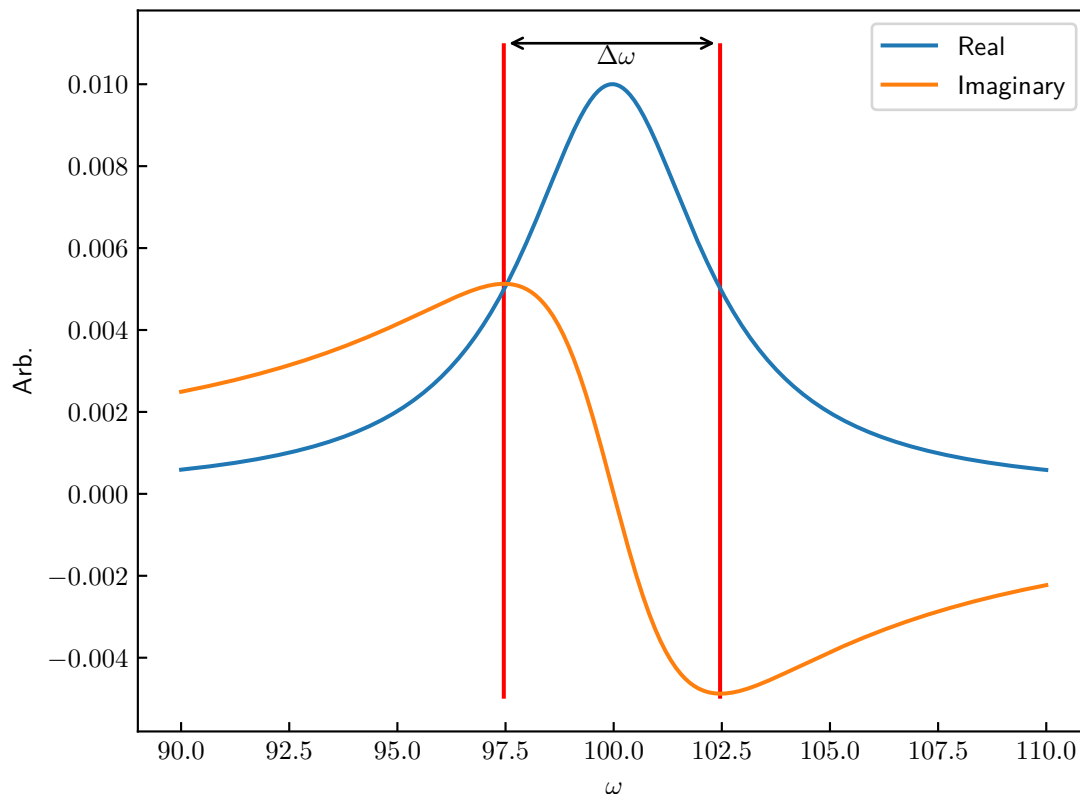
FIGURE 3.1: An example resonance with $k_e = 10000$, $m = 1$ and $\gamma = 5$. The resonance frequency is $\omega_0 = 100$ and has width $\Delta\omega = 5$ which is shown. The quality factor is therefore 20.

Common intrinsic damping mechanisms are clamping losses, the thermoelastic effect and magnetic damping for oscillators driven by the Laplace force [61].

Clamping losses occur due to the construction of the oscillator and are a hard limit on the minimum dissipation and therefore damping. The thermoelastic effect is directly proportional to temperature and can therefore be neglected at the very low temperatures in this work [62]. The magnetic effect is proportional to B^2 and is small compared to fluid damping effects in the fields used for this work [63, 64].

In liquid helium, there are many possible extrinsic damping mechanisms. There can be acoustic losses, where energy is dissipated by emitting sound waves [65]. For dipole emitters the width Δf is dependent on the square of the frequency and for quadrupole emitters Δf is quartic with frequency. Generally, acoustic losses are only relevant for high frequency devices.

For all oscillators in liquid helium there is damping due to the viscosity of liquid helium. We can split the theoretical treatment of viscous damping into two regimes: the
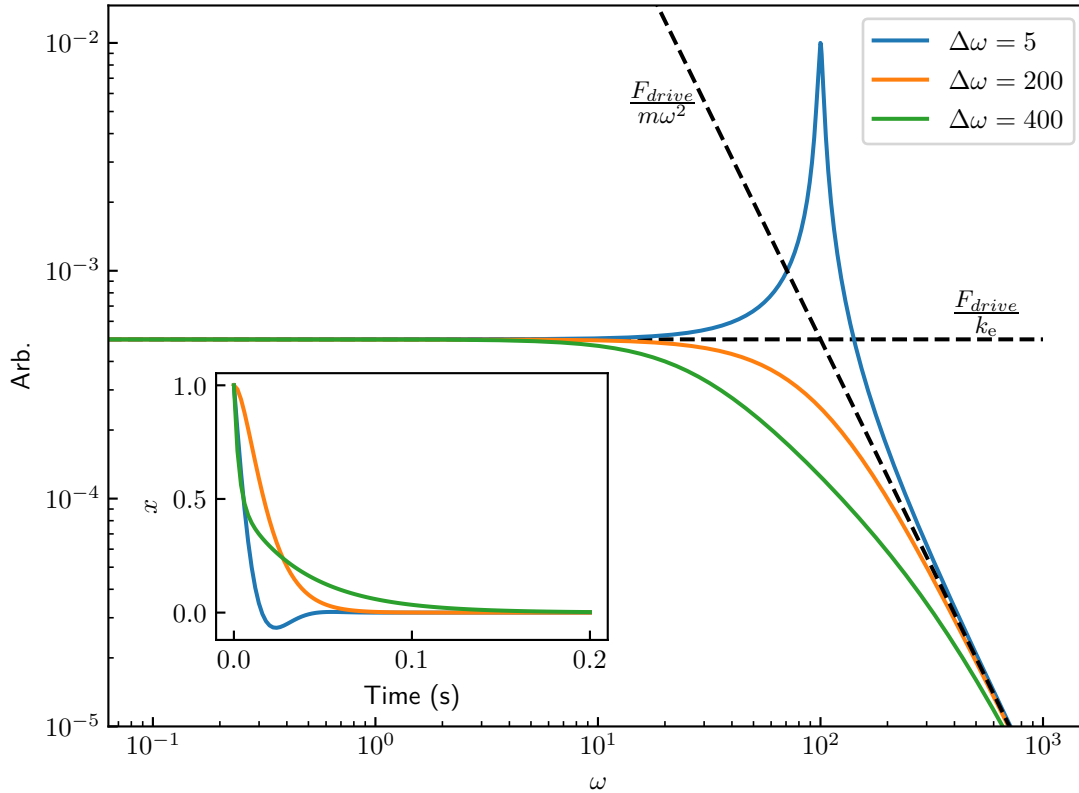
FIGURE 3.2: The magnitude of the same example resonance as Fig. 3.1 except with widths $\Delta\omega = 5, 200, 400$, corresponding to underdamping, critical damping and overdamping, respectively. At frequencies far from resonance the responses are the same, but around the resonance only an underdamped oscillator's response is enhanced. Inset: the free motion starting with position $x(0) = 1$ and initial velocity $\dot{x}(0) = 0$.

hydrodynamic regime and the ballistic regime [61]. The hydrodynamic regime exists in normal fluid and in superfluid conditions where there exists a sufficiently high normal fluid fraction. The ballistic regime exists at low reduced temperatures, typically around $0.3T_c$ and below. These two regimes are detailed in section 3.1.3. Further, damping mechanisms can occur due to the rich array of phenomena available in ^{3}He, such as interactions with quantum turbulence or Cooper pair-breaking [61].

Effects of Damping

Very near T_c, the viscosity of both normal fluid and the normal component in the superfluid phase of ^{3}He is extremely high. Mechanical resonators, especially smaller ones, at these temperatures can be "overdamped". As the normal fluid fraction quickly drops (see

Fig. 2.2), the damping decreases and the resonators become "underdamped". To investigate the effects of damping, we begin by solving the free equation of motion, (3.1) with the driving force $F_{\text{drive}} = 0$,

$$m\ddot{x} + \gamma\dot{x} + k_e x = 0. \tag{3.14}$$

Using a solution of the form $x = x_0 e^{-i\alpha t}$

$$m\alpha^2 + \gamma\alpha + k_e = 0. \tag{3.15}$$

Solving for α

$$\alpha_{+,-} = \frac{-\gamma \pm \sqrt{\gamma^2 - 4mk_e}}{2m}. \tag{3.16}$$

There are three possible physical solutions depending on the square root corresponding to $\gamma^2 > 4mk_e$, $\gamma^2 = 4mk_e$ and $\gamma^2 < 4mk_e$ corresponding to overdamping, critical damping and underdamping respectively. Fig. 3.2 shows the resulting frequency sweeps over several damped-driven oscillators. There is no enhancement of the signal at the resonant frequency for an overdamped oscillator, making it difficult to measure with a frequency sweep.

It was mentioned above that at low damping (when Q-factor is much larger than 1), the maximum in real part of the response and therefore the resonance occurs at the undamped resonant frequency ω_0. However, converting (3.16) into frequency space we can find the damped resonance frequency

$$\alpha_{+,-} = -\frac{\Delta\omega}{2} \pm \sqrt{\frac{\Delta\omega^2}{4} - \omega_0^2}. \tag{3.17}$$

The free motion of an oscillator is shown in the inset of Fig. 3.2. In the underdamped case, we see progressively smaller oscillations until it reaches the equilibrium value. The position is given by

$$x_{\text{ud}}(t) = c_1 e^{-\frac{\gamma}{2m}t} e^{i\omega_{\text{ud}}t} + c_2 e^{-\frac{\gamma}{2m}t} e^{-i\omega_{\text{ud}}t} = e^{-\frac{\Delta\omega}{2}t}\left[c_3 \cos(\omega_{\text{ud}}t) + c_4 \sin(\omega_{\text{ud}}t)\right], \tag{3.18}$$

where

$$\omega_{\text{ud}} = \sqrt{\omega_0^2 - \frac{\Delta\omega^2}{4}} \tag{3.19}$$

is the damped resonant frequency, c_n are constants.

In the critical damping and overdamped cases, the system returns exponentially to the equilibrium, never going beyond it again. For the overdamped case, the oscillator

returns to equilibrium slower than critical damping. The governing equations of motion are

$$x_{\text{od}}(t) = c_1 e^{\alpha_+ t} + c_2 e^{\alpha_- t} = e^{-\frac{\Delta\omega}{2}t} \left[c_3 \cosh\left(\omega_{\text{od}}t\right) + c_4 \sinh\left(\omega_{\text{od}}t\right) \right], \text{ and} \tag{3.20}$$

$$x_{\text{cd}}(t) = e^{-\frac{\gamma}{2m}t} \left(x(0) + \dot{x}(0)t + x(0)\frac{\gamma}{2m}t \right). \tag{3.21}$$

Here, the overdamped resonant frequency is

$$\omega_{\text{ud}} = \sqrt{\frac{\Delta\omega^2}{4} - \omega_0^2} \tag{3.22}$$

but one must remember that in the case of overdamping there is no enhancement of the signal by a Q-factor and no free oscillations. Therefore, the system doesn't really resonate.

The constants c_n can be found by considering the initial position $x(0)$ and velocity $\dot{x}(0)$.

3.1.2 RLC Circuit Resonance

A parallel RLC (resistor-inductor-capacitor) circuit undergoes resonance in an analogous way to the mechanical mass-spring model [66]. Fig. 3.3 shows a simple parallel RLC circuit, also known as a tank circuit. From Kirchoff's current law, the sum of the current through each component must be equal to the total drive current. The current through the resistor is V_{RLC}/R, the current through a capacitor is the capacitance C time the derivative of the voltage $\dot{V}_{\text{RLC}}$ and the current through an inductor is the integral of the voltage with respect to time divided by the inductance L. Thus, a time varying "equation of motion" for a drive current I_{drive} can be written

$$C\dot{V}_{\text{RLC}} + \frac{V_{\text{RLC}}}{R} + \frac{1}{L}\int V_{\text{RLC}}dt = I_{\text{drive}}e^{iwt}. \tag{3.23}$$

With the same form as (3.1) the RLC circuit undergoes a similar resonance. We can simply relate the terms to the mechanical mass-spring model. The capacitance C is equivalent to the mass m, resistance R is equivalent to the inverse of the damping γ and the inverse of inductance L is the spring constant. The resonant frequency is then

$$\omega_0 = \sqrt{\frac{1}{LC}}. \tag{3.24}$$

Similarly, the quality factor and width can be found. The quality factor is

$$Q = R\sqrt{\frac{C}{L}}. \tag{3.25}$$
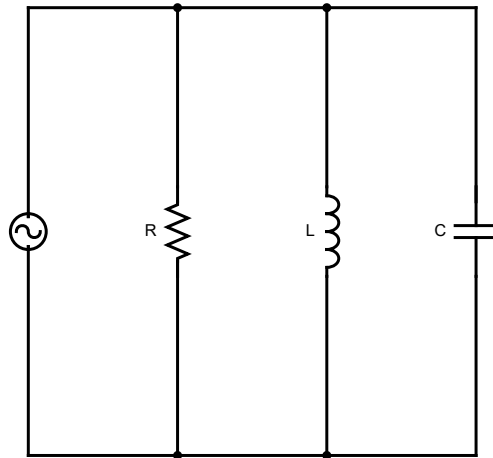
FIGURE 3.3: A simple parallel RLC resonating circuit.

3.1.3 Oscillators in Liquid Helium

Hydrodynamic Regime

In the hydrodynamic regime, the damping occurs from viscous drag due to the viscosity of the remaining normal fluid fraction. Additionally, a finite layer of normal fluid will cling to a moving object within this regime, known as the viscous penetration depth δ. This layer of normal fluid will move with the object, increasing the effective mass of the object. Thus, the effects on the resonance of the mechanical oscillator are twofold: a reduction in the resonant frequency due to the added mass of liquid that must be displaced, and the increasing of the resonance width due to viscous drag [54, 60, 61].

The added mass of an oscillating object with volume V can be modelled as [54]

$$m_{\text{eff}} = m + \beta_1 \rho_{\text{He}} V + \beta_2 \rho_{\text{n}} S \delta \tag{3.26}$$

where ρ_{He} is the total density of liquid helium-4 or helium-3 and V and S are the volume and surface area of the oscillator, respectively. β_1 and β_2 are dimensionless constants that depend on the geometry of the oscillator and are usually left as fitting constants. They are typically close to unity [54]. The first term here corresponds to the "backflow": the amount of fluid that must be displaced as the object moves. This is roughly equal to the volume of the object. The second term is related to the amount of normal fluid that moves along with the oscillator as part of viscous penetration depth. The viscous penetration depth is

$$\delta = \sqrt{\frac{\eta}{\pi \rho_\mathrm{n} f_\mathrm{H}}}. \tag{3.27}$$

Assuming the spring constant does not change, dividing the vacuum frequency f_v and hydrodynamic frequency f_H as calculated by (3.2) gives the ratio

$$\left(\frac{f_\mathrm{v}}{f_\mathrm{H}}\right)^2 = 1 + \beta_1 \frac{\rho_\mathrm{He}}{\rho_\mathrm{osc}} + \frac{\beta_2 S}{m} \sqrt{\frac{\rho_\mathrm{n} \eta}{\pi f_\mathrm{H}}}. \tag{3.28}$$

To calculate the damping, we take the Stokes' drag force for an infinitely long cylinder in the high frequency limit. The drag force is

$$F = C S v \sqrt{\pi \rho_\mathrm{n} \eta f_\mathrm{H}}. \tag{3.29}$$

C is a geometrical constant, which is equal to 2 for an infinitely long cylinder. The damping is given by $\frac{dF}{dv}$ and therefore the width is

$$\Delta f_\mathrm{H} = C \frac{S}{2\pi m} \frac{\eta}{\delta} \left(\frac{f_\mathrm{v}}{f_\mathrm{H}}\right)^2. \tag{3.30}$$

For a cylinder with diameter $2R$ we can write the mass in terms of its density and volume: $m = \rho_\mathrm{osc} V$. Since the ends are excluded, the ratio S/V is then simply $2/R$. This means for cylindrical objects, the hydrodynamic damping is inversely proportional to the radius of the object.

The total width is the sum of the intrinsic width determined by measurements in vacuum and the hydrodynamic width,

$$\Delta f = \Delta f_\mathrm{v} + \Delta f_\mathrm{H}. \tag{3.31}$$

At extremely low temperatures, the frequency shift of oscillating objects still occurs due to the backflow term. However, the normal fluid fraction approaches zero and thus both the total viscosity and the viscous penetration depth terms also approach zero.

Ballistic ^{3}He-B and Andreev Reflection

In the ballistic regime of the B phase, the hydrodynamic approach breaks down [51, 61]. Instead, we can model the oscillator as a 1D scattering problem with a rarefied gas of quasiparticles moving with group velocity v_g. The quasiparticles scatter with and reflect off the oscillator. Due to the superfluid gap, this reflection must involve exchange momentum of $2p_\mathrm{F}$. The difference between the number of quasiparticles hitting the front and back of the oscillator as it moves with velocity v gives rise to the damping force. The oscillator is modelled as a flat paddle with surface area S.

Far from Object   Near Object
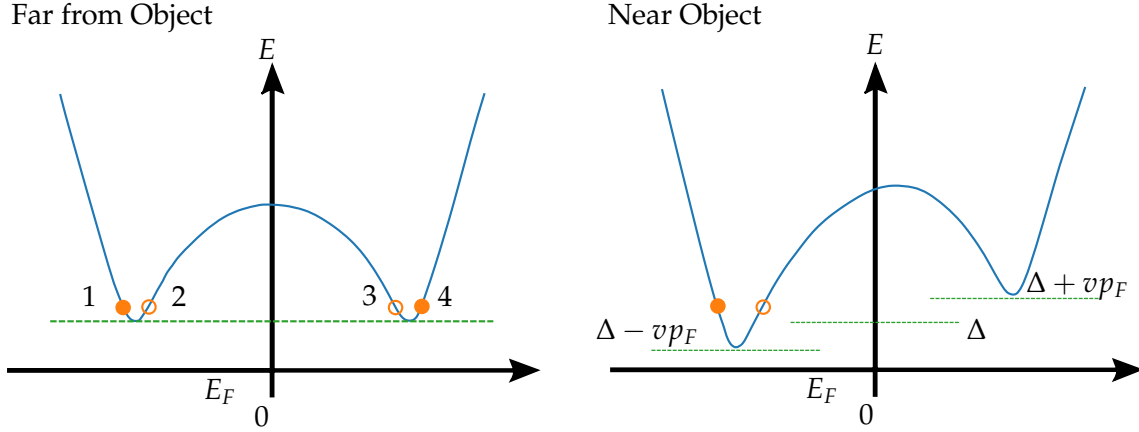
FIGURE 3.4: The dispersion curves for superfluid far from an object moving with velocity v, and near the object moving with velocity v. The right-hand side branch near the object has a much higher velocity. Quasiparticles and quasiholes on the right-hand side far from the object therefore have no available states to move into, and cannot perform the simple scattering with the object. Instead, they must undergo Andreev reflection.

A naive model takes only the velocity of the moving object into account and not the local velocity field produced by the moving wire. Using (2.10), the naive prediction is then simply the difference between the forces on the front and back of the paddle

$$F_{\text{damping}} = \underbrace{\frac{1}{2}S\langle n(v_{\text{g}} + v)\rangle}_{\text{front}} - \underbrace{\frac{1}{2}S\langle n(v_{\text{g}} - v)\rangle}_{\text{back}} = 2Snvp_{\text{F}}. \tag{3.32}$$

The velocity profile of the superfluid close to the oscillator, which morphs the dispersion curve by a Galilean transformation, is shown in Fig. 3.4 [5]. The object drags some fluid with it, and therefore fluid near the wire is also moving at velocity v. Quasiparticles and quasiholes in branches 3 and 4 need energy $\Delta_{\text{B}} + p_{\text{F}}v$ to reach the paddle, thus, the quasiparticle density from these are not equal to $\int_{\Delta_{\text{B}}}^{\infty} g(E) f(E, T) \, dE$ but $\int_{\Delta_{\text{B}} + p_{\text{F}}v}^{\infty} g(E) f(E, T) \, dE$. All the quasiparticles and quasiholes from branches 1 and 2 are free to reflect, so this scattering process is left unchanged. The retroreflective scattering process in ^{3}He is known as Andreev reflection.

Once these corrections are taken into account, the damping force is

$$F_{\text{damping}} = 2Sp_{\text{F}}v_{\text{g}}N\frac{p_{\text{F}}v}{k_{\text{B}}T} \tag{3.33}$$

for low velocities ($vp_{\text{F}} << k_{\text{B}}T$). N is given by (2.24). To simplify extension to higher dimensions, a proportionality constant C_1 is introduced. Recalling (3.1) the damping force is $F_{\text{damping}} = \gamma v$. Combining this, (3.9) and (3.33) gives

$$\Delta f = \frac{C_1 S}{\pi} \frac{v_g N p_F^2}{m \, k_B T} = \frac{C_1 S}{\pi} \frac{v_g p_F^2 g(E)}{m} e^{-\frac{\Delta_B}{k_B T}}. \tag{3.34}$$

In the low temperature limit $g(E) \approx g(E_F)$. It is then convenient to place all the constants into one constant

$$C' = \frac{C_1 S}{\pi} \frac{v_g p_F^2 g(E_F)}{m}. \tag{3.35}$$

Adding the vacuum damping Δf_v of the oscillator, the final expression for the width is therefore

$$\Delta f = \Delta f_v + C' e^{-\frac{\Delta_B}{k_B T}}, \tag{3.36}$$

which we can rearrange for thermometry purposes:

$$T = \frac{\Delta_B}{k_B \ln\left(\frac{C'}{\Delta f - \Delta f_0}\right)}. \tag{3.37}$$

Since this result is only valid for slow velocities, we perform thermometry measurements only at velocities below $1 \, \mathrm{mm \, s^{-1}}$, where response of the oscillator is well-fitted by a Lorentzian. The extent of the linear response in terms of driving force and velocity can be found by performing an amplitude sweep described in 3.3.2.

For full 3-D calculations for both specular and diffuse scatterings, see [67, 68].

3.1.4 Velocity Enhancement and Critical Velocity

It was mentioned previously that the critical velocity above which the superfluid state is destroyed due to a moving object is the Landau velocity v_L. The predicted velocity is $27 \, \mathrm{mm \, s^{-1}}$. The observed critical velocity of actual moving objects in the superfluid is much lower due to the velocity field around a moving object. As discussed above, the local velocity field of the superfluid flow around tilts the dispersion curve by a Galilean transformation.

We can model the flow using the well-known potential flow of an incompressible, inviscid fluid around an infinitely long cylinder. The fluid is moving at initial velocity v_0 in the x direction. The cylinder has a radius R_0. The boundary conditions are simple. Far away from the cylinder, $r = \infty$, the fluid flow is not warped at all by the object: $\mathbf{v}(r = \infty, \theta, z) = v_0$. There must be no flow inside the cylinder or perpendicular to the cylinder at the boundary: $\mathbf{v}(R_0, \theta, z) \cdot \mathbf{Y} = 0$, where $\mathbf{Y}$ is a unit vector perpendicular to the cylinder's surface.

Since the z-direction is of no consequence for an infinitely long cylinder, we can consider only the 2D problem of the cross-section. In Fig. 3.6, we see that in the rest frame of
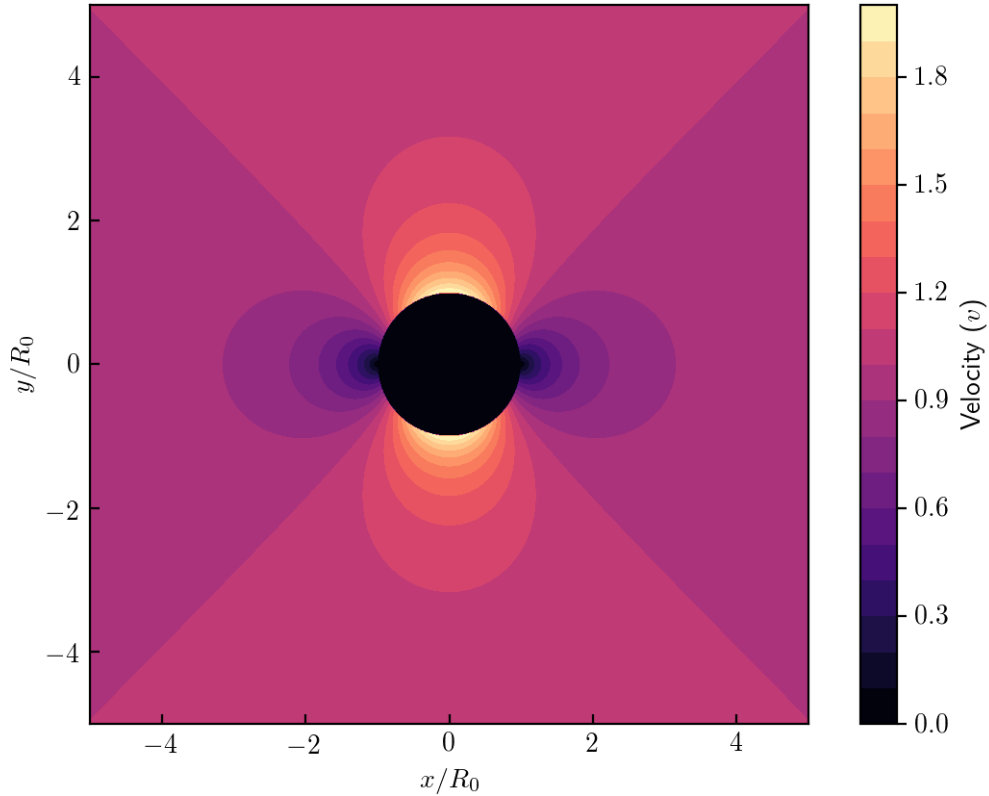
FIGURE 3.5: The potential flow of an incompressible, inviscid fluid within the boundaries of a cylinder cross-section moving at velocity $-v$ in the cylinder's frame. The maximum enhancement of the velocity is $2v$ at the top and bottom of the cylinder. The cylinder has radius R_0.

a cylinder moving at velocity $-v$ in the x direction, the fluid moves at different velocities relative to the cylinder within the vicinity. At the boundary of the cylinder, it reaches a velocity of $2v$ at the top and bottom of the cylinder.

Due to the tilting of the dispersion curves the onset of a large damping force occurs when the condition $\Delta - p_{\mathrm{F}}v = 2p_{\mathrm{F}}v$ is met, shown in Fig 3.6, which is understood through the Lambert model [5]. On any surface in ^{3}He there exists Andreev bound states which are localised to regions with a strong spatial dependence on the energy gap [69, 70]. Andreev first considered the quasi-electrons and quasi-holes in a thin layer of normal metal between the surface of an insulator and the same metal but in its superconducting state. A similar situation exists with the thin layer of normal ^{3}He as the energy gap goes from its bulk value to zero in the direction perpendicular to the surface of an object in ^{3}He over a distance of the order of the coherence length from that surface. The quasiparticles and quasiholes in the layer of normal fluid have the normal liquid ^{3}He (the red curve in Fig. 2.4). For any quasiparticle with energy $E < \Delta$, we can see that it can never enter
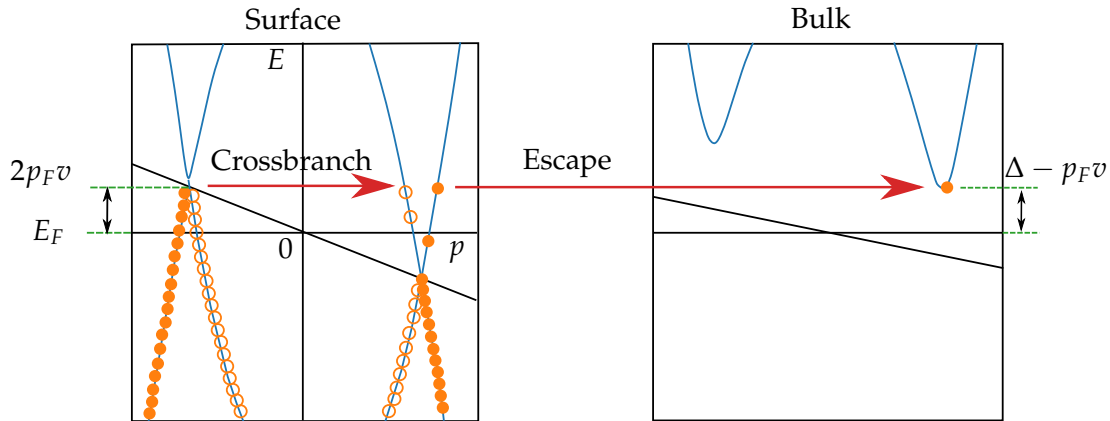
FIGURE 3.6: The dispersion curves for a gas of SABS on the surface of an object moving at velocity v such that the fluid flow is enhanced, and in the bulk superfluid. At v_c quasiparticles and quasiholes that can undergo the crossbranch process can then escape into the bulk, dissipating energy. [5]

the superfluid area, in the same way quasiparticles in the right-hand side branches of the dispersion curve in Fig. 3.6 could not enter the region near the wire. Again, the quasiparticles can only retro-reflect off the energy potential. In the case of the thin layer of normal fluid, this is the only process available for left or right hand side branches. These quasiparticles or quasiholes can never cross into the superfluid, therefore they are "bound" to the surface and are known as surface Andreev bound states (SABS). These states are predicted to have majorana like properties [71].

When the dispersion curves begin to tilt due to the movement of the object, then there becomes an escape process available for quasiparticles or quasiholes who can undergo the crossbranch process. Due to the difference between the local flow and the bulk flow, the dispersion curves tilt at different rates. Choosing the maximum local flow at the top and bottom of a cylinder ($2v$), the crossbranch process begins when $2p_\mathrm{F}v = \Delta - p_\mathrm{F}v$. The critical velocity for a cylinder can then be calculated as

$$v_\mathrm{c} = \frac{\Delta_\mathrm{B}}{3p_\mathrm{F}} = \frac{v_\mathrm{L}}{3}. \tag{3.38}$$

3.1.5 High Field Vibrating Wire Thermometry

At moderate and high fields ($> 100\,\mathrm{mT}$) the bulk A phase is stabilised at low pressures for a large temperature region. As discussed is section 2.2.4, the A phase has a non-uniform energy gap with two nodal points. This entails that quasiparticles can always be excited by pair-breaking and a moved object always experiences some effective drag, and that the drag force experience by a moving object such as a vibrating wire is dependent on the local texture for both the hydrodynamic and ballistic cases [13, 72, 73].

However, this does not mean vibrating wire thermometry can not be used at all. When the field is much higher than the required field to overcome the preferred alignment of $\hat{\mathbf{d}}$ and $\hat{\mathbf{l}}$ caused by the dipole interaction, in the absence of other effects, we can assume the direction of the magnetic field defines the texture. Thus, the texture will be the same for any magnetic field much larger than a few millitelsas, as long as the direction of the magnetic field is the same. In this case, one can use some known points for thermometry: the superfluid transition, the A_1—A transition and the A—B transition. There will be an abrupt change in resonant width of a wire at these points, which give a rough idea of the temperature in time. Second, if the heating to the fluid remains constant in time one can extrapolate backwards from the temperature in the normal fluid phase where accurate thermometry is possible. In section 2.2.2 it was discussed that the viscosity of the normal liquid ^{3}He is proportional to T^{-2}. The oscillator at this temperature will be in the hydrodynamic regime. From (3.27), (3.28) and (3.30) the damping can be calculated and roughly proportional to T^{-1}. Fig. 3.7 shows a temperature dependence calibration of the resonance width of a tantalum VWR with a vacuum resonant frequency of 4721.25 Hz and diameter of 124 µm, which is a large enough to not be overdamped. The backwards extrapolation can then be compared to the known points and the accuracy can be determined.

3.2 Devices

In this section, the mechanical probes used in the experimental cell are introduced. Many of these devices such as vibrating wire resonators (VWRs) and quartz micro-tuning forks (QTFs) are commonly used both in Lancaster Ultra Low Temperature experiments and elsewhere [51, 53, 55]. Newer technologies such as more complicated microelectromechanical systems (MEMS), nanoelectromechanical systems (NEMS) and carbon nanotubes (CNTs) have started to make their way from the wider physics research to the ultra-low temperature and quantum fluids communities, although mostly in superfluid ^{4}He [59].

3.2.1 The Flopper

The flopper is a large goalpost-shaped superconducting vibrating wire resonator (VWR). Shown in Fig. 3.8 (a). From its long leg size relative to the crossbar and low resonance frequency, the wire became known as the "flopper" or "flopper wire" [75]. The original dimensions of the flopper had legs of about 25 mm length and a crossbar of 9 mm in length. The wire diameter was 128 µm and made of single core superconducting NbTi (diameter 100 µm). In this work, a new flopper was made to allow the attachment of a NMR coil around a cylindrical sample of the nematic aerogel Nafen to the crossbar. The new flopper has 24 mm long legs and a crossbar 8 mm long. The wire used was 70 µm
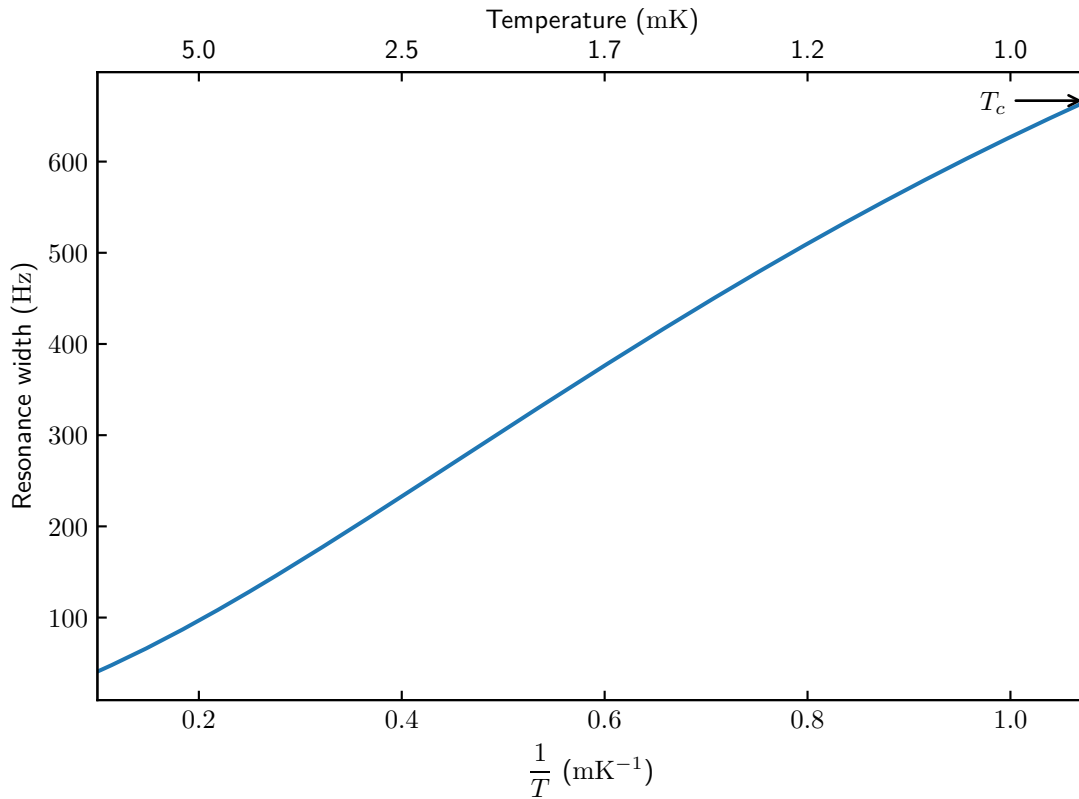
FIGURE 3.7: Calculation for the resonant width of a 124 μm diameter tantalum wire with a vacuum resonant frequency of 4721.25 Hz using hydrodynamic theory and viscosity measurements in [74].

diameter single-core NbTi clad in copper with a ratio of approximately 1.5 Cu: 1 NbTi. To distinguish the devices, the new flopper will be referred to as the NMR-flopper in this thesis.

The flopper has a low quality factor when immersed in superfluid. Normally a disadvantage, a low quality factor means that the device is not very sensitive to small changes of the superfluid. However, if one moves the flopper with a certain velocity and suddenly stops, there is comparatively little subsequent movement or "ring-down" vibrations [75]. The quick stopping time can be exploited effectively by using a direct current drive to move the flopper at a quasi-uniform velocity between two points, rather than alternating current drive to create oscillatory motion.

(a) (b)
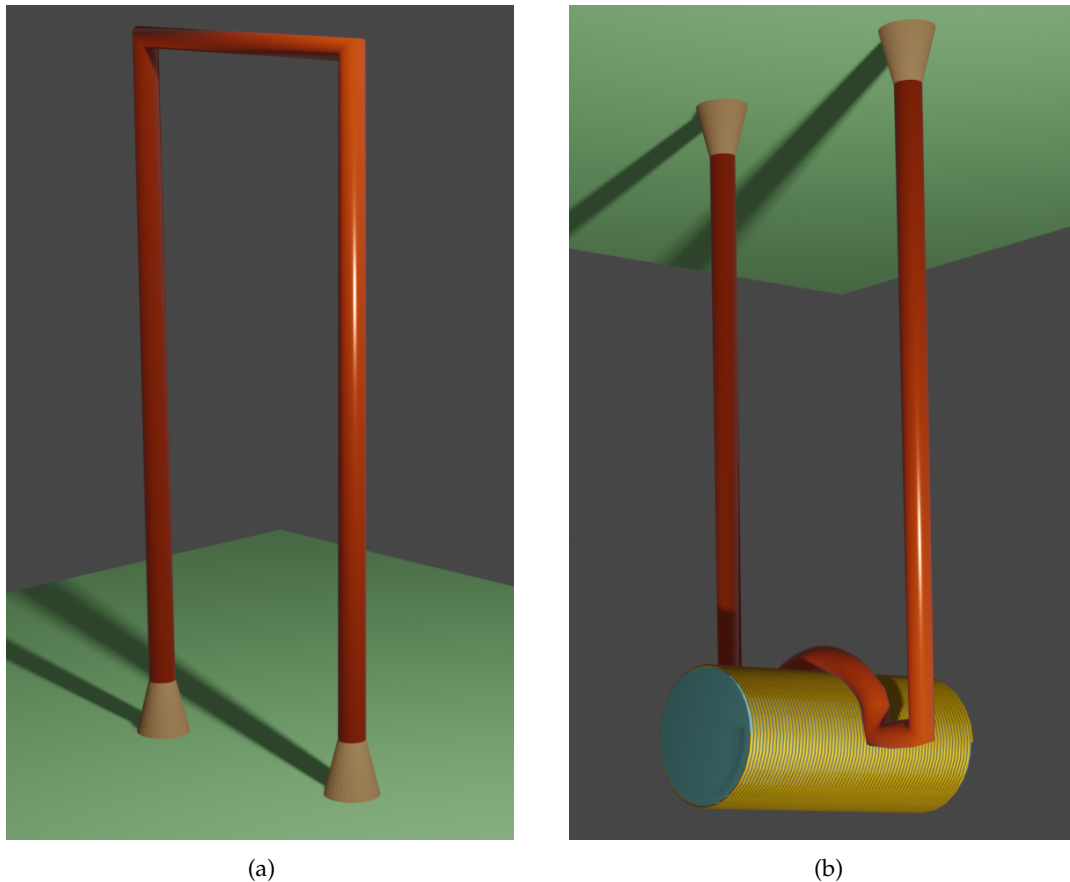
FIGURE 3.8: 3D sketches of the large wires known as the flopper. (a) The old design as just a moving wire, which was used in investigating faster than Landau velocity [6] and for measuring the Kapitza resistance in Chapters 5 and 6. (b) The new inverted design with the copper NMR coil and nafen aerogel.

Driving at Quasi-Uniform Velocity

The method for moving at quasi-uniform velocities requires smooth acceleration and deceleration pulses [76]. Any current through the flopper crossbar in a magnetic field perpendicular to the crossbar creates a Laplace force which will move the crossbar. For oscillatory motion, an alternating current is used. For quasi-uniform velocity, a direct current is used.

The direct current starts at an initial value, which defines the initial position of the flopper. The position is changed according to a complicated profile. A simple linear ramping up (increasing) of the drive current I has discontinuities in the acceleration and deceleration at the end of a ramp, which lead to strong oscillations at the end of a ramp despite the low Q-factor [75]. Hence, the position function is chosen as
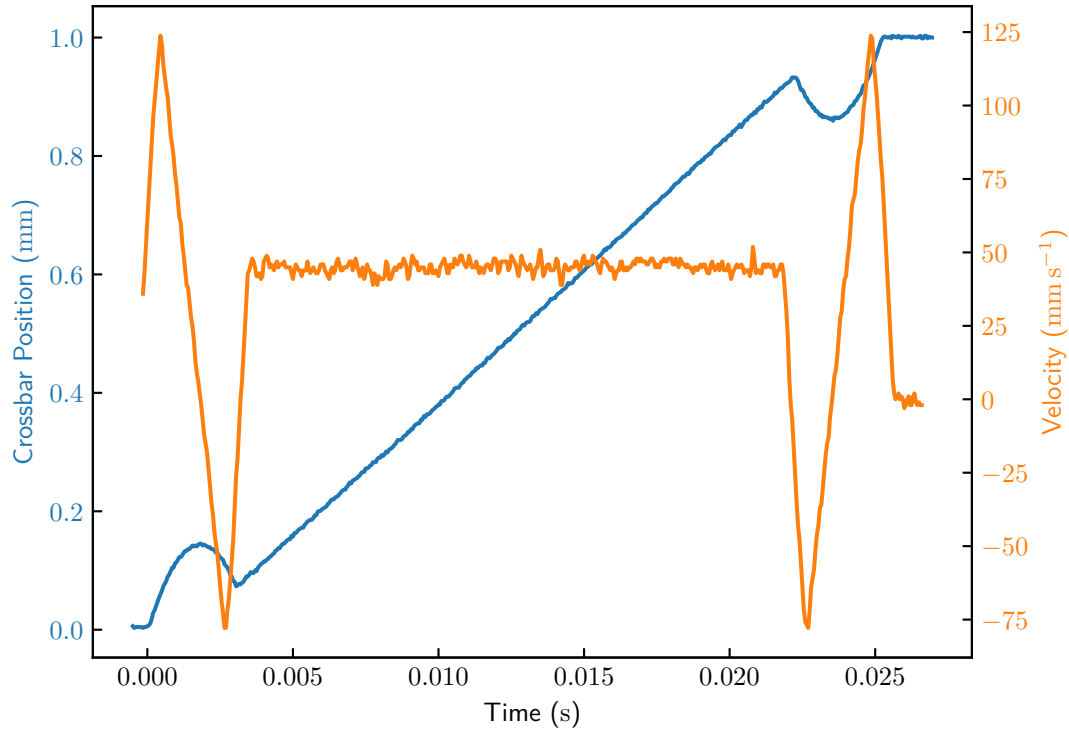
FIGURE 3.9: A $45\,\mathrm{mm\,s^{-1}}$ ramp of the old flopper, with the position detected by an EMF measurement of the position detection coils using a lock-in amplifier. The initial acceleration and the deceleration periods are shown. There is no oscillation in the position from the flopper after stopping.

$$x(t) = \begin{cases} vt_{\mathrm{acc}}\left(1 - \frac{t}{2t_{\mathrm{acc}}}\right)\left(\frac{t}{t_{\mathrm{acc}}}\right)^3 & \text{for } 0 < t \leq t_{\mathrm{acc}} \\ vt & \text{for } t_{\mathrm{acc}} < t \leq t_{\mathrm{ramp}} - t_{\mathrm{acc}} \\ d_{\mathrm{ramp}} - vt_{\mathrm{acc}}\left(1 - \frac{t}{2t_{\mathrm{acc}}}\right)\left(\frac{t}{t_{\mathrm{acc}}}\right)^3 & \text{for } t_{\mathrm{ramp}} - t_{\mathrm{acc}} < t \leq t_{\mathrm{ramp}} \end{cases} \quad (3.39)$$

where t_{acc} is the acceleration time, v is the desired uniform velocity, d_{ramp} is the distance moved over and t_{ramp} is the total time the ramp takes. The distance moved is defined by the initial and final values of the current. The position function and resulting current function is chosen to minimise the strong oscillations.

Faster than Landau Velocity

These "DC ramps" of a direct current to move the flopper at quasi-uniform velocity led to a unique discovery. It was determined the damping force on a wire moving at uniform
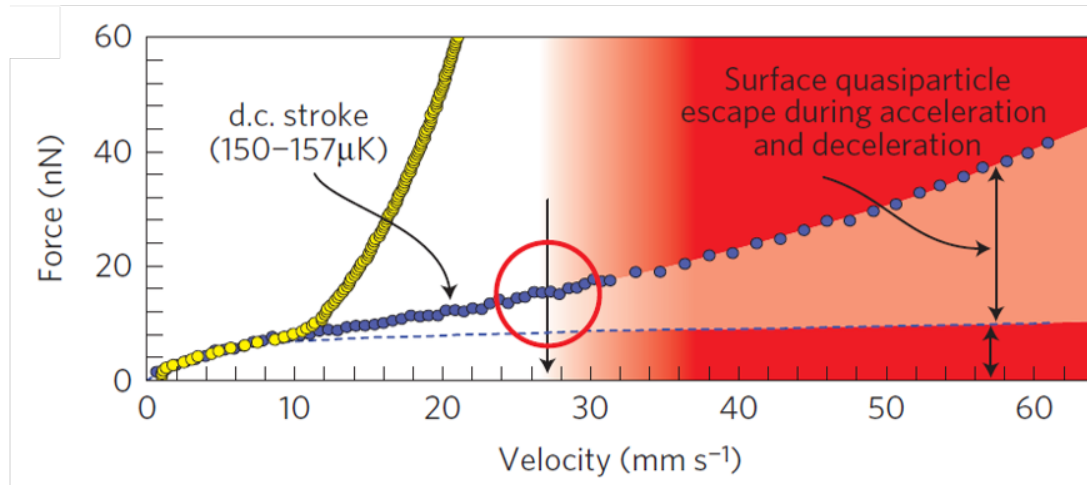
FIGURE 3.10: The difference in damping force on the flopper with AC drive oscillatory motion and DC drive ramps as the velocity increases. For the oscillatory motion v_c is clearly seen. The blue dotted line shows the thermal background due to finite temperature. The red circle and arrow indicates v_L. Figure from [6].

exceeding the Landau velocity is much lower than expected and orders of magnitude lower than damping seen for equivalent velocities in oscillatory motion, (see Fig. 3.10) [6]. There is neither the large onset of damping force seen by the AC driven motion at $v_c = 9\,\mathrm{mm\,s}^{-1}$ or at the full Landau velocity.

The originally proposed explanation was that this damping was due to the escape of quasiparticles occupying surface Andreev bound states (SABS) that exist on the wire surface during acceleration and deceleration periods. In the flopper experiment, the proposed mechanism of dissipation is that when the wire is moving, the normal fluid dispersion curve tilts by the Galilean transformation similar to Fig. 3.6. At v_c, some SABS have enough energy to move into the superfluid state if they are on the correct side. They undergo a cross-branch process and then escape into the bulk, shown in Fig. 3.10. Eventually, these SABS with enough energy have all escaped, and there is no more dissipation. Compared with oscillatory motion, in which the dispersion curves will reverse the tilt and then dissipation can occur in the opposite direction.

The Lambert model of dissipation could be repeated for AC motion indefinitely, depending on how long it takes for the SABS to replenish themselves. Chapter 5 presents an investigation into this model and the dissipation caused by SABS.

Adding Aerogel and NMR Coil

The NMR coil was formed from annealed high purity Teflon-coated copper. The coil is created around a metallic rod wrapped in Teflon tape and annealed for 24 hours at a
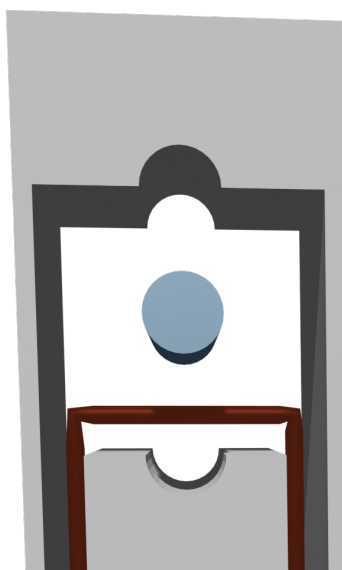
FIGURE 3.11: The shaping devices used for the flopper. The flopper wire is pressed between the two Teflon cubes, with a metal rod on one side within the gap. It is possible to create shapes with either the flopper having an inward or outward semicircle, depending on whether the flopper is above or below the rod.

temperature of 440 °C. This improved the residual-resistance ratio (RRR) from approximately 80 to 250. At higher temperatures the Teflon coating evaporates and the coil will short, and longer times was found to have little effect on the RRR, although it sometimes resulted in some of the Teflon coating deforming. Before annealing, the total diameter is 75 µm with the copper inner diameter 50 µm. The final coil was 4 mm in diameter and 7 mm long with 75 turns.

The nafen sample was cut with a high-speed cutting disk tool from a larger sample of nafen-92 (density 92 kg m^{-3}). Whilst cutting the sample, an air pump was used to remove small strands. The sample was cut to fit tightly within the coil.

To make space for the aerogel and coil a flopper with a semicircular space in its crossbar was needed. The semicircle is centred at the midpoint of the crossbar. The flopper is constructed using a Teflon former and a cylindrical metal rod, shown in Fig. 3.11. The former is two blocks with a hole for the rod. The desired wire is passed through the Stycast-paper base and stretched over the lower forming block. Weights were used at the end of the wire to provide tension. The rod is placed over the wire, then the upper block is place on top and the wire is compressed into shape. This results in the circle pointing inwards, to avoid the NMR RF coil being inside the current loops of the flopper once it is glued.
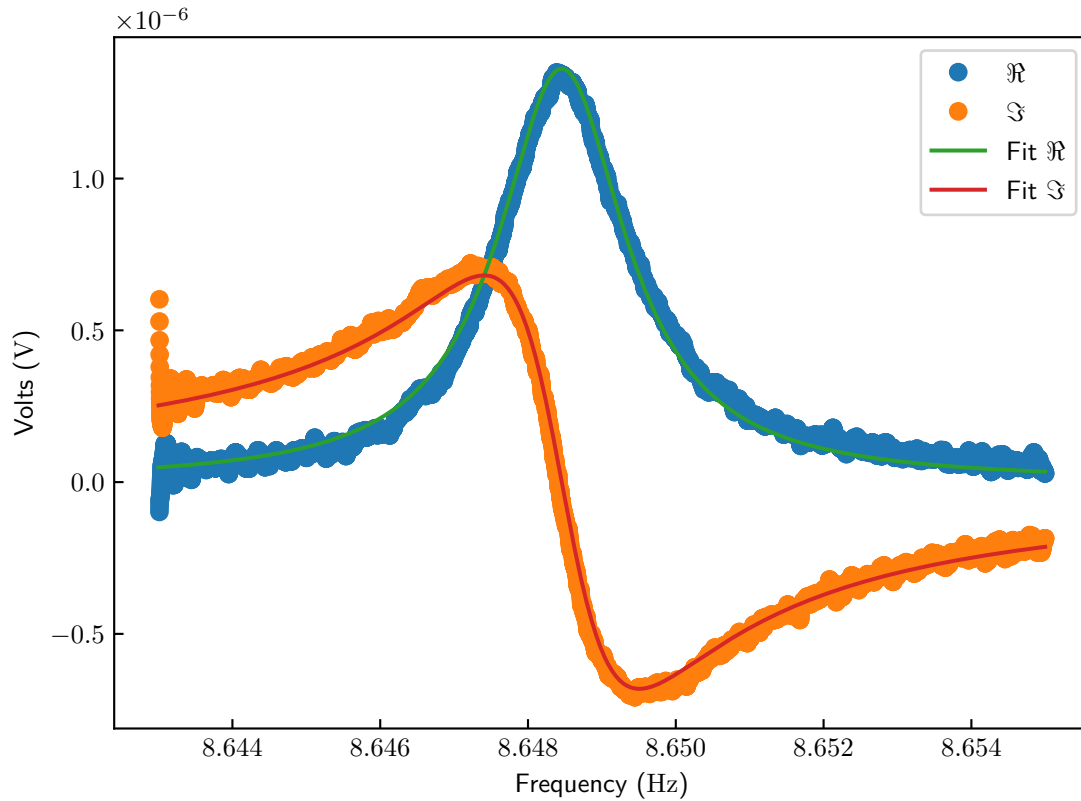
FIGURE 3.12: A frequency sweep of the NMR-flopper in vacuum at 4.2 K. The solid lines represent fits. The central frequency is $f_0 = 8.648$ Hz with a quality factor $Q = 4119$. There is some ringing at the beginning of the sweep.

We tested many types of wire, with and without coils. The wire decided on was single core NbTi clad in copper, with a ratio of 1.5 Cu to 1 NbTi. The original wire diameter was 100 μm. The wire was drawn to decrease the diameter to 70 μm. Drawing a wire results in some of the wire becoming curled, which can be treated by annealing the wire.

Finally, the coil is glued to the flopper using Araldite. The leads to coil were twisted into a twisted pair and varnished, and made slack so as not to restrict the NMR-flopper's movement. A sketch of the NMR-flopper is shown in Fig. 3.8.

The NMR-flopper is upside-down compared to the old flopper to stabilise the motion. Thus, the new flopper becomes similar to that of a pendulum. The resonant frequency of a simple pendulum of a mass at the end of a massless string with length L_{osc} is well known to be

$$f_0 = \frac{1}{2\pi}\omega_0 = \frac{1}{2\pi}\sqrt{\frac{G}{L_{\text{osc}}}}. \tag{3.40}$$

With the acceleration due to gravity $G = 9.81\,\mathrm{m\,s^{-1}}\,\mathrm{s}$, the resonant frequency $f_0 = 3.2\,\mathrm{Hz}$. Consequently, we can expect a much lower frequency. Another side effect of adding a crossbar mass was that the quality factor increased greatly. Fig. 3.12 shows a frequency sweep of the NMR-flopper taken at 4.2 K in vacuum. The quality factor is so high that the signal shows ringing effects for frequency points after the resonant frequency, even for sweeps over an hour long.

The frequency of the NMR-flopper is almost thrice that of the simple pendulum. Modelling it as a physical pendulum (i.e., including the mass of the string and the volume of the end-mass) gives a higher but similar frequency as the simple pendulum model. Instead, the more complicated approach of a hanging cantilever (or "stiff pendulum") with end mass can be taken. This takes into account the rigidity and stiffness of the wire legs and the large mass of the NMR-flopper crossbar. We look at the vibrational mode of just one leg. The mass of the pendulum is the total mass of the coil and crossbar, shared between the two.

The problem of a stiff pendulum is extremely complex and requires computational methods to solve. Naguleswaran computed solutions to the dimensionless natural frequency ω_0 of the nth mode for a hanging cantilever with different boundary conditions[77]. Values are computed depending on the dimensionless gravity parameter Γ and the dimensionless end-mass v. The dimensionless end-mass is the ratio of half of the mass of the aerogel, NMR coil and crossbar to the mass of one leg. The end mass of the aerogel sample can be calculated as

$$M_{\mathrm{e}} = \frac{M_{\mathrm{crossbar}} + M_{\mathrm{coil}} + M_{\mathrm{aerogel}} + M_{\mathrm{glue}} + M_{\mathrm{He}}}{2}. \tag{3.41}$$

The crossbar is made of $70\,\mu\mathrm{m}$ diameter NbTi wire clad in copper with a ratio of 1.5 copper to 1 NbTi. The average density of this wire is then $7960\,\mathrm{kg\,m^{-3}}$. The total mass is then $M_{\mathrm{crossbar}} = 270\,\mu\mathrm{g}$ with a mass per unit length $\mu_D = 30\,\mathrm{mg\,m^{-1}}$, which can be used to calculate the mass of one leg also. The coil is made of Teflon covered copper wire. The copper core has diameter $50\,\mu\mathrm{m}$ and the total diameter is $75\,\mu\mathrm{m}$. There are 75 turns of the coil made around a 4 mm diameter rod. The coil mass M_{coil} is 21.7 mg. The mass of the aerogel is simply the volume of the sample times the density, giving $M_{\mathrm{aerogel}} = 8.1\,\mathrm{mg}$. The mass of the glue is unknown and we initially neglect it. Thus, the end mass in vacuum is $M_{\mathrm{e}} \approx 15\,\mathrm{mg}$.

The mass of the helium fluid is found similarly to the hydrodynamic equations (3.26). In this case, the added mass comes from the volume of normal fluid trapped inside the aerogel and $\beta_1 = 1$. The penetration depth is comparatively small and can thus be neglected, $\beta_2 = 0$. Accordingly, the mass of the helium $M_{\mathrm{e}} = \rho_n 1.98 V_{aerogel}$.

From the values tabulated by Naguleswaran in [77], if the dimensionless end-mass v is between 1 and 100, and $\Gamma \approx 0.0$ (as it is for the NMR-flopper) then the dimensionless

natural frequency for the first mode can be approximated by the relationship

$$\Omega_0 = \frac{1.7}{\sqrt{v}}. \tag{3.42}$$

For the resonant frequency of the first mode we find the predicted resonant frequency of the flopper in vacuum as

$$f_0^{\mathrm{v}} = \frac{\omega_0^{\mathrm{v}}}{2\pi} \approx 6.8\,\mathrm{Hz}. \tag{3.43}$$

Comparatively, in normal fluid we can add the mass of all the helium. The density of normal fluid $\rho_n = \rho_{He} = 81.8\,\mathrm{kg\,m^{-3}}$. The helium mass in normal fluid is then $M_{He} = 7.1\,\mathrm{mg}$. The predicted resonant frequency is thus

$$f_0^{\mathrm{He}} \approx 5.9\,\mathrm{Hz}. \tag{3.44}$$

NMR Circuit and Setup

The NMR circuit is a simple tank circuit, using a cryogenic amplifier developed by V. V. Zavjalov *et al.* and a differential amplifier at room temperature [78]. The tank circuit resonance is excited by a signal generator denoted as the master generator. A 10 pF capacitor is used as a simple DC filter before the RLC resonance circuit. The output of the differential amplifier is measured by a high frequency SR844 lock-in amplifier.

The RLC circuit was designed to have a frequency equal to the Larmor frequency of helium in a magnetic field around 30 mT. From (2.38) this requires a frequency $f_{\mathrm{L}} = 1\,\mathrm{MHz}$. The RLC circuit used is shown in the dotted oval in Fig. 3.13. With 75 turns and a diameter of about 4 mm, the inductance of the coil is about 10 μH. By (3.24) this results in a frequency of $f_0 \approx 1.3\,\mathrm{MHz}$. Due to the resistance of the coil (shown in Fig. 3.13 by the resistor in series) and the resistance of the wires, the actual frequency is shifted down to 948 kHz. The width of the resonance at low temperatures is 5 kHz, giving a Q-factor of 190.

The actual NMR spectrum is measured using a differential amplifier. A second generator is set to produce a signal at the resonant frequency of the tank circuit and phase locked with the master generator. The master generator excited the tank circuit and created the small oscillating RF field. The slave generator is used to compensate the signal, so that the output of the differential amplifier is close to zero when the magnetic field is far below the magnitude required for the Larmor frequency to be equal to the tank circuit resonant frequency. The field is then varied past the required field Larmor frequency and back again, rather than varying the frequency. When the field is close to the required field for resonance, there is an absorption of the RF signal which changes the output of the differential amplifier. Fig. 3.14 shows examples of the resulting absorption spectrum from
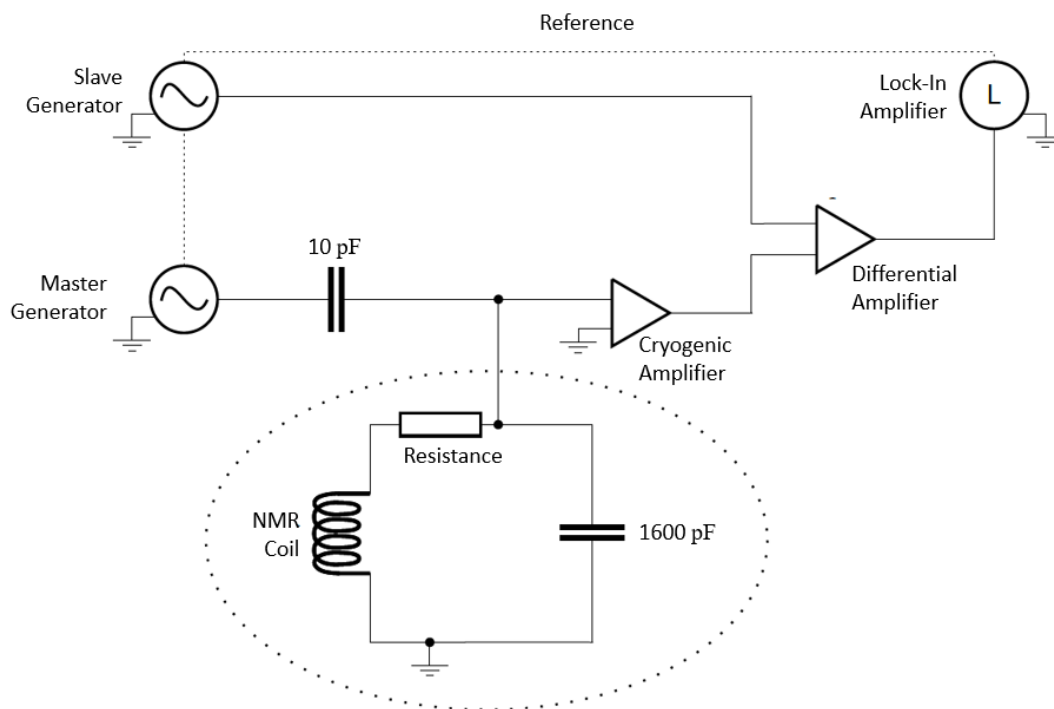
FIGURE 3.13: Circuit diagram for the NMR setup. The Master Generator is fed into a tank circuit out lined by the dotted oval, which produces an electrical resonance and an oscillating RF field through the coil. The Slave Generator is phase-locked with the Master Generator and the frequency is set to the resonance. The signal from the Slave is adjusted to minimise the sum of the two signal in the differential amplifier.

the resonance. The field sweeps are equivalent to frequency sweeps but with inverted directionality. When the static field B_{ext} goes from low-to-high, the equivalent frequency sweep is from high-to-low.

3.2.2 Vibrating Wire Resonators

Vibrating wire resonators (VWRs) are one of the most commonly used devices. They consist of superconducting wire with a circular cross-section. The wires can be created in a goalpost shape with a straight crossbar joining two straight legs, as with the flopper. Alternatively, they can be made as a semicircular loop attached between the two legs. The wire diameter ranges between $1\,\mu m$ and $200\,\mu m$, and the leg spacing is typically above $1\,mm$.

The wires involved in this work were two semicircular wires with larger diameters known as Outer Cell Tantalum and Inner Cell Tantalum (OCTa and ICTa), which were used only for thermometry. Also contained in the experimental cell were a series of smaller wires. The largest of the small-diameter wires was a $13.5\,\mu m$ diameter wire, then
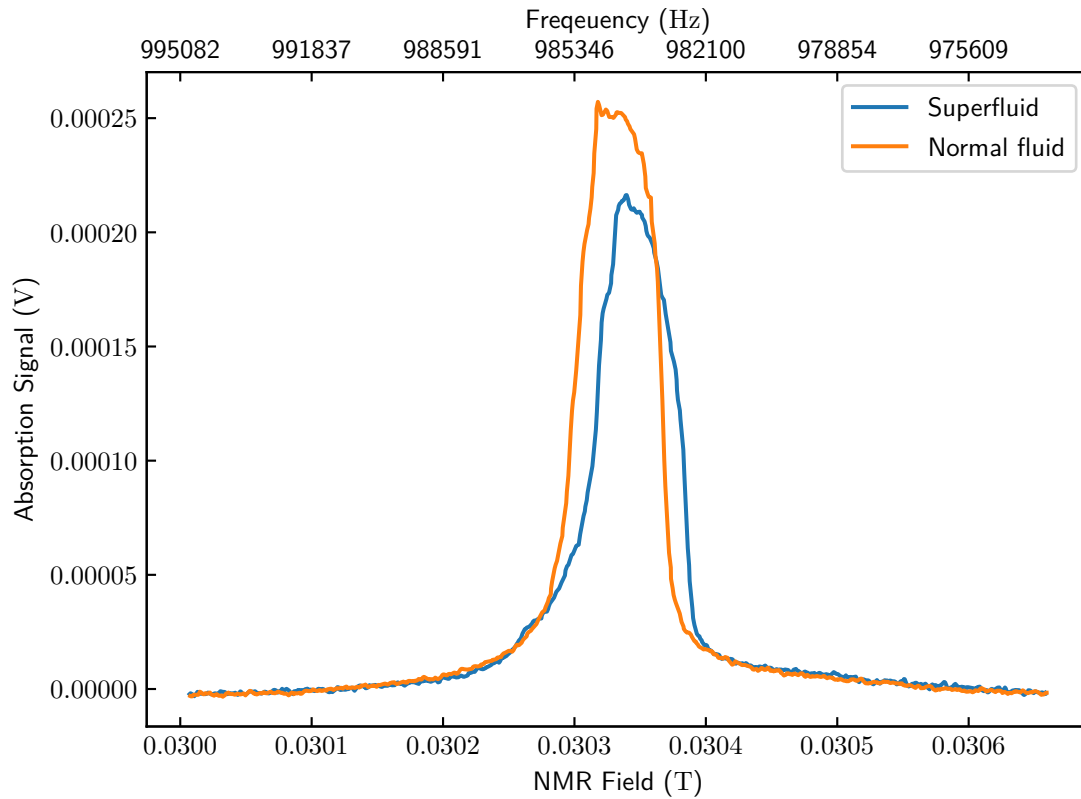
FIGURE 3.14: NMR absorption signals in both ^{3}He-B and normal fluid ^{3}He at zero pressure. The superfluid data is shifted slightly and has a small amplitude, as one would expect from the lower magnetisation in the *B*-phase if some bulk liquid signal is seen from the coil.

a wire with diameter of 4.5 μm known commonly as "triple micro" or "$\mu\mu\mu$" but in this thesis just by their diameter. These are also commonly used for thermometry purposes [51]. In addition, we constructed some sub-micron diameter wires for use in the new experimental cell. These two wires had diameters of 0.9 μm and 0.4 μm diameter wire.

Loop Measurement

All the VWRs are driven by the magnetomotive method. An alternating drive current results in an alternating Laplace force on the wire, creating an oscillating motion. The Laplace force on a wire in magnetic field **B** driven by current $\mathbf{I_{drive}}$ with leg spacing D is [57]

$$\mathbf{F} = \mathbf{B} \times \mathbf{I_{drive}} \cdot D. \tag{3.45}$$
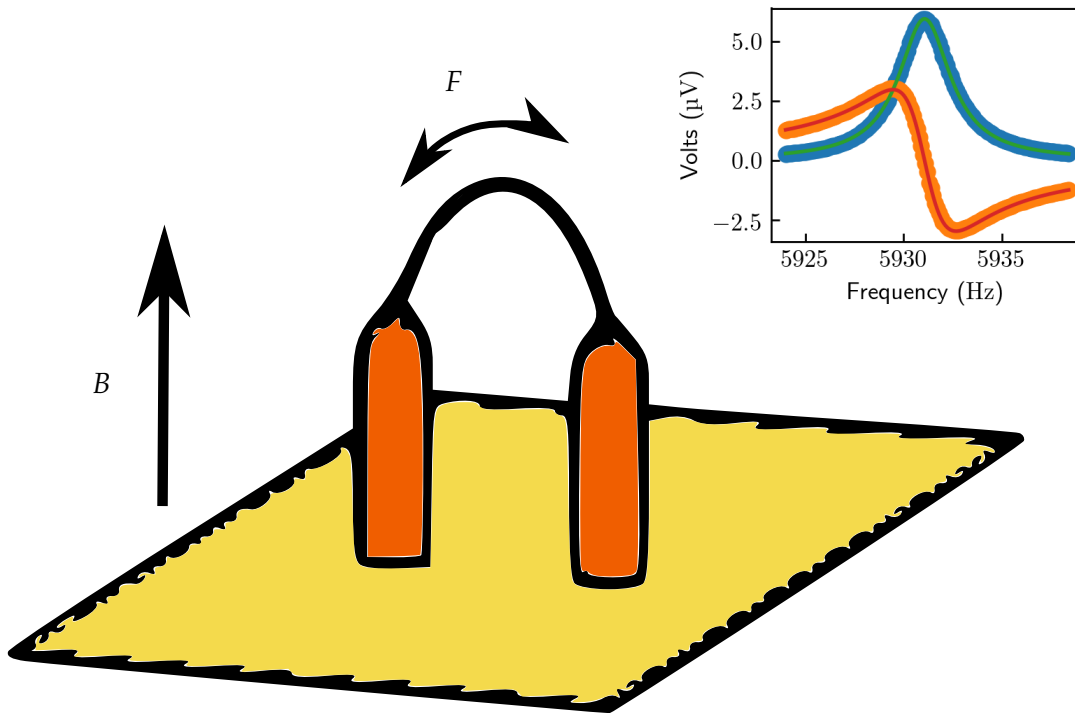
FIGURE 3.15: A sketch of a semicircular loop VWR commonly used for the smaller diameter wires. The wire is driven by the Laplace force induced by an alternating current in the presence of the perpendicular magnetic field B. Inset: The resonance of the 0.9 μm diameter wire in vacuum at 4 K. As with Fig. 3.12, dots represent the raw signal and the solid lines represents fits.

The motion of the wire can be detected by the Faraday voltage induced by the change in field of the area enclosed by the loop

$$V = \frac{\mathrm{d}(\mathbf{B} \cdot \mathbf{A})}{\mathrm{d}t}. \tag{3.46}$$

The area of a semicircle is $A = \pi \frac{D^2}{8}$ and the rate of change is related to the velocity of the wire as $\frac{2v^2}{D}$. With a static magnetic field $\mathbf{B} = B\hat{\mathbf{z}}$, the voltage is related to the velocity by

$$v = \frac{4V}{\pi B D}. \tag{3.47}$$

This voltage can be measured and converted into a velocity using the above formula. Naturally, for a straight crossbar the factor $\frac{4}{\pi}$ does not appear. The HWD can be calculated

from (3.45) and (3.46) as

$$\text{HWD}_\text{vwr} = \frac{B^2 D^2}{8m}.$$

(3.48)

3.2.3 Quartz Micro-Tuning Forks

Quartz micro-Tuning Forks (QTFs) are well-defined, easy to operate and easily available from commercial outlets. Quartz is a piezoelectric material that creates a voltage and current when undergoing stress deformations. Micro-fabrication can develop many forks with high precision. The high precision allows frequencies from a broad set of ranges to be chosen with a similar precision. QTFs are shaped similar to a regular musical tuning fork, as shown in Figure 3.16. There are two prongs or legs with length L_osc and cross-sectional area A_QTF attached to a substrate. The frequency is well described by [54, 79]

$$f_n = \frac{1.875^2}{2\pi L^2} \sqrt{\frac{E_\text{Y} I_\text{qtf}}{\rho_\text{q} A_\text{QTF}}}.$$

(3.49)

I_qtf is the moment of inertia, $E_\text{Y} = 97\,\text{GPa}$ is the Young's modulus of quartz, and $\rho_\text{q} = 2650\,\text{kg}$ is the density of quartz.

Each prong contains an electrode. The electrodes can be used to apply an AC waveform. Depending on the electrode position on each prong, the waveforms excites a flexural resonance, deforming the quartz and inducing a piezoelectric current which can then be detected. The current is dependent on the deformation and therefore resonance; the faster the prongs move, the higher the current.

Tuning forks have a so-called fork constant a that relates the ratio of current I per unit velocity of the fork in the linear regime

$$v = \frac{I_\text{qtf}}{a}$$

(3.50)

or the force F to the voltage, V_qtf

$$F = \frac{a V_\text{qtf}}{2}.$$

(3.51)

It is possible to calculate the fork constant a from the HWD as the drive voltage is known and the current is the measured by the height. Substituting (3.50) and (3.51) into (3.12)

$$\text{HWD} = \frac{a^2}{4\pi m}.$$

(3.52)

The effective mass of a tuning fork is

$$m = 0.24267 \rho_\text{q} L_\text{osc} bh$$

(3.53)
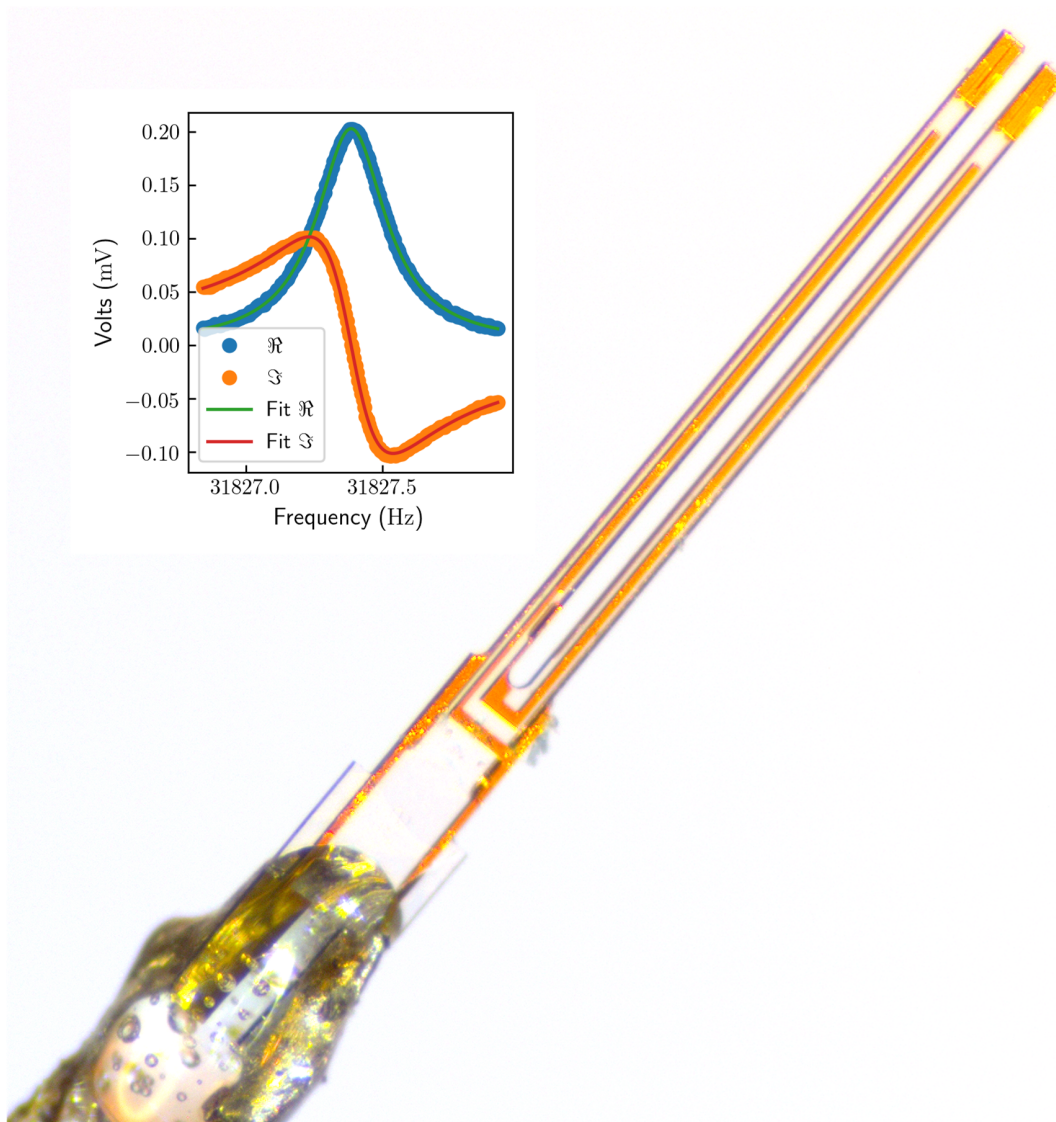
FIGURE 3.16: A photo of a QTF with thickness $b = 25\,\mu$m. The dimensions and electrodes are shown. The fork is soldered to two wires, which are secured by Araldite adhesive. Inset: frequency sweep of the fundamental mode of the $25\,\mu$m fork TF3 in vacuum at $4\,$K. $\Delta f = 0.31\,$Hz and $f_0 = 31\,827.4\,$Hz.

where L_{osc}, b, h are fork prong dimensions and density of quartz $\rho_{\text{q}} = 2.648\,\text{kg}\,\text{m}^{-3}$. The fork constant can be determined optomechanically using a laser Doppler velocimetry [79]. Doing so gives good agreement with the electromechanical determinations.

3.2.4   NEMS

Nano-electromechanical Systems (NEMS) are devices that have at least one important spatial dimension below 1 μm. They are commonly used as resonators. During the construction of our new cell, we added space for five doubly-clamped nano-beams of different lengths and two sub-micron diameter VWR loop resonators. The beams are simple prismatic beams that operate in much the same way as a vibrating loop: an alternating current is passed through in a perpendicular magnetic field, creating a Laplace force and subsequent movement [59].

As nano-sized devices are much smaller they have higher force and mass sensitivity, and generally higher resonant frequencies (see below), allowing them to access the MHz range of frequencies, previously not used in liquid ^{3}He. A further physical interest is that the nano-beams had width and height dimensions approaching the coherence length in superfluid ^{3}He, about 80 nm. How a probe that has dimensions similar to the size of the coherence length and an amplitude much smaller interacts with the superfluid is particularly interesting question.

The disadvantage of nano-beams are that they tend to have much higher losses than slightly larger devices such as micro-tuning forks. Particularly, their high frequencies mean that acoustic damping is a large problem [60]. To get around this problem, the sub-micron VWRs are made similar to the traditional way, outside the clean room [51]. These devices have lengths of the order of 1 mm, and therefore have a much lower resonant frequency.

Construction of Sub-Micron Diameter Wires

To construct a small diameter wire, copper-clad multi-filament superconducting NbTi wire is used. The original wire is total diameter 130 μm. First, the wire is drawn through dies to ensure the filaments are the desired size, reducing the total wire diameter. Second, the wire is bent into the semicircular loop and glued in place by placing both ends of the wire through Stycast paper. Often, the wire is wrapped around a mould with the desired leg spacing to create the loop.

Third, the copper cladding must be removed by etching the loop in nitric acid. Once the filaments are exposed, all but one must be plucked. For the sub-micron diameters, such as the 0.9 μm and 0.4 μm wires, this is often done whilst the loop is submerged in alcohol and then left to dry, as the surface tension when pulling the wire out of the acid can break the wire. It is also possible to glue the ends of the NbTi wire to the legs, adding some tension to the wire.
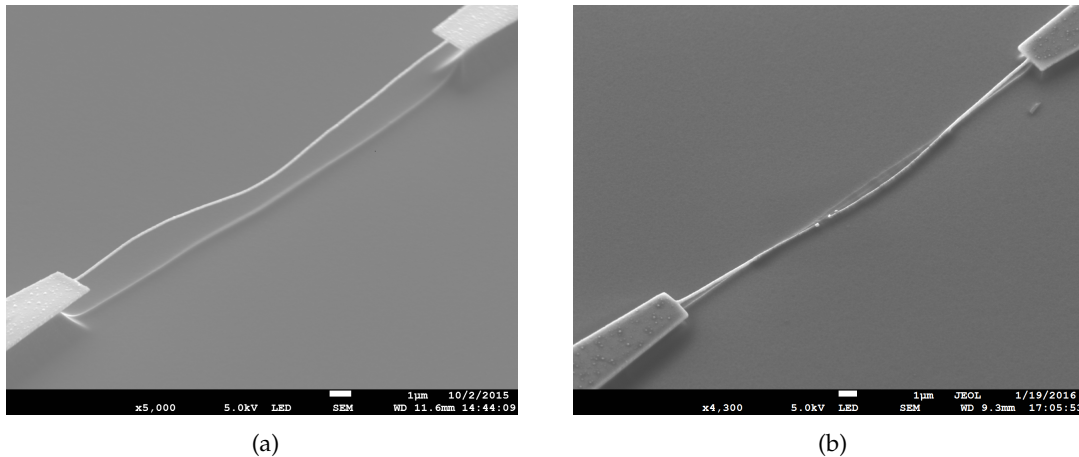
FIGURE 3.17: Scanning Electron Microscope images of (a) a successful nanobeam from those used in superfluid ^{4}He [59] and (b) a collapsed nanobeam.

Nanobeam Fabrication and Failure

The beams were fabricated by means of applying two masks to a silicon wafer and using electron beam lithography to pattern the masks. Silicon is then etched according to the pattern, and Aluminium is deposited through the mask onto the thin remaining silicon bridge. Finally, the masks are removed. This leaves a large aluminium layer on the silicon bridge. The mismatch between the silicon and aluminium expansion coefficient causes a tension that increases the beam frequency [59].

The nanobeams were investigated for quite some time. Whilst resonances were found, they were found to be fairly independent of parameters that usually effected the mechanical resonance of beams. For instance, a lack of magneto-motive damping was seen. However, some beams showed a clear superconducting transition, demonstrating electrical conductivity through the beam. The scanning electron microscope (SEM) of nano-beams produced in the same batch in Figure 3.17 demonstrates the clear reason. The beams had collapsed along the floor of the beam but some had retained their conductivity.

One possible reason is the over-etching of the silicon caused the silicon bridge to collapse before or during aluminium deposition.

3.2.5 Carbon Nanotube

One can imagine a carbon nanotube as essentially the tube one would get when rolling up a single atomic layer or a few multi-layered sheets of carbon. As such, carbon nanotubes are extremely small devices, often having lengths sub-micrometer and diameters about 10 nm. This makes them extremely sensitive to mass and excitations in a system. Due to their small size, they have high mechanical resonant frequencies, in the tens or hundreds

of GHz [80]. Due to their method of growth however, they do not have high losses one would associate with a tradition nanobeam made to a similar size and can have Q-factors over 30000 [80].

A carbon nanotube also represents a good opportunity to measure a larger mechanical device in its quantum ground state. The temperature required to achieve this is $T < \frac{hf}{k_B}$. Furthermore, the larger the Q-factor, the longer lived a quantum state will be. Finally, the diameter of a carbon nanotube is well below the coherence length of the superfluid ^{3}He.

Unfortunately, the carbon nanotube used in this work was either broken before use in our experimental cell or broken sometime during the setup or testing period.

3.3 Measurement Types

There are several ways of measuring oscillators. The most fundamental way is to apply a sinusoidal drive at a range of frequencies. In the following, the common measurement types used in this work are presented.

3.3.1 Frequency Sweep

The most common and basic measurement method is a frequency sweep. Here, an alternating drive current with a constant amplitude is applied. The frequency at which the current is applied can then be increased or decreased. The result is that given by (3.5) and (3.6). Figs. 3.12, 3.15 and 3.16 all contain frequency sweeps. In reality, there is a "background" in the frequency sweep, in both the real and imaginary components. The background is usually a linear function of frequency or a constant offset, and it can be found during the fitting procedure and subtracted later.

The electrical circuit for performing such measurements differs slightly by oscillator. Circuit diagrams are shown in Appendix A. For VWRs, a voltage signal generator is passed through a resistor, then through a step-down transformer into the VWR. The resulting electromotive force (EMF) can be picked up by using a step-up transformer, amplifier and a lock-in amplifier. The lock-in amplifier is phase locked with the original signal generator.

The tuning forks again use a signal generator and lock-in amplifier, however they do not need transformers. The signal is reduced by attenuators (if required) and the resulting signal is converted by means of an I-V converter with a gain setting.

The damping of the oscillator directly limits the time taken for a frequency sweep. The response time of an oscillator is inversely proportional to the resonance width

$$\tau_w = \frac{1}{\pi \Delta f}. \tag{3.54}$$

Therefore, for each measured point on a frequency sweep, one should wait τ_w time to prevent ringing effects. At extremely low temperatures, some very lightly damped devices may take hours to measure correctly, whilst a device with high damping will take a much shorter time.

3.3.2 Tracking Mode

Once the resonance frequency, phase, HWD and background are known from a frequency sweep, a resonator can be operated in "tracking mode". In this mode the drive current is set to the resonant frequency. From equation (3.6) we note that in the correct phase the imaginary part of the frequency sweep must be equal to zero at the resonance.

We can then measure the ratio of the imaginary signal V_y to the real signal V_x. Substituting the damping γ for the width from (3.9) gives

$$\frac{V_y}{V_x} = \frac{\Im(\dot{x}_0)}{\Re(\dot{x}_0)} = \frac{\omega_0^2 - \omega^2}{\Delta\omega \times \omega}. \tag{3.55}$$

During the tracking mode, we can introduce feedback in the form of a phase-locked loop to adjust the frequency of the driving signal generator. From 3.1, V_y is: zero when the frequency is equal to the resonance frequency, negative at frequencies above the resonance frequency and below $\omega_0 + \dfrac{\Delta\omega}{2}$ and positive at frequencies below the resonance frequency $\omega_0 - \dfrac{\Delta\omega}{2}$. By using V_y/V_x in a proportional–integral–derivative controller algorithm we can keep the signal on resonance.

Amplitude Sweeps

A common way of using the tracking mode is to increase the drive whilst keeping the same frequency. The increased drive results in larger velocities and displacements. In the linear regime, one can plot the force against velocity and expect a linear relationship. In non-linear regimes, (3.1) no longer applies and the force-velocity relationship changes. A log-log force velocity will see this as a "kink" as it goes from a straight line of gradient one to a line of different gradient. In the case of damping by turbulence, the kink line should have gradient 0.5. Andreev reflection also results in a non-linear force against velocity relation when in the ballistic regime.

For this reason, amplitude sweeps are generally used to determine the range of linear response for an oscillator, where (3.1) applies. Subsequent measurements are then used in this range.

Chapter 4

Experimental Techniques and Apparatus

In this chapter, the different experimental designs for this work are shown and techniques used for refrigeration are described. The Chapter shows the layout of the two experimental cells used. The first experimental cell housed the old flopper. The second experimental cell was made by recycling the old experimental cell: cutting the lower portion and replacing it with a new cell. This cell houses the NMR-flopper and the sub-micron VWRs. Some devices, for example Outer Cell Tantalum (OCTa) and Inner Cell Tantalum (ICTa) are common to both cells.

4.1   Refrigeration

The experiments in this work take place in a custom–built dilution refrigerator with an adiabatic nuclear demagnetisation stage. Both dilution refrigeration and nuclear demagnetisation are discussed extensively in the literature [13, 81, 82]. For details of a design of a Lancaster specific custom-built fridge, one can see [83] and for the specific fridge used in this experiment [84]. Therefore, only a very brief description of the dilution refrigeration is given here, with a slightly more detailed description of nuclear demagnetisation.

A dilution refrigerator exploits the spontaneous separation of liquid ^{3}He-^{4}He mixtures at low temperature (about $870\,\text{mK}$). At zero temperature, there is a layer of the lighter ^{3}He liquid above a dilute 6.5% ^{3}He–93.5%^{4}He mixture in the part of the fridge known as the mixing chamber. Cooling power is generated by transferring ^{3}He atoms from the pure layer into the dilute layer, in a process similar to evaporation.

Once separation is achieved, extra ^{3}He can be added into the system by pumping it in. This ^{3}He liquefies and joins the pure layer, creating a nonequilibrium concentration at the phase boundary between the pure and diluted layers. ^{3}He will then cross the phase boundary. The dilute phase has a higher entropy, thus there is an increase in entropy. From the second law of thermodynamics, this process then requires some thermal energy, which is taken from the surroundings.

Above the mixing chamber is the still volume. It is connected to the dilute phase at the bottom of the chamber and heated to about $0.5\,$K. At this temperature, ^{3}He is predominately evaporated from the mixture due to its higher vapour pressure. There is therefore a vapour of 90% or more ^{3}He and a liquid mixture of less than 1% ^{3}He. [13] The vapour can be pumped out, cleaned and then pumped back into dilution refrigerator. The principle operation is then to initially condense and cool a ^{3}He-^{4}He gas mixture into liquid until separation in the mixing chamber. This is done by a variety of high impedances and heat exchange with pre-cooling unit [13]. ^{3}He is then extracted from the still and cycled back in, driving the nonequilibrium concentration at the phase boundary. Continuous circulation of ^{3}He provides a continuous cooling power which reaches a base temperature of a few millikelvins.

4.1.1 Nuclear Demagnetisation

Nuclear demagnetisation is a cooling process that involves using the nuclear spins of a paramagnetic material as a refrigerant [81, 82]. In a magnetic field and at low temperature the nuclear spins undergo Zeeman splitting and separate into different energy levels. Our nuclear refrigerant of choice is copper. The nuclear spin of the stable isotopes of copper, ^{63}Cu and ^{65}Cu, is $I = 3/2$. There are then $2I + 1 = 4$ energy levels. The entropy of the nuclear spin system is

$$s_n = R_g \ln\left(2I + 1\right) - \frac{\lambda_n B^2}{2\mu_0 T^2},$$ (4.1)

for R_g the ideal gas constant, λ_n is the nuclear molar Curie constant and μ_0 is the Bohr magneton.

Since the entropy of the Copper nucleons is a function of the ratio of the magnetic field over the temperature, if one thermally disconnects the copper refrigerant using a superconducting heat switch and then reduces the magnetic field the demagnetisation process is isentropic. Therefore, for the entropy to remain constant whilst the field decreases, the temperature of the nucleons must also decrease. We can write the final temperature of the nuclei in terms of the initial and final magnetic fields, and the initial temperature. At low fields the interaction between the nuclear moments of neighbouring Cu nuclei are no longer negligible. The nuclear interactions can be simplified as a small internal magnetic field B', which presents a hard limit on the final field:

$$\frac{T_{\text{final}}}{T_{\text{initial}}} = \frac{\sqrt{B_{\text{final}}^2 + B'^2}}{\sqrt{B_{\text{initial}}^2 + B'^2}}.$$ (4.2)

In reality, the final temperature of the nuclei is higher than T_{final} as there is always some heat leak into the system, shown in Fig. 4.1. One large source of heating during a
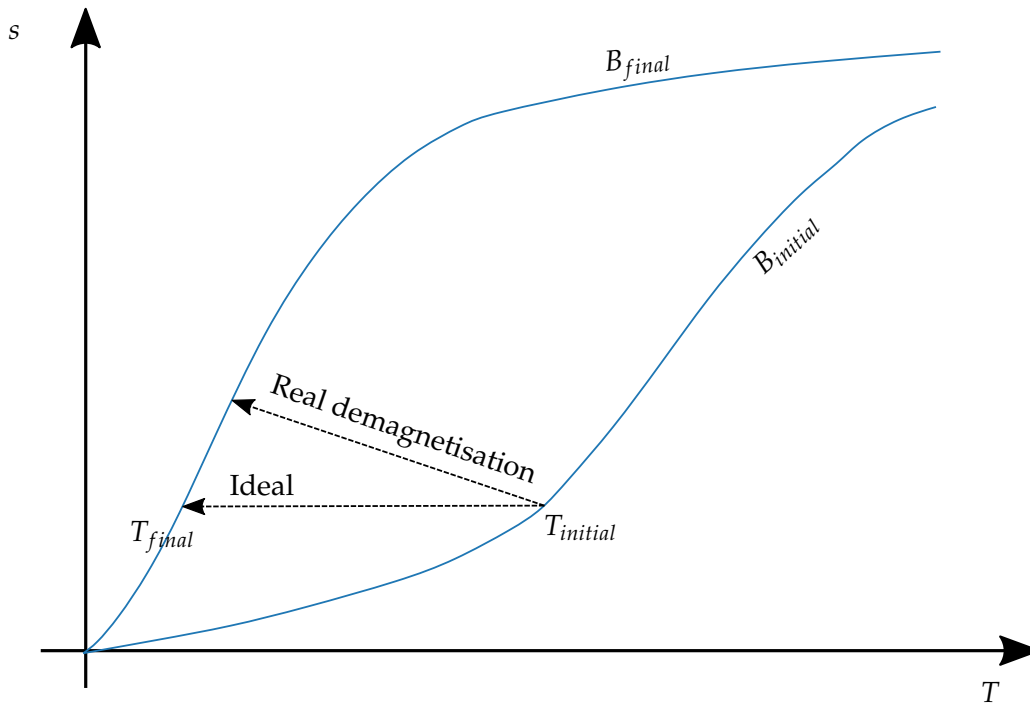
FIGURE 4.1: A nuclear demagnetisation cycle. A real demagnetisation process does have some parasitic heat leaks into the system, which leads to a higher final temperature than the theoretical T_{final}.

real demagnetisation cycle is the Joule heating from eddy currents created in the copper by the changing magnetic field [85].

4.1.2 Kapitza Resistance in Nuclear Demagnetisation

Since the nuclear demagnetisation process applies to the nuclear spin system in the Copper refrigerant, to cool the helium sample heat must flow from the liquid helium to the nuclear refrigerant. There are several thermal baths with independent temperatures it must go through [81, 85]. First, there is the liquid helium sample. Heat then transfers through to the metallic phonons in the refrigerant. After that, heat must transfer from the phonons via the eletron-phonon interaction to the Copper electrons, then finally into the nuclei by the hyperfine interaction. This means the final temperature of the liquid ^{3}He sample will be even higher than that of the Copper nuclei.

The heat conduction between the solid metal and liquid ^{3}He is limited by the thermal boundary resistance R_{K}, known as the Kapitza resistance. The heat flux between the two materials with contact area A can be defined as

$$\dot{q} = \frac{\Delta T}{A R_{\mathrm{K}}}. \tag{4.3}$$

The existence of Kapitza resistance between liquid helium and solid metal has had a strong effect on the design of helium refrigerators. The Kapitza resistance increases as temperature decreases. Hence, refrigeration becomes increasingly difficult the lower the temperature.

Nakayama breaks down the effect of temperature on Kapitza resistance for the helium liquids into three regimes [86]:

- $T > 1\,\mathrm{K}$: R_{K} is anomalously low and similar to solid helium's.

- $10\,\mathrm{mK} \leq T \leq 200\,\mathrm{mK}$: R_{K} follows the prediction of acoustic mismatch theory, $R_{\mathrm{K}} \propto T^{-3}$ [87]

- $1\,\mathrm{mK} \leq T < 10\,\mathrm{mK}$: R_{K} is again anomalously low, turning to a possible T^{-2} or T^{-1} relationship. There is a suspected magnetic channel of heat transfer mediated by solid ^{3}He adsorbed on the surface of the metal.

To combat the effects of the Kapitza resistance at low temperatures, a process known as sintering is undertaken to increase the surface area of metal in contact with the liquid helium [81, 82, 86]. Metal powders or flakes are fused together at high temperatures and pressures, creating a rough sponge-like surface with a large "microscopic" surface area [88, 89]. The larger surface area allows more contact with the liquid helium and thus more heat transfer, without taking up large amounts of space.

Copper plates used as coolants in nuclear demagnetisation experiments commonly have silver sinter coatings to enhance the cooling power of the nuclear refrigerant. Without the silver sinter, these experiments would either simply not work or take an unreasonably long time to reach a desirable temperature. This also slightly modifies the heat flow, as heat must flow from electrons in the sintered silver to electrons in the copper refrigerant.

4.1.3 Kaptiza Resistance in the B Phase

A further regime for superfluid ^{3}He should be added. For superfluid ^{3}He, a range of differing R_{K} have also been found. Previous measurements at Lancaster and measurements made by Parpia at Cornell found a Kapitza resistance exponentially dependent on temperature, $T \propto e^{-\frac{\Delta_{\mathrm{B}}}{k_{\mathrm{B}} T}}$ [27, 90, 91]. The exponential dependence is suspected to be because the heat transfer is dominated by quasiparticle collisions with the metal. However, later measurements have found simple power laws. All sets of measurements have been performed over varying temperatures and pressures.

If the value of Kapitza resistance behaved according to the acoustic mismatch theory (see [86]), the Kapitza resistance would still be too great. The leading hypothesis to explain the discrepancy in superfluid and normal fluid below $10\,\mathrm{mK}$ is due to a magnetic channel of heat exchange between magnetic $^3\mathrm{He}$ and magnetic particles or impurities in the metal powder [86]. Whilst Leggett and Vuorio originally developed this theory due to anomalous measurements of the Kapitza resistance between cerium magnesium nitrate and helium at relatively high temperatures, this theory can be applied to metals at lower temperatures [86, 92]. The origin of this channel is dipole-dipole interaction between the nuclei refrigerant's spins and the $^3\mathrm{He}$ nuclei. In reality, helium will adsorb on the surface of a cold solid. Solid $^3\mathrm{He}$ is a strongly para-magnetic material and a complex dynamic between liquid $^3\mathrm{He}$, solid $^3\mathrm{He}$ and sintered metal is responsible for the whole Kapitza resistance [93].

Whilst early measurements saw no magnetic field dependence for R_K at low fields, Perry *et al.* found a field dependence in Platinum powders [94]. Osheroff and Richardson found a field dependence in the more commonly used silver sinter at fields up to $200\,\mathrm{mT}$ but no further [95]. Detailed investigations in the magnetic impurities of different powders used for sinter have since been carried out by König *et al.* [96–98]. They found evidence for the amount of magnetic impurities in a silver sinter affecting the Kapitza resistance.

Covering the surfaces with solid $^4\mathrm{He}$ is commonly done in NMR experiments to remove the signal from solid $^3\mathrm{He}$ [7, 8, 36]. Moreover, covering the experimental surfaces with non-magnetic $^4\mathrm{He}$ to increase surface specularity has become popular [28, 29, 99]. The removal of the solid layer of $^3\mathrm{He}$ should have a great impact on the cooling power of the demagnetisation stage by removing the magnetic channel as $^4\mathrm{He}$ has no nuclear magnetism. In an experiment similar to the one presented in this thesis in Chapter 6, Mizutani and Suzuki found the R_K to increase when solid $^4\mathrm{He}$ was added to $\mathrm{HoVO_4}$ and $\mathrm{TmVO_4}$ between $2\,\mathrm{mK}$–$20\,\mathrm{mK}$ [100]. Similarly, increasing the field also increased the resistance.

The effects on nuclear demagnetisation experiments should not be understated. The time required to reach the target temperatures should increase, and it may not be possible to reach some temperatures at all. Reaching the ballistic regime without pressurising may prove an impossibility if this magnet channel is indeed responsible for the anomalously low Kapitza resistance.

4.2 Inner Cell Design and Reconstruction

4.2.1 Cell Recycling

To reach ultra-low temperatures of $T < 200\,\mathrm{\mu K}$, experiments at Lancaster use a "nested" cell. Fig. 4.2 shows the nested cell design with the inner cell used for experiments in
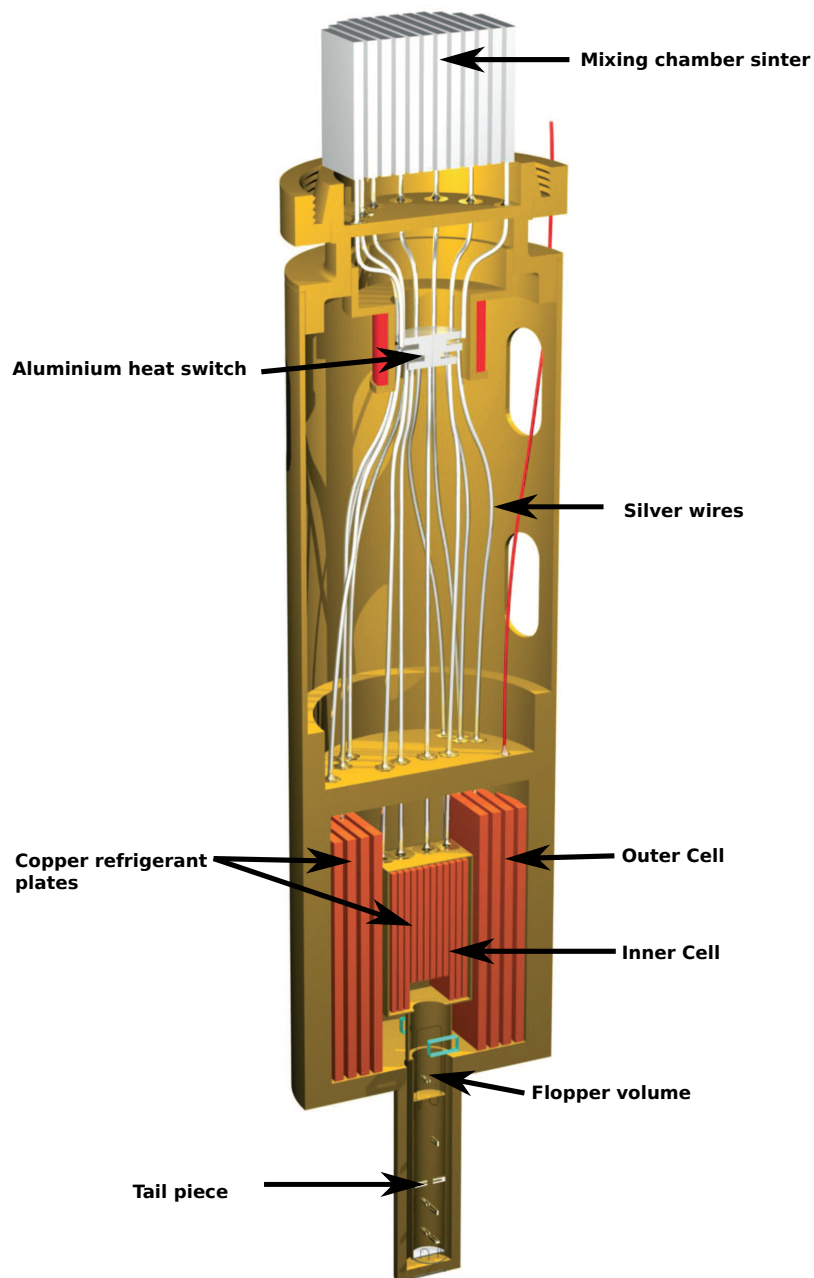
FIGURE 4.2: The Lancaster nested-cell demagnetisation stage. The mixing chamber contains sinter plates which are thermally connected through a superconducting Aluminium heat switch controlled by its own magnet solenoid. The outer cell wall is constructed of Stycast-filled araldite shells, whilst the inner cell wall is constructed of Stycast-soaked paper. The experimental cell shown here is the one used for flopper experiments and in Chapter 6, which was replaced by the method described here for experiments in Chapter 5.

Chapter 5 and 6. The nested cell comprises an experimental cell of two separate layers, both filled with liquid ^{3}He. The outer cell is defined by a hard Stycast wall and contains most of the copper plates used as refrigerant for nuclear demagnetisation. The outer cell contains just one VWR as a thermometer, known as OCTa and acts as an extra thermal shield for the inner cell.

The inner cell sits within the outer cell. At the top, there is space for more copper plates for nuclear demagnetisation. Below that is the experimental volume of the cell. The whole cell is made from Stycast-soaked paper. The cells share the same helium filling line, and therefore the inner cell can still be pressurised as there will be no pressure difference across the inner and outer cells. Both cells are thermally connected to the mixing chamber by silver wire attached to the copper plates through an aluminium superconducting heat switch.

Experiments in Chapter 5 required the design and building of a new experimental cell for the new NMR-Flopper device. Rather than remove both cells entirely and construct an entirely new cell, it was decided to simply replace the Stycast-paper section of the old inner cell. This required the opening and rejoining of the bottom of the outer cell.

The cell was detached from the mixing chamber and placed upside-down in the centre of a rotating turntable. The outer cell tailpiece was cut with a Dremel rotary cutting tool held in a fixed position whilst the cell was rotated on the disc. A new outer cell wall was constructed from Araldite. The wall was made of three concentric shells, with gaps to be filled with Stycast when gluing back to the rest of the original outer cell. Each shell was a different height, allowing a cap to be placed on top of the innermost gap after filling with Stycast and then glued on when filling the outermost gap.

Once the cell was opened, the tailpiece of the inner cell was cut out, the old Flopper device was removed and a new inner cell tailpiece was put in place. The devices at the top of the experimental volume before the tailpiece (ICTa, a 4.5 μm VWR, a 13.5 μm VWR and a QTF) were left and are common to both experimental cells.

4.2.2   New Inner Cell Design

The new tailpiece was originally designed to be much shorter and mainly house the NMR-flopper, allowing the outer cell to also be shorter. However, the new tailpiece soon came to house many devices: five nanobeams, a CNT, two sub-micron VWRs and a 25 μm QTF. A small external antenna was glued to the inside of the wall, but its use creates a large amount of heat. Instead, an external set of gradient coils are used and described below.

A schematic of the new experimental cell is shown in Fig. 4.3. The NMR-flopper is in roughly the same position as before but upside down. In the middle section is the CNT chip, placed vertically. The CNT is driven and detected by capacitive means, and
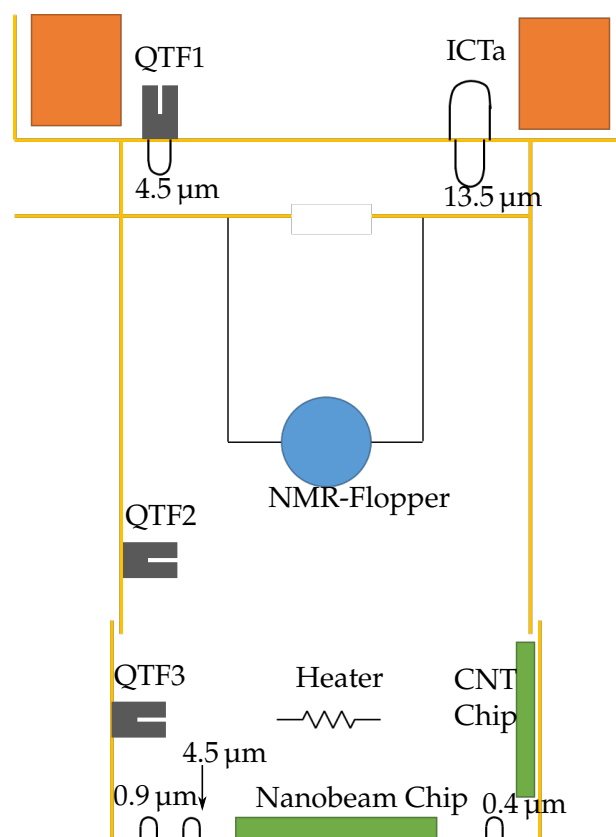
FIGURE 4.3: Schematic of the reconstructed cell with NMR-flopper. The upper part of the cell near the copper refrigerant is unchanged, housing ICTa and two other VWRs used as thermometers. The QTF1 here is also recycled from the previous cell. The old separation between the tailpiece was used to floor the old flopper device, and was removed, being replaced with the NMR-flopper. The bottom cap contains the nanobeams, the CNT chip, two sub-micron diameter VWRs and a tuning fork with a leg thickness of 25 µm.

therefore didn't require being oriented perpendicular to the magnetic field. At the bottom is a stycast plate holding a printed circuit board with three nanobeam chips glued and bonded. The plate has three holes allowing space for the nano-VWRs and a 13.5 µm wire. This whole plate is then glued over with stycast to prevent leaks.

Outside the outer cell, a set of two connected co-rotating gradient coils are located across from each other on the axis of the NMR coil. The coils serve as position detection for the NMR-flopper. The RF signal produced by the coil is picked up by the NMR coil on the flopper. When it is closer to a particular coil, the signal changes in magnitude and sign.

NEMS Grounding

Whilst the nano-beams had collapsed, it may be worth mentioning the scheme used to ground the devices whilst soldering them to the rest of the fridge. Soldering can potentially produce electrostatic discharge which can destroy the small devices. The observation of superconducting transitions in the beams indicates the metallic connection of the beam had not been destroyed by such a voltage.

The different ends of the nanobeams were bonded at the top of the chip but were shorted at the back. A rectangle was left in the stycast-paper plate holding the beams at the bottom, allowing the short connects to be cut and destroyed before sealing with another piece of stycast-paper and gluing over with stycast. The wires from the bond pads were then also shorted by a circular piece of wire, pre-soldered to every nanobeam wires. The shorts mean that any current created by soldering would not pass through the nanobeam but instead travel around the loops. In actuality, two loops were used. One was held at the mixing chamber on the drive side of the nanobeam circuit (if the nanobeam is the centre of the circuit), the other at the top of the fridge on the measurement side of the nanobeam circuit.

4.2.3 Flopper Position Calibration

To detect the motion of the old flopper during a DC ramp two coils wound in the same direction were mounted in the outer cell on the inner cell wall in the direction of motion of the flopper [75]. As well as sending a DC drive, a small, off-resonance high frequency 96.4 kHz signal is mixed into the drive. The two coils on the outer cell can pick up this signal via mutual induction, which increases as the flopper gets closer to a coil. A slow calibration motion is used and the signals of the two pickup coils are monitored. In this motion the flopper is moved until it hits a wall, and then moved in the reverse direction until it hits the other wall. Knowing the dimensions of the inner cell and using the small angle approximation allows for the position to be calibrated, and further a spring constant to be determined. The velocity can be calculated by differentiation.

In practice, the EMF induced by the motion of the wire in the same way as a VWR provided a much less noisy signal and therefore more precise measurement of the velocity. Therefore, the coils were only used for the initial calibration of the spring constant for the old flopper.

For the new NMR-flopper, the same principle was used but with a reversed relationship, and the two coils were connected in the same circuit by a wire. The NMR circuit can be driven via the coils through mutual induction. The response of the NMR circuit is measured instead. Since the NMR coil is large and the amplification of properties of resonance are used, the signal can have a much lower signal-to-noise ratio than the old
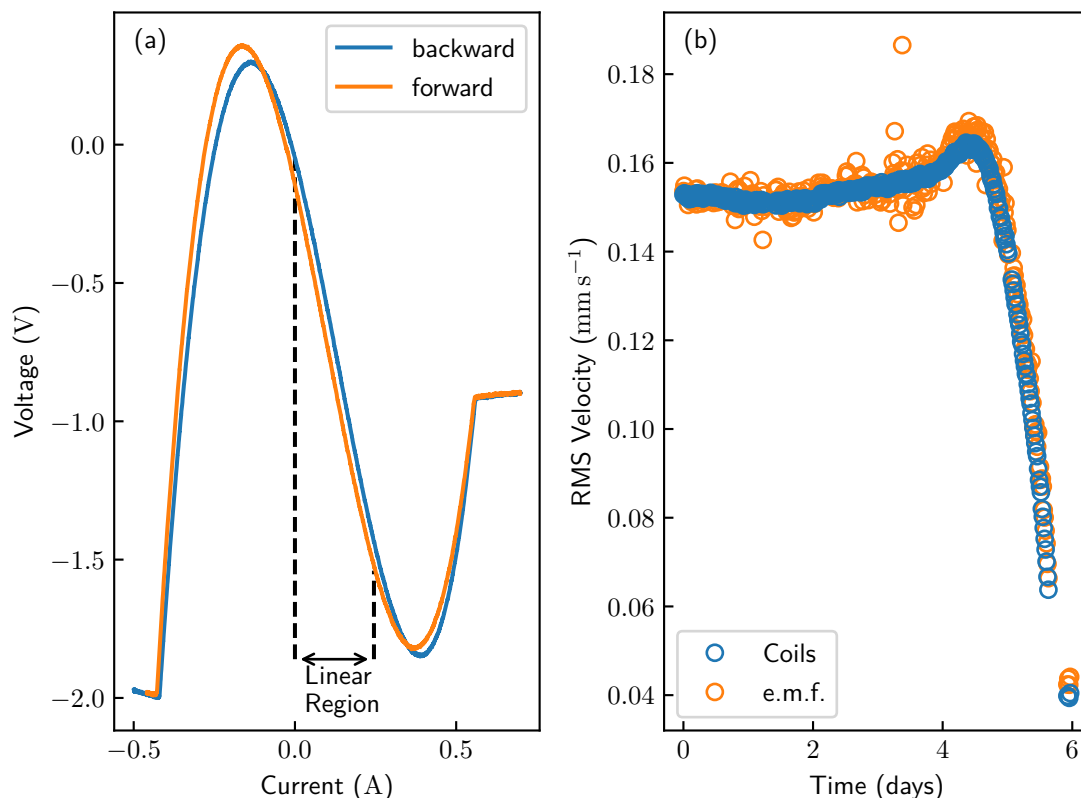
FIGURE 4.4: Position calibration of the NMR-flopper. (a) The flopper is slowly swept with a DC drive from each side of the wall whilst the external coils drive the NMR circuit. The difference in backwards and forwards motion is suspected to be due to the motion of trapped magnetic flux lines in the superconducting wire (see section 5.2.3). (b) A comparison of using the EMF and a fit to the linear region of the position calibration (coils) for measuring the velocity response of the NMR-flopper. See Chapter 7 for details.

flopper coils. Fig. 4.4 shows a typical wall-to-wall response and then the velocity calculated from a series of fixed frequency sine-wave drive currents (see Chapter 7) by the position detection compared to the velocity calculated from the EMF as done for a VWR. In our measurements, we only use the current end points and the distance travelled as the inner cell radius (18 mm) and the coil length (7 mm) to calculate the total distance travelled as 11 mm. We then stay in only the linear portion shown in Fig. 4.4 (a), and assuming the distance changes linearly here. We convert the voltage detected by the NMR circuit using a linear fit.

In Fig. 4.4 (b) we can see firstly there is good agreement, and that we can achieve better signal-to-noise ratio. The precision of this method is limited simply by the systematic error, rather than the signal noise.

4.3 NMR Magnets

A static magnetic field of 30.4 mT is required for an NMR resonance with a Larmor frequency $f_L = 948$ kHz given the gyromagnetic ratio γ for ^{3}He. Furthermore, the field needs to be extremely homogeneous within the aerogel region. Although the rate of decay of the transverse magnetisation τ_2 gives a minimum NMR linewidth, in practice the NMR linewidth is much more likely to be determined by the field homogeneity. If the field is slightly different in the different regions of the aerogel sample, then the helium in these regions will resonate at very slightly different frequencies, creating a larger line width in the NMR signal.

To create a homogeneous magnetic field, two new superconducting magnets were created: a static main NMR magnet was created to provide the 30.4 mT field needed for NMR, and a gradient magnet to control the field homogeneity.

The main magnet is made of 142 μm diameter superconducting NbTi wire and comprised of three connected parts. The top and bottom have 171 turns and eight layers, whilst the larger middle section has 1264 turns and four layers.

The gradient magnet comprises just two connected parts, in the same position as the top and bottom of the main magnet. It used the same wire and each part was 171 turns with just a single layer in design. Fig. 4.5 shows a simulation of the overall magnetic field created by a current of 1 A in the main magnet and 5 A in the gradient magnet. The calculated field in the NMR region is 33.65 mT A^{-1}.

4.4 Adding Helium-4

As mentioned in section 2.3.2, the polar phase in nafen-90 can only be stabilised when there is no paramagnetic surface ^{3}He. Second, pre-plating means there is no NMR signal from solid ^{3}He. To prevent ^{3}He from forming on the surfaces, one can pre-plate the surfaces with just over two monolayers ^{4}He as ^{4}He has a lower adsorption energy and is thus preferably attracted to the surface.

4.4.1 Helium-4 Pre-plating

To pre-plate the surface ^{4}He a small amount of ^{4}He gas is seeded into the cell and left to form layers. The amount of ^{4}He gas is based on the surface area of the whole cell and the area density of ^{4}He monolayers. The area density of the first two monolayers is roughly 0.1 Å^{-2} [101]. The surface area is dominated by the total area of the silver sinter on the copper plates, which totals about 437 m^2. One can then calculate the required volume of ^{4}He from the number of helium atoms.
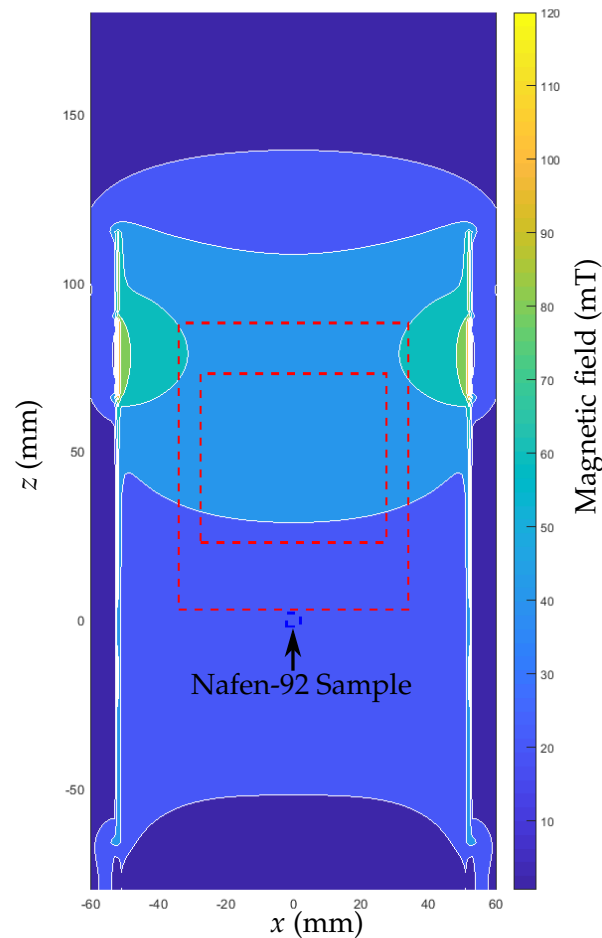
FIGURE 4.5: A simulation using the final wound properties of the NMR magnet (1 A supplied) and gradient magnet (5 A supplied) in the area around the experimental cell. The red dashed boxes show the position of the Copper demagnetisation plates for the outer and inner cells. The blue dashed box shows the position of the aerogel sample.

The pressure inside the cell as the gas can be monitored by the smaller VWRs. The devices can sense even small changes in the pressure. The gas is seeded in slowly and the VWR resonance response is monitored in tracking mode. When in gas, the frequency decreases and width increases according to hydrodynamic theory, but then the gas solidifies and the wire returns to its previous resonance width. When the wire doesn't return to its vacuum resonance, there is a small equilibrium pressure and saturated solidification has been achieved.

We can verify there is no solid ^{3}He once the cell is filled and at temperatures below 100 mK. Here, the normal fluid will obey Landau Fermi liquid theory, meaning the magnetic susceptibility is a constant equal to (2.15). If there is solid ^{3}He, the susceptibility of a paramagnet follows the well-known Curie law

$$\chi_s = \frac{C_T}{T} \tag{4.4}$$

where C_T is the Curie temperature and the total susceptibility will be the sum of χ_N and χ_s.

Since by (2.40) the integral of the absorption spectrum of an NMR signal is equal to the susceptibility, if there is an inverse temperature dependence of the absorption signal then there is solid ^{3}He, whilst if it is constant there is no solid ^{3}He. This check only applies to the cell with the NMR-flopper, and unfortunately was not possible for the experiments described in Chapter 5 and section 6.1.

4.4.2 Adsorption Purifier

Due to the spontaneous phase separation, helium-3 at ultra-low temperatures is the purest material in the universe, as liquid ^{4} will spontaneously separate and every other material is frozen. However, when warming up to higher temperatures, it is difficult to separate ^{3}He and ^{4}He.

The experiments with ^{4}He pre-plating were the first ever done at Lancaster, and therefore a new purifying system had to be designed and built. After an experimental run with ^{4}He pre-plating, we separate the mixed helium gases by again exploiting the difference in adsorption energies. This method takes after the Moscow group and is simpler than the rectification method, which requires the condensation of the mixture.

The design is simple and Fig. 4.6 shows the schematic. The mixture is slowly pumped out through a needle valve with a charcoal cryopump immersed in liquid ^{4}He. The needle valve is used as there appears to be an ideal pressure for the efficiency of the separator, which is fairly low [102]. After the needle valve, it goes through the purification chamber, made of spiralled copper-nickel tube packed with activated charcoal also immersed in liquid ^{4}He. As ^{4}He has a lower adsorption energy, it preferentially adsorbs onto the charcoal. In this way, ^{4}He is removed from the mixed gas and the purified ^{3}He gas passes through into the cryopump.

A leak detector is used to monitor the relative percentages of the outputted gas. Once the purification chamber reaches saturation, the percentage of ^{4}He in the output gas increases greatly. The purifying process is stopped when this rise begins, and the purified ^{3}He is removed from the cryopump and stored in a barrel. The remaining mixture of ^{4}He and ^{3}He gas can be stored in the auxiliary "dirty barrel".

The performance of the purifier is shown in Fig. 4.7. A leak detector employs a mass spectrometer. The mass spectrometer's accelerating voltage determines whether it detects ^{3}He gas, ^{4}He gas and hydrogen gas, and then the detector measures the throughput of that gas [103]. In Fig. 4.7 the readings of the mixture before and after purifying is shown as we sweep the voltage of the mass spectrometer. A background reading must
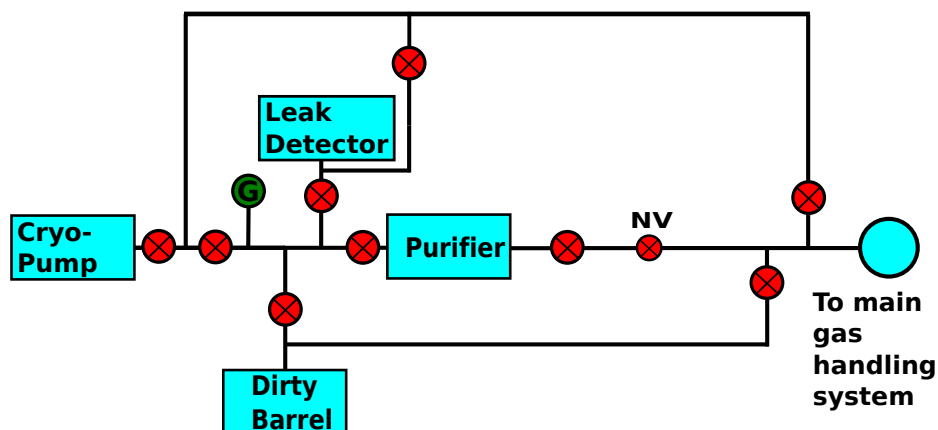
FIGURE 4.6: Schematic of the purification system. Red circles with cross indicates valves and the green G indicates a pressure gauge. The valve with NV is a needle valve, used for fine control of the gas flow. The cryopump used is a charcoal pump.

be taken before, where the leak rate against without any throughput is determined. The background is subtracted from subsequent calculations. The peaks for ^{4}He and ^{3}He are shown.

We see that the purifying system works very well, with a factor of 167 reduction in the percentage of ^{4}He gas. The design of this system is very simple and mobile. It can be used for any fridge in Lancaster and be easily replicated in another laboratory.
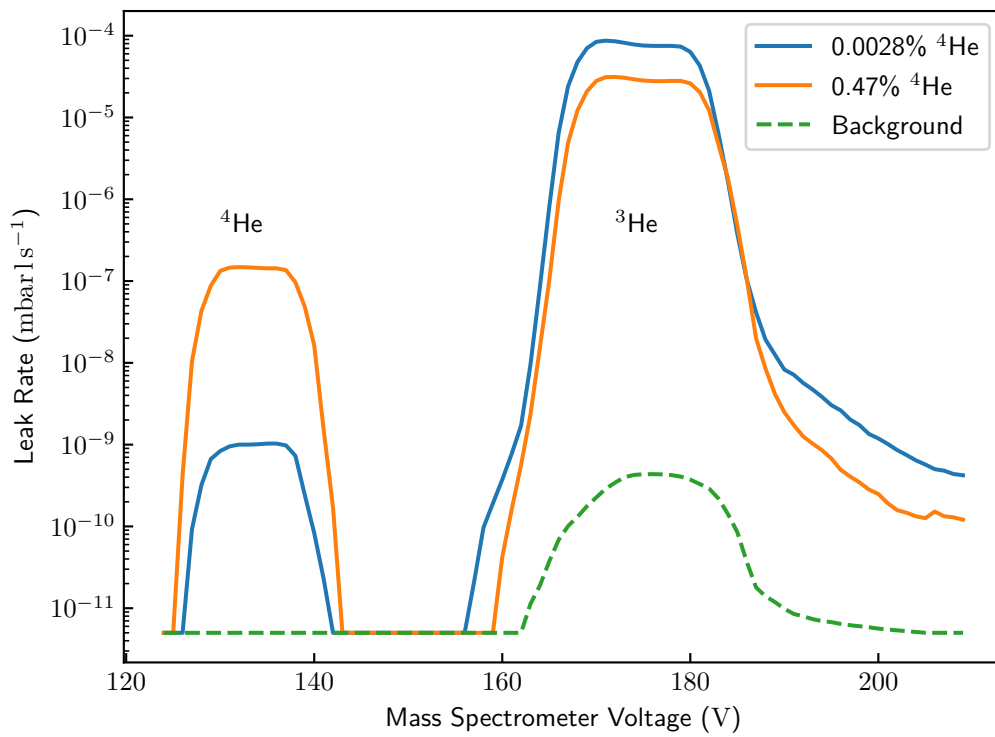
FIGURE 4.7: The ^{3}He and ^{4}He leak rates as detected by the mass spectrometer before purifying (orange) and after purifying (blue). The percentages of ^{4}He are shown respectively.

Chapter 5

Faster than Landau Experiment

In Chapter 3 we discussed the experiment in which the flopper is moved at quasi-uniform velocities above the Landau velocity v_L by the DC ramp method [6]. A nearby VWR thermometer and QTF thermometer measured the heat released by the bursts, and the force on the wire was inferred. This was compared to the damping force on the wire during oscillatory motion by an AC drive. For AC drive, there was a sudden and large increase in the damping force on the wire at $9\,\mathrm{mm\,s^{-1}}$, the predicted critical velocity for a cylinder. For DC ramps, there was no sudden onset of large damping on the wire and only a smooth increase. Whilst the amount of damping was larger than the thermal background due to collisions with the quasiparticle population in the ballistic regime, it was only a modest increase and the damping increased smoothly.

The suspected reason was that when the wire was travelling above the critical velocity, a certain amount of quasiparticles occupying SABS on the wire could begin escaping into the nearby bulk superfluid [5, 6]. This process leads to some dissipation and the damping force. Once they had all escaped, the process ends and no more states can be dissipated. In this chapter we detail an experiment exploring this model and investigate some dynamics of the surface-bound quasiparticles on the wire. This work a continuation of experiments in [104] and makes use of those results. All experiments in the following were carried out at saturated vapour pressure. The main results of this experiment are published in *Nature Communications* [105].

5.1   Model of Dissipation

We begin with a thought experiment based on the model of dissipation. First, we consider the 1D Lambert model of dissipation for several velocities, as discussed earlier in sections 3.1.4 and 3.2.1, and explained in [5]. At velocity $v < v_c$, there is a crossbranch process available to the surface-bound quasiparticles but no escape process. At velocities between v_c and the full Landau velocity v_L, the escape process becomes available for only the quasiparticles able to make the crossbranch process. To make the crossbranch process, a quasiparticle has to reverse the direction of its momentum almost elastically, for example
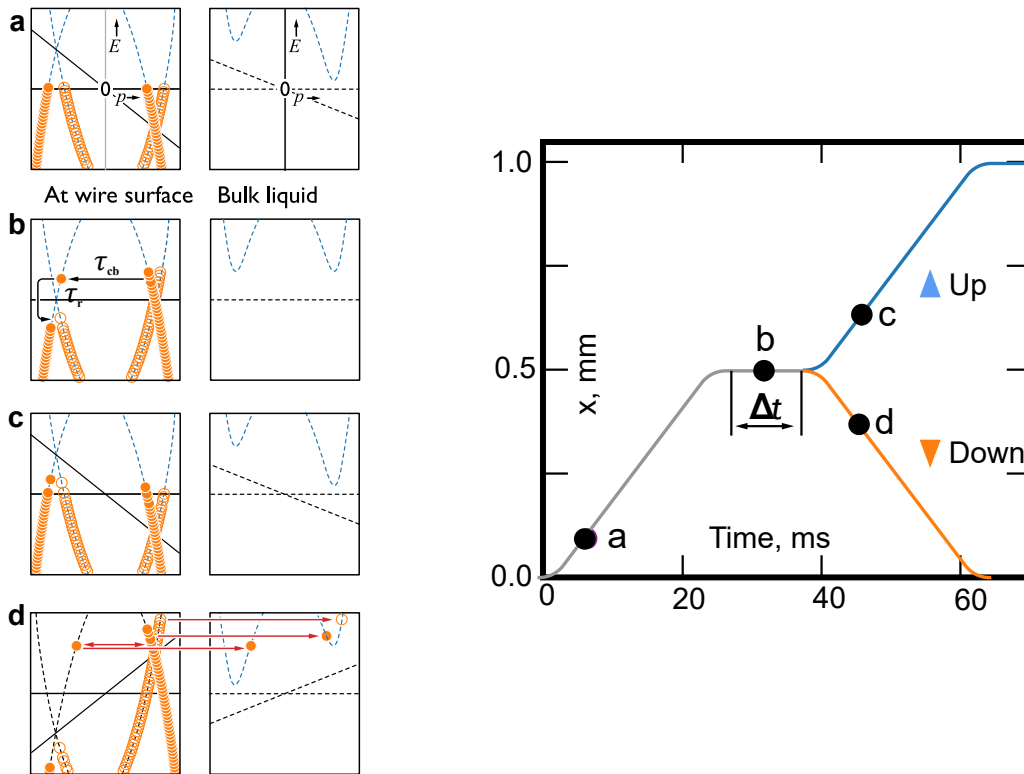
FIGURE 5.1: On the right is a schematic showing the difference of the up and down ramps at a velocity higher than v_c. On the left are the dispersion curves corresponding to the lettered positions on the ramp. (a) Halfway on the first half of the ramp. The surface states that can escape to bulk have done so and are now depleted. (b) The motion is stopped, the dispersion curves return to normal and the quasiparticles begin to reach equilibrium again. (c) The beginning of an up ramp after waiting a short amount of time. There was not enough time for the surface states to reach equilibrium, and therefore the surface states are still mainly depleted. (d) The beginning of a down ramp by reversing the direction after a short waiting time. The reversed direction of the dispersion curve tilt means there is an overpopulation of surface states on the RHS branch, allowing many more escape processes to undergo, increasing the damping.

from $-p$ to $+p$. The escape process results in dissipation into the system and a drag force on the flopper. At velocities $v > v_L$, the escape process becomes possible for some states even without making the crossbranch process. Eventually, the quasiparticles with high enough energy to escape will become depleted and the escape process ends (Fig. 5.1 (a)). There is no more dissipation.

The escape of quasiparticles into bulk increases the local quasiparticle population of the bulk superfluid. This increases the number of quasiparticle collisions on a thermometer, and is equivalent to if we had heated up the superfluid by some amount. It is important to remember that when talking about heating detected by thermometers in the

following sections, we are equivalently talking about the increase in quasiparticle density.

5.1.1 Alternating Direction

Now we can ask: what happens if we were to suddenly reverse the direction of the wire? In this case, there is a very large amount of quasiparticles that are available to escape or crossbranch and escape.

Instead of suddenly reversing the direction, we can stop, wait some time Δt and, after waiting, reverse the direction. The right-hand side of Fig. 5.1 shows the profile of these ramps. During the waiting period, the dispersion curves reset and then there are two thermalisation processes happening as the quasiparticles begin to equilibrate. First, the cross branch process happens again, then a relaxation process occurs, shown in Fig. 5.1 (b). The timescale of these two processes are τ_{cb} and τ_r, for crossbranch and relaxation, respectively.

Once we have waited some time, we can choose to either reverse the direction, or continue in the same direction. The ramps with a reversed direction we call "down" ramps, and with a continued direction "up" ramps. If we do not wait any time at all, the quasiparticle branches on the left-hand side and right-hand side will not have time to reach equilibrium again. In this case, we expect to see a large difference in the damping as the states that can escape are still depleted for the up ramps, but there is an overpopulation of quasiparticles that can escape for the down ramps (Fig. 5.1 (c) and (d)). If we wait a long time, the quasiparticles will repopulate and reach an equilibrium between both branches.

In summary, we expect the down ramps to dissipate more heat into the system at low waiting times. We expect no difference in drag force on the wire between up ramps and down ramps as the waiting time goes to infinity. We also expect the dissipation from ramps with a long waiting time to be less than the dissipation of down ramps with no waiting time, and more than up ramps with long waiting time.

5.2 Measurements

We compared DC ramps at several temperatures between $160\,\mu K$ and $225\,\mu K$ in superfluid ^{3}He-B at saturated vapour pressure, just at the edge of the ballistic regime. Fig. 5.2 is a zoomed in version of Fig. 4.2 showing the relevant devices in the experimental cell.

In the measurement, each ramp is measured whilst the thermometers are operated in resonance tracking mode. The resonance properties are recorded in the time before, during and immediately after the ramp. The exact same ramp is repeated a few times at this temperature before moving onto the next ramp type. In analysis, the response of the VWR and QTF thermometers are averaged. Fig. 5.3 shows a typical response from
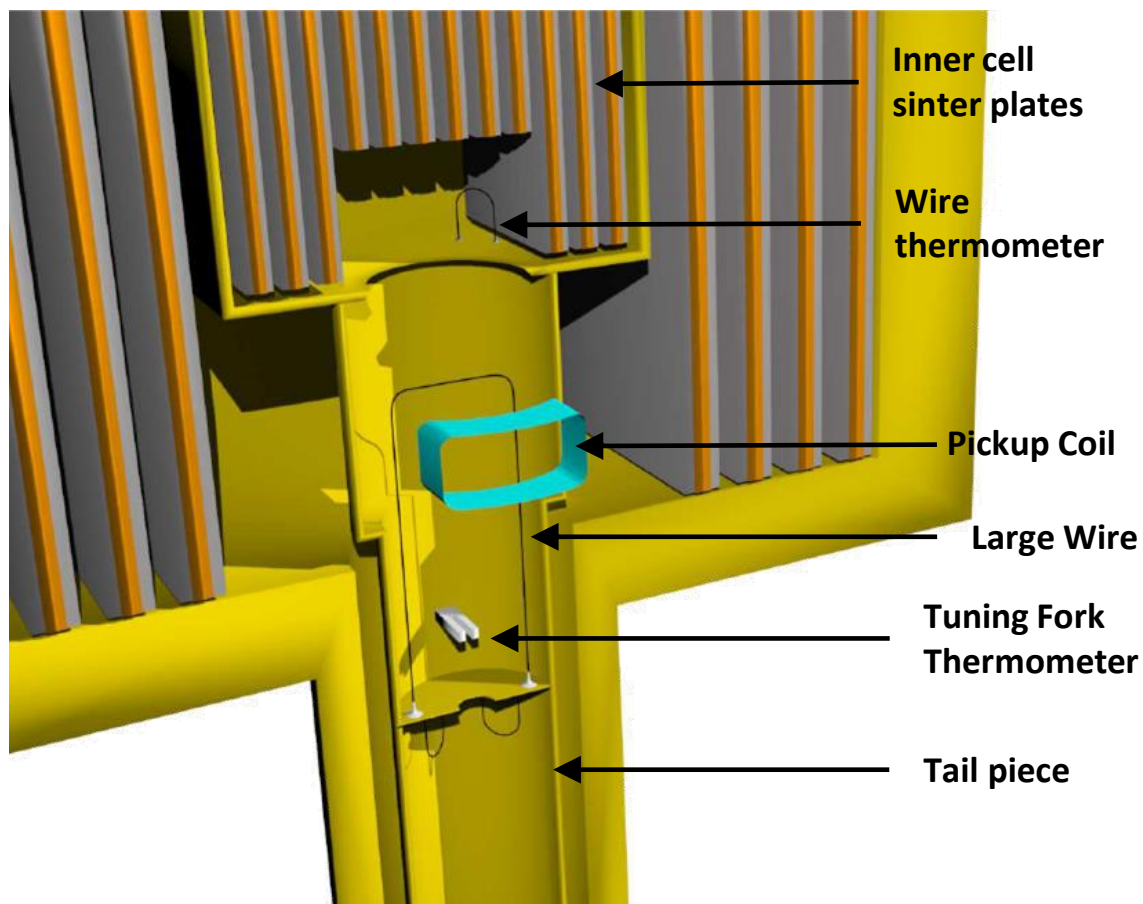
FIGURE 5.2: A zoomed 3D sketch of the top of the inner cell and devices used for this experiment and the Kapitza resistance analysis in Chapter 6. The inner cell contains eighty thin and eight thick copper plates that are sintered with silver powder. The geometric volume formed by cutting the plates (see Fig. 6.6) cell contains the 4.5 μm vibrating loop wire. A cylindrical volume containing the flopper and quartz tuning fork is connected via a circular cutout to the bottom of the geometric volume. The cylindrical volume also has a tailpiece separated by a small hole.

the two thermometers to a ramp. The time dependence of the thermometer response is analysed in Chapter 6 to find the Kapitza resistance.

Many of the measurements were made previously and the effects of varying the ramp parameters of velocity, acceleration time and waiting time have been analysed [104]. The effects are as follows: increasing acceleration time increases the total dissipation; increasing velocity increases the amount of heating; decreasing acceleration time excites higher resonance modes of the flopper (particularly below 2 ms). A ramp with a distance more than 1 mm experience large effects of magnetic heating (see the velocity dependence results).

For this thesis, new measurements were made with 2.5 layers of ^{4}He pre-plating. The
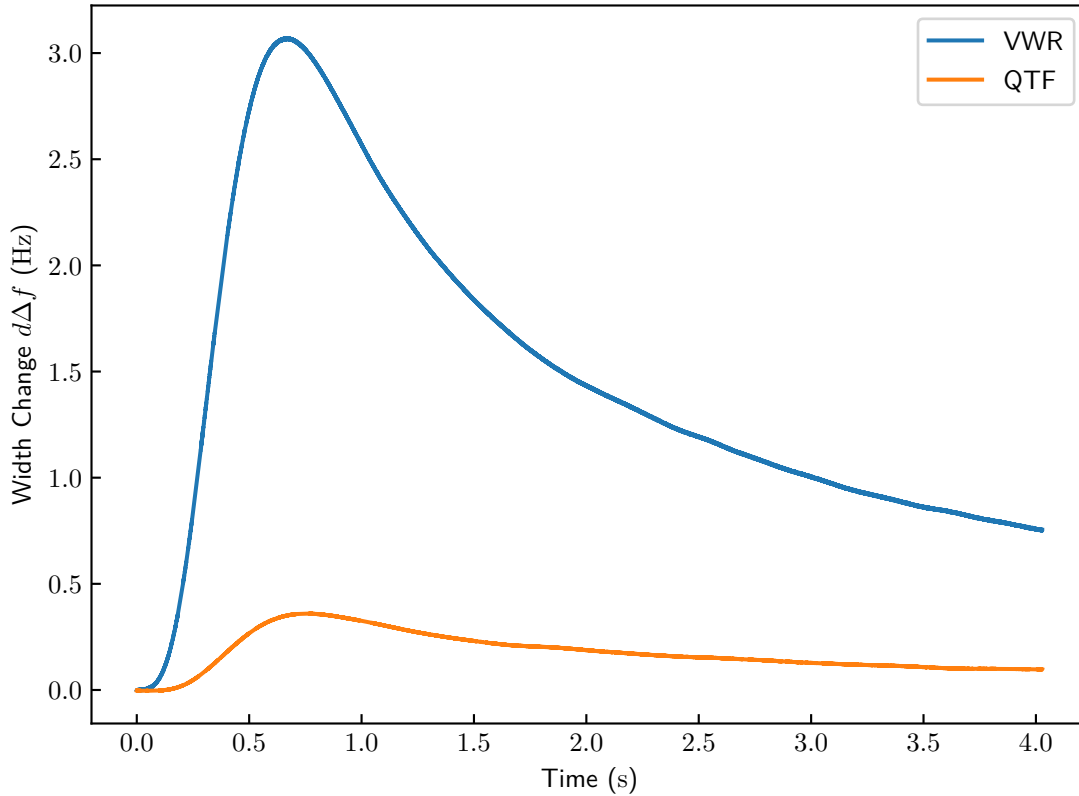
FIGURE 5.3: The change in width $d\Delta f$ of the 4.5 μm VWR and QTF thermometers as a response to a 45 mm s^{-1} up ramp with a total distance of 1 mm with 2.5 monolayers of ^{4}He pre-plating. The base width are 25.9 Hz and 3.22 Hz for the VWR and QTF respectively, corresponding to a temperature of 194±1 μK. The VWR reacts quicker due to its higher width, as expected from (3.54).

main focus was velocity dependent measurements which were not taken in previous experimental runs, but three sets of waiting time measurements were taken. These waiting time measurements are compared with previous measurements using the same total distance of 1 mm, acceleration time of 3 ms and velocity of 45 mm s^{-1}. The ramps were stopped at halfway, 0.5 mm, for the waiting period. A ramp with $\Delta t = 0$ will still have two separate halves, but with no instructions to wait after finishing the first half. The waiting time measurements are compared with previous waiting time measurements with the same acceleration time, total distance and velocity.

These three waiting time measurements are compared to similar previous measurements of waiting time. The total distance is the same, and the acceleration periods are from 3 ms–5 ms, but most commonly 3 ms is used. This is within the good range of acceleration values and has effect on the analysis presented here, as we are only concerned

about the waiting time dependence of the dissipation, not the magnitude.

For the velocity measurements, the ramps analysed here have the same distance, acceleration time and stopping point as above. The ramp velocity was varied between $2\,\mathrm{mm\,s^{-1}}$ and $50\,\mathrm{mm\,s^{-1}}$ and there were three wait times $0\,\mathrm{ms}$, $0.05\,\mathrm{s}$ and $0.1\,\mathrm{s}$.

To convert the change in resonance width $d\Delta f$ to the amount of heat energy released, we use a previous calibration for the $4.5\,\mathrm{\mu m}$ wire [106]. The calibration was made by using AC motion pulses with similar durations to a DC ramp and monitoring the resonance as it is in tracking mode. The EMF and drive current of the flopper are measured, and the energy is calculated. In the calibration, it is assumed all the energy dissipated is released as heat into superfluid ^{3}He-B. The calibration is [106]

$$q = 88.6\,\mathrm{pJ}(d\Delta f - 0.46\,\mathrm{Hz})^{0.26}. \tag{5.1}$$

A second option is to calculate the heat energy from thermodynamics. Integrating the heat capacity of the B phase (2.25) between the initial and max temperature of the thermometer gives results for the energy released with the same order of magnitude at low changes in width, but relies on knowing the correct volume of superfluid ^{3}He. In Chapter 6 the possible volumes used for the heat capacity are discussed in more detail.

5.2.1 Waiting Time Dependence

Fig. 5.4 shows two of the new waiting time measurement in terms of the heat energy q produced and detected by the VWR for up (q_{up}) and down (q_{down}) ramps. We see that the expectation that the down ramps dissipate more energy into the system is matched. The difference in dissipation released by the two ramp sequences increases as the waiting time increases, which was predicted by our simple model. However, the difference doesn't reach zero and actually reverses. The difference in Fig. 5.4 at long waiting times is of the same order of magnitude as the values of the magnetic heating constant a discussed below.

We can fit the heating from up and down ramps with a simple exponential decay plus an offset. Since $\Delta q = q_{\mathrm{down}} - q_{\mathrm{up}}$ is negative at long waiting times, we fit q_{up} and q_{down} separately but with the same decay time constant τ_{d} rather than fit the difference. This time constant is plotted in Fig. 5.5. The time constant is the same at all temperatures measured.

The surface conditions may play an important role in the dynamics of the surface states, but here the 2.5 layers of solid ^{4}He pre-plating had no effect on the time constant. From [71], this should have increased the specularity from entirely diffuse to a specularity between 0.2 and 0.5, (where 1 is fully specular, 0 is diffuse and -1 fully retro-reflective). The average time constant is $6\,\mathrm{ms}$ with a range of $6\,\mathrm{ms}$. Therefore, $\tau_{\mathrm{d}} = 6 \pm 3\,\mathrm{ms}$.
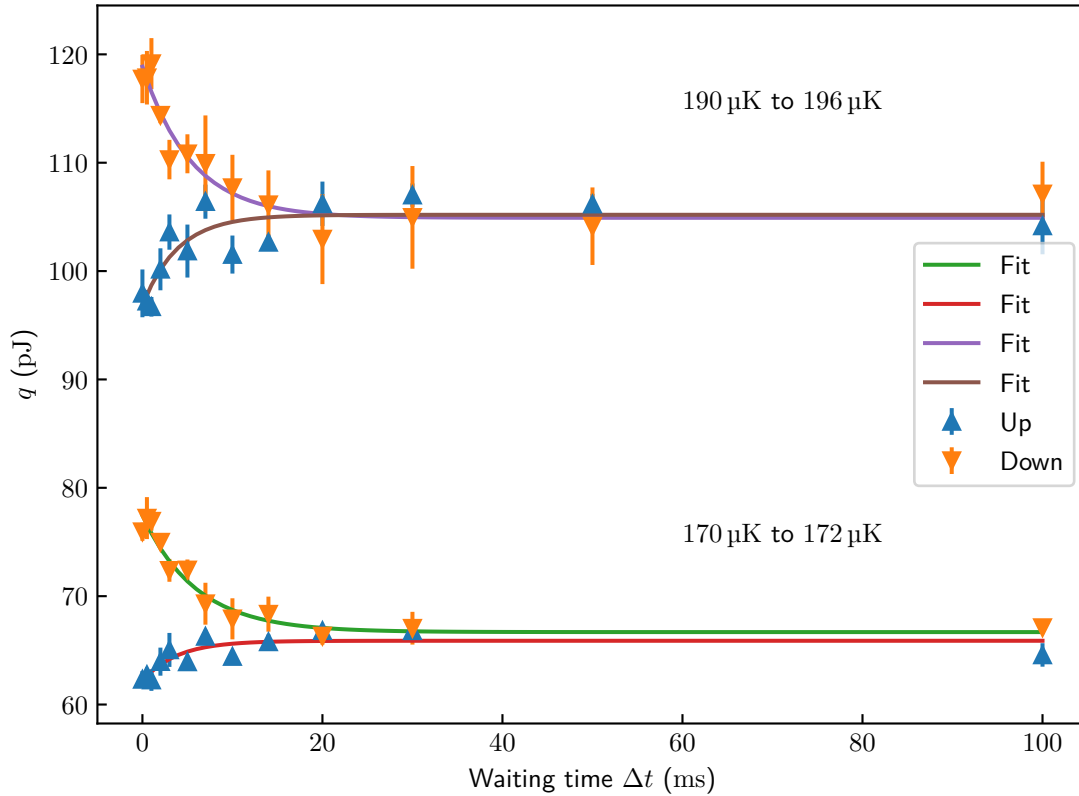
FIGURE 5.4: Two waiting time measurements with 2.5 layers of ^{4}He pre-plating. The magnetic field is 130 mT in both cases. The solid lines represent exponential decay fits with an offset. Each temperature set uses the same time constant. The difference between the offsets is similar to values of the magnetic heating constant a in (5.2). The errors are estimated from the error in the change in width. The waiting time measurements are similar to those in [104], with which we perform the same analysis.

Interpreting the Decay Constant

The fitted decay constant can refer to either of the two time constants related to the two processes in Fig. 5.1, the crossbranch or the relaxation process, τ_{cb} and τ_r. We argue that decay constant is a measurement of τ_{cb} only by considering our model for two limits of τ_r.

If $\tau_r = 0$, then a SABS would crossbranch and immediately fall in energy. We would expect a second surface state to immediately follow, and the whole process would be essentially limited by τ_{cb} and how many particles there are that are needed to cross. If $\tau_r = \infty$, then we would expect a diffusive process. And in this case, the time would still be determined by τ_{cb}. That is to say, we can only have measured τ_{cb}.

To test for τ_r it would be best to use AC motion. The Lambert model predicts that there
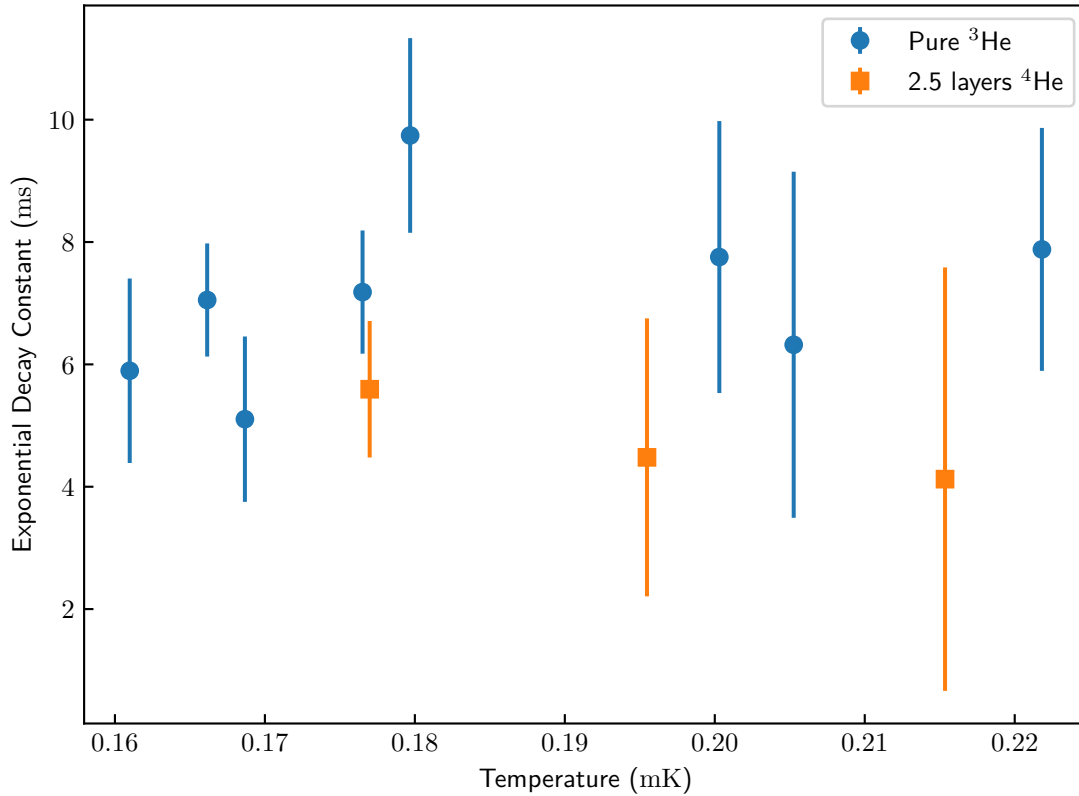
FIGURE 5.5: The exponential decay time constant τ_d does not change with the temperature. The 2.5 layers of ^{4}He pre-plating does not appear to have any effect. From the average and range, $\tau_d = 6 \pm 3\,\text{ms}$.

will be a reduction in the critical velocity when the frequency of the motion approaches $1/\tau_r$ [5]. At frequencies higher than this, the repeated tilting of the dispersion curves allows some surface states to increase in energy until the point they can just escape to bulk, which can onset much earlier than v_c. Since v_c depends on the local flow and therefore geometry of the device, this requires using the same geometry with different frequencies to properly test. To do so, one can use higher modes of an oscillator. Other groups at Lancaster have not seen a reduction in v_c using the second modes of a quartz tuning fork up with a frequency up to 158 kHz [105].

The process τ_r therefore must be extremely fast, with a time constant less than 7 μs. An alternative model for supercritical velocity has been proposed by Kuorelahti, Laine, and Thuneberg [107]. As a mechanism for supercritical superflow, they find that the Landau velocity can be increased for a macroscopic cylinder with a radius larger than the coherence length and the damping effect reduced. However, this increase is only about
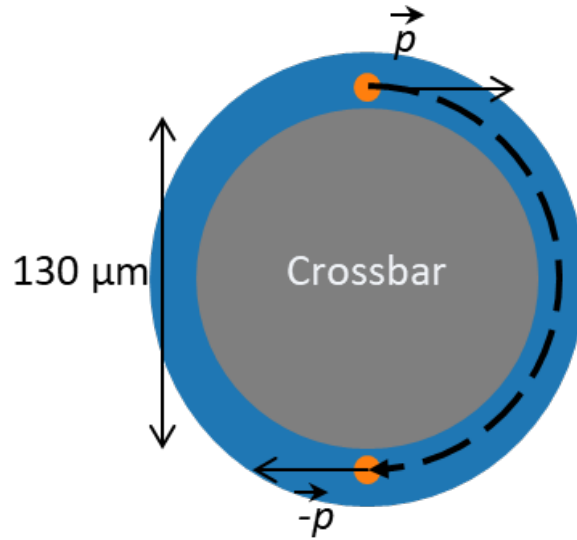
FIGURE 5.6: An illustration of the cross-section of the flopper crossbar (grey circle) with a surface state (orange dot) trapped inside the surface layer (blue). At the top of the crossbar, this SABS has the wrong momentum to join the bulk superflow and must move around the entire wire.

$1.12v_{\mathrm{L}} = 30.4\,\mathrm{mm\,s^{-1}}$ and the damping reduction found was not enough to explain results of the original experiment [6, 107]. Their model is however preliminary, and does not include many effects at the surface, such as Andreev reflection. Nevertheless, they suppose that surface quasiparticles collide with the wire with a time constant equal to the coherence length divided by the Fermi velocity. They approximate this constant as $1 \times 10^{-9}\,\mathrm{s}$. The extremely fast time constant here is used as an argument against the Lambert model. The idea here is that the very short bound state dynamics can not be perturbed by the much longer time scales of our acceleration period (or oscillation period for AC motion). Hence, the bound states remain in equilibrium through the motion and another mechanism is needed to explain the results of this thesis. However, if we have correctly identified that there are actually two processes, and one of them is relatively slow, this would explain how one can create nonequilibrium populations of bound states between branches.

It would be fruitful to explore the possibility of a reduced v_{c} caused by reaching a higher frequency than $1/\tau_{\mathrm{r}}$. To do so requires high-frequency resonator devices, such as MEMS and NEMS.

Mechanism for the Decay Constant

If we take the decay constant as a measurement of the replenishment rate of the surface bound states, there needs to be some physical process of how this is possible. One proposal is that bound states from elsewhere can crawl up the legs of the wire to the crossbar, driven by a concentration gradient [104]. The legs are 25 mm long. We can identify three velocities in ^{3}He. The Fermi velocity $v_F \approx 60 \, \text{m s}^{-1}$, the group velocity $v_g \approx v_F/3$, and Landau velocity $v_L = 27 \, \text{mm s}^{-1}$. Using the leg length, only the group velocity seems promising, giving about 1 ms time. This simple calculation does not include any surface effects, and it is possible the process is diffusive, which would increase the time. An effective test would be changing the length of the legs. An alternative test is to use a floating device which has no legs or attachment to other surfaces at all. Replenishment would then be impossible, and a device for this is currently under construction [108].

A second possible interpretation is that surface bound quasiparticles need to be in a position with the matching direction of momentum to join the bulk. An illustration is given in Fig. 5.6. In this simple drawing, a quasiparticle on the top of the wire has momentum in the wrong direction to join the bulk. It must make travel to the bottom of the wire, where the momentum will be in the correct direction. According to [109] and [110], surface states should have a velocity less than or equal to the Landau velocity. A simplified picture goes that v_L is a kind of escape velocity: if they had greater than Landau velocity, they would already be able to escape to the bulk.

Following this, the time required to traverse half the wire is simply πR_0. This gives a travel time of 7.5 ms. This is well within the range of values calculated for our device.

5.2.2 Velocity Dependence

When examining the velocity dependence, there was an unusual effect. Fig. 5.7 shows the heating at different ramp velocities response with the different ramps types with zero waiting time. Most experiments were done with only down and up ramps, but this data is representative of those and qualitatively the same. At high velocities for the up ramps and down ramps, the expected relationship is true. The down ramps indeed produce more heating. At low velocities, where we should expect no difference, the relationship is strangely reversed. The cause of this is a suspected magnetic heating effect.

5.2.3 Magnetic Hysteresis Heating Effect

In order to investigate the effects of the SABS, which should exist at zero temperature, we need to remove the effects of thermal background of bulk quasiparticles. Ordinarily, a
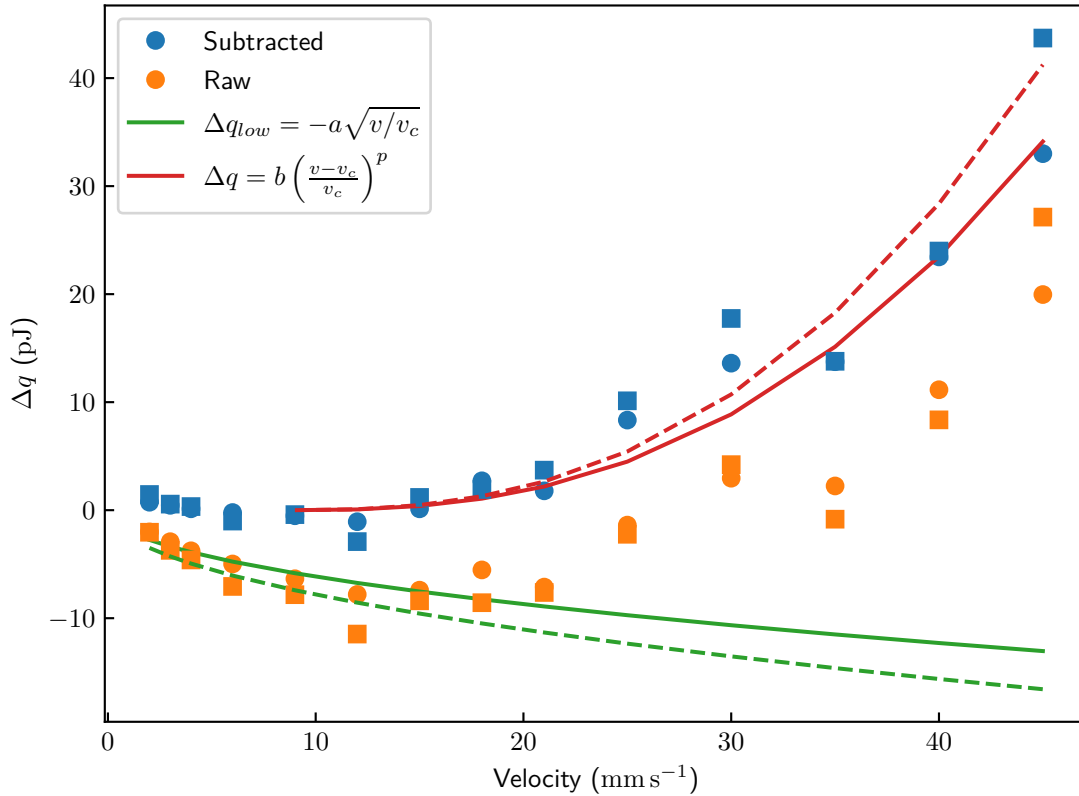
FIGURE 5.7: Two velocity measurements with Δt showing the original $\Delta q = q_{\text{down}} - q_{\text{up}}$ (orange data) which is fitted below v_c with (5.2). This is subtracted to attain the heating due to surface states (blue data), which is fitted above v_c by (5.3). After subtraction of the magnetic hysteresis, below v_c there is no heating and then there is a smooth increase. The magnetic field for both was 130 mT. The temperatures are 185 μK–195 μK (circle and solid lines) and 197 μK–209 μK (squares and dashed lines).

simple way of doing that would be to plot the difference in heating Δq. There is no directional dependence of damping in the ballistic regime, so both type of ramps with identical velocity and the same background temperature should have the same background damping. This subtraction should then leave only damping processes with a directional dependence. This subtraction is shown by the orange data in Fig. 5.7. There is a positive Δq at high velocities, but a negative Δq at low velocities.

To explain the data at low velocities, it was supposed that there is a magnetic hysteresis effect [104]. The flopper wire is made of a type-II superconductor, which can pin magnetic flux lines [13]. As a type-II superconductor, the wire will be in a state of flux penetration. As the wire moves, the flux moves relative to the wire, creating some damping. The motion of these flux lines leads to some slightly extra dissipation [111].
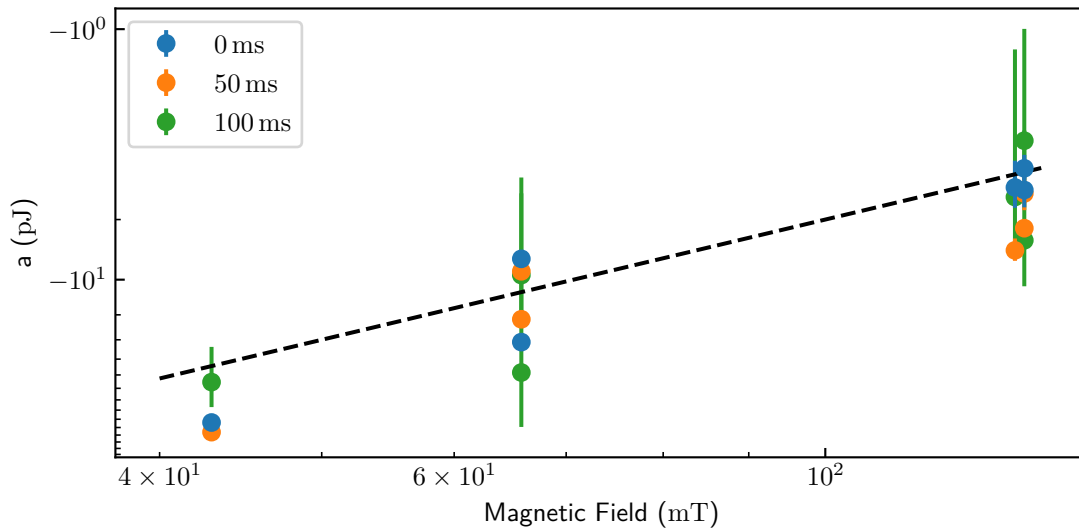
FIGURE 5.8: The constant a used to fit the magnetic effect at velocities below v_c with (5.2). The colours refer to Δq velocity measurements with $\Delta t = 0\,\text{ms}$, $50\,\text{ms}$ and $100\,\text{ms}$. The black dashed line is a guide for the eye and corresponds to $a = \dfrac{-5.0\,\text{pJ}}{B^2}$.

The consequence of the damping due to the flux lines seems to be that the down ramps do not move quite as far as up ramps, and therefore do not collide with as many thermal bulk quasiparticles as up ramps.

We fit the low velocity data with an empirical power law, which is

$$\Delta q_{\text{low}} = a \sqrt{\frac{v}{v_c}}. \tag{5.2}$$

The fitting constant a for several datasets is shown in Fig. 5.8 and seems to follow a magnetic field dependence close to B^{-2}, which indicates this difference is indeed likely due to some magnetic effect.

5.2.4 Damping from Bound States

Once we fit the empirical magnetic law, we can subtract it. Performing this subtraction gives us the blue data in Fig. 5.7. This picture matches much more closely to the expected picture, with Δq being large at high velocities and roughly zero at low velocities. This data is fitted with an empirical law

$$\Delta q = b \left(\frac{v - v_c}{v_c} \right)^p \tag{5.3}$$

b is different depending on the dataset but falls within the range $0.4\,\text{pJ}$–$1.2\,\text{pJ}$ and $p = 2.5 \pm 0.5$. Lambert's model calculates $p = 2$ for high velocities, although this is not for our reversal ramps where the bound states could be depleted [5].

5.3 Conclusions

In this experiment we presented a simple Lambert-style model of the supercritical superflow explained in terms of the dynamics of surface bound states on the crossbar of the flopper. Using this model, we compared moving the flopper at supercritical velocities primarily with two types of motion. An initial direction of motion was chosen, and then stopped. After stopping, the same direction was repeated, or the direction was reversed.

Measuring the difference in dissipation between these two ramps allows us to exclude the dissipation from collisions with bulk superfluid quasiparticles, which is not direction dependent. A further correction for a magnetic dissipation effect had to be made. Once this was carried out, the data clearly shows that there is a difference between the two ramp types when we wait for only small times. This difference appears at v_c, as predicted by Lambert's model [5]. In the absence of other possible explanations that would be direction dependent, we conclude that the extra dissipation seen above v_c for quasi-uniform velocity ramps is due to the escape of surface-bound quasiparticles to the bulk superfluid.

By varying the waiting time, we found that the difference between up and down ramps at long waiting times is simply the magnetic hysteresis. By fitting the heating produced by each type of ramp as a function of waiting time with an exponential decay, we found the time constant of the crossbranch process identified in Lambert's model.

We should emphasise the preliminary and simple nature of this model. In this work, it is shown as a simple 2D problem. However, this simple Lambert model has predicted the behaviour of several phenomena, and provides a qualitatively accurate explanation of the faster than Landau velocity observed in Fig. 3.10 and reported in [6]. Furthermore, an alternative model developed by Kuorelahti, Laine, and Thuneberg predicts an enhanced Landau velocity at $\sim 1.12 v_\text{L}$ for a moving macroscopic cylinder and does not have a mechanism understanding the difference between up and down ramps [107]. In our velocity measurements, no such enhancement was found.

As yet, the nature of the physical process leading to the crossbranch processes τ_cb is unknown. Hopefully this can be done with further analysis and experiment. One experiment is currently being designed, with plans to move a floating sphere [108]. If the quasiparticles replenish by moving up the legs, this process will become impossible. A second test of Lambert's model is the prediction of a reduced critical velocity at frequencies higher than the second relaxation process, $f > 1/\tau_\text{r}$. The critical velocity depends on the local flow around the oscillator, so it would be convenient to have the same shape

oscillator. Using MEMS and NEMS in ballistic superfluid ^{3}He-B present an excellent opportunity to test this prediction.

Chapter 6

Thermometric Experiments

This chapter details experimental results in relation to the response of vibrating wire thermometers. First, measurements of Kapitza resistance between liquid ^{3}He and copper covered with sintered silver are reported, which are published in *Physical Review B* [112]. This is compared to both with and without a surface layer of ^{4}He covering the sinter.

As mentioned in the section 4.1.3, the temperature dependence of Kapitza resistance in the superfluid phase has been controversial. In the ballistic regime of ^{3}He-B, early measurements by Parpia at Cornell and at Lancaster showed an exponential temperature dependence but a later investigation by Voncken *et al.* investigate a power law and found a T^{-2} or T^{-3} dependence the most likely [27, 90, 91, 113]. Replicating the results of one of these experiments would improve our understanding of heat exchangers for designing low temperature experiments.

The chapter also presents some preliminary measurements of the sub-micron diameter vibrating wires as we explore their possibilities as bolometers in superfluid ^{3}He. In superfluid ^{4}He, nanoscale devices have been successfully employed as ultra-sensitive probes from less than 10 mK to the superfluid transition temperature [59, 62]. However, the coherence length is smaller than a nanometer in superfluid ^{4}He [1]. In superfluid ^{3}He the coherence length ranges from 20 nm to 80 nm depending on pressure [26]. One VWR has a diameter of just 400 nm, and the coherence length could affect the damping on the wire. The measurements presented here were carried out at saturated vapour pressure, where the coherence length is 80 nm [26].

6.1 Measurements

In this section we analyse the thermometer response to DC ramps presented in the previous chapter. In the experiments, the DC ramps released a heat burst. In the following analysis, only up ramps with zero waiting time described in Chapter 5 are analysed. The heat burst from a ramp is measured by two nearby thermometers: a 4.5 μm diameter VWR and a QTF. The original set up is shown in Fig. 5.2. The resonance widths of the thermometers are measured continuously as they are left in the tracking mode described in

3.3.2. Naturally, the resonance widths of the thermometers increase during the ramp, before decaying back to a base temperature. The analysis for Landau velocity only requires the height of the response, but analysing the full response can be used to illuminate the thermal interaction between superfluid ^{3}He-B and silver sinter.

Before a DC ramp, the bulk quasiparticle population is in thermal equilibrium with the thermal bath. The thermometers are resonating with a base resonance width of Δf_base.
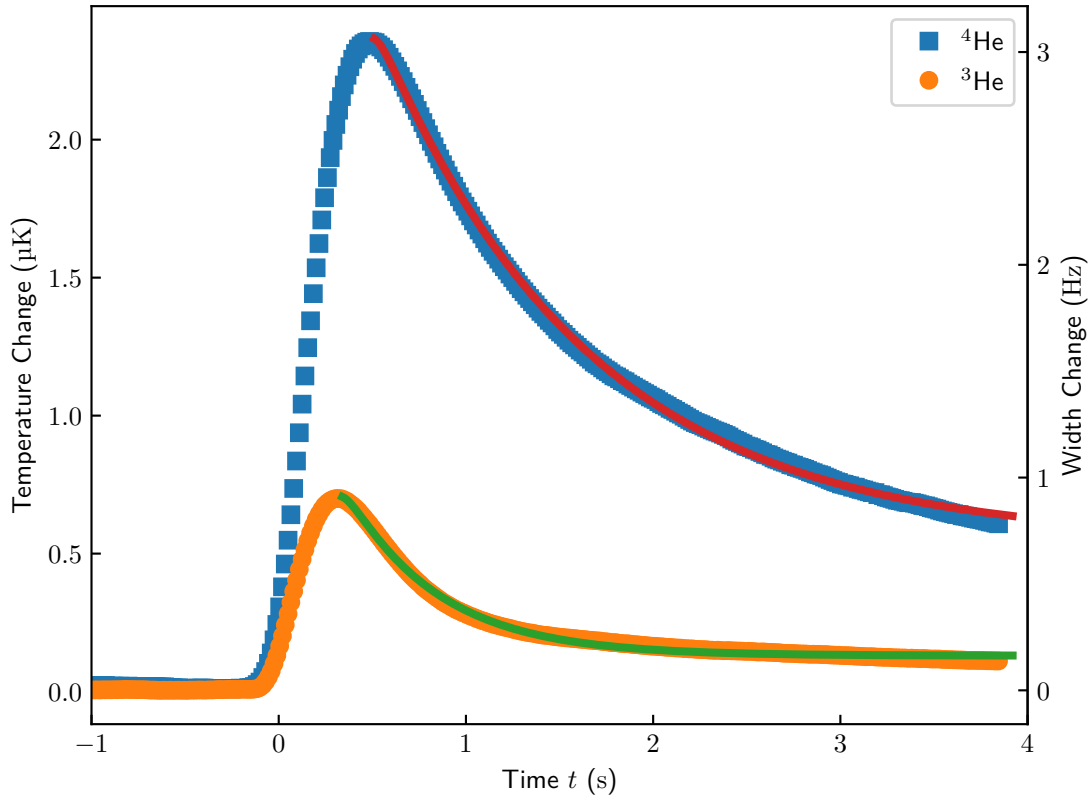
FIGURE 6.1: The response of the VWR with diameter 4.5 µm for pure ^{3}He and two layers of solid ^{4}He coverage on the cell surface at temperatures of 197 µK ($\Delta f_\text{base} = 30.4$ Hz) and 193 µK ($\Delta f_\text{base} = 25.9$ Hz), respectively. The corresponding width change for the ^{4}He data is given by the right y-axis. The ^{3}He data was measured at a slightly different temperature, and hence the width change is 5% larger for a given temperature change. Solid lines represent the fits from Eq. (6.1).

After a DC ramp is started, the released heat goes directly into the liquid and increases the bulk quasiparticle population, detected by a rapid increase in thermometer width up to a peak value. The quasiparticles excited begin colliding with surfaces. In the ballistic regime these collisions are either near-elastic or the quasiparticles lose enough energy to recombine as a Cooper pair. We expect an exponential decay of the quasiparticle density

until thermal equilibrium is again reached, measured by the thermometer width reaching the base value. Figure 6.1 shows a typical response of a thermometer width to a DC pulse that we model as [114]

$$\Delta f = \Delta f_{\text{base}} + H \frac{\tau_{\text{b}}}{\tau_{\text{b}} + \tau_{\text{w}}} \left(e^{-t/\tau_{\text{b}}} - e^{-t/\tau_{\text{w}}} \right). \tag{6.1}$$

Here, H is a constant describing the amplitude of the width response and τ_{w} is the response time of the thermometer, determined by the resonance width and is approximately equal to $1/(\pi \Delta f_{\text{base}})$ (see (3.54)). The decay time constant τ_{b} is related to the heat capacity given by (2.25) [27]

$$R_{\text{K}} = \frac{\tau_{\text{b}}}{C_B}. \tag{6.2}$$

The thermal conductivity of the stycast cell walls is extremely low. Therefore, we expect only collisions with sintered copper plates to result in recombination. The inner cell contains 8 copper plates of thickness 1.1 mm and 80 copper plates of thickness 0.2 mm which are used as a refrigerant for nuclear demagnetization. Ulvac brand silver powder of 70 nm particle size is sintered to both sides of each copper plate with a filling factor of 0.5 and results in a microscopic surface area of 80 m^2 [89].

6.1.1 Comparison of ^{3}He and ^{4}He Plated Cells

Fig. 6.2 shows the time constants extracted from the measured response of the 4.5 μm wire to ramps at different temperatures. Unfortunately, the QTF was too noisy to provide useful measurements in the ^{3}He run. However, between those measurements and adding ^{4}He a low temperature attenuator was added to the QTF circuitry, much improving the signal quality. The QTF provides similar results in the case of ^{4}He measurements as the VWR does to identical ramps for ^{4}He pre-plated cases. The ramps are up ramps with velocity 45 mm s^{-1} over a total distance 1 mm with an acceleration period of 3 ms. They have waiting time $\Delta t = 0$, see Fig. 5.1 for details. For this analysis these ramps are functionally equivalent to a constant ramp without stopping in the middle, as according to (6.1) the time dependence is not dependent on the magnitude H and acceleration time is much shorter than the response time of the oscillator.

The decay constant τ_{b} extracted for ^{4}He pre-plated surfaces is 1.0 ± 0.1 s which is approximately double the 0.5 ± 0.1 s constant observed in pure ^{3}He. Similar results were obtained for the QTF thermometer for pure ^{4}He, with the same average. From (6.2) this means that ^{4}He plating has effectively doubled the Kapitza resistance. Furthermore, the
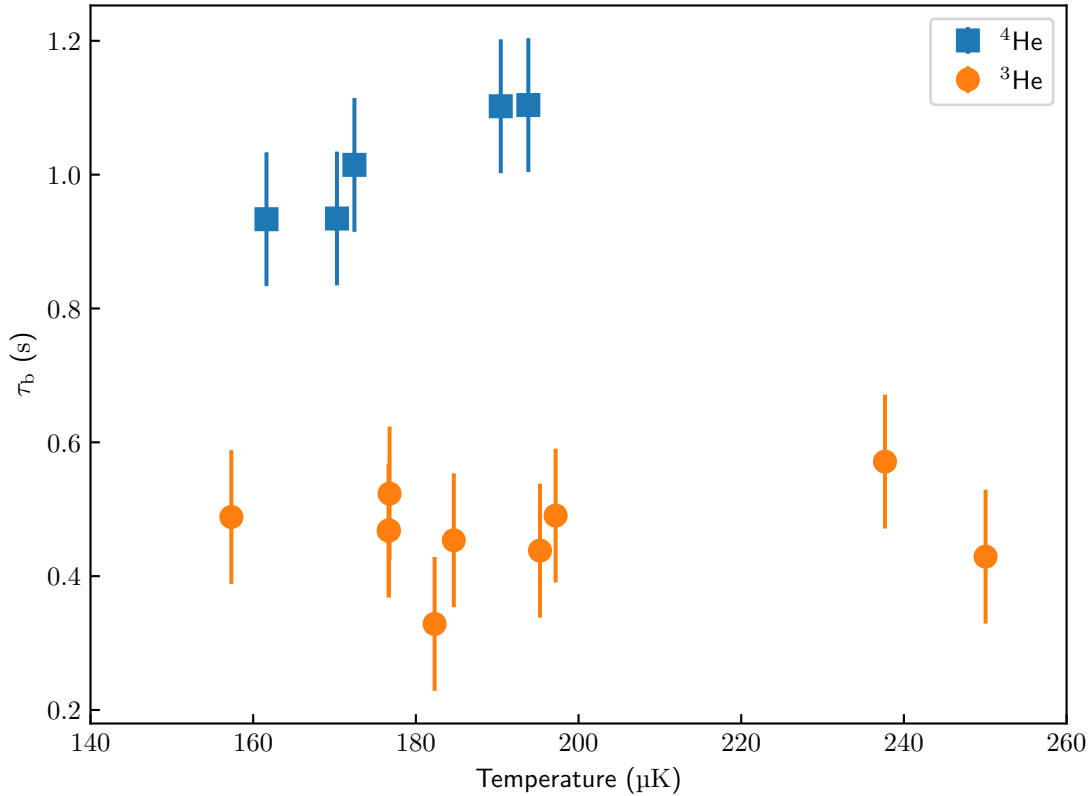
FIGURE 6.2: The quasiparticle relaxation time constant τ_b as measured by the vibrating loop thermometer. The average τ_b is $0.5 \pm 0.1\,\mathrm{s}$ and $1.0 \pm 0.1\,\mathrm{s}$ for solid ^{3}He and solid ^{4}He coverage, respectively. Absence of discernible variation over temperature is consistent with an exponential dependence of R_K.

thermalization time constant τ_b is independent of temperature for both types of coverages, which is demonstrated in Fig 6.2. According to (6.2), this demonstrates an exponential temperature dependence on Kapitza resistance in both cases, and leads to the conclusion that pre-plating with solid ^{4}He doubles the Kapitza resistance.

DC ramps with varying velocities for the same 1 mm distance and 3 ms time constant were measured with ^{4}He plating. From Fig. 6.3 we can see that the velocity of the ramp does not affect the time constant. Therefore, the height of the peak, or in physical terms, the heat released into the superfluid, does not seem to affect the time constant, as one would expect in the ballistic regime.

What is interesting is the difference between the higher and lower fields. The measurements show a consistent difference. The 65 mT measurements have an average time constant $\tau = 1.0 \pm 0.1\,\mathrm{s}$ whilst the 130 mT has an average time constant of $1.2 \pm 0.1\,\mathrm{s}$ for the entire span. More startlingly, the effect is happening in the ^{4}He plated data but this
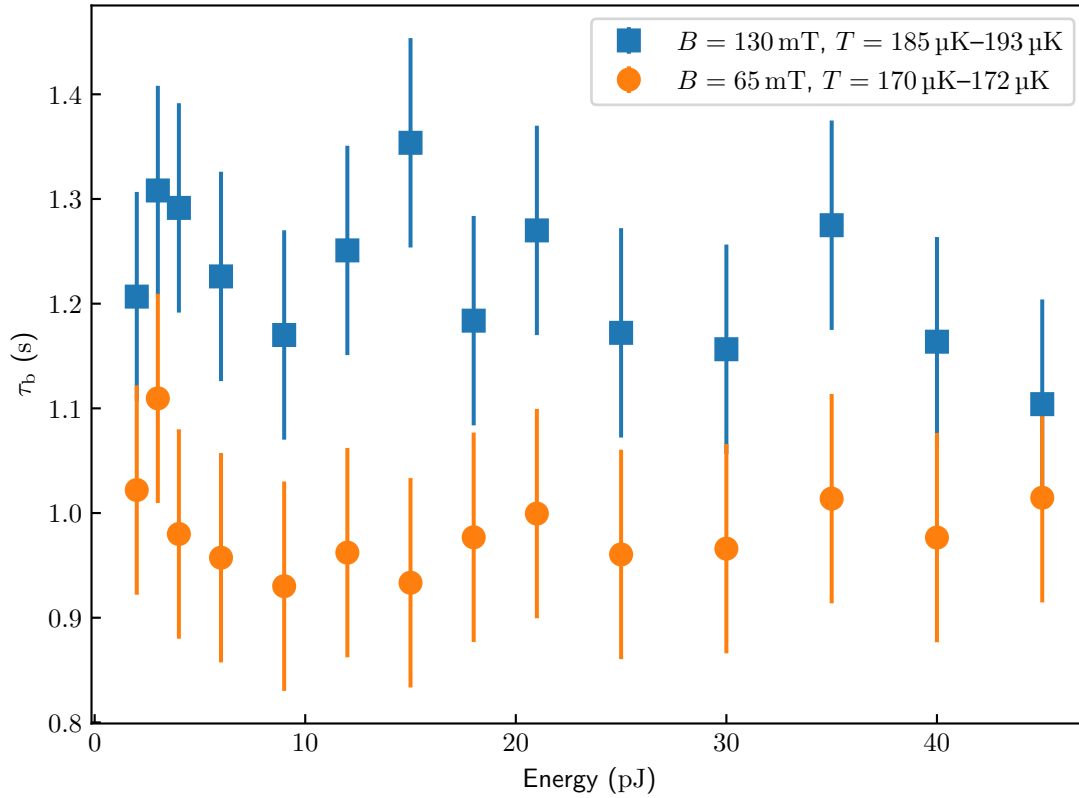
FIGURE 6.3: The time constants extracted from fits as velocity of the DC ramps is increased in two different field and temperature regimes. The average time for the lower field is 1.0 ± 0.1 s and for the higher field 1.2 ± 0.1 s.

does not necessarily suggest there is still solid ^{3}He on the surfaces. In a study of Kapitza resistance for metals with impurities, Avenel *et al*. note that the Kapitza resistance with one monolayer of ^{4}He was identical to Kapitza resistance with pure ^{3}He [115], hence it is likely we have over one layer. Moreover, in a study comparing 99.99% pure platinum and 99.999% platinum, Bishop, Mota, and Wheatley found that the two values proportional to R_K were independent of ^{4}He up to 480 ppm [116]. At 635 ppm the Kapitza resistance increases consistently up to 7000 ppm, depending on the impurity level. Unfortunately, they lacked knowledge of their geometry and do not calculate the number of layers.

The field dependency in some way provides evidence for the existence of a magnetic channel. The original proposal was simply the dipole-dipole interaction between nuclear dipoles in the liquid ^{3}He and electronic dipoles in the solid [92]. It is possible that solid ^{3}He only enhances the coupling, but it is not completely prevented without ^{3}He. Osheroff and Richardson found a similar 20% increase in the Kapitza resistance as they increased the magnetic field up to 200 mT [95]. Osheroff and Richardson also used the 70 nm Ulvac

brand of silver powder. Perry *et al.* saw that Kapitza resistance between ^{3}He-N and pure ^{3}He-covered platinum was insensitive to magnetic field in our range of magnetic fields [94].

In this chapter, we convert the velocity energy range by the heat capacity method, different from the calibration method presented as (5.1) in Chapter 5. First, one converts the thermometer widths into a temperature by means of (3.37). The heat required to raise the temperature is then

$$q = \int_{T_{\text{base}}}^{T_{\text{peak}}} C_{\text{B}} dT. \tag{6.3}$$

Both methods provide similar values at low velocities but deviate at high velocities. Using (6.3) the energy range tested over is from 5 pJ to 100 pJ.

A final concern is that the heat capacity of the solid helium on the cell walls may effect the results, as in [117]. The heat capacity of the solid helium at the temperatures presented is much smaller than the heat capacity of the liquid for our cell.

6.1.2 Comparison to Previous Measurements

As Lancaster has used the same technique found in [89] for making silver sinter with the same Ulvac powder, it is possible to compare to the previous measurements of Kapitza resistance by Carney *et al.* and Castelijns *et al.* [90, 91]

To calculate the Kapitza resistance using (6.2), the relevant volume of ^{3}He has to be calculated. The possible options are the volume of the whole inner cell or the volume of ^{3}He bordered by the sintered copper plates and the cell walls, localised within the vicinity of the flopper. That is to say, not including the ^{3}He between the copper plates.

During Carney's 1989 experiments, they also investigate heat transport through sintered plates, from a distant heater (say volume A) to the experimental volume (say volume B), shown in Fig. 6.4. Volume A has a heater and several 10s of sintered plates between it and volume (B), with a VWR thermometer. They found that even at extremely high heat flux, there was only a small temperature rise eventually detected by the VWR thermometer in B. At low heat flux there was no detected temperature rise in the thermometer even after a long period of waiting time.

Thus, it was decided to take into account only the localised ^{3}He. The tailpiece was also neglected due to being connected by only a tiny hole. Despite this, the choice for the value of the volume does not change the overall conclusion of the following results much, and the Kapitza resistance would be the same order of magnitude. This volume was used to calculate the energy range for the velocity measurements and gives similar values to the calibration, although again, the other volumes would still keep it within
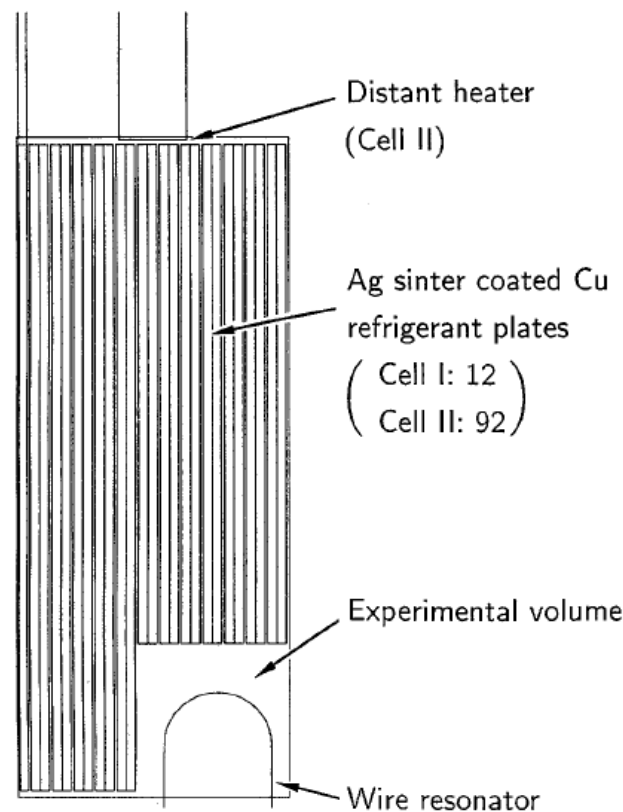
FIGURE 6.4: Sketch of the experimental cells used in earlier Lancaster experiments [90, 91], referred to as Cell I and Cell II, respectively. The experimental volume in both experiments contains several wires that can be used as detectors or heaters, and even resistance heaters in the case of [90]. In the case of Cell I the copper plates were 1 mm thick with about 0.5 mm of sinter on one face, whilst in Cell II the plates were 0.1 mm thick with 0.1 mm sinter on both sides of each plate.

an order of magnitude. The method for measuring R_K by Carney and Cousins did not depend on the choice of volume.

When comparing the data, one would expect a similar value of Kapitza resistance times area $R_K A$ (or heat conduction per area) for each set of data. As with the volume chosen, the choice of area is not obvious. There are three possibilities: the total "interfacial" area, the "microscopic" area or the "geometric" area. Table 6.1 shows a comparison of the possible three sets of geometries for the three datasets. The interfacial area is the total area of the copper plates, calculated as if the sinter does not enhance the area. The microscopic area is the area created by the sponge-like sinter surface, calculated by knowing the total mass of sinter used on the plates and measurements of the area per unit mass made ($0.83 \, \mathrm{m^2 \, g^{-1}}$) by Keith and Ward [89].

Cell	Volume (cm^3)	Sinter Area			Sinter Mass (g)
		Interfacial (m^2)	Microscopic (m^2)	Geometric (cm^2)	
This work	8.6	0.21	80	36	96
Castelijns *et al.* [90]	1.0	0.011	22	3.0	28
Carney *et al.* [91]	1.0	0.17	41	3.0	49

TABLE 6.1: Experimental cells for each measurement. The interfacial area is the area of all plate faces covered in sinter and microscopic area is the area of the sintered powder's sponge-like surface. Geometric area is the sintered plate surfaces that face the experimental volume containing the large wire with no other sintered surfaces between it and the volume (see text). The experimental volume quoted for this work excludes the tail piece, in which a small hole limited heat flow into the tail piece volume. However, the tail piece volume is not large and its inclusion would not change the results significantly.

The geometric area is complex to define. It is the area of sinter that is in contact with the chosen experimental volume of ^{3}He. In Fig. 5.2 we could say that the back, front and top are sinter "walls" that are in contact with volume. The area of these walls would then be the geometric area.

Thus we treat this area as if there are no gaps between the plates. Of course, in reality there are small gaps. Even more complicated is the structure of the plates are not at a uniform depth, but instead have a ridge-like structure. The inner cell contains eighty 0.2 mm thick and eight 1.1 mm thick copper plates with dimensions 49 mm by 28 mm. To create the box at the top of the experimental area, a rectangle is cut out of each of the middle plates. The rectangles cut out are of alternating dimensions to create the ridge-structure. Figure 6.6 shows the full pattern of the dimensions.

Fig. 6.5 shows the Kapitza resistance multiplied by the geometric area for our pure ^{3}He in Fig. 6.2, the data from Lancaster in 1986 and 1989. The zero pressure data for 1986 and 1989 has been refitted with the same $T^{c_2}e^{-\Delta_B/k_B T}$ form as the original fits but with a fixed BCS gap

$$q = p_1 T^{p_2} e^{-\frac{1.76 k_B T_c}{k_B T}}. \tag{6.4}$$

The inverse of the derivative is then used to calculate R_K, as per (4.3). For [90], $p_1 = 5.87 \times 10^{-10}$ and $p_2 = -0.836$ and for [91], $p_1 = 1.25 \times 10^{-8}$ and $p_2 = -0.54$. These fits are as good if not better than the previous fits. The R-squared value of fit to the 1985 data is 0.99, whilst it was 0.98 for the previous fit. Appendix B gives some details of statistical measures of best fit.
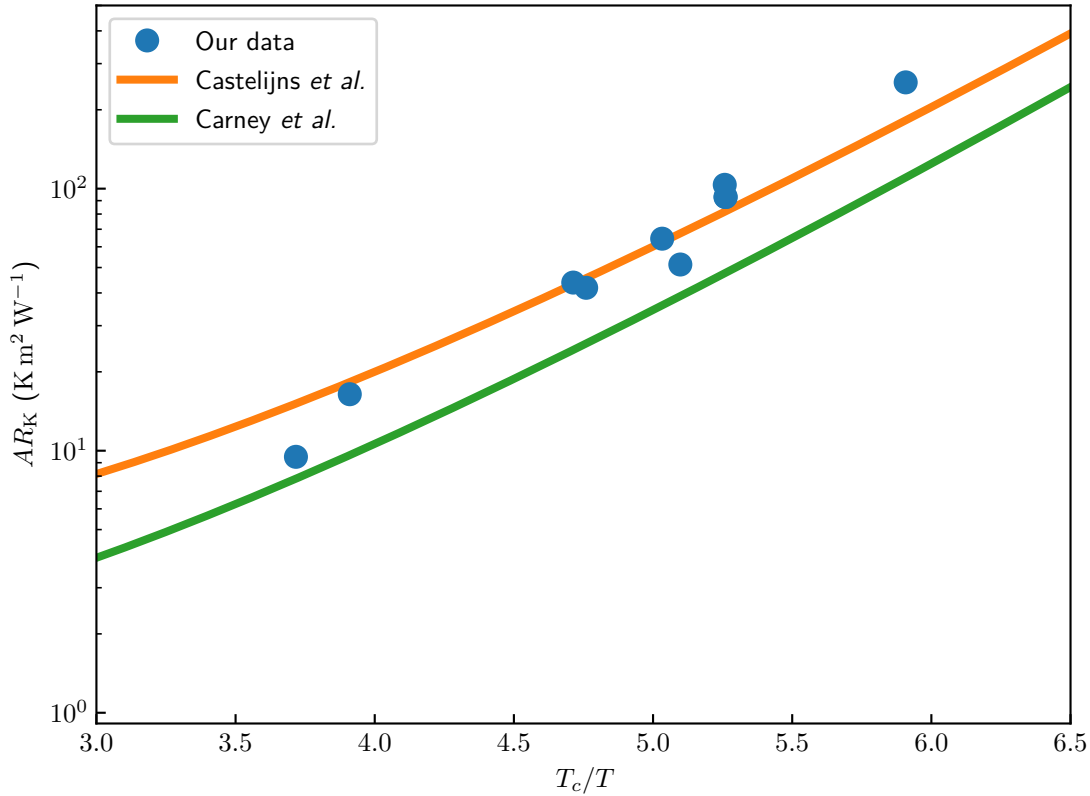
FIGURE 6.5: The effective thermal boundary resistance R_K multiplied by the "geometric" sinter scattering area A for quasiparticles created by the wire as a function of inverse temperature. $T_c = 929\,\mu\mathrm{K}$ is the critical temperature of superfluid ^{3}He at zero pressure. The gold and red lines are fits using (6.4) for data from [90] and [91], respectively, and converted into thermal boundary resistance. For comparison, our data shown is only in pure ^{3}He. They lie mostly on the gold line, or between the two lines if the tailpiece volume is included.

The area used is the geometric area. The geometric area is in fact the only area that gives the broad order of magnitude agreement one would expect. The fact that the geometric area is the only area suggests that in the ballistic regime of ^{3}He-B, the quasiparticles don't "see" the entire sinter area. Perhaps to a quasiparticle, the sinter appears mainly as a wall of normal fluid, solid helium and metal. The pore size of sintered metals is roughly equal to the coherence length of the superfluid in our conditions, 80 nm.

Consider a quasiparticle in a box, with the ceiling being a sinter wall with which a collision results in recombination. The other walls and floor are plastic, with recombination collisions so rare as to be effectively impossible. The quasiparticle travels with group velocity v_g which is approximately $20\,\mathrm{m\,s^{-1}}$ at these temperatures and pressure. With distance d_c between the walls, the time it takes to traverse from one wall to another
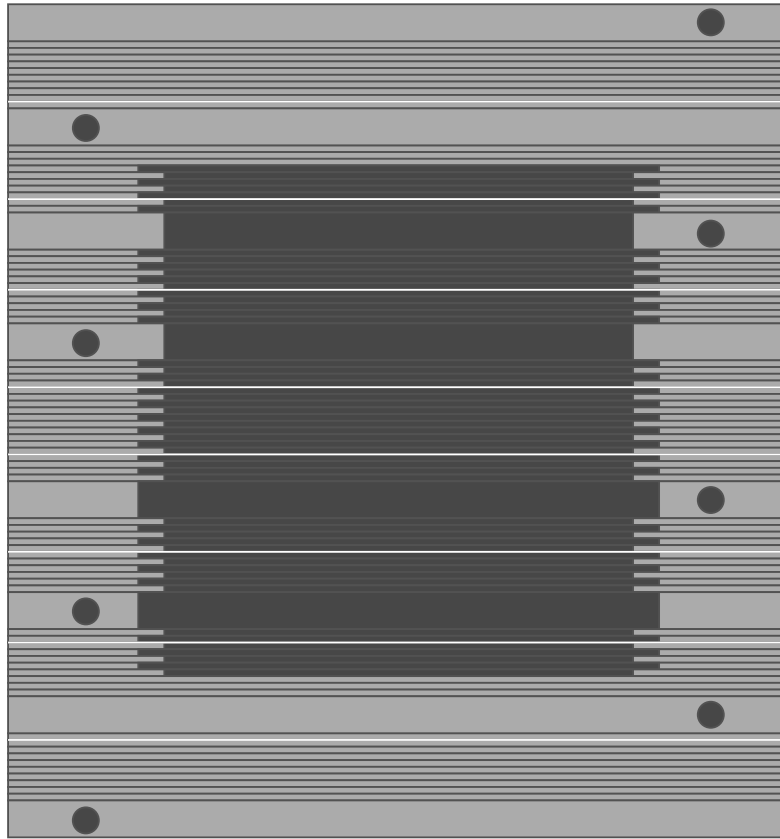
FIGURE 6.6: The arrangement of sintered copper plates in the inner cell as viewed from underneath. The inner cell contains eighty 0.2 mm thick and eight 1.1 mm thick copper plates with dimensions 49 mm by 28 mm. A 2 cm by 2 cm by 1 cm cube is formed by cutting the middle plates. The cuts from these plates are in an alternating pattern of a 1.9 cm by 1.1 cm rectangle followed by a 2.0 cm by 1.0 cm rectangle to create 1 mm protrusions that increase the surface area without changing the volume. The thick plates have holes for attaching silver wires from the mixing chamber plate. The white gaps indicate a piece of cigarette paper.

is roughly $t_{\text{col}} = d_{\text{c}}/v_{\text{g}}$ and the average time taken for there to be no more collisions is approximately τ_{b}. Therefore the probability of collision successfully leading to recombination is $P = \frac{t_{\text{col}}}{6\tau_{\text{b}}}$. This gives an estimate on the order of 1000 collisions needed for a quasiparticle to lose its energy with the sinter and recombine.

However, this is a much too simplified model to explain fully the dynamics of heat conduction by quasiparticle collisions. First, in the calculation of the geometric and interfacial areas we made no distinction between parts of copper plates covered by sinter and those not.

Second, we are unsure of how the gaps between the plates affect the collisions. Surely

some quasiparticles will fall into these gaps. We know from the volume A to B heat conduction experiment by Carney *et al.* that at some high heat flux some quasiparticles likely get through these gaps. The 1986 experimental cell used just twelve 1 mm thick copper plates with a square cut out of seven to create an experimental volume. In 1989, Carney *et al.* used ninety-two 0.1 mm thin plates. As previously described, we have eight thick and eighty thin plates. Our data lies towards Carney *et al.* in 1989, and is closer to midway between the two with the tailpiece volume included.

In their efforts to explain possible differences, Carney *et al.* used a similar model to our simple quasiparticle collisions with a box calculation but also stipulated the possibility of an effective "capture rate". The capture rate is how likely a quasiparticle recombines upon colliding with a particular surface. Adding sinter improves the capture rate. A "wall" actually being the ends of several sintered plates with gaps between would also have a different capture rate. It would be interesting to perform a conduction experiment similar to that in Carney *et al.* In the original experiment, both the plates and quasiparticle travel direction from the distant heater are vertical. Instead, the plates could be arranged horizontally rather than vertically to test if there is indeed a difference in capture rates if there are gaps. Mixed arrangements could also be tried, such as most plates vertical but with one or a few horizontal in the middle. Alternatively, more thermometry could be placed along the direction of travel and between plates, to determine how far a quasiparticle travels.

Unfortunately, it was difficult to extend the comparison to other measurements. For example, Parpia uses bronze flakes rather than silver powder [27]. Details of the experimental geometry are often difficult to find but make a large difference to the final analysis.

For the experiments made by Voncken *et al.*, they used a platinum NMR thermometer to monitor the temperature of the cell or sinter T_s, and a VWR thermometer to measure the pressure of the liquid T_l [113]. In their analysis, they plot the difference of the $T_l^n - T_s^n$ against temperature, where $n = 1, 2\,3$.

There are a few significant differences, which they also note. First, the experimental cell is designed such that, apart from a small space for the VWR thermometers, it is packed with silver sinter. The sinter is thermally connected to the refrigerant plates, but they are not directly in the cell. This means the cell temperature changes quite drastically when they apply heat to the liquid, whereas for our cell the change is slow and the cell temperature is close to a constant. In their model, they come to the conclusion that there is normal fluid trapped in the sinter due to the small pore size. In their one dimensional model, they therefore use the properties of normal fluid for the temperature dependence of heat conductivity. Since their cell is packed with sinter, the relative percentage of normal fluid would be much larger. In our experiment, R_K would be dominated by the superfluid quasiparticles because the ratio of superfluid is much higher compared to the normal fluid trapped leading to an exponential dependence, whereas in their experiment

the opposite could be true.

Second, they lose sensitivity at the lowest temperatures, as the intrinsic width of the VWR become comparable to the damping. Finally, they use a different silver sinter for their sinter, so one would not expect an exact agreement. There is a large difference between the Kaptiza resistance and different types of silver sinter. König *et al.* performed several measurements of impurities in different brands of silver powder used for making sinter [96–98]. They concluded that Ulvac powder has a larger content of magnetic impurities and a lower Kapitza resistance at millikelvin temperatures. We, Osheroff and Richardson, Castelijns *et al.* and Carney *et al.* all used the 70 nm Ulvac powder, which has the highest magnetic impurity content of all brands and sizes measured by König *et al* [90, 91, 95]. Voncken *et al.* use a powder from Inabala Corp., Vacuum Metallurgical Ltd [113].

6.2 Nanowires as Thermometers

With the construction of the new inner cell, 400 nm and 900 nm VWRs were added. Nanowires and nanobeams have a much higher mass-sensitivity [59]. At temperatures near T_c the viscosity of ^{3}He means such devices are much too overdamped to gain information from a frequency sweep for thermometry purposes. At lower temperatures, they may be more responsive to small changes in temperature.

As discussed in section 3.1.3 the resonance width is caused by damping due to quasi-particle collisions. The damping is enhanced by Andreev reflection and follows the exponential relationship (3.33). Since the proportionality constant C is of order unity, devices should experience a similar damping force normalised by the diameter. Using the full 3D specular calculation for the devices allows us to estimate the expected maximum damping force for a given temperature and geometry [68]:

$$\frac{F}{2R_0} = 2p_F^2 v \frac{4\pi p_F h}{m_3} e^{-\frac{\Delta_B}{k_B T}}.$$ (6.5)

The wires were first measured with in vacuum, with the inner cell connected to the mixing chamber, which had reached its base temperature close to 4 mK, to ascertain the intrinsic width of the resonators. The wires have then been measured in the ballistic regime of ^{3}He-B at zero pressure. The wires were plated with ^{4}He and the quasiparticle reflections should therefore be close to specular. Fig. 6.7 shows the normalised damping force of the several thermometers at 220 µK in the cell as a function of the characteristic size of the device.

One can see the 400 nm device is almost an order of magnitude lower than the predicted maximum value and much smaller than the average for the other devices. There is a possible drop off for 900 nm device. The relationship is more or less the same at various
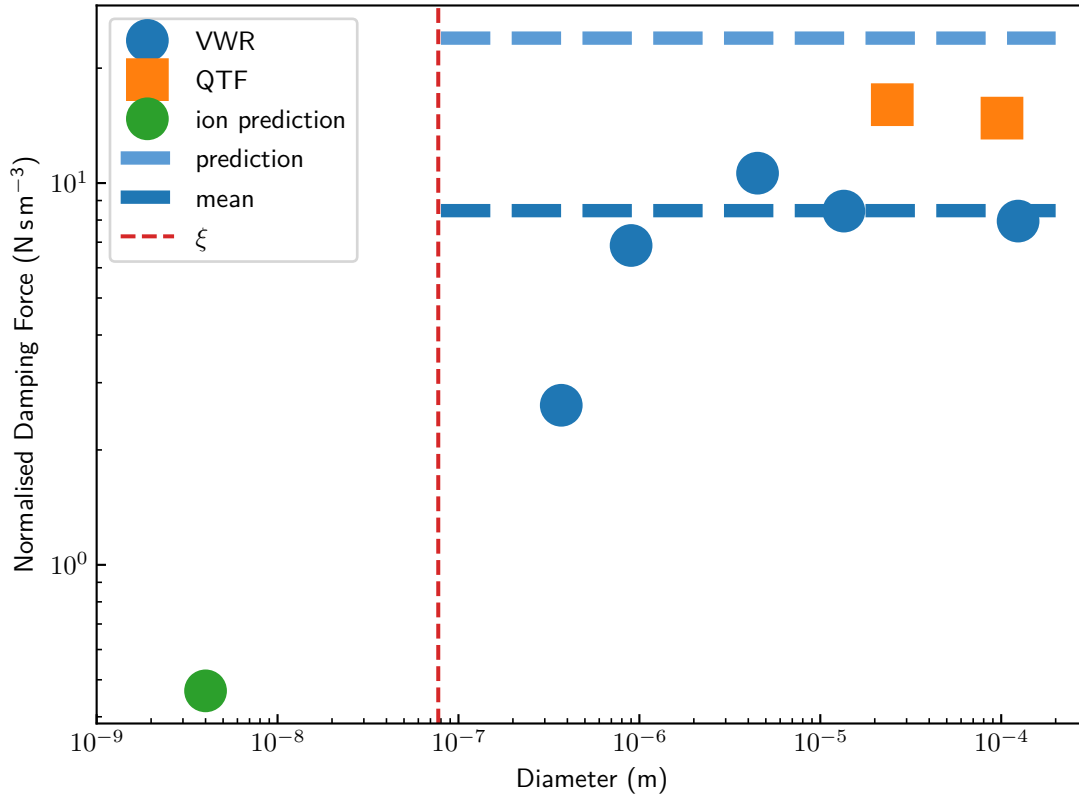
FIGURE 6.7: The normalised damping force of various probes in the cell at 220 μK at zero pressure. The specular reflection prediction for this temperature according to (6.5) is shown. The drag force of ion at this data has been extrapolated from data in [118]. The naive prediction without Andreev reflection effects included would be $0.002\,\mathrm{N\,s\,m^{-3}}$.

temperatures. Also plotted is the extrapolated drag force for an electron bubble extrapolated to the same reference temperature [118]. The electron bubble radius is much smaller than the coherence length and could provide a reference value for devices smaller than the coherence length. Finally, a simple scattering mechanism without Andreev reflection as described by (3.32) would give a normalised sensitivity of about $0.002\,\mathrm{N\,s\,m^{-3}}$. The ratio of 4.5 μm wire and 400 nm wires' normalised damping force is 3.5.

This difference could be due to 400 nm having a very strange geometry, but this seems unlikely. An alternative physical explanation could be that the flow enhancement around the cylinder has reduced. The coherence length in ^{3}He-B at zero pressure is $\approx 80\,\mathrm{nm}$, and thus $\frac{R_0}{\eta} \approx 2.5$. In these cases, they could exhibit much different damping phenomena compared to the larger devices. The effect on the velocity profile of the superflow around the wire and the potential barrier coming into the wire was derived by Evgeny Surovtsev

[1]

First, Surovtsev rewrites the order parameter of the B phase (2.19) near a wire in polar co-ordinates (r, θ) as

$$A_{\mu j} = e^{i\Theta}(\Delta_\perp(r)n_\mu n_j + \Delta_\parallel(r)(\delta_{\mu j} - n_\mu n_j)) \tag{6.6}$$

where n_μ and n_j are components of the matrix $\hat{\mathbf{n}}_R$ which is fixed perpendicular to the cylinder, and we have split the gap into its components parallel and perpendicular to the surface, and we have assumed it depends only on the radius. Surovtsev also assumes that the superflow does not influence the surrounding texture, which is valid for low velocities. Using Ginzburg-Landau expansions and the fact the superflow must be irrotational, the differential equation to solve is

$$\left(3\Delta_\perp^2 + 2\Delta_\parallel^2\right)\frac{\partial^2\Theta}{\partial r^2} + \left(\frac{(3\Delta_\perp^2 + 2\Delta_\parallel^2)}{r} + 6\Delta_\parallel\frac{\partial\Delta_\parallel}{\partial r} + 4\Delta_\perp\frac{\partial\Delta_\perp}{\partial r}\right)\frac{\partial\Theta}{\partial r} + \frac{4\Delta_\parallel^2 + \Delta_\perp^2}{r^2}\frac{\partial^2\Theta}{\partial\theta^2} = 0. \tag{6.7}$$

The boundary conditions are the same as the simple incompressible, inviscid model above. That is to say, $v = v_0$ far away and $v = 0$ perpendicular to the cylinder at $r = R_0$.

At large diameter devices $R_0 \gg \xi$, the energy gaps $\Delta_\perp = \Delta_\parallel = \Delta_B$. Since Δ_B is a constant at a given temperature, in this regime the model simplifies into the same governing equation as that of the incompressible, inviscid fluid model in Fig. 3.5.

More complex, however, is the situation for wires with a diameter such that $R_0 \sim \xi$. Here, we take a model function for the gap values of the order parameter as the gap going to zero at the boundary over a distance defined by the coherence length

$$\Delta_{\perp,\parallel} = \Delta_B - \delta_{\perp,\parallel}e^{\left(\frac{R-r}{\xi}\right)}. \tag{6.8}$$

The constants $\delta_\perp$ and $\delta_\parallel$ depend on the scattering conditions. The simplest case is specular reflection, where $\delta_\perp = \Delta_B$ and $\delta_\parallel = 0$. Solving for the purely specular case numerically results in a varying flow profile relative to the wire size, plotted in Fig. 6.8.

---

[1]This analysis was delivered in personal communications. A website with contact details is available here: https://kapitza.ras.ru/arhiv/people/surovtsev/Welcome.html.
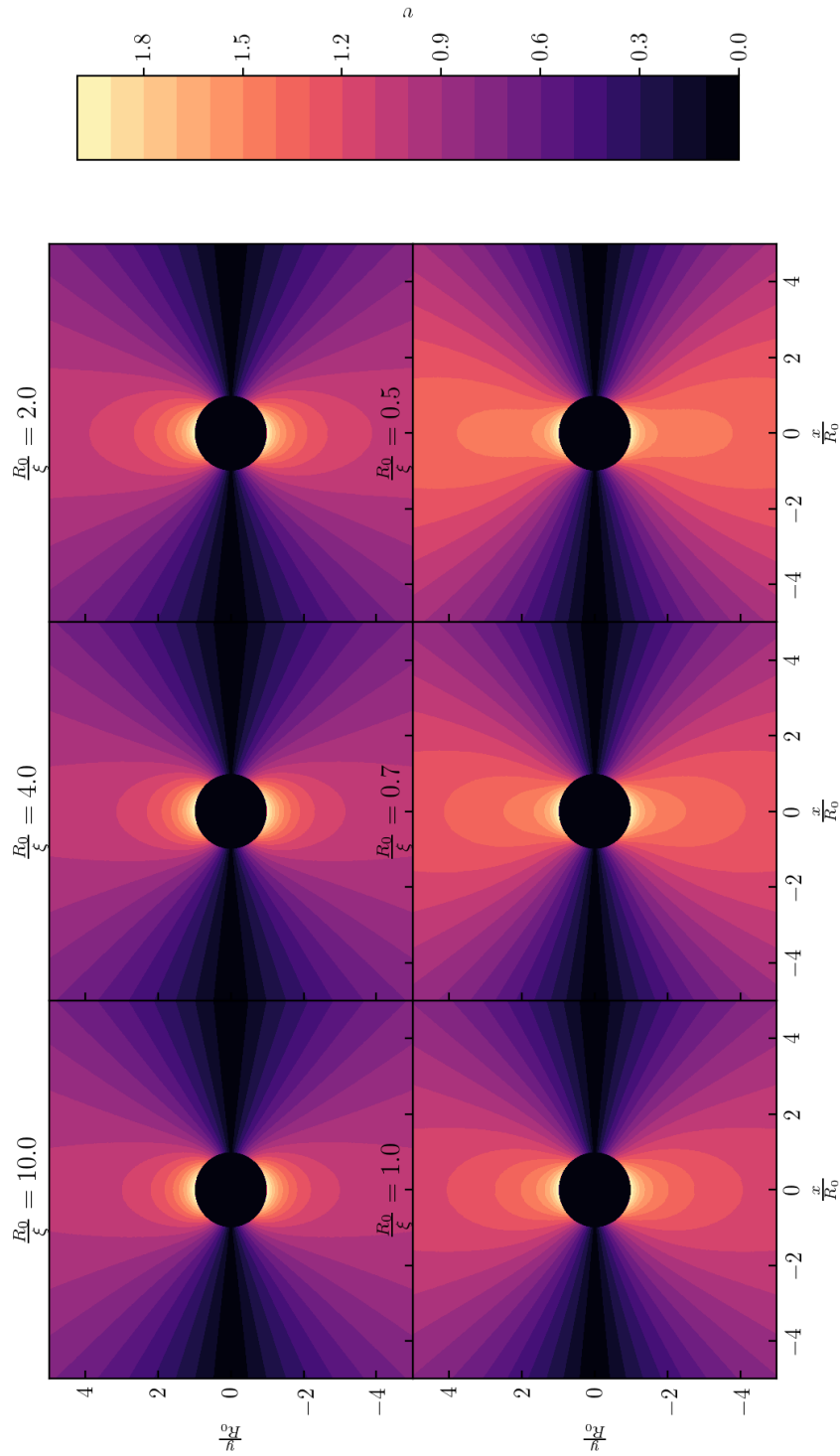
FIGURE 6.8: The flow velocity of superfluid within the vicinity of a small radius cylinder. The smallest radius is equal to 0.5ξ, and therefore has diameter equal to the coherence length. Whilst there is not much change for the larger cylinders (top left and centre) compared to Fig. 3.5, the region of faster flow at the top and bottom of the cylinder reaches further out (relative to the radius) for the smaller diameters.
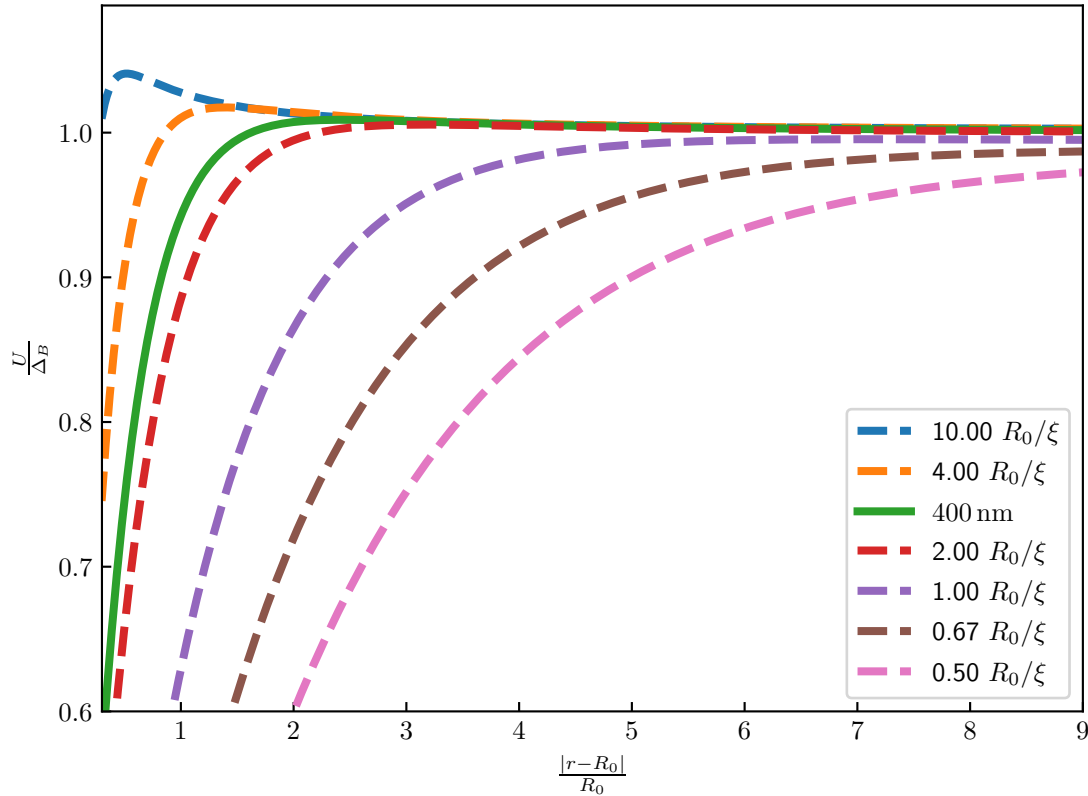
FIGURE 6.9: The potential energy of superfluid near a cylinder of *R*. The same values as Fig. 6.8 are plotted in dotted, whilst the 400 nm diameter wire is plotted as a solid line. A potential barrier is formed when the wire is much larger than coherence length.

Such a morphing of the flow velocity and order parameter near the wire has a large effect on the potential barrier that causes Andreev reflection. Surovtsev estimates this by considering a quasiparticle with momentum $\mathbf{p} = (-p_\mathrm{F} - \delta p, 0)$ for Cartesian coordinates. The particle is moving directly perpendicular to the surface of the wire. For the wire moving with velocity $(-v_0, 0)$ the potential barrier can be estimated as the perpendicular gap plus the relative velocity of superflow multiplied by the Fermi momentum: $\Delta_\perp + (v_0 - v_\mathrm{s}(r))p_\mathrm{F}$. Fig. 6.9 shows calculations of the potential barrier as $\frac{R}{\eta}$ decreases. We can see this barrier reduces as the radius of the wire becomes comparable to the coherence length and even becomes an attractive well. Therefore, there will be a lack of Andreev reflection for such a quasiparticle.

Furthermore, both the 400 nm and 900 nm wires have the reduced critical velocities shown in Fig. 6.10. The 4.5 μm wire has the expected critical velocity $v_\mathrm{c} = 9\,\mathrm{mm\,s^{-1}}$. This could be due to approaching the coherence length, however it could also be due to a much more mundane reason. It could indicate dirt, some kink in the wire, a shape
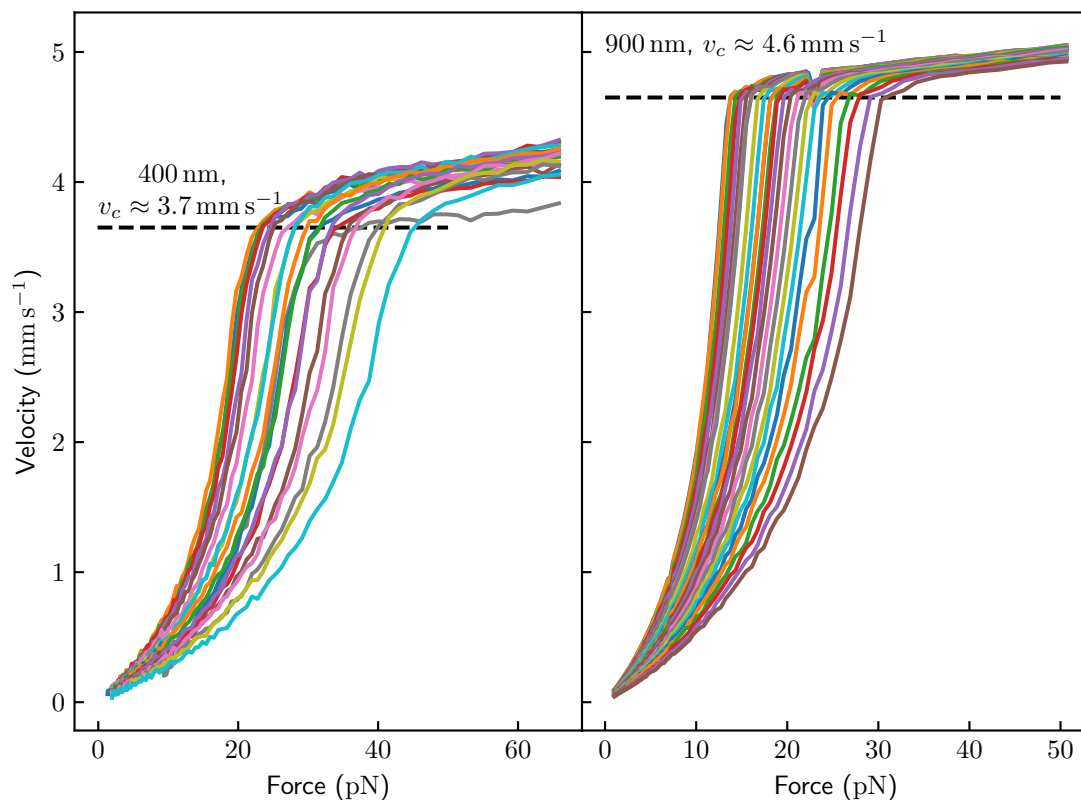
FIGURE 6.10: Amplitude sweeps in a magnetic field of 84 mT for the nanowires as temperature increases from 178 μK to 191 μK. The critical velocities are less than the usual $v_c = 9\,\mathrm{mm\,s^{-1}}$.

slightly different from a loop or some unetched copper causing a strange geometry.

6.3 Conclusions

The flopper experiments have illuminated cooling mechanisms important for the future of ultra-low temperature experiment design. The analysis prevents strong evidence that in the ballistic regime of ^{3}He-B that Kapitza resistance is dominated by quasiparticle collisions with sintered copper plates. Comparisons with previous measurements indicate that simply increasing the amount of sinter in an experimental cell will not yield much improvement in cooling power once an experiment has started. Since the probability of a collision resulting in recombination, on the order of 1000 collisions are needed for the average quasiparticle to recombine. If an experiment produces a localised heating (and thus an increase in the local quasiparticle population) one should focus on increasing the area of sintered surfaces a quasiparticle created in this local area can easily scatter too.

One way of increasing this area is to employ the alternating narrow and wide sinter plates to create a ridge like surface. The early experimental results were likely the logic behind this design, as opposed to the straight design used in those experiments. Another possibility is to use copper plates with prismatic sloped edges, which also have sinter on them. This design is soon to be tested at Lancaster in a new experiment.

Adding surface layers of ^{4}He was found to increase the Kapitza resistance. Some experiments require large amounts to achieve surface specularity may struggle to reach low temperatures, at least in a reasonable time. The higher Kapitza resistance is likely due to the weakening of a magnetic channel of heat transfer, as solid ^{4}He is non-magnetic. Similarly, it seems that the amount of magnetic impurities in the silver powder used is an important factor.

It would be beneficial to extend the scope of the measurements by increasing the temperature range and probing different phases. This requires sensitive and accurate thermometers for a higher temperature range. Similarly, the VWR thermometry technique cannot be used in the A phase. The A phase has nodal points in the energy gap, and therefore quasiparticle populations differ depending on the texture. The method of heat transfer from superfluid ^{3}He-A to sinter at ultra-low temperatures is an interesting question for further work, since the propagation of quasiparticles is significantly different [73]. One would assume it is unlikely that the result in the B phase would then apply, but earlier measurements of the A phase found an exponential dependence on temperature similar to that in the B phase between 230 μK and 450 μK at zero pressure [67].

As for the preliminary measurements on the vibrating wires, a potentially counter-intuitive result was found. Whilst the small diameter wires are expected to have a high mass-sensitivity in general, they may actually have a lower damping force for the same temperature in the ballistic regime of a superfluid. The warping of the velocity potential and energy gap near an object that approaches the coherence length could result in a weaker effect for Andreev reflection, leading to an overall loss in sensitivity. While these devices may be useful in observing interesting physics from approaching the coherence length, their value as sensitive thermometers may be limited. As an object becomes smaller than the coherence length, they may become essentially point-like objects [107]. Under this assumption, they would therefore not disrupt the superflow at all and the energy gap perpendicular to the surface would also not go to zero. Therefore, they such an object would not undergo Andreev reflection, resulting in a much lower damping [107].

It is currently unclear whether the sub-micron VWRs have anomalously low damping due to the effects of the coherence length on the flow and energy potential around the wire, or if it is a mundane reason such as a geometric defect. It is possible to pressurise the cell to confirm this effect. Pressurising will decrease the coherence length and change the ratio of R/ξ. This should therefore change the potential barrier according to Fig. 6.9 and therefore the damping force due to Andreev reflection.

Additionally, due to their low frequency, the sub-micron diameter wires present a good opportunity to investigate a new regime. Studies of mechanical oscillators in the hydrodynamic regime of liquid helium have hitherto focused on the limit where the viscous penetration depth δ is much greater than radius [57]. With resonant frequencies on the order of 1 kHz, much lower than resonance frequencies of MEMS and NEMS previously studied, the sub-micron wires can have $\delta \gg R$. These measurements can be done in liquid ^{3}He or ^{4}. Furthermore, they could also be done in gaseous helium, but an independent pressure gauge is necessary to accurately control the density of the helium gas.

Chapter 7

^{3}He in a Nematic Aerogel Experiment

In this chapter, we detail experiments entirely using the newly built cell and NMR-flopper device. The experiments took place in two regimes, low magnetic field and high magnetic field. The objective of low magnetic field was to use NMR to detect features in the polar phase. It would be possible to confirm and complete the phase diagram found by Dmitriev *et al.* discussed in Fig. 2.8 for the low temperature and low pressure region in the bottom left [7].

Furthermore, the NMR can be used to examine textural defects in the several phases [2]. By moving the NMR-flopper and therefore aerogel beforehand, vortices and half-quantum vortices could be generated, as well as possible textures induced by the flow. After stopping, NMR can be performed to examine the defects and their dynamics. The population of HQVs with relation to the amplitude of the movement, and the population decay in time, can hopefully be measured. In this chapter the current performance of the NMR setup is presented and whether HQVs could be measured is determined.

In the high magnetic field, movement of the flopper is hopefully used to detect the β phase. The properties of resonance of the device could be used to detect the superfluid fraction and therefore the β phase [10]. Finally, any dependence of superflow on the velocity of moving is to be found, in an effort to search for the predicted threshold velocity effect. The bulk of the chapter concerns measurements in high field in search of the β phase and a threshold velocity for superflow.

7.1   NMR Measurements

We performed nuclear magnetic resonance measurements at temperatures around and above $0.6T_c$ and in a field of around $30\,\text{mT}$ by inputting a current of $900\,\text{mA}$ into the main NMR magnet. Once the resonance was found by sweeping the magnetic field around $900\,\text{mA}$, increasing currents were applied to the gradient field magnet to increase field homogeneity. A reduction in the width of the NMR signal is observed. Fig. 7.1 shows the absorption of several NMR field sweeps, as a function of Lamor frequency of the
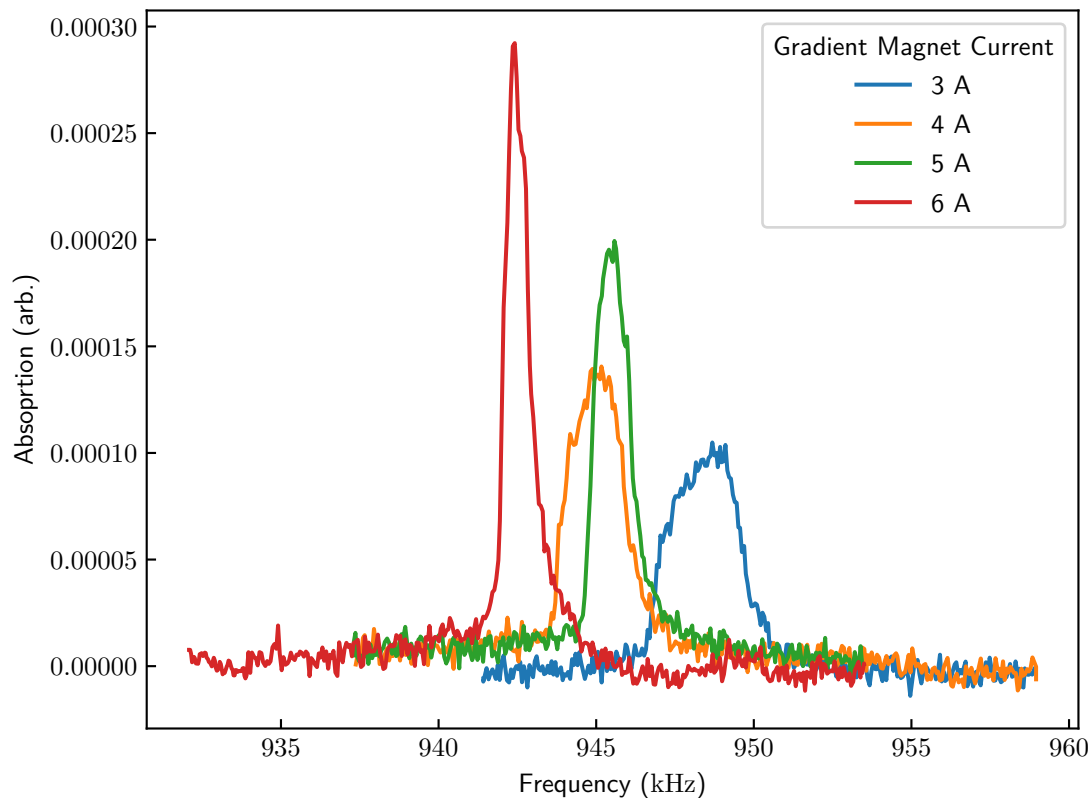
FIGURE 7.1: The NMR absorption spectrum as the current in the gradient field magnet is increased. The NMR absorption line width is decreasing and amplitude increasing as the gradient magnetic field increases, indicating the field inside the aerogel is becoming more homogeneous.

given field. We can see the frequency width of the signal decreases as the gradient current increases.

6 A is the maximum current our power supply could provide. The signal width is about 2 kHz. Unfortunately, at currents of 5 A and above, the gradient magnet will eventually quench and become normal again. Quenching heats the dilution refrigerator, as the magnets are thermalised on the still radiation shield, and the superfluid quickly heats well into the normal phase, effectively ending any measurement. Quenches in the gradient magnet can also quench the main NMR magnet and temporarily stop circulation as the pumps used to circulate mixture are overloaded. Therefore, we operate the gradient magnet at 4 A. Since it is possible to use higher currents on the gradient magnet for a time before it quenches, only a small part of the gradient field magnet or its wiring must have exceeded its critical current, until this part heats enough to create an avalanche process of heating and quenching.

One can estimate the resonance width needed to observe HQVs from (2.46) and measurements made by Autti *et al.* [8]. For the $\mu = \pi/2$ configuration, Autti *et al.* saw a frequency shift $(\omega_{\text{sat}} - \omega_{\text{L}}) \times \dfrac{\omega_{\text{L}}}{4\pi^2}$ of approximately -1×10^9 Hz to -3.5×10^9 Hz (see the blue curve in Fig. 2.12 (b)) with a measured Λ of 0.93 ± 0.07. Rearranging (2.46) and using our own Larmor frequency we can approximate the frequency shift a HQV peak would occur at using

$$-\left(\frac{\omega_{\text{sat}} - \omega_{\text{L}}}{2\pi}\right) = \frac{2\pi}{2\omega_{\text{L}}} \times 1 \times 10^9 \, \text{Hz}. \tag{7.1}$$

Using the relationship between frequency and angular frequency $f = \omega/2\pi$ we find the minimum frequency shift for our setup, occurring near T_c, should be approximately 500 Hz. This increases to around 1750 Hz at low temperatures. The amplitude of the HQV satellite peak is expected to be much lower than the main peak, meaning with our magnetic field inhomogeneity, near T_c the peak will not be visible.

In theory, it might be possible to see the satellite peak at low temperatures, at least as a distortion of the main peak. However, after the introduction of the NMR magnets there was a large increase in the heat leak and temperatures below $0.5T_c$ were not achievable.

Much effort was made to find the source of the heat leak. There were very few changes from early test measurements in which measurements of the sub-micron diameter VWRs in the ballistic B phase presented in Chapter 6 were made. These measurements were made before the NMR magnets had been finished, and before the grad coil used for detecting the NMR-flopper position were glued. Between these experimental runs, there were several big changes: more ^{4}He was added; the magnets and their wiring were added, gradient antenna coils for the position detection were added and finally a mu-metal magnetic shield was added. Several smaller fixes adjustments to wiring would have also been made. Heat leaks from the gradient antenna and the NMR magnets were not found. The mu-metal is on the still radiation shield, thermally disconnected from the cell by the heat switch. It is possible the extra ^{4}He has had an effect.

7.1.1 Normal Phase Susceptibility

The NMR line was measured at temperatures between 5 mK and 30 mK to determine the temperature dependence of the normal fluid susceptibility. The susceptibility can be measured by integrating the absorption of the NMR spectrum. Integrating (2.40) gives simply $\dfrac{\pi}{2}\chi$.

Following (2.15) the normal phase of liquid ^{3}He should have no temperature dependence. If there is any solid ^{3}He the signal should follow the Curie temperature dependence T^{-1}. Fig. 7.2 shows a plot of the numerical integral of the absorption spectrum of the measured curves with respect to temperature. The numerical integration was carried
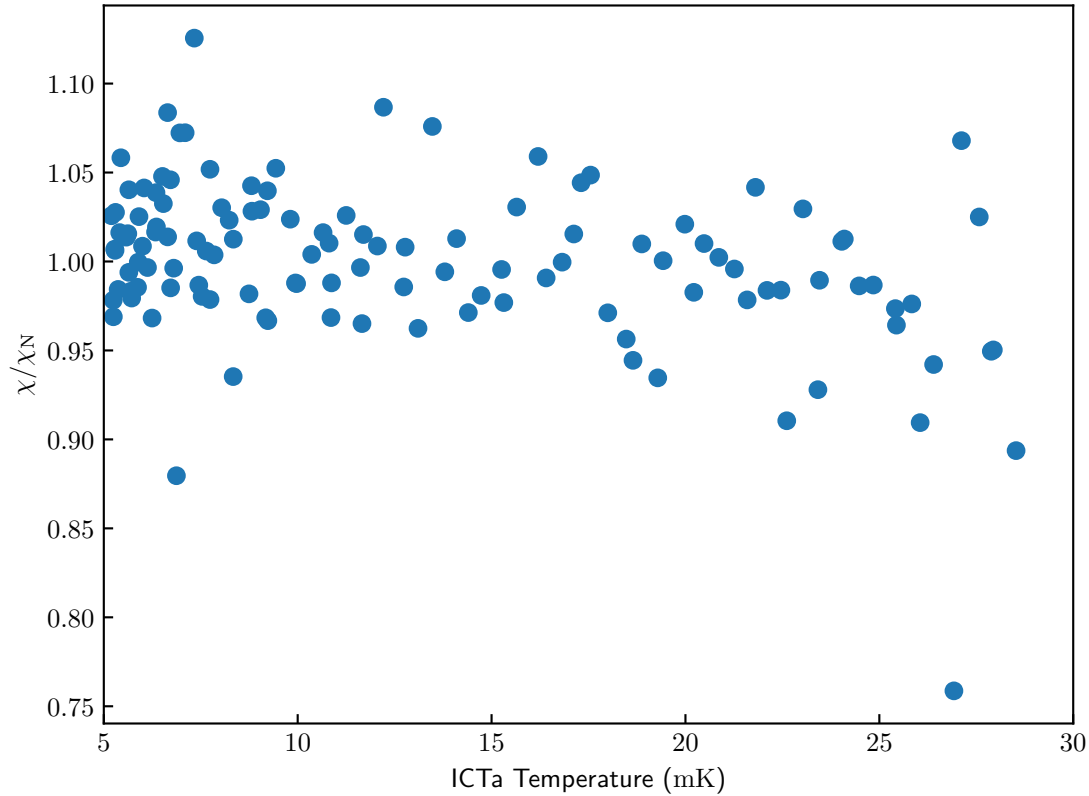
FIGURE 7.2: The ratio $\dfrac{\chi}{\chi_{\mathrm{N}}}$ measured from the integral of absorption of the NMR spectrum by Simpson's rule for ³He-N. The pressure is saturated vapour pressure.

out using Simpson's rule. We can conclude from this that the susceptibility is constant and all surfaces have been covered with solid ⁴He.

7.1.2 Superfluid Susceptibility

The main NMR line was then followed between $0.6T_{\mathrm{c}}$ to well above the superfluid transition temperature. Again, the absorption spectrum is integrated and normalised to the value above the superfluid transition in Fig. 7.3.

Here we can see that there is a decrease in the magnetic susceptibility. Such a drop is a hallmark of the bulk B phase due to the presence of $\frac{1}{\sqrt{2}}\,(\uparrow\downarrow + \uparrow\downarrow)$ pairs. Both the P and A phase have only $\uparrow\uparrow$ and $\downarrow\downarrow$ pairs and therefore do not see a reduction in the magnetic susceptibility. Whilst the drop is not as extreme as in the pure bulk phase, a smaller drop in B-like phases in isotropic aerogels has been previously reported that can be well-supported by the suppression of spin-spin scattering by the aerogel strands [119].
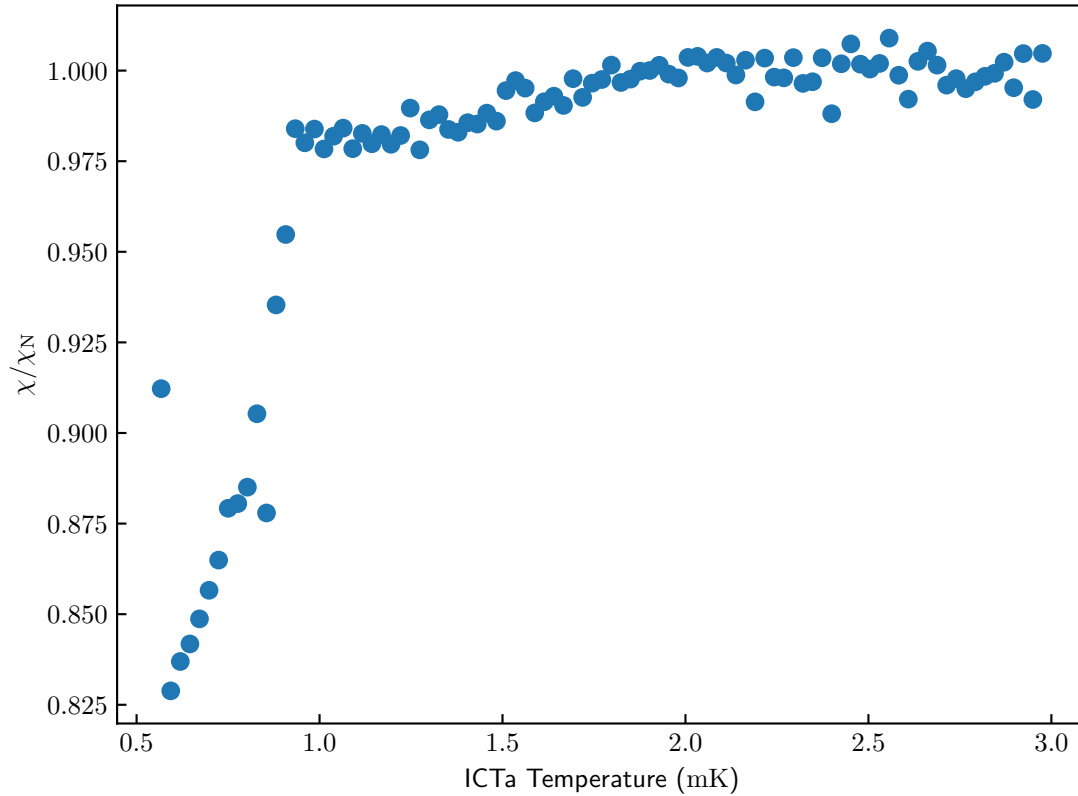
FIGURE 7.3: The ratio $\dfrac{\chi}{\chi_N}$ measured from the integral of absorption of the NMR spectrum by Simpson's rule. The pressure is saturated vapour pressure and $T_c = 929\,\text{mK}$. There is a decrease in the magnetic susceptibility in the superfluid phase, which is normally associated with the B phase.

According to Fig. 2.8 (b), we should be in the polar phase and polar distorted A phase for the temperature range in Fig. 7.3. The NMR coil is a tight fit around the aerogel and only some small amount of bulk near the edges of the coil should be visible. Therefore, it seems unlikely that the coil is detecting a larger volume of liquid outside the aerogel than inside the aerogel. We can assume that at least a significant proportion of the signal is from superfluid inside the aerogel. From previous measurements of nafen-92 (see Fig. 2.8 (b)), the only B-like phase is the distorted B phase. The transition to the distorted B phase is below $0.6T_c$ [7]. It is possible the aerogel sample is damaged and not as isotropic as we would have liked.

7.2 Mechanical Oscillator Frequency Sweeps

Originally, frequency sweeps were performed on the NMR-flopper. It quickly became apparent from frequency sweeps near T_c (Fig. 7.4 (a)) that the NMR-flopper was heavily overdamped and would be difficult to extract information from by fitting a Lorentzian. Without the enhancement of a peak from resonance, the signal from mechanical motion is very small and difficult to distinguish from electrical noise. Whilst this general problem can be solved by taking longer for measuring points and averaging, in practice this slows down the measurement. The heat leak meant very few measurements could then be taken. Furthermore, the response time of a resonator is proportional to the inverse of the resonance width. The oscillator will respond fairly quickly to changes in the properties of liquid helium surrounding it due to increasing temperature. If the temperature changed substantially over a single slow frequency sweep, then it could be difficult to fit. The low frequency of the device was also difficult to work with. There is a strange electrical response measured by the lock-in amplifier at these frequencies. The response was found when testing by measuring the signal from the signal generator directly. The phase below 2.5 Hz appeared to change continuously and below 1 Hz some of the signal is lost.

Frequency sweeps at relatively high temperatures in the normal phase where the viscosity is low were performed. A second resonance can be seen in the device, quite close to the first resonance, in Fig. 7.4 (b). This resonance does not seem to appear in vacuum measurements and also becomes overdamped, with its resonance shifting to lower frequencies and becoming wider. The main resonance and second mode can interfere with each other. It is possible to create a double Lorentzian fit, but these fits only seem to fit decently to intermediate temperatures. For these reasons more creative approaches were taken.

During the design, testing and creation of the NMR-flopper this second mode was not observed. A replica device has been built and immersed in ^{4}He, and frequency sweeps do not display this mode. Finite Element Analysis was carried out in SolidWorks, but due to a lack of information on the mechanical properties of NbTi and nafen and the fact that the real device has imperfections such as bent legs, this simulation did not produce qualitatively good results even for the frequency of the first mode. Finally, calculations by Naguleswaran also do not predict a second mode so close in frequency to the first [77].

7.3 Constant Frequency Measurements

The NMR-flopper was driven with a sinusoidal AC drive at a fixed frequency and amplitude for a period of 300 seconds. The measurement would be repeated over a large stretch of time after the demag as the cell temperature increased, with several drives.
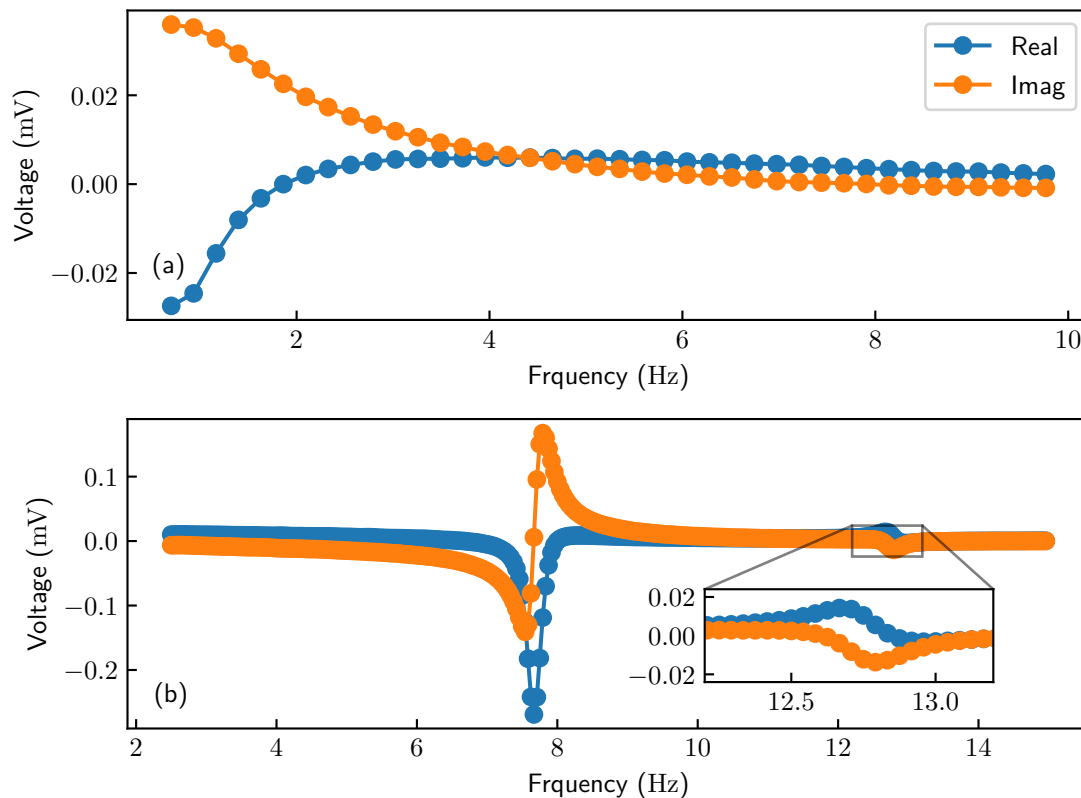
FIGURE 7.4: Raw frequency sweeps of the NMR-flopper in liquid helium at saturated vapour pressure and (a) near T_c where it is overdamped and (b) far above T_c. The ICTa thermometer resonance width is (a) 768 Hz, the magnetic field is 172 mT, the drive is 68 mV. For (b) ICTa thermometer resonance width is 4.24 Hz, the magnetic field is 31 mT, the drive is 4 V

As with vibrating wires, the Laplace force due to an alternating current in a magnetic field creates a sinusoidal (or sinusoidal-like) motion of the NMR-flopper. However, the frequency was not swept and the frequency chosen was deliberately chosen as an off-resonance frequency, and is not even necessarily near the resonance frequency.

The magnitude of the drive used was chosen by initially moving the NMR-flopper from one wall of the cell to the other, with its position monitored by the gradient coils as described in Chapter 4 and shown in Fig. 4.4 (a). A maximum drive was then chosen to be within the range of drives that provided a linear signal.

During a fixed frequency drive measurement, the position is monitored by the driving the NMR resonance with the gradient antenna coils. Monitoring the position naturally produces a corresponding sinusoidal-like wave, shown in Fig. 7.5. From this resulting signal, the amplitude and phase of the wave could be extracted by means of Fourier analysis. Alternatively, one could fit a sine wave to the signal. Finally, we also monitored
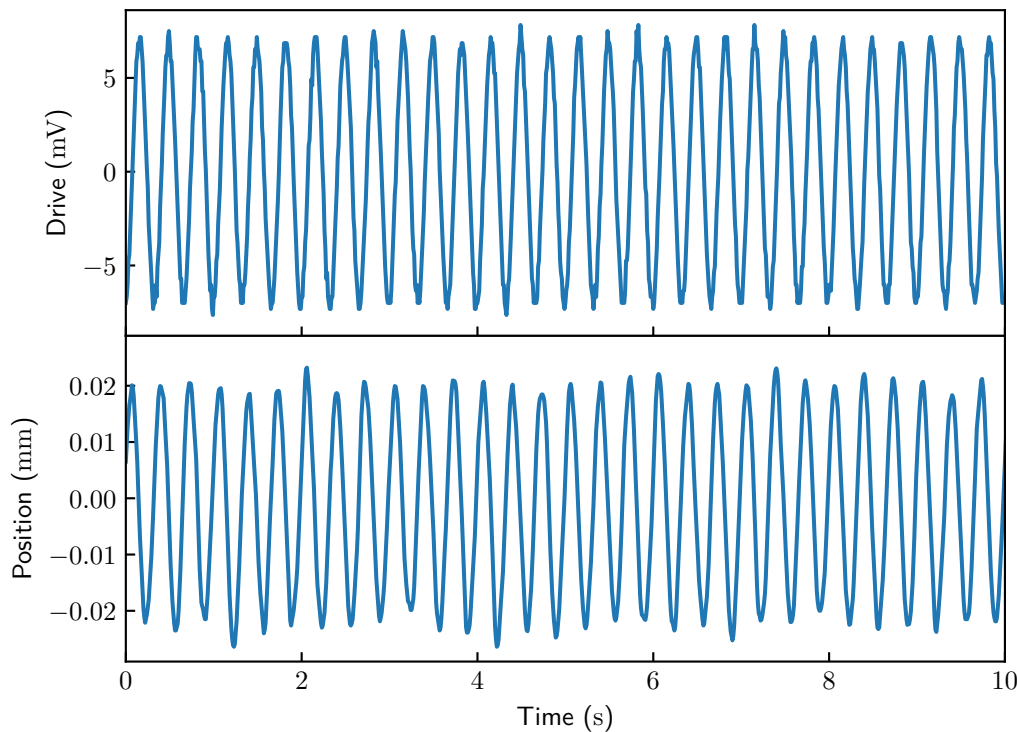
FIGURE 7.5: An example of the drive signal and the resulting response measured by the NMR coil. Only the first ten seconds of a 300 second measurement is shown for clarity. This measurement had a peak-to-peak drive of 14 mV and a fixed frequency of 3 Hz.

the e.m.f. produced using a separate lock-in amplifier. The circuitry is shown in Appendix A. Comparing the measured velocity of the wire by the e.m.f. and by position detection gives a good agreement (see Fig. 4.4). However, the noise for the phase and amplitude data given by Fourier analyses of the signals was much lower than the other two methods (see Fig. 4.4 (b)).

The drive signal was also monitored and recorded, allowing the real drive voltage applied to the NMR-flopper to be known but more importantly the phase difference between drive and response for each 300 s measurement. In fact, it is possible to separate each measurement into smaller sections to increase the time-resolution of the data, at the cost of noise.

Due to the predicted threshold superfluid velocity, at which only above certain velocities does the β phase behave superfluid, we wished to investigate the response at both low and high velocities. There were two ways of doing so: altering the frequency of the 300 second measurement, or altering the drive. We most commonly chose to use several

drives (up to six) in a repeating order. The higher drives produced noticeable heating as recorded by ICTa's resonance width (shown in the inset of Fig. 7.6 or the oscillations in Fig 7.11). Thus, we chose to alternate between high and low drives in these patterns to prevent over heating. For example, a 50 mV (high) drive 300 second measurement, then a 10 mV (low) drive 300 second measurement, then a 40 mV (fairly high) drive, then a 30 mV drive, and so on. In some measurements we changed both the frequency and the drive. However, there was not any noticeable differences from just changing one parameter.

Measurements were made by initially demagnetising to a high field, where the bulk B phase is not stable. A measurement was started once the temperature seemed to have settled after demagnetisation. The measurement was left to continue for several days. Once the bulk helium has moved into the normal phase, the measurement was stopped and a second demagnetisation was carried out. This process was to half of the original field, where the bulk B phase is stable. Then a second measurement at a lower field was carried out. Often, a measurement would be briefly paused for one to two hour periods, to allow the helium bath to be refilled. Occasionally, the controlling computer restarted, or a power cut happened, pausing a measurement for a much longer period.

In general, we can separate the results into these two distinct groups: high field measurements ($> 312\,\text{mT}$) and low field measurements ($\leq 312\,\text{mT}$). Data at high fields overall produced a similar temperature dependence when comparing normalised amplitude, as did data at lower fields, but they are distinct from each other, in part due to the A-B transition only being present in the low fields. It is also important to note all magnetic fields presented from here onwards are the maximum magnetic field. Due to differences in position, ICTa is in a field 98% of the total magnetic field, and the NMR-flopper crossbar 95% of the total magnetic field.

Thermometry

Taking accurate thermometry for this type of measurement turned out to be uniquely difficult. The temperature dependence of the ICTa resonance width is well known in the B phase and normal phase, but there is no data in the A phase. Whilst typically one could perform a backward calibration from the normal phase if the heating is constant throughout, when the drive of the sine-wave measurement was increased, the amount of heating produced by the measurement also increased. In Fig. 7.6 the resonance width of ICTa as a function of time is plotted. In this measurement a cycle of increasing drives were used. We can see the clear pattern of heating and cooling in the ICTa width, corresponding to when higher drive measurements are made. When the cycle finishes, it returns to a lower drive. For this reason alone, the heating rate due to the measurement is not constant. This pattern also seems much less distinct when in the normal phase.
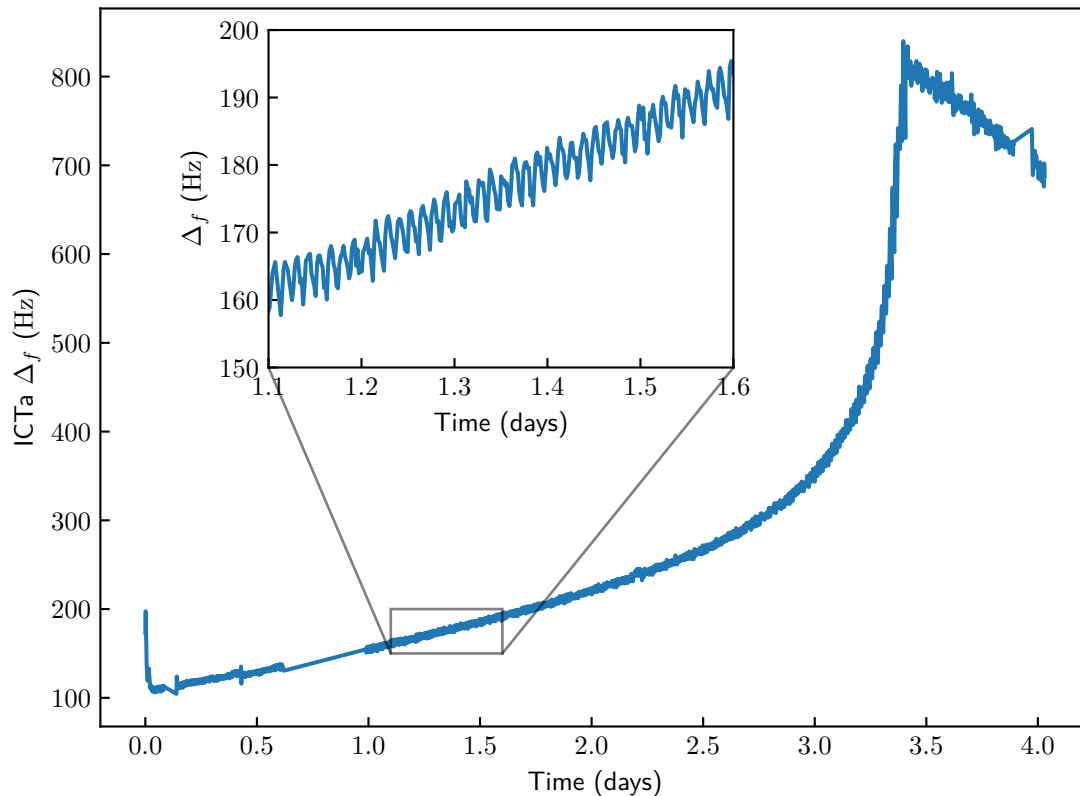
FIGURE 7.6: The resonance width of the ICTa VWR thermometer as a measurement takes place in a magnetic field of 453 mT.

Whilst it may be possible to assume there is an average heating rate from the measurement across the different drives, the measurements in high field were often stopped very soon after entering the normal phase to allow a second demagnetisation to a lower field. Roughly, from (4.2), halving the field would reach half the temperature. Due to imperfections in the system, temperature dependent thermal resistances between the copper nucleons and liquid helium, and some heat leaks, in reality is a higher temperature is reached. Therefore, to reach a low enough temperature for superfluidity again and provide a reasonable temperature range, we had to demagnetise very soon after going beyond T_c.

Since backward extrapolation for higher field data is simply not possible, and there is a non-constant heating from the measurement itself (and any pauses), we instead present the data in general as a function of the ICTa thermometer resonance width. An advantage of this method is that we have a direct comparison of the two oscillators in the same bulk liquid. A deviation of the behaviour of the NMR-flopper with respect to ICTa must be explainable in terms of the oscillator's mechanical properties (its geometry or lower
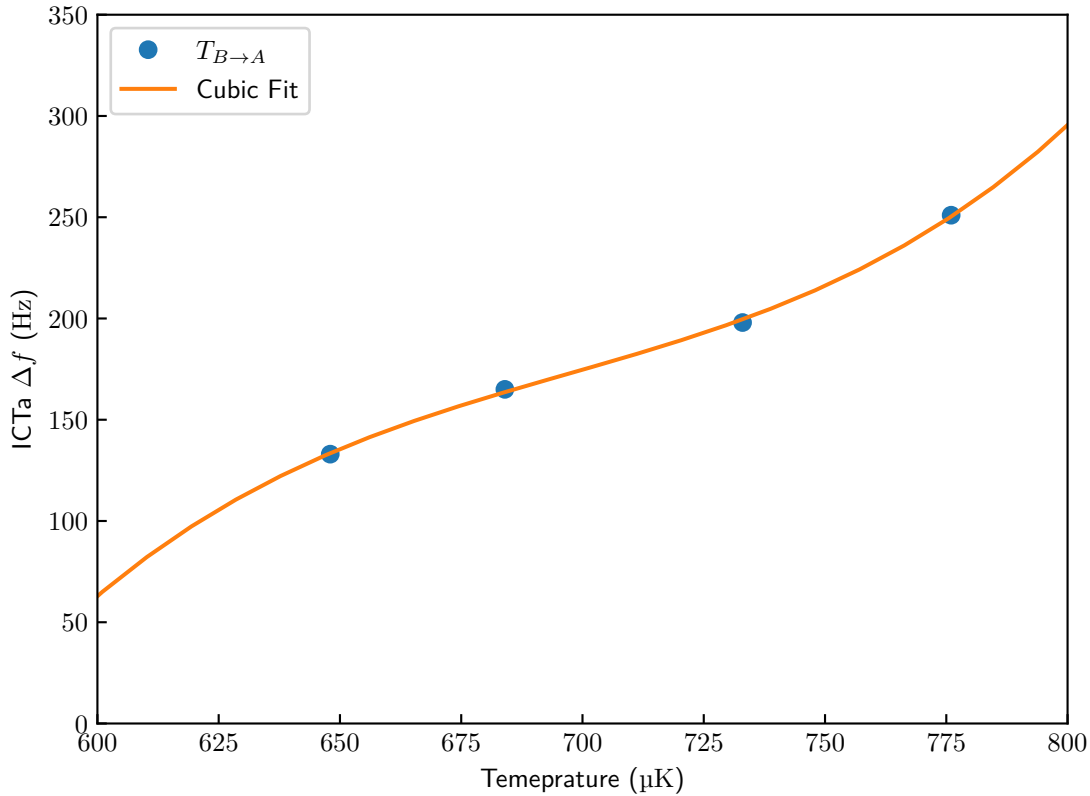
FIGURE 7.7: Known-point thermometry calibration curve based on the B
to A phase transition observed by a discontinuity in the ICTa width on
warming for several magnetic fields.

frequency), or in the properties of the superfluid in aerogel.

Additionally, the ICTa resonance width at the B phase to A phase transition and at T_c
were reproducible with a low drive signal to ICTa. Therefore, we can attempt to use the
warming B→A and cooling A→B transitions at different magnetic fields for known point
thermometry. The downside of this is that the low drive signal means the signal-to-noise
ratio is lower than desired. Fig. 7.7 is a calibration curve for the A→B transitions. This
method is only valid in this range and even then, we can not expect it to be particularly
accurate.

7.3.1 Lower Fields

In the lower fields, we can rearrange (2.36) to find the temperature width of the β phase.
At SVP $T_c = 929$ mK and the aerogel transition temperature is $\approx 0.92T_c$. The fields used
ranged from 120 mT to 240 mT. The expected temperature width of the β phase is there-
fore approximately 5 µK to 10 µK, similar to values for the A_1 phase [12].
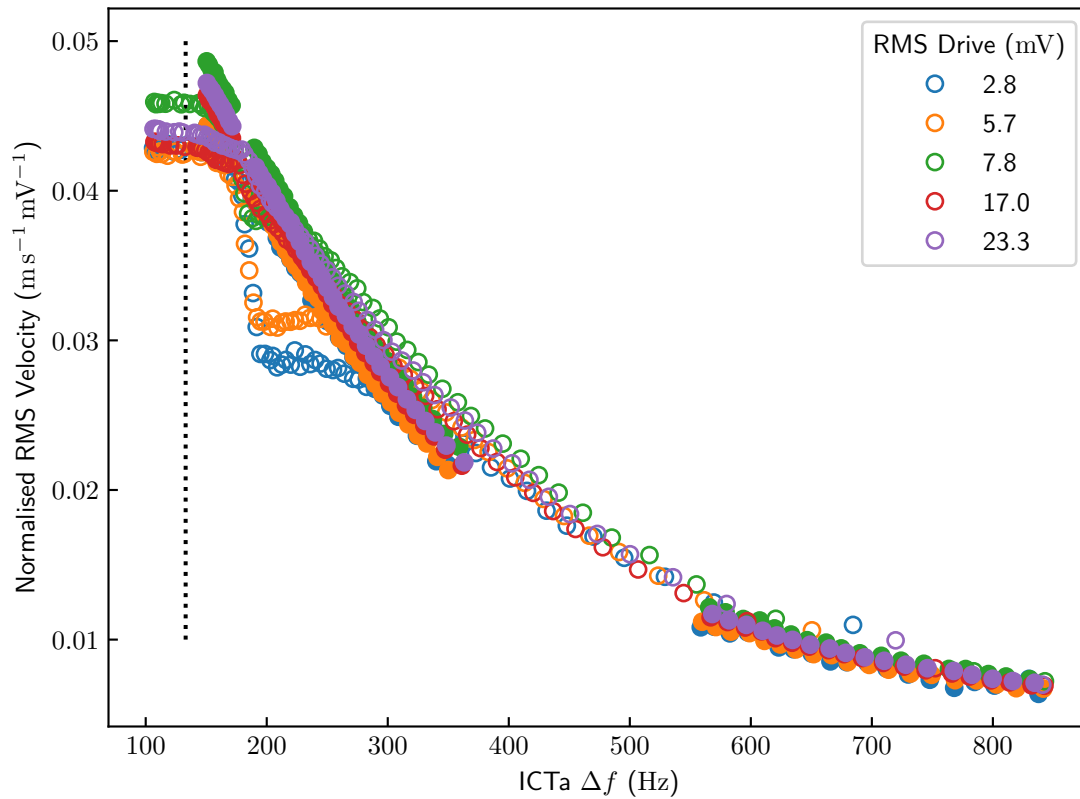
FIGURE 7.8: The RMS velocity of a 300 second sine-wave measurement, normalised by the drive signal amplitude. The magnetic field is 234 mT and the fixed frequency is 3 Hz. The solid circles indicate normal fluid data and the open circles indicate superfluid. The black dotted lines correspond to the B→A transitions on ICTa, shown in Fig. 7.7.

Velocity

First, we compare the velocity amplitude for each measurement across several drives by normalising the root mean squared (RMS) velocity by the drive $v_{\mathrm{rms}}/V_{\mathrm{drive}}$. In Fig. 7.8 the data is plotted against the resonance width of ICTa, and marks the resonance width at which the B→A transition was detected by ICTa on warming as part of a known point thermometry for measurements in a few fields. Fig. 7.8 measurement is typical of low field measurements.

First, we note a transition that is seen at the low ICTa widths. This is likely the bulk B to A transition, and is close in ICTa width to the bulk A to B transition seen on cooling. The lower drives see it sharper as they produce less heating. But before this transition the behaviour is odd. The normalised amplitudes are equal and remain constant until this transition. If the NMR-Flopper's mechanical behaviour was governed only by B phase

dynamics, the normalised velocity would be decreasing as the temperature and normal fluid fraction increased. Furthermore, we know that ICTa width is behaving as expected, so it is possibly not some purely bulk superfluid process. We can even compare to a similar ICTa width in the normal phase. When the ICTa width is the same in either the normal or superfluid phases, the viscous force and therefore viscosity should be equal. Here we see the expected behaviour that as ICTa width and therefore damping becomes lower, the NMR-Flopper's velocity increases.

Past the B→A transition, we note that at lower drives the device is oscillating at a much lower relative velocity whilst the highest two drives follow a smooth curve. As the temperature increases and the ICTa width increases, these lower drives eventually join this smooth curve. The velocity at which the lower drives rejoin the main curve is a critical velocity that will be investigated later. This smooth curve that the high drives follow appears to be almost the same as the curve followed by all drives in the normal phase.

Phase

According to (3.10), a changing phase difference indicates either a moving resonant frequency, a changing resonance width, or both. Examining the change of phase difference produces a similar picture to examining the amplitude. Fig. 7.9 shows the corresponding phase data to the amplitude data in Fig. 7.8.

We again see the B→A transition and a similar pattern: the two higher drives follow a smooth curve after the transition, and almost completely follow normal phase data. The lower drives seem even more separated and join only after a while. What is a notable difference here, however, is that the phase difference does not seem to be wholly constant at low temperature before the B→A, unlike the amplitude.

For the data in the B phase, let us assume that the resonant frequency is above the measurement frequency and the oscillator is not overdamped. The superfluid fraction in the bulk B phase is well understood, and we know that the viscosity is indeed changing from the ICTa measurements. We know the NMR-flopper is not overdamped from previous frequency sweeps and later drop measurements, detailed below. Then we can compare the following scenarios as the temperature increases. (1) Both damping and resonance frequency are changing, but the resonance frequency is close. (2) Neither is changing. (3) The resonance frequency has increased to a value far higher than the fixed frequency. Alternatively, (3) could be that resonance width has decreased, meaning the resonance is now relatively far away. Likely it is a combination of both effects.

In scenario (1), the simultaneous change in damping and resonant frequency implies that they must change such that the effects on velocity cancel each other out. This seems unlikely, especially as we have performed measurements at two fixed frequencies (2 Hz
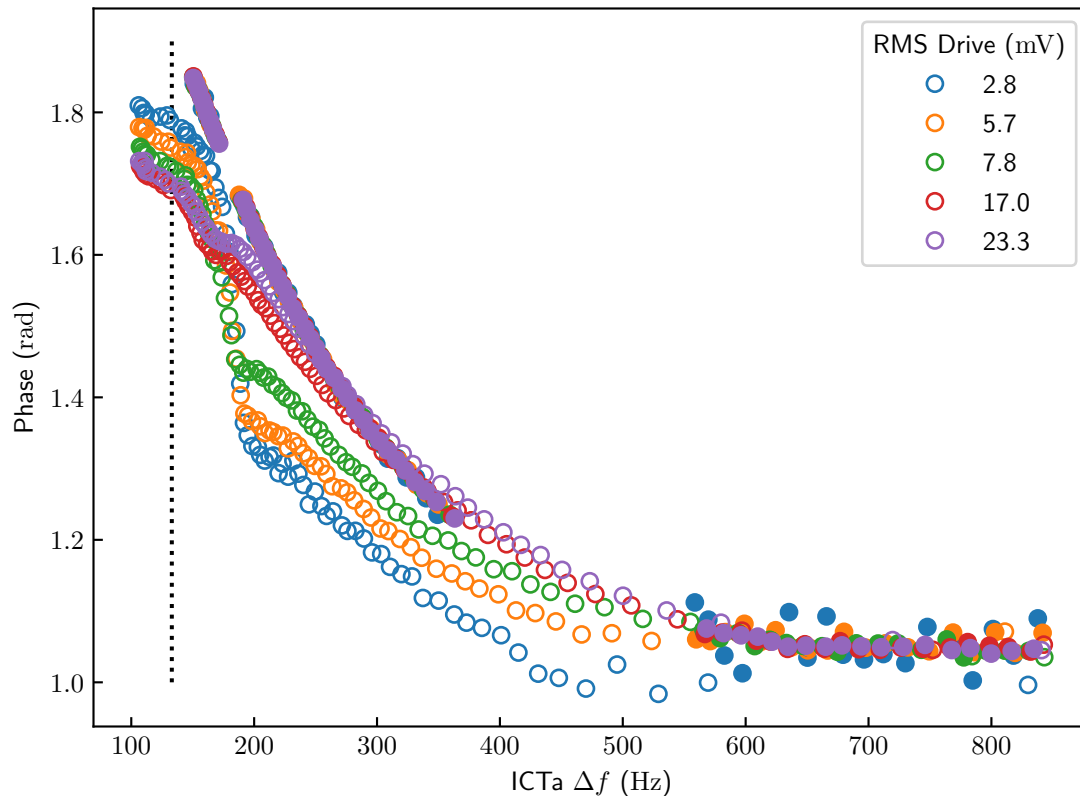
FIGURE 7.9: The phase of a 300 second sine-wave measurement. The magnetic field is 234 mT and the fixed frequency is 3 Hz. The solid circles indicate normal fluid data and the open circles indicate superfluid. The black dotted line corresponds to the B→A transition on ICTa for this field, shown in Fig. 7.7.

and 3 Hz). If (2) was true, the phase wouldn't be changing. Therefore, (3) must be true, and the resonance frequency has suddenly increased far above the fixed frequencies.

Higher Harmonics

A perfect sine wave has no harmonic components. When performing a Fourier transform of the measured sine wave to find the amplitude, one can also perform it around the higher frequencies of nf, where $n = 1, 3, 5 \ldots$ to find the odd harmonics. Naturally, the Fourier transform of a perfect sine wave should have zero amplitude at these frequencies. Whilst the signal noise will result in a non-zero Fourier amplitude, this should be much lower than any Fourier amplitude from the actual mechanical response, if such a response exists. Examining the Fourier amplitude allows us to see any increases in the Fourier amplitude. We also tested for Fourier amplitudes in the drive signal, at even harmonics
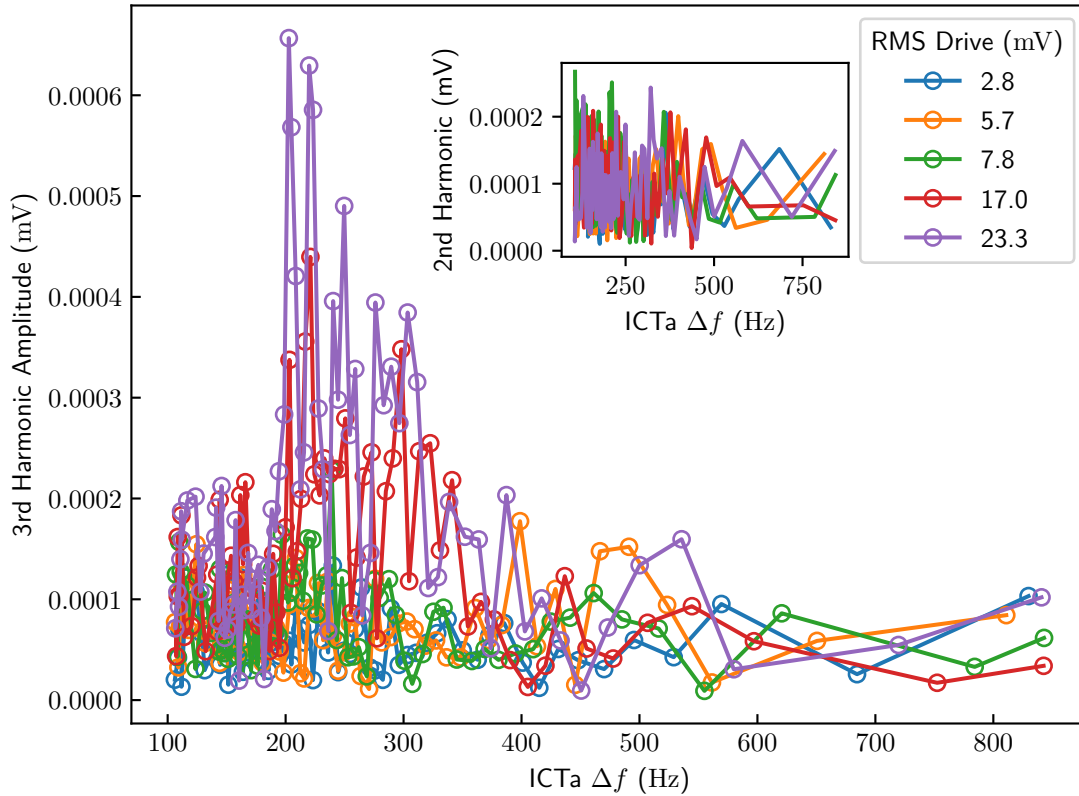
FIGURE 7.10: The amplitude of the 3rd harmonic second sine-wave measurement in millivolts. The magnetic field is 234 mT and the fixed frequency is 3 Hz. Only superfluid data is shown. Inset: The amplitude of the second harmonic in superfluid, which is constant.

($n = 2, 4, 6 \ldots$) and at a random frequency at an integer multiple of the fixed frequency were also examined.

Fig. 7.10 shows the $n = 3$ harmonic of the low field data corresponding to Fig. 7.8. As can be seen, a significant increase in the Fourier transform of the $n = 3$ harmonic for the two highest drives, 24 mV and 33 mV, is present after the entry into the A phase. This amplitude then decreases at an ICTa width around 320 Hz, similar to the width at which the 4 mV drive rejoins the curve.

If we were to normalise the 3rd harmonics by the drive as we did the velocity of the fundamental frequency, the normalised amplitude of lower drive signals would be larger than the normalised amplitudes of the 17.0 mV and 23.3 mV amplitude drives. This indicates that the 3rd harmonic amplitude of these drives is lower than the noise of the measurement, if they exist. The harmonics $n = 2$ were also measured (Fig. 7.10 inset), but this amplitude showed no features and was much lower than $n = 3$ and was closer in value to a random frequency. No changes were noticed in the drive signal for any of

the drive amplitudes used.

7.3.2 Higher Fields

At higher fields the picture is similar to that in lower fields, however without the B→A phase transition present since only the A phase is stable in these fields. Fig. 7.11 shows the normalised velocity amplitude and phase of a representative sine-wave measurement in a magnetic field of 453 mT. There is here a large difference between lower drives and the higher drives again, most notable with the 5.0 mV drive. Eventually, as temperature increases, all sine-wave amplitudes begin to follow the same curve again.

Interestingly, there appears to be a maximum velocity reached for every drive, something not seen before in the low-field measurements. This feature is perhaps interrupted by the B phase for the lower field measurements. For the two lowest drives, their velocity initially seems constant. There seems to be no discontinuity in the highest drive and steadily increases, despite the maximum in velocity. The data sets at high ICTa widths are much closer to the same phase when compared with low field data.

Finally, the normalised amplitude of the 3rd harmonic for each wave is also plotted in Fig. 7.12. The reason for normalising by the drive shall become clear below. As the temperature increases, the normalised 3rd harmonic decreases for all drives. This seems to happen at the same point for all drives. Again, the 2nd harmonic of each drive was also measured, but this amplitude showed no features and was much lower than $n = 3$.

7.3.3 Critical or Threshold Velocities?

There are two possible interpretations of the velocities here. One is that of a traditional critical velocity v_c, where the damping force increases and often becomes non-linearly dependent on velocity. The second is a type of threshold velocity. A description of the outcomes of them both follow.

Interpretation as a Critical Velocity

Under a standard critical velocity approach, the damping increases. Typical mechanisms for critical velocity are pair breaking, an abrupt change in the superfluid fraction (for example, due to a phase change) and the onset of quantum turbulence. The increase in damping shifts the resonance frequency to a lower frequency.

Considering the simpler high field case where there is no B phase, initially the lower drives are below the critical velocity, and the higher drives are above the critical velocity. The resonance frequency of the device for the higher drives would effectively be lower. Suppose at $v > v_c$ the lower resonance frequency is much closer to the fixed drive frequency of the measurement than when the device is below critical velocity. In this case,
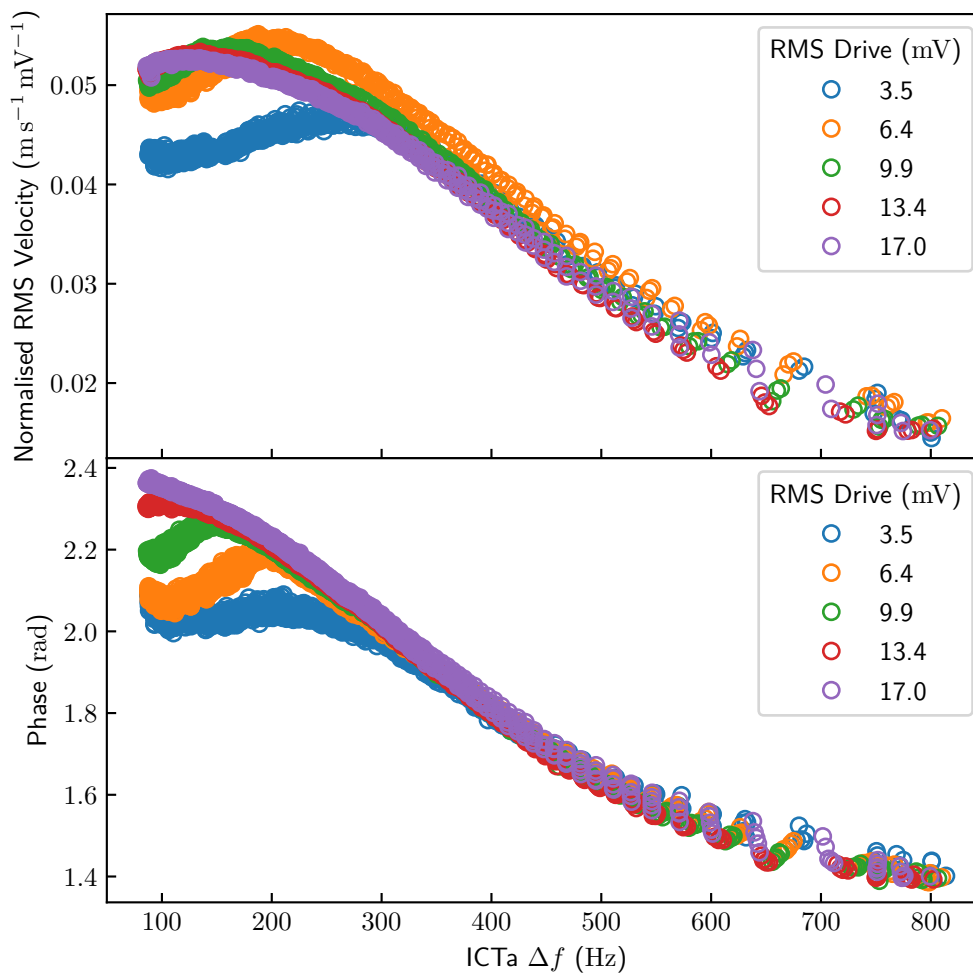
FIGURE 7.11: The velocity and phase of a high field sine-wave measurement. $B = 453\,\mathrm{mT}$ and $f = 2\,\mathrm{Hz}$. Only superfluid data is shown for clarity and as only 54 measurements were made in normal fluid before demagnetising again. The transition appears slightly earlier on ICTa as the NMR-flopper is positioned lower than ICTa and is only at 95% of the total magnetic field.

the normalised velocity for the higher drives would be higher, as they are closer to the resonance and see the enhancement. The lower drives would initially be further away from the resonance, with a reduced normalised velocity.

Under this interpretation, as temperature increases the critical velocity would have to decrease, such that the lower drives also break the critical velocity to catch up and rejoin
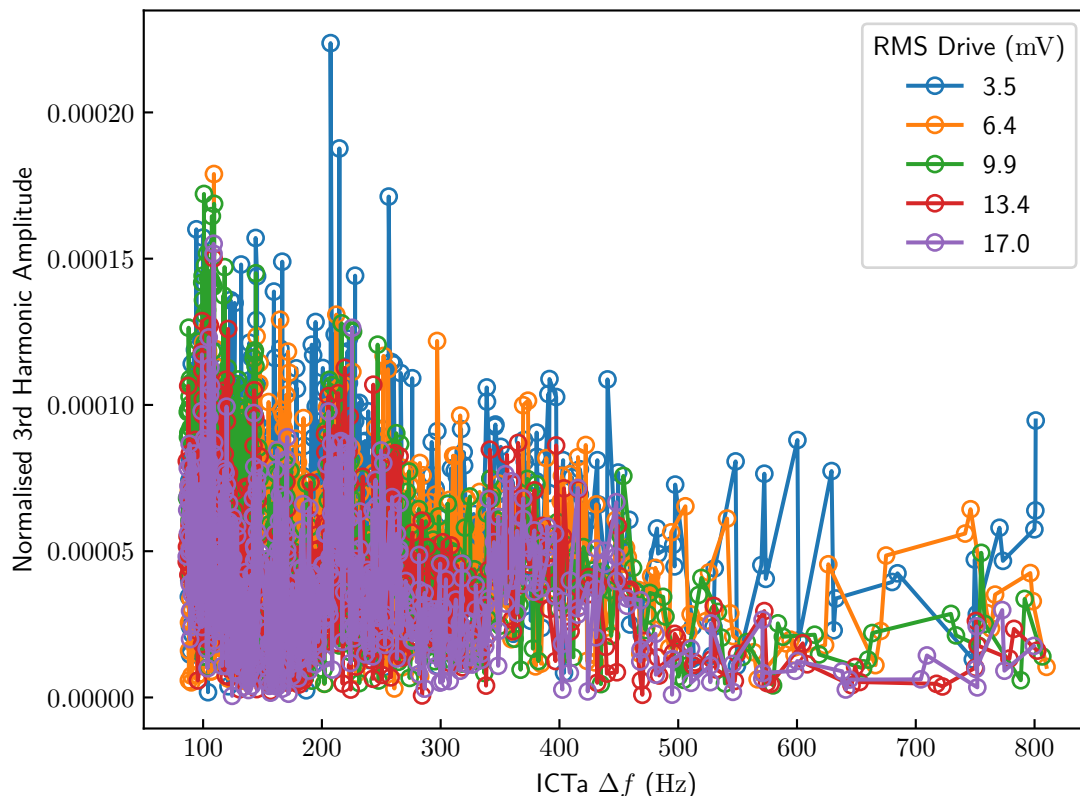
FIGURE 7.12: The amplitude of the 3rd harmonic second sine-wave measurement normalised by the drive. $B = 453\,\text{mT}$ and $f = 2\,\text{Hz}$. A rolling average with a window of 5 is used.

the same general curve. This is the opposite temperature dependence expected for the critical velocity v_d given by (2.37) at which the superflow energy is larger than the dipole energy [37]. Also, we must note under this shifting-frequency model that the oscillator is almost certainly underdamped. Recalling Fig. 3.2, for an overdamped oscillator, the amplitude at frequencies lower than the resonance frequency is close to a constant.

Previous hydrodynamic measurements of the superfluid fraction of ^{3}He in the A phase found that the apparent superfluid fraction decreases as the velocity is increased [10]. This effect was attributed to a textural change in the superfluid. As the velocity increases, the $\hat{\textbf{l}}$ vector inside aligns parallel to the flow. This increases the superfluid fraction inside the aerogel, as the superfluid gap goes to zero at points parallel to $\hat{\textbf{l}}$ (see Fig. 2.5). In those measurements, the axis of the aerogel cylinder is not orientated parallel to the superflow and the aerogel is isotropic. The magnetic field in our measurements is also much higher. The preferred alignment of $\hat{\textbf{d}}$ is perpendicular to the magnetic field.

The direction of superflow is parallel to the axis of the aerogel cylinder and perpendicular to the field, and so will tend to align $\hat{\mathbf{l}}$ also perpendicular to the field. The preferred alignment from the dipole interaction is $\hat{\mathbf{l}} \parallel \hat{\mathbf{d}}$, which is possible with our direction of superflow and magnetic field, and therefore we do not expect the textural alignment effects of the magnetic field and superflow to compete with each other. A hysteresis was also observed, attributed to the increased expelling of defects such as vortices as velocity increased. There is no hysteresis at all in our measurements. Our measurements take place in a much higher magnetic field.

7.3.4 Interpretation as a Threshold Velocity

The second possible interpretation of the difference between lower drives and higher drives for both fields involves a threshold velocity v_t. Under this interpretation, there is no superflow below the threshold velocity and therefore the damping of the wire is larger for a lower velocity. We can identify two possible mechanisms for a threshold velocity. One is velocity needed to orient the superflow parallel to the aerogel [10]. Another is that the β phase contains only ↑↑ Cooper pairs but the A phase contains both ↑↑ and ↓↓ Cooper pairs. In this case, around the aerogel the dipole energy of the A phase in a magnetic field (or A$_2$ phase) will not be minimised. In this case, the degeneracy is not lifted. The superflow energy must be greater than the dipole energy for superflow to occur at all.

We can interpret data as at first, the threshold velocity is only small, and only the lowest drive in Figs. 7.8 and 7.11 are below this velocity. It is impossible to know whether this is the "turn on" point, or whether this is just the first velocity to go below such a drive. As the temperature decreases, the threshold velocity increases, and other lower drives slowly drop below the threshold velocity. This seems to readily explain the feature of the velocity graphs. It may also offer a partial explanation of the 3rd harmonic data.

At high temperatures and at all drives, the NMR-flopper oscillates at a velocity above the threshold (or there is no threshold). In this case, the sine wave is normal and the $n = 3$ harmonic amplitude is low, caused only by measurement noise. Now consider an oscillating motion for a sine wave with an amplitude above the threshold velocity. For parts of the oscillation period, the velocity is between zero and the threshold velocity ($0 < |v| < v_t$), but at some point it will cross the threshold ($|v| \geq v_t$) and therefore the damping will decrease and the velocity will increase further, leading to a larger overall amplitude. A larger third harmonic amplitude happens when a more significant proportion of the sine wave is morphed. This explains why the third harmonic amplitude for the 33 mV seems to increase near the same point the first harmonic amplitude of the 4 mV drive stops increasing (in temperature decreasing direction).
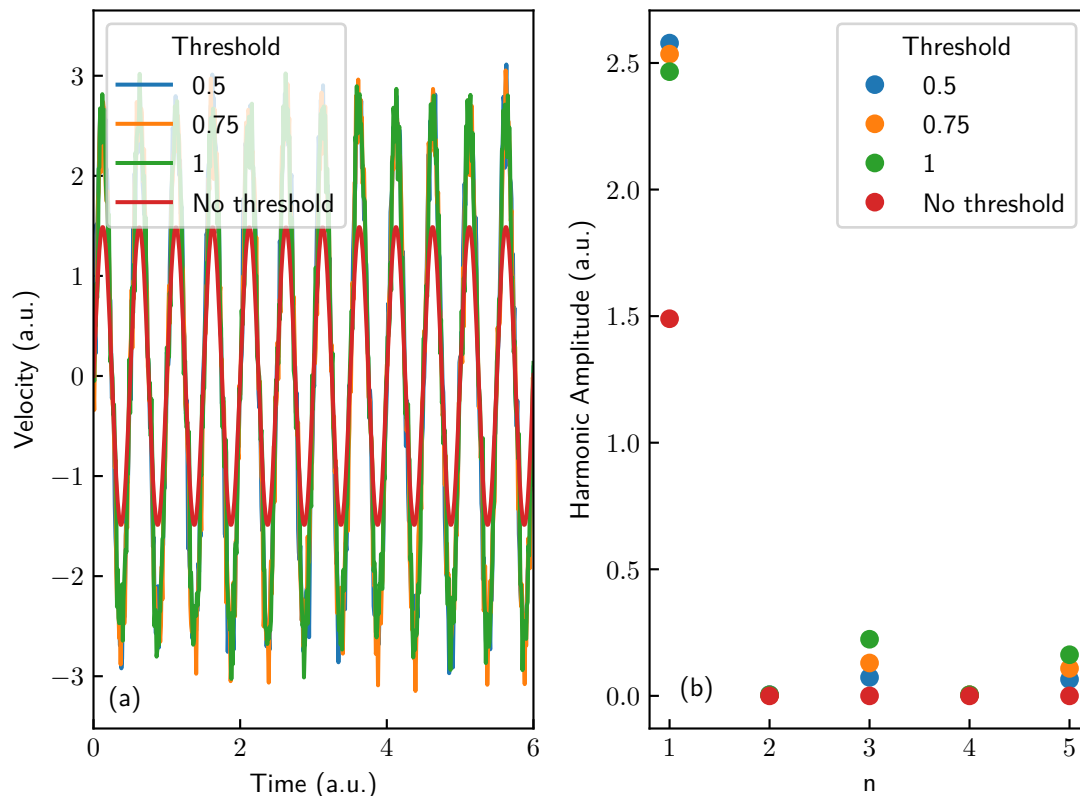
FIGURE 7.13: (a) The simulated sine-waves and the "velocity" the threshold velocity occurs at. All sine-waves have frequency of $f = 2$ and go on for time $t = 100$. The amplitude of the original sine-wave is 1.49. Above the threshold, the damping is reduced by half increasing the amplitude to 2.5. Random noise was added to each wave by a normal distribution centred at zero with a standard deviation of 0.1. (b) The Fourier amplitude of each harmonic nf found by the same slow Fourier transform as a real measurement.

In Fig. 7.13 (a) four simple model waves are created and in (b) shows the amplitude of the different harmonics. All model waves are originally created with the same damping, resulting in a velocity wave 1.49 in amplitude. Each wave is 100 seconds long, with a frequency of 2 Hz. For three of the waves, when the velocity reaches above a threshold (0.5, 0.75, 1 or one third, one half and two thirds), the damping decreases to half its value, increasing the velocity of the wave. The fourth wave has no threshold and is just the original for comparison. Finally, noise is added to each wave.

From Fig. 7.13 (b) we can see that there are odd harmonics created by a sine-wave response where the damping is halved after crossing a threshold but there is no even harmonics, which matches observations for the 2nd and 3rd harmonics. We also observe a distinct pattern. Aside from $n = 1$, the odd harmonic amplitudes increase as the threshold

is increased. In real terms, the more time the response is below the threshold, the higher the 3rd harmonic amplitude. If this is the case it explains why Fig. 7.12 the normalised harmonics of the lower drives are larger.

On the other hand, for the first harmonic the relationship is reversed. A lower threshold always results in a higher amplitude. One would expect a signal where most of the sine-wave is above the threshold to have a slightly larger first harmonic, and therefore one should expect to see the normalised velocity for lower drives slightly below the normalised velocity of higher drives in areas where they appear to follow the same temperature dependence. Looking at the velocities 7.11 and 7.8, the opposite is true. The fact that a lower drive is offset above the highest drive holds for all measurements we made, and is shown more clearly below in Fig 7.14.

Phase Diagram

It is possible to create a phase diagram by determining the ICTa width at which a velocity kink is observed somewhat objectively. For this method, we assume that the highest drive is always above the threshold velocity. At the high temperatures and in the normal phase, it was seen clearly that the normalised velocities follow a similar curve. If we assume the highest drive in any particular data set is always above the threshold velocity and it has no obvious critical or threshold velocities kinks, we fit the highest drive data with a polynomial. We can then use the same polynomial, plus some small offset, to fit the normalised velocity data of a second drive. However, when there is a kink we assume a linear function is subtracted from the polynomial that reduces the normalised velocity. By fitting for the ICTa width at which any kinks occur, we find possible transition points.

Fig. 7.14 gives an example of this process for the 9.9 mV drive compared to the highest 17.0 mV drive data shown in Fig. 7.11. As long as there are no obvious critical or threshold velocity kinks in the highest drive data we are comparing the lower drive with, we can assume the process will accurately find kinks. A disadvantage of this method is if there is a potential point in the highest drive data, one can not compare the curve to itself. A potential solution to this is to use data taken in the normal phase. However, not all datasets had data far enough into the normal phase, and there was no observable kink in the data for the highest drive anyway across all datasets.

We have data for fields 219 mT, 234 mT, 312 mT, 406 mT and 453 mT. For most data sets in the high magnetic field, as in Fig. 7.15, there are apparently two kinks. In low field, it is not always clear if there are two kinks, but the same process is used for all data sets. In Fig. 7.15, the temperature-velocity phase diagram is plotted. In (a) all kinks are plotted with their critical ICTa width, with 1 and 2 corresponding to the 1st and 2nd kink shown in Fig. 7.15. In (b), only kink 1 is presented and the ICTa width has been converted to temperature by the known-point thermometry calibration curve above.
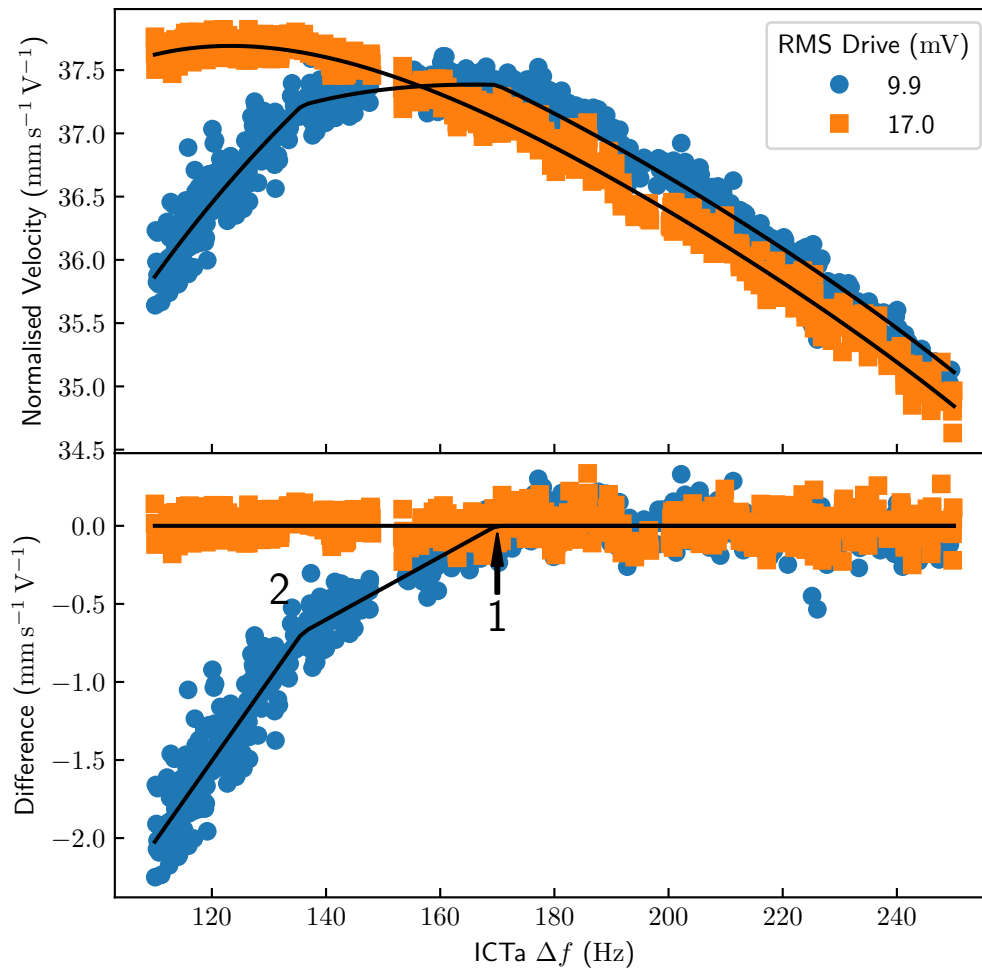
FIGURE 7.14: An example process of finding possible threshold velocity kinks. A polynomial curve is fitted to a high drive dataset and the same polynomial used with an offset to predict the temperature dependence of a lower drive. The lower drive data has two linear functions that are only added to the polynomial before a critical ICTa width, with the critical widths left as fitting parameters. One can see very clearly the effect when flattening the curves.

From Fig. 7.15 (b), a linear function is fitted to the data for the velocity kinks. The fit for kink 1 crosses the temperature axis at $0.92T_c$. This is very close to the aerogel transition temperature $T_{ca} = 0.9T_c$ for nafen-92 [7]. This is evidence that the kink has something to do with a superfluid transition within the aerogel. However, we must note that ICTa
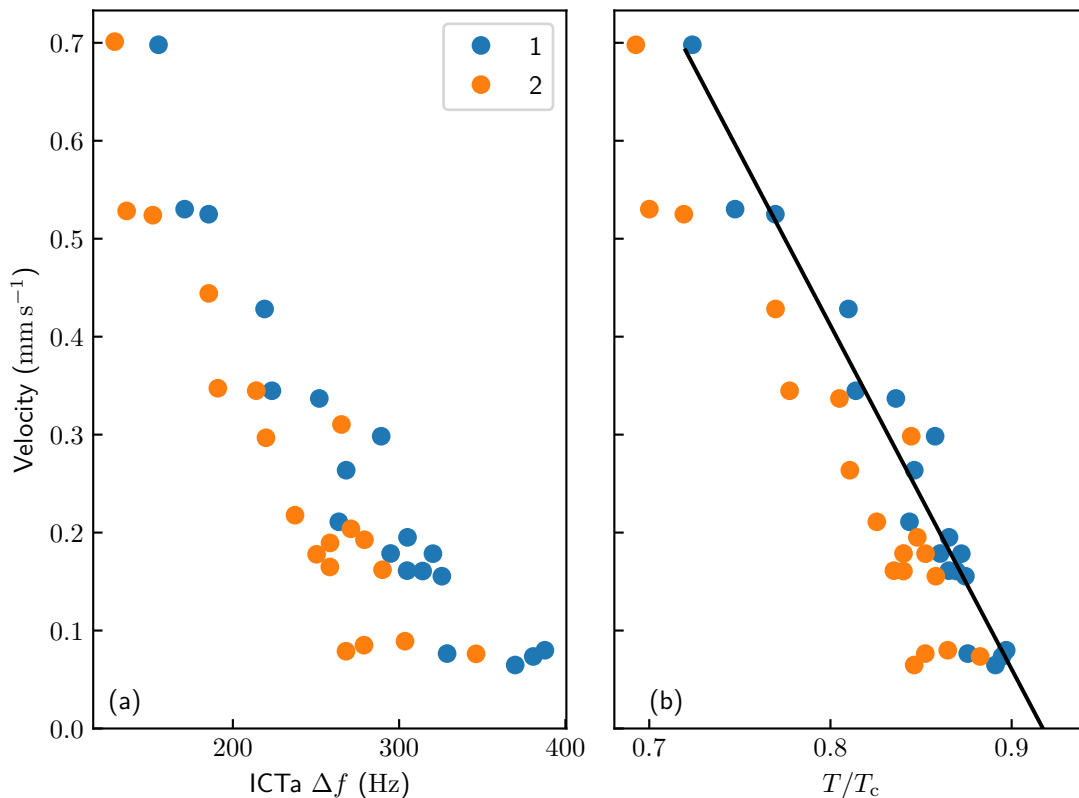
FIGURE 7.15: Temperature phase diagrams for the critical velocity in terms of (a) ICTa resonance width and (b) reduced temperature by calibration from Fig. 7.7. In (a), both kinks 1 and 2 are plotted. The black lines represent a linear fit to the kink 1 data. The velocity is 0 at $0.92T_c$.

known-point calibration in Fig. 7.7 can only be expected to be accurate within our estimated error for ICTa widths between 100 Hz and 300 Hz. Although there can be a large error for the widths outside this range, there are several values within this range and all the data seems to fit well to the line. Second, the error only just outside this range is unlikely to be on the order 100 μK. The error in the temperature calibration is hence not enough to change from the overall conclusion that this transition happens somewhere around the expected aerogel transition of $0.9T_c$, but it is clearly not precise enough to say exactly where this temperature is. The temperature difference between kink 1 and kink 2 varies widely. The data was collected at various fields which would explain some differences, but the difference at high velocities is very large and some tens of millikelvins. This may be due to overheating. For these reasons and the inaccuracy of the temperature calibration at the high-temperature range, it is impossible to draw any conclusions about the physical nature of the second kink and whether it is a phase transition in the aerogel.

7.4   Drop Measurements

The second type of measurement used was a so-called "drop" measurement. The NMR-flopper was held at an equilibrium by a constant DC drive current I_{ini}. The NMR-flopper is then "dropped" at time t_0 to another equilibrium position determined by a DC drive current I_{fin}. The current switch was instantaneous and not smooth, similar to holding a pendulum at a fixed position and releasing it. The free response of the oscillator is then observed by monitoring its position as a function of time. The position is detected by measuring voltage on the detection coils and then converted to a position by the method described in section 4.2.3.

Equations (3.18), (3.20) and (3.21) give the response of a generic oscillator for under-damped, overdamped and critically damped conditions. Although in our case $I_{fin} \neq 0$ and therefore $x(t \to \infty) \neq 0$, this is a simple offset that can be subtracted. We can use the boundary conditions $x(0) = x_0$ and $\dot{x}(0) = 0$ for fitting the response, and the response of the oscillator will be similar to the example plotted in Fig. 3.2. We fit the signal with a python program using the trigonometric and hyperbolic versions of (3.18) and (3.20) respectively. With our initial conditions the constants c_3 and c_4 are

$$c_3 = x_0, \qquad (7.2) \qquad\qquad c_4 = \frac{x_0 \Delta\omega}{2\omega_{ud,od}} \qquad (7.3)$$

with the appropriate underdamped and overdamped resonant frequencies.

As with the constant frequency sine-wave measurements, a small drive is applied to the gradient coil and the position is detected by a lock-in amplifier measurement of the voltage response generated on the NMR coil. The voltage was measured through the digital filter of the lock-in amplifier, which is equivalent to four simple exponential decay filters with a time constant $\tau_f = 10\,\text{ms}$ (see Appendix B.3). Whilst this is relatively inconsequential for a low frequency sine-wave or a signal with a response time much longer than 10 ms, the NMR-flopper typically reached its new equilibrium within a few hundred milliseconds in the most overdamped of cases.

The response for a first-order exponential decay filter with time constant τ to the position $x(t)$ measured by the voltage on the detection coils can be found from

$$\dot{y}_1 = \frac{x - y_1}{\tau_f} \qquad (7.4)$$

with the initial condition $y(0) = x(0)$ which gives the simple exponential decay. Once we have solved the equation for the first filter, we can use the output $y(t)$ as a new input $x(t)$ for the next filter and repeat the process. We can iterate the process over J filters (see Appendix B.3). The response for an underdamped oscillator to any number of filters J with the same time constant is

$$y_J = e^{-\frac{\Delta\omega}{2}t} \left[A_J \cos(\omega_{\mathrm{ud}}t) + B_J \sin(\omega_{\mathrm{ud}}t) \right] + \sum_{j=0}^{J} \left(1 - A_{J-j}\right) \frac{(t/\tau_{\mathrm{f}})^j}{j!} \tag{7.5}$$

and for an overdamped oscillator

$$y_J = e^{-\frac{\Delta\omega}{2}t} \left[A_J \cosh(\omega_{\mathrm{od}}t) + B_J \sinh(\omega_{\mathrm{od}}t) \right] + \sum_{j=0}^{J} \left(1 - A_{J-j}\right) \frac{(t/\tau)^j}{j!}. \tag{7.6}$$

The constants A_J and B_J are given by the series

$$A_J = u_F A_{J-1} - v_F B_{J-1} \tag{7.7}$$

$$B_J = u_F B_{J-1} \pm v_F A_{J-1} \tag{7.8}$$

and the multipliers u_F and v_F are

$$u_F = \frac{1 - \tau\Delta\omega/2}{(1 - \tau\Delta\omega/2)^2 \pm (\omega_{\mathrm{ud,od}})\tau)^2} \tag{7.9} \quad v_F = \frac{\tau\omega_{\mathrm{ud,od}}}{(1 - \tau\Delta\omega/2)^2 \pm (\omega_{\mathrm{ud,od}})\tau)^2}. \tag{7.10}$$

For underdamping, the $\pm$ signs are positive, and for overdamping, the $\pm$ signs are negative. Fig. 7.16 shows a measurement and a fit of both an underdamped and overdamped responses from the NMR-flopper below T_c. The fits are with $J = 4$ and $\tau = 10\,\mathrm{ms}$. The NMR-flopper is held at the position corresponding to the initial drive current for a few seconds before the drop time, from which we take x_0. We measure for a long time after the NMR-flopper returns to equilibrium, and from here take the offset to be subtracted. Therefore, the only fitting parameters are the resonance width and the natural resonant frequency ω_0. The actual change in position (with no filters) of the oscillator is also plotted in Fig. 7.16 based on the fitted resonance frequency and width. The velocity can be measured from the time derivative of the position. We can vary the drop distance to change the velocity the device reaches. The advantage of this method versus constant frequency measurements is we can directly easily obtain the resonant frequency and damping of the device, similar to doing a frequency sweep, which can then be used to measure the superfluid density.

7.4.1   Saturated Vapour Pressure

Drop measurements were first carried out at saturated vapour pressure at ultra-low temperatures. At this pressure, two slow-warming measurements were made with magnetic fields of 273 mT and 468 mT. Fig. 7.17 shows the response at 468 mT for the oscillator's damping and the resonance width and the oscillator's undamped (natural) resonance frequency. As one can see there is a clear phase transition to T_c but also a large increase in the damping just before. This large increase in damping corresponds roughly to the location of the A_1 phase. In fact, phase transitions seem to be detected slightly earlier
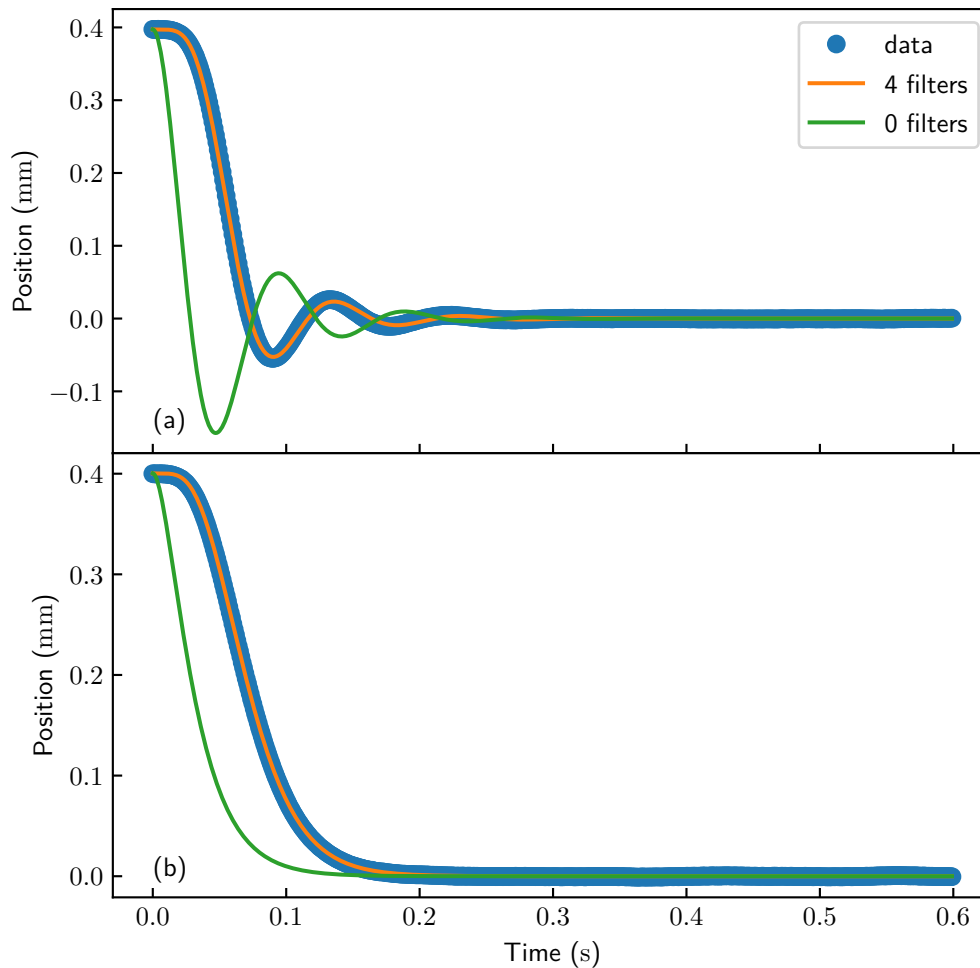
FIGURE 7.16: Two examples of a drop measurement when the NMR-flopper is (a) underdamped and (b) overdamped. The lock-in time constant was set 10 ms and the filter -24 dB, indicating a series of 4 filters. x_0 is taken from the average of values before the measurement and is 0.400 mm. The fit parameters are (a) $f_0 = 11.0$ Hz and $\Delta f = 6.25$ Hz and (b) $f_0 = 9.80$ Hz and $\Delta f = 20.7$ Hz.

by the NMR-flopper than ICTa. The same effect was found in the sine-wave measurements. We can attribute this to the heating being produced by measurements as being more localised creating some overheating, and the magnetic field not being uniform in the z-direction. The presented field is the maximum field provided by the main demagnetisation magnet, which occurs roughly in the middle of the Cu plate refrigerants. The
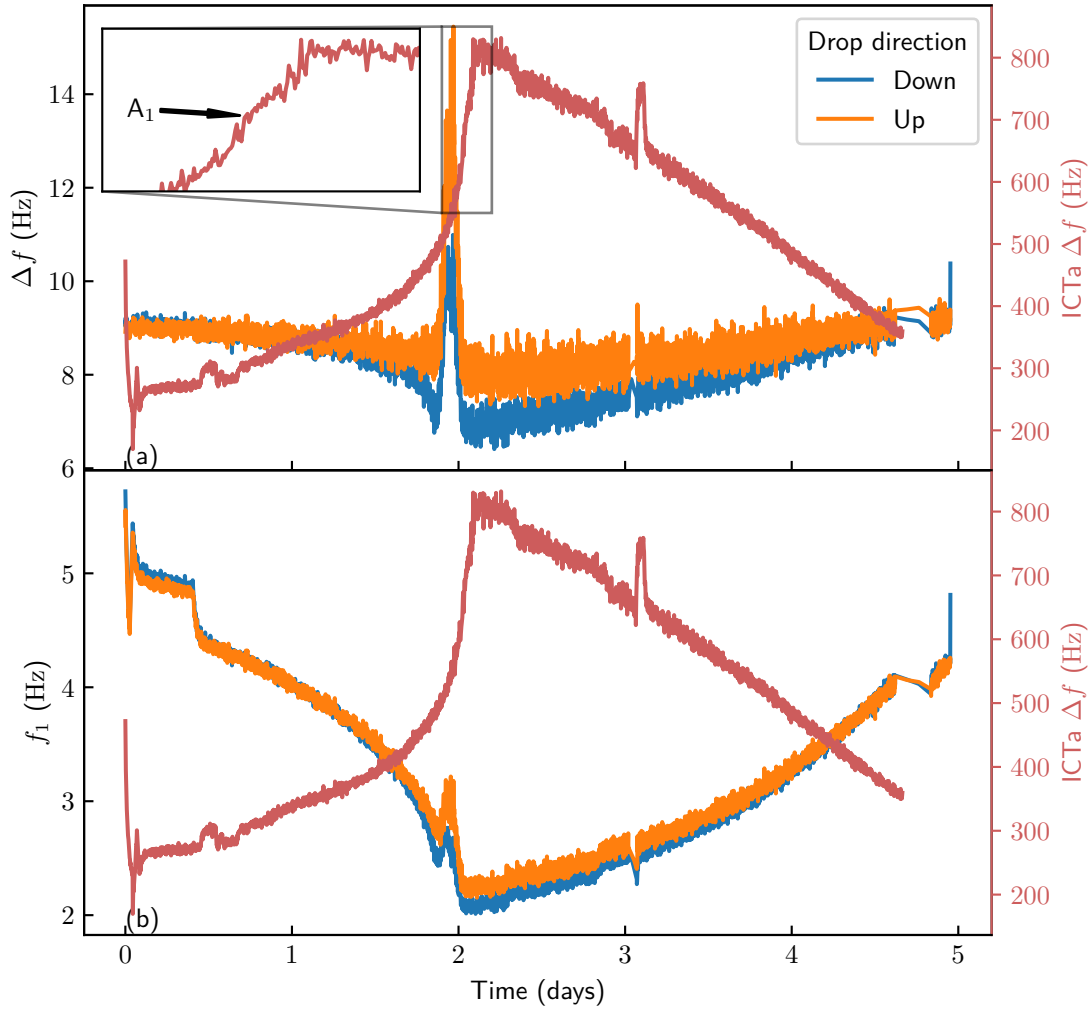
FIGURE 7.17: Drop measurements as a function of time after nuclear de-magnetisation and the cell temperature has settled. The cell is left to warm up and the temperature is monitored by the ICTa thermometer in red. A rolling average with a window of 3 is used. (a) The resonance width as a result of fitting by (7.5) and (7.6). (b) The resonance frequency. We assume this is the fundamental mode f_0. The A_1 phase transition is zoomed in on ICTa.

location of ICTa means that the field is calculated to be at 98.4% of this field [106]. The old flopper crossbar was in a similar position, but since the inversion, the NMR-flopper crossbar will be at $\approx 95\%$.

What is strange about the A_1 transition detected on the NMR-flopper large spike in the damping just before T_c is that it is much higher than damping in the normal phase. This is possibly caused by the superflow within the oscillator as the phase changes, causing a large change in the local texture. The texture changes and energies involved are

difficult to calculate because there are multiple competing effects on the texture: the orientation of $\hat{\mathbf{l}}$ due to the aerogel, the orientation of $\hat{\mathbf{l}}$ due to the magnetic field and the orientation $\hat{\mathbf{l}}$ due to the superflow.

The other noticeable difference is the difference between dropping the NMR-flopper upwards and dropping the NMR-flopper downwards. This difference is most likely due to some asymmetry in the device. First, the NMR-flopper is not perfect and has some asymmetry in the legs. Second, the coil may have been slightly imbalanced. Third, in one direction the flopper is moving against gravity. Fourth, the aerogel sample may be asymmetric. What is strange is that the difference seems to be more pronounced around T_c in the superfluid phase than in the normal phase, which may indicate the aerogel is symmetric, and the superfluid inside the aerogel is asymmetric.

Examining the frequency dependence with temperature we learn important properties of the device with regard to the fixed-frequency sine wave measurements. The fixed-frequency measurements were most commonly performed with frequencies of 2 Hz and 3 Hz. Between some temperature range, around the T_c, the frequency of the NMR-flopper is below 3 Hz. For 2 Hz measurements we can assume the point is always below the resonance frequency, but for any 3 Hz measurements the resonance frequency crosses the fixed-point.

7.4.2 5 bar Pressure

The decision was made to pressurise the experimental cell by adding more liquid ³He to increase the temperature width of the β phase. According to (2.36) the temperature width is linear with field and equal to $2T_{ca}\eta_a B$. From previous measurements of the phase diagram (Fig. 2.8) [7], the aerogel transition temperature increase from $T_{ca} \approx 0.9T_c$ to $T_{ca} \approx 0.95T_c$. Furthermore, T_c increases 0.929 mK to 1.48 mK [12]. Not only does this increase the temperature width of the β phase, but we no longer need to demagnetise to as low fields to reach the superfluid temperature. This allows us to perform measurements at even higher fields, further widening the temperature width of the β phase if it is stabilised in our system [37]. We performed drop measurements in magnetic fields ranging from 0.5 T–1 T, resulting an estimated $\Delta T_\beta =$ 28 μK–56 μK.

Upon performing the drop measurements, an extremely unusual phenomenon happened, as the NMR-flopper resonance frequency was found to increase to roughly double in both normal and superfluid. Since the frequency doubled in both superfluid phases and the normal fluid phase it seems entirely mechanical. There is no reasonable explanation for this effect. It is not clear how the pressure of the fluid can strongly effect the properties of the resonator, unless the pressure changed the mechanical properties of the material or the shape of the object somehow.
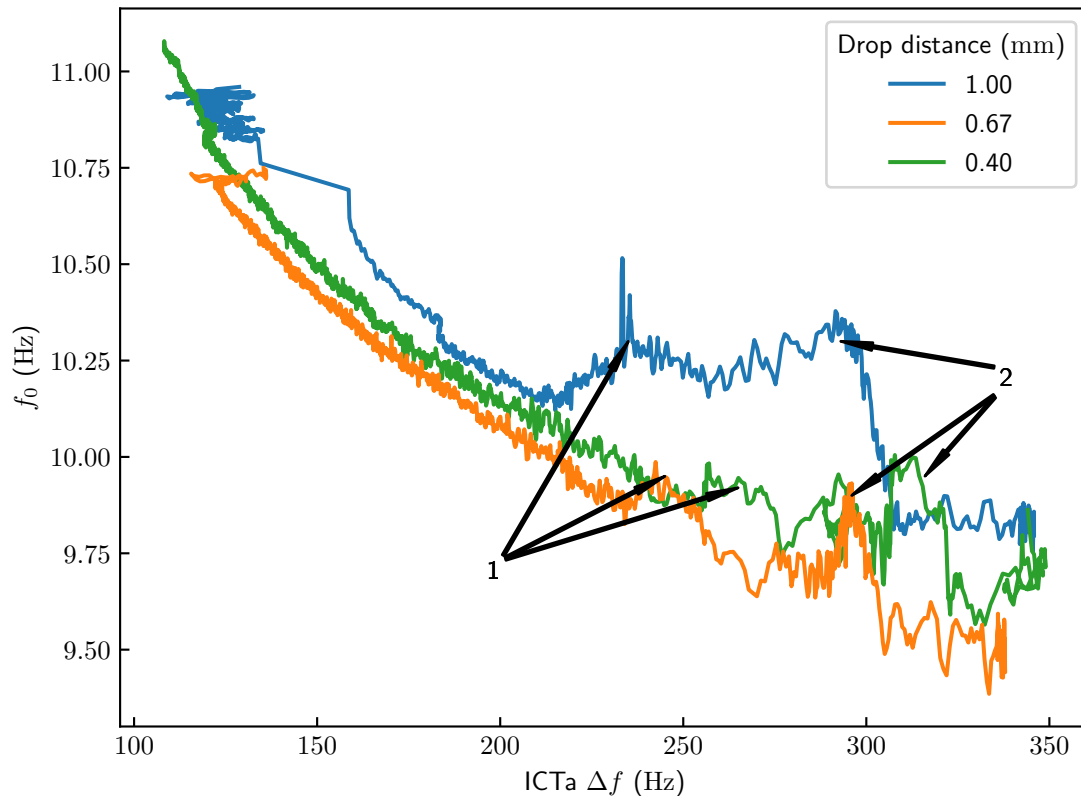
FIGURE 7.18: The undamped resonance frequency of the NMR-flopper af-
ter a downwards drop as the cell temperature slowly warms. Temperature
is measured by the ICTa resonance width. The data displayed is up un-
til T_c. A rolling average with a window of 3 was used for the 1 mm and
0.67 mm drops, and a window of 5 for the 0.4 mm drops. The two peaks
are labelled.

Fig. 7.18 shows plots of the resonance width as function of ICTa width for measure-
ments with different drop distance in a magnetic field of 940 mT. Due to the differences
that appear between upwards and downwards drops, for clarity only downwards drops
are plotted. Just before the transition to the normal phase there seems to be a double peak
in the resonance frequency. It is also apparent in the resonance width, although less no-
ticeable. In time, these transitions occur just before A_1 and normal transitions are detected
by ICTa, which is consistent with the constant frequency measurements.

The velocity response of the NMR-flopper for a drop measurement in each peak is
shown in Fig. 7.19. The velocity at the first peak is slightly faster than the second peak in
all cases even though the frequencies are very similar, indicating the damping is larger in
the second peak.

We need to distinguish between several possibilities: (1) each peak is a phase unto
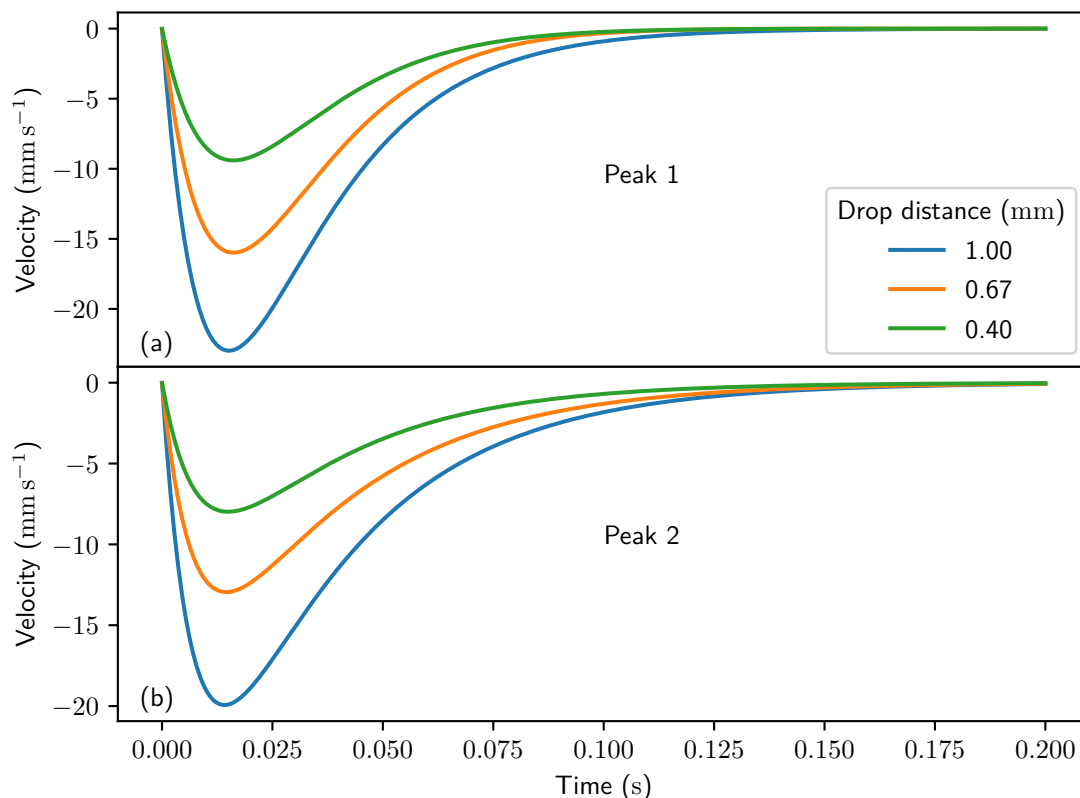
FIGURE 7.19: The velocity of a typical drop measurement for (a) the first peak and (b) the second peak as labelled on Fig. 7.18. The velocity is found by differentiating the position as determined by the fit parameters with respect to time. The maximum speeds are (a) $23.0\,\mathrm{mm\,s^{-1}}$, $20.0\,\mathrm{mm\,s^{-1}}$ and $16.0\,\mathrm{mm\,s^{-1}}$ and (b) $13\,\mathrm{mm\,s^{-1}}$, $9.4\,\mathrm{mm\,s^{-1}}$ and $8\,\mathrm{mm\,s^{-1}}$, for drop distances of $1\,\mathrm{mm}$, $0.67\,\mathrm{mm}$ and $0.4\,\mathrm{mm}$ respectively.

itself, with the first being a phase in the aerogel (β), the second being a phase in the bulk (A_1) or (2) each peak represents entering and leaving a single phase. In the case of (2), we need to then further distinguish whether this is the β or A_1 phase, since until now we have assumed that the NMR-flopper is indeed sensitive to the bulk $A\rightarrow A_1$ transition.

Temperature Calibration

To distinguish between these possibilities, we begin by backwards extrapolating in time the temperature as measured by ICTa in the normal phase to produce a relationship between time and temperature. We can then compare it to the known transition temperature of $1.478\,\mathrm{mK}$ at $5\,\mathrm{bar}$. This backwards extrapolation is more complicated as the discontinuity in ICTa appears at various widths depending on the field, with the difference some tens of Hertz. There is no single calibration that matches all fields. Δf is linear with the
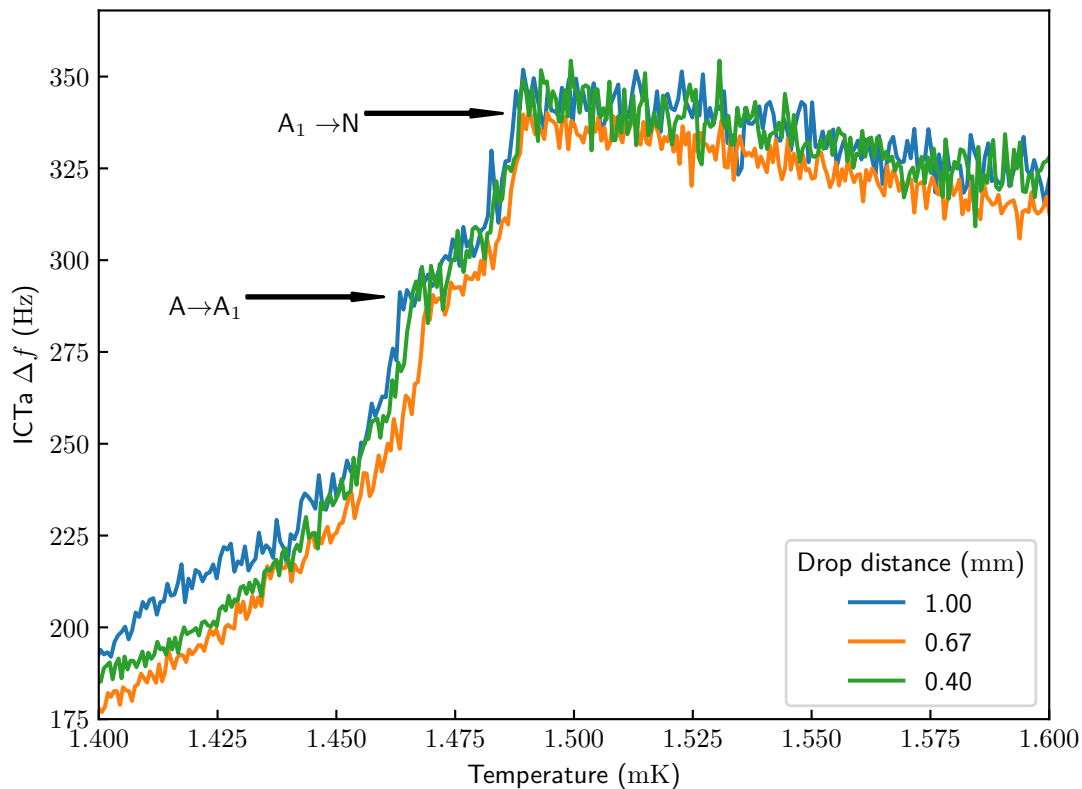
FIGURE 7.20: The resonance width of the ICTa thermometer as a function of temperature after using backwards extrapolation from the normal phase and known point thermometry at T_c for drop measurements in a magnetic field of 937 mT. The first kink in the width is the A_1 phase transition, and the second is T_c.

inverse temperature so if we assume the difference in width is constant with time, the width difference can be considered simply as an offset. Therefore, the heating rate (the gradient of the temperature with respect to time) is accurate. A recalibration with regard to the actual time ICTa went through T_c can be performed. The actual relationship of time and temperature can be checked against the A_1 transition given by [12] in Fig. 2.6.

The maximum magnetic field is 937 mT, and the flopper is at a position where field strength 95% of the maximum magnetic field. In this field, and at a pressure of 5 bar, the A_1 width should be $\approx 22 \, \mu K \, T^{-1}$ and therefore $T_c = 1.478 \, mK + 0.011 \, mK$ [12]. Fig. 7.20 demonstrates the ICTa calibration procedure described above. Each drop measurement has an A_1 phase temperature width of $\sim 22 \, \mu K$. The difference between the lowest and highest temperatures the A_1 phase kink appears at can be used as an estimate for the error. This difference is $5 \, \mu K$.

After calibrating, it is possible to plot the undamped frequency shown in Fig. 7.18 as
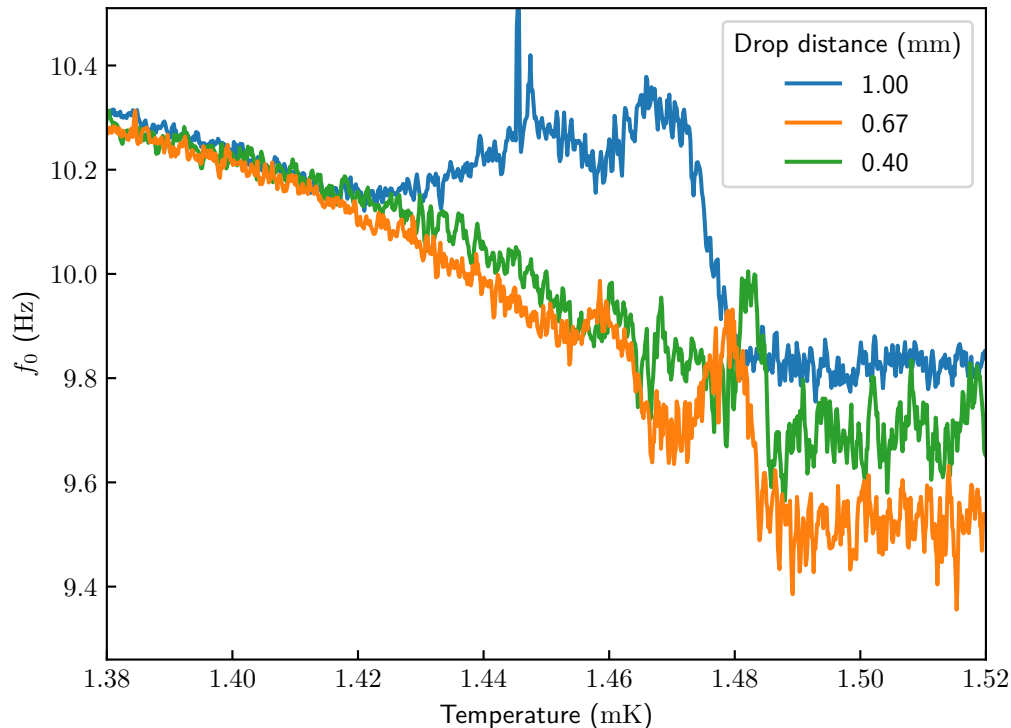
FIGURE 7.21: Undamped resonance frequency f_0 as a function of temperature for downward drop measurements in a magnetic field of 937 mT.

a function of temperature instead of ICTa width. From Fig. 7.21 there is a definite difference between the double peak for a drop distance 1 mm and the two lower distances. The overall temperature width is much larger than the A_1 width. From the beginning of the first peak to the end of the second, the temperature width is 57 µK±7 µK. Each peak is wide enough on its own to be the A_1. As mentioned above, the aerogel transition temperature at 5 bar is approximately $0.95T_c$, which is 1.4 µK. Therefore, the first peak also begins roughly in the correct position for the β phase.

There is little difference between the undamped resonant frequencies of the two lower amplitude drops. For the 0.67 mm and 0.4 mm drops the width is 30 µK±7 µK, still larger than the A_1 phase. Considering peak-centre to peak-centre, the width would be much closer to 20 µK. But for these drops neither peak on its own has a large enough temperature width on its own to be the A_1 phase, unlike in the case of the 1 mm drops.

FIGURE 7.22: The NMR-flopper resonance frequency near bulk T_c from drop measurements with a drop distance of $\sim$ 0.7 mm in several magnetic fields. Rolling averages with windows (a) 5, (b) 3, and (c) 3 are used.

Magnetic Field Dependence

A more useful way of identifying any phase transitions would be to follow the temperature widths of the peaks and the beginning and end. Given there may be a difference between higher and lower distances, drops with similar distances should be grouped together.

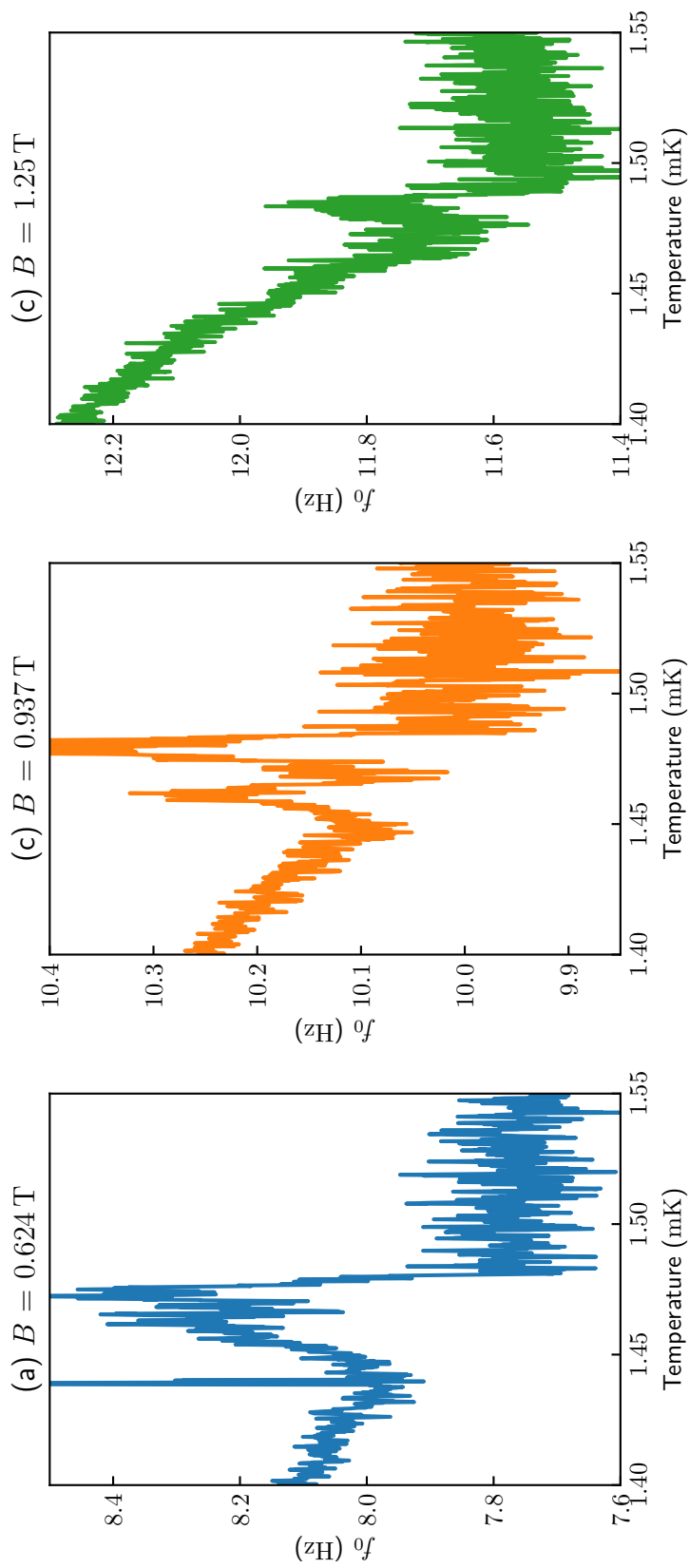Fig. 7.22 shows three drops measurements with a drop distance ~ 0.7 mm in distance at different fields. In checking the ICTa calibration for each measurement, the A_1 was found to vary with field according to [12]. Again, the 0.67 mm measurement was the furthest from the expected A_1 width, so the temperature error is still approximated as 5 μK. From the measurements, we can see the double peak is not particularly consistent among the data. It seems present in (a) and (b), but not present in (c).

Furthermore, there is no clear magnetic field dependence in the width of the peaks or the distance between the peaks. (a) and (c) look extremely similar yet the magnetic field has increased by 50%. This should result in a 50% increase in the phase width for both A_1 and β phase. For drops with a distance of over 1 mm there were measurements for three different fields, and the result were similar. There was no field dependence found, and one measurement didn't show any sign of a double peak.

What is consistent among both groups of measurements is that the frequency seems to depend on magnetic field at all temperatures. The average resonant frequency increases as field increases, going from (a) to (c). When the width is plotted instead in Fig. 7.23, there is no overall increase in the width as with f_0. Since there is no change in the damping measured by the width, it is likely the increase in frequency is caused by an increase in the effective stiffness. It has previously been found that VWRs resonance frequency increases as magnetic field increases due to the pinned flux lines present in the superconducting wire [63, 64].

In Fig. 7.23, we do also notice a field dependence in the width of a potential phase transition. The phase width of the 1250 mT drops seems about 30 μK, which is a result that matches the expectation for the A_1 phase. Both the 624 mT and 937 mTdata shows a higher width in the superfluid phase. Both of these datasets were the two that displayed a double peak most clearly. This leads us to suspect that the double peak is a result of some interaction within the A_1 phase, rather than the β phase.

7.5   Conclusions

In this chapter we first presented NMR measurements at low magnetic field. NMR can be used to fingerprint the polar phase and detect HQVs. In the normal phase, there was no temperature dependence of the magnetic susceptibility, confirming we had pre-plated the surfaces with enough ^{4}He to remove the signal of solid ^{3}He. Below T_c the magnetic
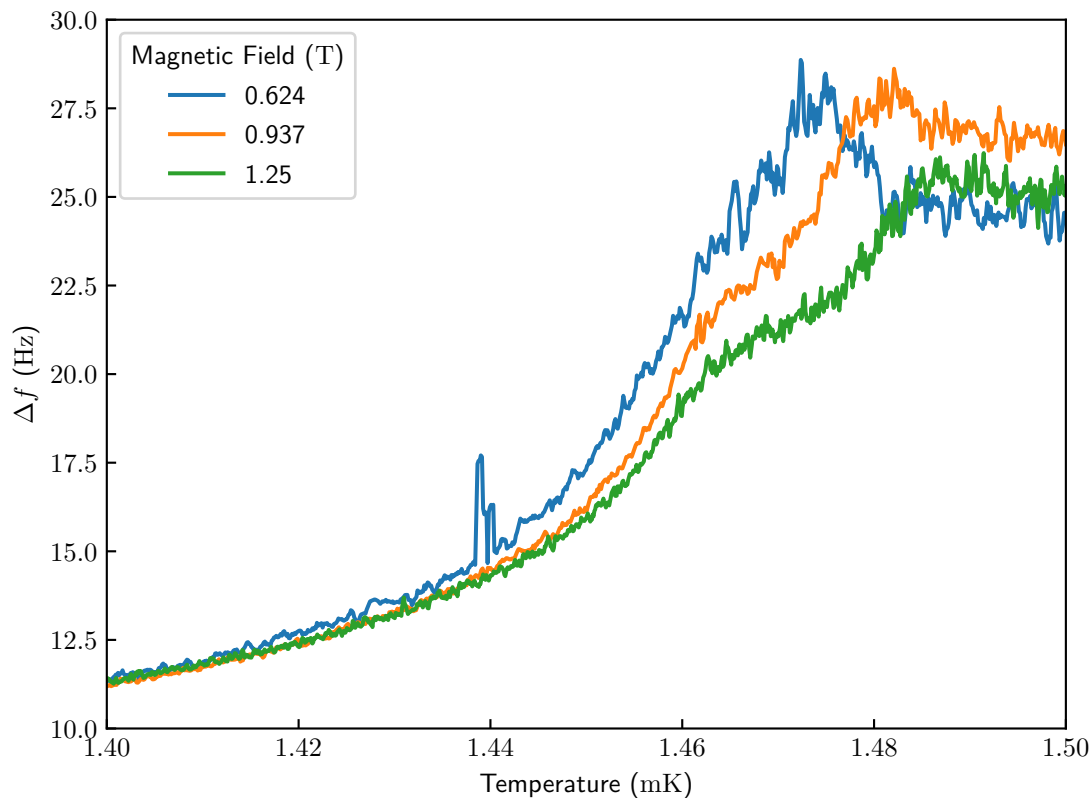
FIGURE 7.23: The NMR-flopper resonance frequency near bulk T_c from drop measurements with a drop distance of ~ 0.7 mm in several magnetic fields. Rolling averages with a windows (a) 5, (b) 3 and (c) 3 are used.

susceptibility dropped, an indication of the non-equal spin pairing B phase. The current state of measurements shows our width is larger than the expected frequency shift of any HQVs at the temperatures measured. They do indicate that HQVs could be detected at much lower temperatures, although the HQV peak would overlap with the main peak. There is hope for improvement, however, if the gradient magnet can be driven to higher fields. An alternative possibility, since the capacitors in the NMR RLC circuit are located outside the cell, they could be changed to reduce the resonant frequency and thereby increase the frequency shift of the HQV peak.

We have also described our efforts to discover the β phase in superfluid ³He in a nematic aerogel using mechanical motion of the NMR-flopper. The NMR-flopper is heavily overdamped near T_c. Instead of frequency sweeps, two other measurement types were used. Despite our best efforts, we have not yet found evidence of the pure β phase. Instead, we have found a series of odd effects. First, there is apparently no change in the velocity of the NMR-flopper driven by a constant force when the bulk superfluid is in

the B phase as the temperature increases. Second, there are some possible threshold or critical velocities whilst the bulk liquid is in the A phase. Plotting a temperature-velocity phase diagram and extrapolating, we see that these velocities begin around $0.9T_c$, the expected polar phase transition. Since, in general the transition temperature of any phase of superfluid ³He is reduced in aerogels, this can not be taken as evidence of the polar phase. Finally, there is sometimes a double-peak in the undamped resonant frequency of the NMR-flopper at temperatures just below T_c and higher damping in the A phase than in the normal phase. These two phenomena seem to be related, as measurements that show a double peak often show a higher damping.

Chapter 8

Summary

This thesis has presented work on two main experiments in superfluid ^{3}He. The first experiment was a continuation of a previous experiment, using new results, techniques and analysis, taking place in superfluid ^{3}He-B. The second was a newly built experiment exploring superfluid ^{3}He confined in an aerogel.

8.1 Faster than Landau Experiments

In the first experiment, the dissipation mechanism of a large superconducting wire known as the flopper as it was moved faster than the critical Landau velocity in superfluid ^{3}He was investigated. Previously, it was discovered that there is no large onset of damping seen with oscillatory motion at the critical velocity or the Landau velocity. Instead, a small increase is seen. A tentative model was proposed, that the only damping comes from surface-bound-states on the wire. In a previous work, an attempt at discovering the replenishment rate of the surface states was made by moving the wire, waiting and repeating the movement in the same direction (up ramp) or reversing the direction (down ramp).

In this work, we pre-plated the cell with 2.5 layers of solid ^{4}He to increase the surface specularity. This was not found to affect the dynamics of the surface states. We have reanalysed the old data with a slightly different technique, fitting two separate exponential decay curves to the heating of the up ramps and down ramps as the waiting time is varied, rather than trying to fit the difference. This is because there is a direction dependent magnetic heating effect, which results in the heating of the two ramps being slightly different. We conclude there is no temperature dependence to the time constant τ of the exponential decay. An argument that this time constant represents the time constant for a surface state to undergo a crossbranch process, where it changes its momentum, was presented.

We varied the velocity of these ramps and analysed the difference in dissipation between down ramps and up ramps as the velocity was increased. When there is no wait time between the first and second half of each ramp, from the Lambert model there

should be a large difference in heating between the two ramps, beginning at $v_c = v_L/3$. By removing the effects of magnetic heating, we demonstrated that there is no extra dissipation due to surface states below v_c and indeed there is an increase in the dissipation above at $v \geq v_c$, following a v^2 dependence. Since the bulk superfluid quasiparticle contribution to the dissipation is not direction dependent, it is effectively removed by plotting the difference. Therefore, this extra dissipation can only be due to the surface states.

Furthermore, an analysis of the thermometer response used to measure the heating generated by the flopper was carried out. By measuring the time decay of the response back to a base temperature, the Kapitza resistance could be measured. The Kapitza resistance between liquid helium and sintered metal has long been controversial, especially at ultra-low temperature. Our measurements found an exponential dependence of the Kapitza resistance on temperature, agreeing with previous measurements made at Lancaster and Cornell. As the previous measurements were made with the same sinter recipe, the Kapitza resistance multiplied by the area (or the heat conductance per area) should be roughly similar. Surprisingly, the area that gives even an order of magnitude estimate is the geometric area: the area available for quasiparticles to scatter. This finding may be useful to future demagnetisation experiments, when designing the shape and structure of the nuclear refrigerant to maximise the cooling power.

Finally, the Kapitza resistance was found to double when 2.5 monolayers of solid ^{4}He were added. As solid ^{4}He is non-magnetic, and solid ^{3}He is paramagnetic, this is evidence for the magnetic channel of heat transfer between silver sinter and superfluid helium.

8.2 The Search for the β Phase

The experimental cell used above was rebuilt for a new experiment. The polar phase of superfluid ^{3}He was recently stabilised for the first time in a nematic aerogel known as nafen. At high magnetic fields, the β phase should also be stable, which, at the time of beginning the experiment, had not been stabilised. As with the bulk A_1 phase, this phase consists of only Cooper pairs with both spins parallel to the field. Half quantum vortices (HQVs) can also be stabilised with this phase. HQV are best detected by Nuclear Magnetic Resonance (NMR) at low magnetic fields, whereas the β phase cannot be detected by NMR. Instead, it can be detected by the change in the superfluid density.

To this end, a new oscillating device was created. The nafen aerogel was fit inside an NMR coil and glued to a vibrating wire, very similar in design to the flopper. Mechanical vibrations allow us to probe the superfluid density and possibly nucleate HQVs at low temperatures.

Sadly, the β phase has not been discovered with this device in high magnetic fields, and there are some limitations to the NMR side of the experiment that will make it difficult to observe HQVs without going to very low temperatures. More optimistically, there have been some strange effects seen whilst in the bulk A phase that are likely due to the superfluid phase in the aerogel, including a possible threshold or critical velocity. Secondly, the NMR circuit frequency can be lowered, and the NMR peak shift of the HQVs can be increased to within our resolution fairly easily.

Additionally, new sub-micron diameter vibrating wires were measured in superfluid ^{3}He-B below $200\,\mu$K. These wires experience much lower damping than expected from the standard treatment of wires in the ballistic regime. This is possibly due to a lack of Andreev reflection, as the wire radius approach the coherence length of the superfluid. However, it's also possible there is kink, or unetched copper on the wire after the manufacturing process. The wires have been compared in helium gas at $4\,$K with larger wires, but the results are not any clearer. Hopefully in the future the matter will become more clear: first, it is possible to measure the wires at higher pressure, which will decrease the coherence length and increase the ratio of coherence length to radius. Second, a new experiment has begun which has several of these sub-micron wires, and an independent pressure gauge. We eagerly anticipate superfluid results for these wires.

Appendix A

Measurement Circuitry

Fig. A.1 and Fig. A.2 show simplified measurement circuits used for VWR measurements and QTF measurements, respectively. The signal generators used are Keysight Agilent 33220A or Agilent 33521A. The lock-in amplifiers used are Stanford Research Systems SR830. For VWRs, the drive current is passed through a drive box with a variable resistance (100 Ω to 1 MΩ) and a 6:1 step-down transformer to break ground loops. The signal voltage is amplified by a step-up transformer, which typically is a ratio 30:1. A QTF is instead passed through a series of $-20\,\text{dB}$ attenuators, usually a total of $-60\,\text{dB}$, to reduce the drive voltage. The signal is amplified by a current-to-voltage (I/V) converter. The I/V converter is a Stanford research systems SR570.
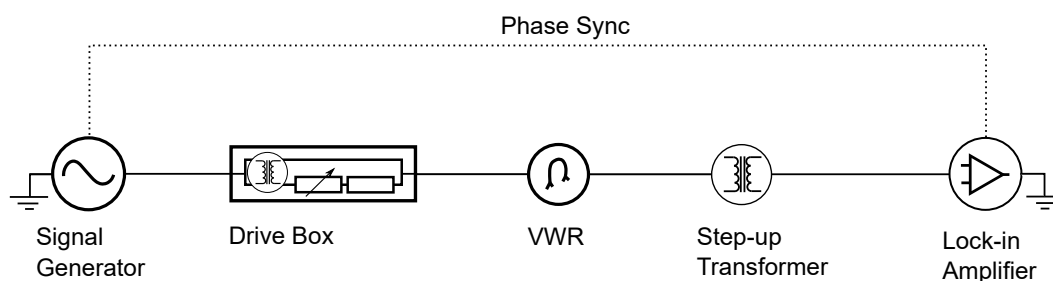
FIGURE A.1: Simplified circuit for a VWR resonator.

The measurement circuits for the flopper and NMR-flopper are in Fig. A.3, Fig. A.4 and Fig. A.5. For AC measurements (the outer signal generator and lock-in amplifier), the principle is the same as a VWR but without the step-up transformer. For the flopper DC ramps, the DC drive is mixed with an off-resonance high-frequency signal to measure the pick-up coil response. The drive voltage is determined by measuring the voltage of an $0.1\,\Omega$ resistor. For the NMR flopper, the NMR tank circuit is driven by the gradient coil via mutual induction. The NMR tank circuit is driven at a fixed frequency of 948 kHz and the response is recorded. In a sine-wave measurement, the DC power supply is still used but programmed by an AC signal generator. Again, the voltage of the resistor is
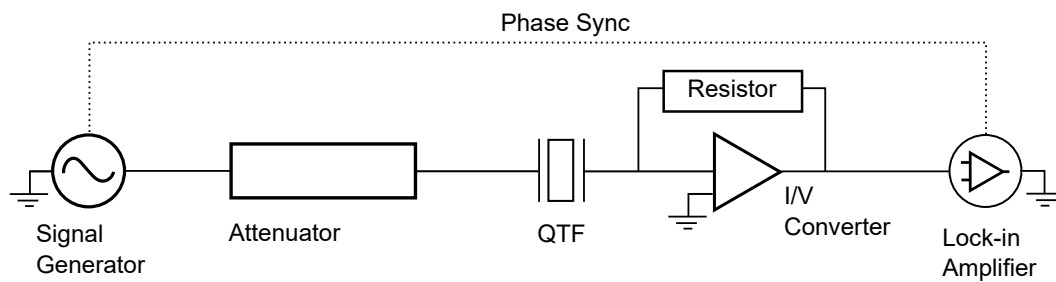
FIGURE A.2: Simplified circuit for a QTF.

measured to monitor the drive signal. Of course, for a drop measurement, only the DC supply is needed. The DC power supply used is a KEPCO Linear Power Supply BOP 20-25M model, which is controlled by a voltage signal from a Digital Acquisition board (DAQ).
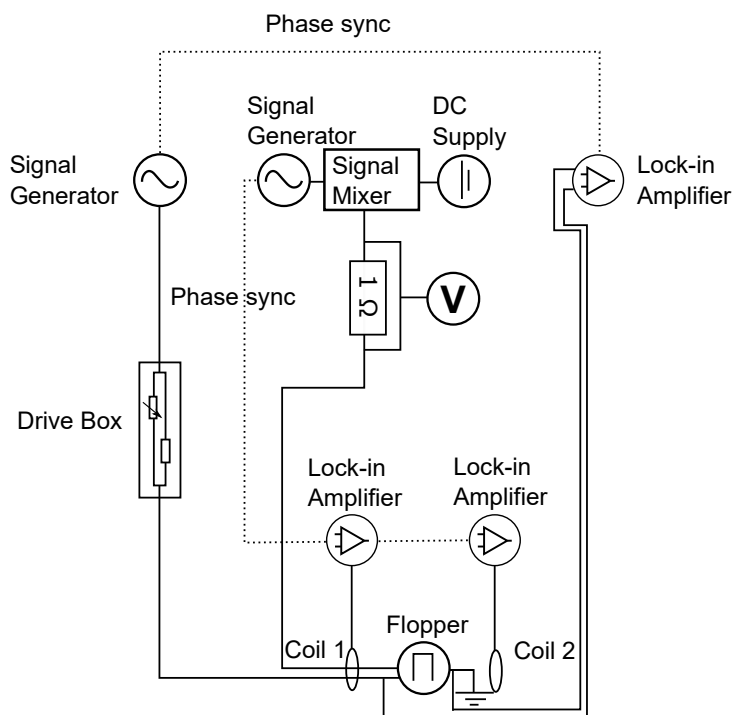
FIGURE A.3: Simplified circuit for AC motion and DC ramps of the flopper. The outer phase loop is for AC motion and is similar for a VWR.
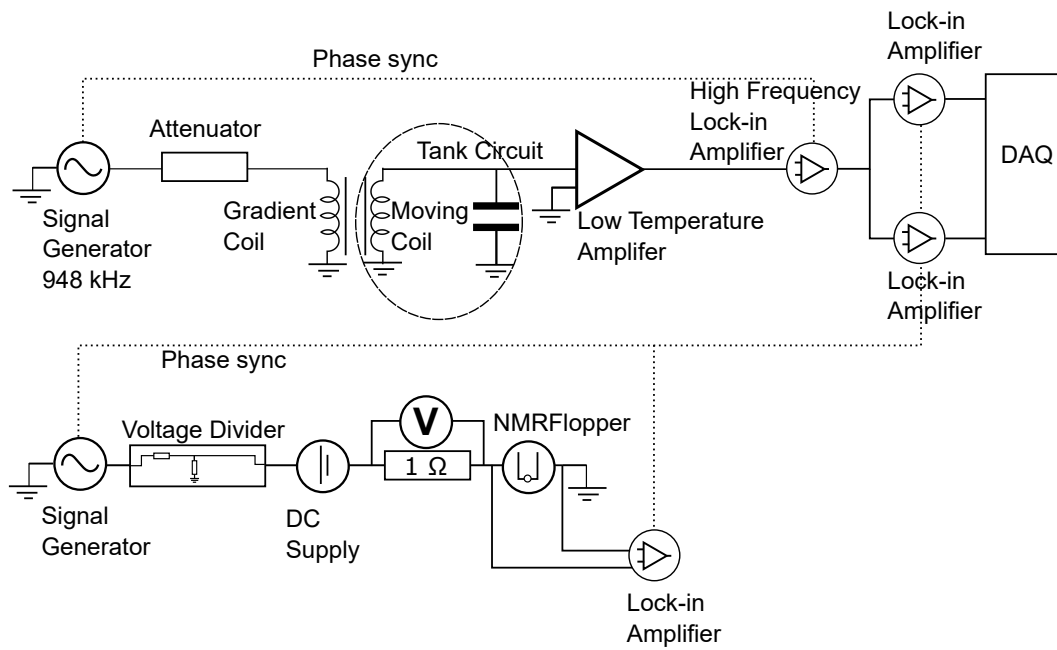
FIGURE A.4: Simplified circuit for a sine-wave measurements in Chapter 7.
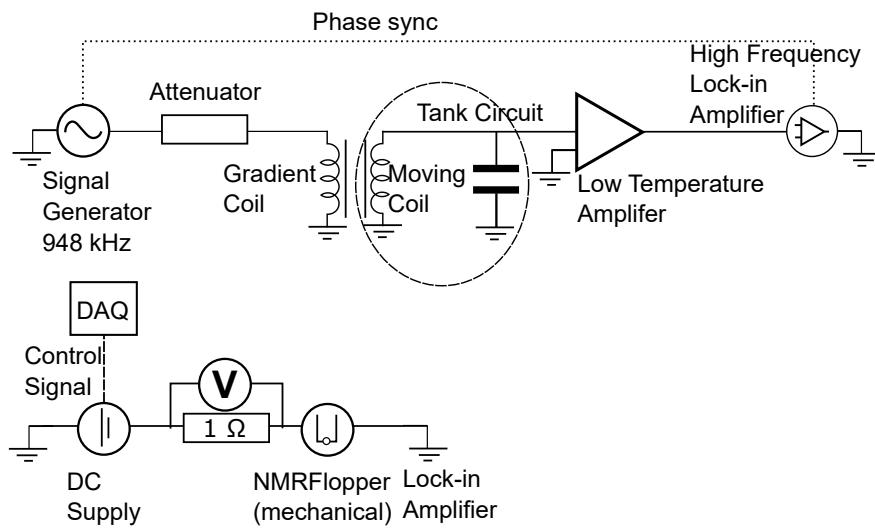
FIGURE A.5: Simplified circuit for drop measurements in Chapter 7.

Appendix B

Statistics

B.1 Goodness of Fits

In this work there are free methods for calculating the goodness of a fit to data. These are: the coefficient of determination (R^2), the Root Mean Squared Error (RMSE) and the Mean Absolute Error (MAE).

B.1.1 Mean Absolute Error

The total MAE simply measures the absolute difference between the measured value of the ith data point y_i and the predicted fit value x_i for the total N data points. It is defined as

$$\text{MAE} = \frac{\sum_{i=1}^{N} |y_i - x_i|}{N}. \tag{B.1}$$

B.1.2 Root Mean Squared Error

The RMSE uses the residual sum of squares (SS_{res}). The residual sum of the squares is defined as the sum of the squared difference between the measured and fit values

$$SS_{res} = \sum_{i=1}^{N} (y_i - x_i)^2. \tag{B.2}$$

For the RMSE, we simply divide SS_{res} by N and take the square root

$$\text{RMSE} = \sqrt{\frac{SS_{res}}{N}}. \tag{B.3}$$

B.1.3 Coefficient of Determination

The R^2 value is said to be a measure of the proportion of variation in the measured values that are predictable by the fit.

It compares the ratio of the residual sum of squares to the total sum of squares (SS_{tot}). The total sum of squares is the sum of the difference between the measured values y_i and the mean $\bar{y}$

$$SS_{tot} = \sum_{i=1}^{N} (y_i - \bar{y})^2. \tag{B.4}$$

The R^2 is then defined as

$$R^2 = 1 - \frac{SS_{res}}{SS_{tot}}. \tag{B.5}$$

One can think of the R^2 of providing a measure comparing how good our fit is to the simplest and most basic fit we can think of, the mean.

B.2 Statistical Moments

Statistical moments can be used to calculate several features of the NMR absorption line, including the central frequency and the width. Statistical moments are analogous to moments in classical mechanics. For a discrete data set that is a function of $f(x)$, the moment is

$$\mu_1 = \sum_{1}^{N} f(x_i) x_i \tag{B.6}$$

which we can use to find the centre by simply dividing by sum of $f(x_i)$

$$\text{Centre} = \frac{\mu_1}{\sum_1^N f(x_i)}. \tag{B.7}$$

This is analogous to finding the centre of mass. The second moment is simply

$$\mu_2 = \sum_{1}^{N} f(x_i) x_i^2. \tag{B.8}$$

To find the standard deviation σ which we use as the width, we use the centred second moment and divide by the sum of the function again

$$\sigma^2 = \text{Var} = \frac{\sum_1^N f(x_i)(x_i - \text{centre})^2}{\sum_1^N f(x_i)}. \tag{B.9}$$

For a continuous function we can replace the sums with integrals between $-\infty$ and $+\infty$.

B.3 Signal Response to a Lock-in Filter

The lock-in amplifiers have a Jth order low-pass filter setting with a time constant τ_f and a roll-off. The roll-off can be 6 dB, 12 dB, 18 dB and 24 dB per octave and determines the order of the filter used. This filtering is performed digitally within the lock-in amplifier. The low pass-filter is a simple exponential filter. Increasing the roll-off from -6 dB per octave is equivalent to passing the response after the first filter through another identical filter. Therefore, the roll-off setting controls the number of filters the original signal is passed through, from $J = 1$ to $J = 4$.

To find the position $x(t)$ of the NMR-flopper, we measure the voltage of the position detection coils. The response $y_1(t)$ of the first simple exponential filter can be defined by

$$\dot{y}_1 = \frac{x - y_1}{\tau_f}. \tag{B.10}$$

Now we introduce the function $u = y_1 e^{t/\tau_f}$ and rearrange (B.10) to get

$$x = T_f \dot{u} e^{t/\tau_f}. \tag{B.11}$$

Since $y_1 = u e^{-t/\tau_f}$ we can write from (B.11)

$$y_1 = \frac{1}{\tau_f} \left(\int x e^{t/\tau_f} dt + C_J \right) e^{-t/\tau_f} \tag{B.12}$$

The constant of integration C_J is determined by the initial condition $y_1(0) = x(0)$. Taking the underdamped solution, we write

$$y_1 = \frac{1}{\tau_f} \left(\int e^{-\frac{\Delta\omega}{2}t} \left[c_3 \cos(\omega_{ud}t) + c_4 \sin(\omega_{ud}t) \right] e^{t/\tau_f} dt + C_J \right) e^{-t/\tau_f}. \tag{B.13}$$

For simplicity, we use the substitution $a_1 = (1/\tau_f - \Delta\omega/2)$. Integrating results in

$$y_1 = \frac{1}{\tau_f} \frac{e^{\frac{\Delta\omega}{2}t}}{a_1^2 + \omega_{ud}^2} \left[(c_3 a_1 - c_4 \omega_{ud}) \cos(\omega_{ud}t) + (c_4 a_1 + c_3 \omega_{ud}) \sin(\omega_{ud}t) \right] + \frac{C_J}{\tau_f} e^{(-t/\tau_f)}. \tag{B.14}$$

We can see that this equation has the same form as the original underdamped equation, except with new constants in front of the sine and cosine functions and the addition of $\frac{c_n}{\tau_f} e^{(-t/\tau_f)}$.

We can then repeat the process for the second filter $y_2(t)$ by using the response of the first filter,

$$\dot{y}_2 = \frac{y_1 - y_2}{\tau_f}. \tag{B.15}$$

Clearly, this will result in another equation with the form of the original underdamped solution but with the addition $\int \frac{c_J}{\tau_f} e^{(-t/\tau_f)} dt + \frac{c_{J+1}}{\tau_f} e^{(-t/\tau_f)}$, where c_{J+1} is the second constant of integration.

We can repeat this process for J filters, as the constants of integration will just result in the addition of an infinite series.

Bibliography

[1] T. Guenault, *Basic superfluids* (CRC press, 2003).

[2] D. Vollhardt and P. Wölfle, *The superfluid phases of helium 3* (Taylor & Francis, London New York, 1990).

[3] C. A. M. Castelijns, K. F. Coates, A. M. Guénault, S. G. Mussett, and G. R. Pickett, "Landau critical velocity for a macroscopic object moving in superfluid ^{3}He-B: Evidence for gap suppression at a moving surface", Physical Review Letters **56**, 69–72 (1986).

[4] D. I. Bradley, P. Crookston, S. N. Fisher, A. Ganshin, A. M. Guénault, R. P. Haley, M. J. Jackson, G. R. Pickett, R. Schanen, and V. Tsepelin, "The Damping of a Quartz Tuning Fork in Superfluid ^{3}He-B at Low Temperatures", Journal of Low Temperature Physics **157**, 476–501 (2009).

[5] C. Lambert, "Theory of pair breaking by vibrating macroscopic objects in superfluid ^{3}He", Physica B: Condensed Matter **178**, 294–303 (1992).

[6] D. I. Bradley, S. N. Fisher, A. M. Guénault, R. P. Haley, C. Lawson, G. R. Pickett, R. Schanen, M. Skyba, V. Tsepelin, and D. Zmeev, "Breaking the superfluid speed limit in a fermionic condensate", Nature Physics **12**, 1017 (2016).

[7] V. Dmitriev, A. Senin, A. Soldatov, and A. Yudin, "Polar phase of superfluid ^{3}He in anisotropic aerogel", Physical Review Letters **115**, 165304 (2015).

[8] S. Autti, V. Dmitriev, J. Mäkinen, A. Soldatov, G. Volovik, A. Yudin, V. Zavjalov, and V. Eltsov, "Observation of Half-Quantum Vortices in Topological Superfluid ^{3}He", Physical Review Letters **117**, 255301 (2016).

[9] E. V. Surovtsev, "Phase Diagram of Superfluid ^{3}He in a Nematic Aerogel in a Strong Magnetic Field", Journal of Experimental and Theoretical Physics **128**, 477–484 (2019).

[10] D. I. Bradley, S. N. Fisher, A. M. Guénault, R. P. Haley, N. Mulders, S. O'Sullivan, G. R. Pickett, J. Roberts, and V. Tsepelin, "Contrasting Mechanical Anisotropies of the Superfluid ^{3}He Phases in Aerogel", Physical Review Letters **98**, 075302 (2007).

[11] V. V. Dmitriev, M. S. Kutuzov, A. A. Soldatov, and A. N. Yudin, "Superfluid β phase in liquid ^{3}He", https://arxiv.org/abs/2012.06302 (2020).

[12] R. Dobbs, *Helium Three* (Oxford University Press, 2001).

[13]C. Enss and S. Hunklinger, *Low Temperature Physics* (Springer Science & Business Media, 2005).

[14]W. Keesom and K. Clusius, "Leiden communication 216b", Proceedings van de Koninklijke Nederlandse Akademie van Wetenschappen **34** (1931).

[15]P. Kapitza, "Viscosity of Liquid Helium below the λ-Point", Nature **141**, 74–74 (1938).

[16]J. F. Allen and A. D. Misener, "Flow of Liquid Helium II", Nature **141**, 75–75 (1938).

[17]L. Landau, "Theory of the Superfluidity of Helium II", Physical Review **60**, 356–358 (1941).

[18]L. Landau, *Collected Papers of L.D. Landau*, edited by D. Ter Haar (Elsevier Science & Techn., Oct. 2013), 858 pp.

[19]J. F. Allen and H. Jones, "New Phenomena Connected with Heat Flow in Helium II", Nature **141**, 243–244 (1938).

[20]L. Tisza, "Transport Phenomena in Helium II", Nature **141**, 913–913 (1938).

[21]D. Betts, B. A. Keen, and J. Wilks, "The viscosity and acoustic impedance of liquid helium-3", Proceedings of the Royal Society of London. Series A. Mathematical and Physical Sciences **289**, 34–45 (1965).

[22]J. Bardeen, L. N. Cooper, and J. R. Schrieffer, "Microscopic Theory of Superconductivity", Physical Review **106**, 162–164 (1957).

[23]P. W. Anderson and P. Morel, "Generalized Bardeen-Cooper-Schrieffer States and the Proposed Low-Temperature Phase of Liquid ^{3}He", Physical Review **123**, 1911–1934 (1961).

[24]R. Balian and N. R. Werthamer, "Superconductivity with Pairs in a Relative p Wave", Physical Review **131**, 1553–1564 (1963).

[25]A. J. Leggett, "Interpretation of Recent Results on ^{3}He below 3 mK: A New Liquid Phase?", Physical Review Letters **29**, 1227–1230 (1972).

[26]J. Serene and D Rainer, "The quasiclassical approach to superfluid ^{3}He", Physics Reports **101**, 221–311 (1983).

[27]J. M. Parpia, "Anomalous thermal boundary resistance of superfluid ^{3}He-B", Physical Review B **32**, 7564–7566 (1985).

[28]L. Levitin, R. Bennett, A Casey, B Cowan, J Saunders, D Drung, T. Schurig, and J. Parpia, "Phase diagram of the topological superfluid ^{3}He confined in a nanoscale slab geometry", Science **340**, 841–844 (2013).

[29]P. J. Heikkinen, A. Casey, L. V. Levitin, X. Rojas, A. Vorontsov, P. Sharma, N. Zhelev, J. M. Parpia, and J. Saunders, "Fragility of surface states in topological superfluid ^{3}He", Nature Communications **12**, 10.1038/s41467-021-21831-y (2021).

[30]W. Halperin, "Superfluid ^{3}He in Aerogel", Annual Review of Condensed Matter Physics **10**, 155–170 (2019).

[31]V. Dmitriev, A. Soldatov, and A. Yudin, "Effect of Magnetic Boundary Conditions on Superfluid ^{3}He in Nematic Aerogel", Physical Review Letters **120**, 075301 (2018).

[32]K. Matsumoto, J. V. Porto, L. Pollack, E. N. Smith, T. L. Ho, and J. M. Parpia, "Quantum Phase Transition of ^{3}He in Aerogel at a Nonzero Pressure", Physical Review Letters **79**, 253–256 (1997).

[33]G. Gervais, T. M. Haard, R. Nomura, N. Mulders, and W. P. Halperin, "Modification of the Superfluid ^{3}He Phase Diagram by Impurity Scattering", Physical Review Letters **87**, 035701 (2001).

[34]G. Gervais, K. Yawata, N. Mulders, and W. P. Halperin, "Phase diagram of the superfluid phases of ^{3}He in 98% aerogel", Physical Review B **66**, 054528 (2002).

[35]J. V. Porto and J. M. Parpia, "Superfluid ^{3}He in Aerogel", Physical Review Letters **74**, 4667–4670 (1995).

[36]D. T. Sprague, T. M. Haard, J. B. Kycia, M. R. Rand, Y. Lee, P. J. Hamot, and W. P. Halperin, "Homogeneous Equal-Spin Pairing Superfluid State of ^{3}He in Aerogel", Physical Review Letters **75**, 661–664 (1995).

[37]E. V. Surovtsev, "Thermodynamic Properties of Superfluid ^{3}He in a Nematic Aerogel in a Strong Magnetic Field", Journal of Experimental and Theoretical Physics **129**, 1055–1061 (2019).

[38]M. H. Levitt, *Spin Dynamics* (Wiley John + Sons, Mar. 2008), 744 pp.

[39]A. M. Zimmerman, M. D. Nguyen, and W. P. Halperin, "NMR Frequency Shifts and Phase Identification in Superfluid ^{3}He", Journal of Low Temperature Physics **195**, 358–364 (2018).

[40]J. Kasai, Y. Okamoto, K. Nishioka, T. Takagi, and Y. Sasaki, "Chiral Domain Structure in Superfluid ^{3}He-A Studied by Magnetic Resonance Imaging", Physical Review Letters **120**, 205301 (2018).

[41]F. Reif and L. Meyer, "Study of Superfluidity in Liquid He by Ion Motion", Physical Review **119**, 1164–1173 (1960).

[42]H. Ikegami, Y. Tsutsumi, and K. Kono, "Chiral Symmetry Breaking in Superfluid ^{3}He-A", Science **341**, 59–62 (2013).

[43]G. P. Bewley, D. P. Lathrop, and K. R. Sreenivasan, "Visualization of quantized vortices", Nature **441**, 588–588 (2006).

[44]W. Guo, M. L. Mantia, D. P. Lathrop, and S. W. V. Sciver, "Visualization of two-fluid flows of superfluid helium-4", Proceedings of the National Academy of Sciences **111**, 4653–4658 (2014).

[45]P. Švančara, D. Duda, P. Hrubcová, M. Rotter, L. Skrbek, M. L. Mantia, E. Durozoy, P. Diribarne, B. Rousset, M. Bourgoin, and M. Gibert, "Ubiquity of particle–vortex interactions in turbulent counterflow of superfluid helium", Journal of Fluid Mechanics **911**, A8 (2021).

[46]D. J. Bishop and J. D. Reppy, "Study of the Superfluid Transition in Two-Dimensional ^{4}He Films", Physical Review Letters **40**, 1727–1730 (1978).

[47]Y. P. Sachkou, C. G. Baker, G. I. Harris, O. R. Stockdale, S. Forstner, M. T. Reeves, X. He, D. L. McAuslan, A. S. Bradley, M. J. Davis, and W. P. Bowen, "Coherent vortex dynamics in a strongly interacting superfluid on a silicon chip", Science **366**, 1480–1485 (2019).

[48]A. Shook, V. Vadakkumbatt, P. S. Yapa, C. Doolin, R. Boyack, P. Kim, G. Popowich, F. Souris, H. Christani, J. Maciejko, and J. Davis, "Stabilized Pair Density Wave via Nanoscale Confinement of Superfluid ^{3}He", Physical Review Letters **124**, 015301 (2020).

[49]M. J. Fear, P. M. Walmsley, D. A. Chorlton, D. E. Zmeev, S. J. Gillott, M. C. Sellers, P. P. Richardson, H. Agrawal, G. Batey, and A. I. Golov, "A compact rotating dilution refrigerator", Review of Scientific Instruments **84**, 103905 (2013).

[50]J. Nyéki, A. Phillis, A. Ho, D. Lee, P. Coleman, J. Parpia, B. Cowan, and J. Saunders, "Intertwined superfluid and density wave order in two-dimensional ^{4}He", Nature Physics **13**, 455–459 (2017).

[51]A. Guénault, V Keith, C. Kennedy, S. Mussett, and G. Pickett, "The mechanical behavior of a vibrating wire in superfluid ^{3}He-B in the ballistic limit", Journal of Low Temperature Physics **62**, 511–523 (1986).

[52]H. Yano, K. Ogawa, Y. Chiba, K. Obara, and O. Ishikawa, "Anisotropic Formation of Quantum Turbulence Generated by a Vibrating Wire in Superfluid ^{4}He", Journal of Low Temperature Physics **187**, 515–522 (2016).

[53]D. I. Bradley, D. O. Clubb, S. N. Fisher, A. M. Guénault, R. P. Haley, C. J. Matthews, G. R. Pickett, V. Tsepelin, and K. Zaki, "Decay of Pure Quantum Turbulence in Superfluid ^{3}He-B", Physical Review Letters **96**, 035301 (2006).

[54]R Blaauwgeers, M Blazkova, M Človečko, V. Eltsov, R De Graaf, J Hosio, M Krusius, D Schmoranzer, W. Schoepe, L Skrbek, et al., "Quartz tuning fork: thermometer, pressure-and viscometer for helium liquids", Journal of low temperature physics **146**, 537–562 (2007).

[55]M. Človečko, E. Gažo, M. Kupka, M. Skyba, and P. Skyba, "High Quality Tuning Forks in Superfluid ^{3}He-B Below 200 μK", Journal of Low Temperature Physics **162**, 669–677 (2010).

[56]D. Schmoranzer, M. J. Jackson, V. Tsepelin, M. Poole, A. J. Woods, M. Človečko, and L. Skrbek, "Multiple critical velocities in oscillatory flow of superfluidHe4due to quartz tuning forks", Physical Review B **94**, 214503 (2016).

[57]D. Schmoranzer, M. J. Jackson, Š. Midlik, M. Skyba, J. Bahyl, T. Skokánková, V. Tsepelin, and L. Skrbek, "Dynamical similarity and instabilities in high-Stokes-number oscillatory flows of superfluid helium", Physical Review B **99**, 054511 (2019).

[58]C. S. Barquist, W. G. Jiang, K. Gunther, N. Eng, Y. Lee, and H. B. Chan, "Damping of a microelectromechanical oscillator in turbulent superfluid ^{4}He : A probe of quantized vorticity in the ultralow temperature regime", Physical Review B **101**, 174513 (2020).

[59]D. I. Bradley, R George, A. M. Guénault, R. P. Haley, S. Kafanov, M. Noble, Y. A. Pashkin, G. R. Pickett, M. Poole, J. R. Prance, et al., "Operating nanobeams in a quantum fluid", Scientific Reports **7**, 4876 (2017).

[60]A. M. Guénault, A. Guthrie, R. P. Haley, S. Kafanov, Y. A. Pashkin, G. R. Pickett, M. Poole, R. Schanen, V. Tsepelin, D. E. Zmeev, E. Collin, O. Maillet, and R. Gazizulin, "Probing superfluid ^{4}He with high-frequency nanomechanical resonators down to millikelvin temperatures", Physical Review B **100**, 020506 (2019).

[61]A. M. Guénault, R. P. Haley, S. Kafanov, M. T. Noble, G. R. Pickett, M. Poole, R. Schanen, V. Tsepelin, J. Vonka, T. Wilcox, and D. E. Zmeev, "Acoustic damping of quartz tuning forks in normal and superfluid ^{3}He", Physical Review B **100**, 104526 (2019).

[62]A. Guthrie, "Nanoscale devices for studying quantum fluids and electrostatic field-effects in superconducting nanoconstrictions", PhD thesis (Lancaster University, 2020).

[63]P. Esquinazi, "Vibrating superconductors", Journal of Low Temperature Physics **85**, 139–232 (1991).

[64]J. H. Naish, A. P. J. Voncken, D. Riese, R. König, J. R. Owers-Bradley, and F. Pobell, "A study of vibrating wires for viscometry in high magnetic fields", Czechoslovak Journal of Physics **46**, 99–100 (1996).

[65]D. Schmoranzer, M. L. Mantia, G. Sheshin, I. Gritsenko, A. Zadorozhko, M. Rotter, and L. Skrbek, "Acoustic Emission by Quartz Tuning Forks and Other Oscillating Structures in Cryogenic ^{4}He Fluids", Journal of Low Temperature Physicss **163**, 317–344 (2011).

[66]R. G. Powell, *Introduction to electric circuits* (Arnold, London, 1995).

[67]S. N. Fisher, G. R. Pickett, and R. J. Watts-Tobin, "A microscopic calculation of the force on a wire moving through superfluid ^{3}He-B in the ballistic regime", Journal of Low Temperature Physics **83**, 225–235 (1991).

[68]M. P. Enrico, S. N. Fisher, and R. J. Watts-Tobin, "Diffuse scattering model of the thermal damping of a wire moving through superfluid ^{3}He-B at very low temperatures", Journal of Low Temperature Physics **98**, 81–89 (1995).

[69]K. Nagai, Y. Nagato, M. Yamamoto, and S. Higashitani, "Surface Bound States in Superfluid ^{3}He", Journal of the Physical Society of Japan **77**, 111003 (2008).

[70]J. A. Sauls, "Andreev bound states and their signatures", Philosophical Transactions of the Royal Society A: Mathematical, Physical and Engineering Sciences **376**, 20180140 (2018).

[71]S. Murakawa, Y. Wada, Y. Tamura, M. Wasai, M. Saitoh, Y. Aoki, R. Nomura, Y. Okuda, Y. Nagato, M. Yamamoto, S. Higashitani, and K. Nagai, "Surface Majorana Cone of the Superfluid ^{3}He-B Phase", Journal of the Physical Society of Japan **80**, 013602 (2011).

[72]S. N. Fisher, A. M. Guénault, C. J. Kennedy, and G. R. Pickett, "The one-dimensional excitation gas in superfluid ^{3}He-A at very low temperatures", Journal of Low Temperature Physics **89**, 481–484 (1992).

[73]G. Pickett, M. Enrico, S. Fisher, A. Guénault, and K. Torizuka, "Superfluid ^{3}He at very low temperatures: a very unusual excitation gas", Physica B: Condensed Matter **197**, 390–396 (1994).

[74]D. C. Carless, H. E. Hall, and J. R. Hook, "Vibrating wire measurements in liquid ^{3}He. I. The normal state", Journal of Low Temperature Physics **50**, 583–603 (1983).

[75]D. I. Bradley, M. Človeč̌ko, M. J. Fear, S. N. Fisher, A. M. Guénault, R. P. Haley, C. R. Lawson, G. R. Pickett, R. Schanen, V. Tsepelin, and P. Williams, "A New Device for Studying Low or Zero Frequency Mechanical Motion at Very Low Temperatures", Journal of Low Temperature Physics **165**, 114–131 (2011).

[76]D. Zmeev, "A method for driving an oscillator at a quasi-uniform velocity", Journal of Low Temperature Physics **175**, 480–485 (2014).

[77]S. Naguleswaran, "The Vibrations Of A "Stiff " Gravity Pendulum With A Particle Bob", Journal of Sound and Vibration **191**, 1–14 (1996).

[78]V. V. Zavjalov, A. M. Savin, and P. J. Hakonen, "Cryogenic Differential Amplifier for NMR Applications", Journal of Low Temperature Physics **195**, 72–80 (2018).

[79]D. I. Bradley, P. Crookston, M. J. Fear, S. N. Fisher, G. Foulds, D. Garg, A. M. Guénault, E. Guise, R. P. Haley, O. Kolosov, G. R. Pickett, R. Schanen, and V. Tsepelin, "Measuring the Prong Velocity of Quartz Tuning Forks Used to Probe Quantum Fluids", Journal of Low Temperature Physics **161**, 536–547 (2010).

[80]E. A. Laird, F. Pei, W. Tang, G. A. Steele, and L. P. Kouwenhoven, "A High Quality Factor Carbon Nanotube Mechanical Resonator at 39 GHz", Nano Letters **12**, 193–197 (2011).

[81]G. K. White and P. J. Meeson, *Experimental Techniques in Low-Temperature Physics* (Oxford University Press, Apr. 2002), 296 pp.

[82]F. Pobell, *Matter and Methods at Low Temperatures* (Springer Berlin Heidelberg, 2007).

[83]D. J. Cousins, S. N. Fisher, A. M. Guénault, G. R. Pickett, E. N. Smith, and R. P. Turner, "T^{-3} Temperature Dependence and a Length Scale for the Thermal Boundary Resistance between a Saturated Dilute ^{3}He-^{4}He Solution and Sintered Silver", Physical Review Letters **73**, 2583–2586 (1994).

[84]M. J. Fear, "Probing the A-phase, B-phase and A-B Interface of Superfluid ^{3}He with Miniature Quartz Tuning Forks", PhD thesis (Lancaster University, 2011).

[85]G. Pickett, "Cooling metals to the microkelvin regime, then and now", Physica B: Condensed Matter **280**, 467–473 (2000).

[86]T. Nakayama, "Chapter 3: Kapitza Thermal Boundary Resistance and Interactions of Helium Quasiparticles with Surfaces", in *Progress in Low Temperature Physics*, Vol. 12 (Elsevier, 1989), pp. 115–194.

[87]R. Peterson and A. Anderson, "Acoustic-mismatch model of the Kaptiza resistance", Physics Letters A **40**, 317–319 (1972).

[88]H. Franco, J. Bossy, and H. Godfrin, "Properties of sintered silver powders and their application in heat exchangers at millikelvin temperatures", Cryogenics **24**, 477–483 (1984).

[89]V. Keith and M. Ward, "A recipe for sintering submicron silver powders", Cryogenics **24**, 249–250 (1984).

[90]C. A. M. Castelijns, K. F. Coates, A. M. Guénault, S. G. Mussett, and G. R. Pickett, "Exponential Temperature Dependence of the Thermal Boundary Conductance between Sintered Silver and ^{3}He-*B* in the Region of Low Normal Fluid Density", Physical Review Letters **55**, 2021–2024 (1985).

[91]J. P. Carney, K. F. Coates, A. M. Guénault, G. R. Pickett, and G. F. Spencer, "Thermal behavior of quasiparticles in ^{3}He-B", Journal of Low Temperature Physics **76**, 417–434 (1989).

[92]A. J. Leggett and M. Vuorio, "On the anomalous CMN-^{3}He thermal boundary resistance", Journal of Low Temperature Physics **3**, 359–376 (1970).

[93]R. C. Albers and J. W. Wilkins, "Spin relaxation of ^{3}He to paramagnetic centers in surfaces at very low temperatures", Journal of Low Temperature Physics **34**, 105–156 (1979).

[94]T. Perry, K. DeConde, J. A. Sauls, and D. L. Stein, "Evidence for Magnetic Coupling in the Thermal Boundary Resistance between Liquid ^{3}He and Platinum", Physical Review Letters **48**, 1831–1834 (1982).

[95]D. D. Osheroff and R. C. Richardson, "Novel Magnetic Field Dependence of the Coupling of Excitations between Two Fermion Fluids", Phys. Rev. Lett. **54**, 1178–1181 (1985).

[96]R. König, T. Herrmannsdörfer, D. Riese, and W. Jansen, "Magnetic properties of Ag sinters and their possible impact on the coupling to liquid ^{3}He at very low temperatures", Journal of Low Temperature Physics **106**, 581–590 (1997).

[97]R. König, T. Herrmannsdörfer, A. Schindler, and I. Usherov-Marshak, "The Origin of the Magnetic Channel of the Thermal Boundary Resistance Between Liquid ^{3}He and Ag Sinters at Very Low Temperatures", Journal of Low Temperature Physics **113**, 969–974 (1998).

[98]R. König, T. Herrmannsdörfer, and I. Batko, "Magnetization of Ag Sinters Made of Compressed Particles of Submicron Grain Size and Their Coupling to Liquid ^{3}He", Physical Review Letters **80**, 4787–4790 (1998).

[99]S. M. Tholen and J. M. Parpia, "Effect of ^{4}He on the surface scattering of ^{3}He", Physical Review B **47**, 319–329 (1993).

[100]N. Mizutani and H. Suzuki, "Magnetic thermal boundary resistance between enhanced nuclear spin systems and liquid ^{3}He", Journal of Low Temperature Physics **86**, 231–256 (1992).

[101]C. E. Campbell, F. J. Milford, A. D. Novaco, and M. Schick, "Helium-Monolayer Completion on Graphite", Physical Review A **6**, 1648–1652 (1972).

[102]V. Dmitriev, L. Levitin, V. Zavjalov, and D. Y. Zmeev, "Separation of ^{3}He from ^{3}He-^{4}He Mixture by means of Adsorption", Journal of Low Temperature Physics **138**, 877–880 (2005).

[103]Various, *Leak Detection Compendium* (Pfeiffer Vacuum GmbH, 2013).

[104]J. Vonka, "Demagnetisation of solid ^{3}He and supercritical superflow", PhD thesis (Lancaster University, 2018).

[105]S. Autti, S. L. Ahlstrom, R. P. Haley, A. Jennings, G. R. Pickett, M. Poole, R. Schanen, A. A. Soldatov, V. Tsepelin, J. Vonka, T. Wilcox, A. J. Woods, and D. E. Zmeev, "Fundamental dissipation due to bound fermions in the zero-temperature limit", Nature Communications **11**, 4742 (2020).

[106]M. Skyba, "Critical flow velocity in superfluid ^{3}He-B", PhD thesis (Lancaster University, 2016).

[107]J. A. Kuorelahti, S. M. Laine, and E. V. Thuneberg, "Models for supercritical motion in a superfluid Fermi liquid", Physical Review B **98**, 144512 (2018).

[108]M. Arrayás, J. L. Trueba, C. Uriarte, and D. E. Zmeev, "Design of a system for controlling a levitating sphere in superfluid ^{3}He at extremely low temperatures", Scientific Reports **11**, 20069 (2021).

[109]M. A. Silaev and G. E. Volovik, "Andreev-Majorana bound states in superfluids", Journal of Experimental and Theoretical Physics **119**, 1042–1057 (2014).

[110]T. Mizushima, Y. Tsutsumi, T. Kawakami, M. Sato, M. Ichioka, and K. Machida, "Symmetry-Protected Topological Superfluids and Superconductors —From the Basics to ^{3}He—", Physical Society of Japan **85**, 022001 (2016).

[111]W. Ruesink, J. P. Harrison, and A. Sachrajda, "The vibrating wire viscometer as a magnetic field-independent ^{3}He thermometer", Journal of Low Temperature Physics **70**, 393–411 (1988).

[112]S. Autti, A. M. Guénault, A. Jennings, R. P. Haley, G. R. Pickett, R. Schanen, V. Tsepelin, J. Vonka, D. E. Zmeev, and A. A. Soldatov, "Effect of the boundary condition on the Kapitza resistance between superfluid ^{3}He-B and sintered metal", Physical Review B **102**, 064508 (2020).

[113]A. P. J. Voncken, D. Riese, L. P. Roobol, R. König, and F. Pobell, "Thermal boundary resistance between liquid helium and silver sinter at low temperatures", Journal of Low Temperature Physics **105**, 93–112 (1996).

[114]C. Winkelmann, J. Elbs, Y. M. Bunkov, E. Collin, H. Godfrin, and M. Krusius, "Bolometric calibration of a superfluid ^{3}He detector for Dark Matter search: Direct measurement of the scintillated energy fraction for neutron, electron and muon events", Nuclear Instruments and Methods in Physics Research Section A: Accelerators, Spectrometers, Detectors and Associated Equipment **574**, 264–271 (2007).

[115]O. Avenel, M. P. Berglund, R. G. Gylling, N. E. Phillips, A. Vetleseter, and M. Vuorio, "Improved Thermal Contact at Ultralow Temperatures between ^{3}He and Metals Containing Magnetic Impurities", Physical Review Letters **31**, 76–79 (1973).

[116]J. H. Bishop, A. C. Mota, and J. C. Wheatley, "Thermal Boundary Resistance between Pt and Liquid ^{3}He at Very Low Temperatures", in *Low Temeprature Physics - LT 13* (Springer US, 1974), pp. 406–410.

[117]J. Elbs, C. Winkelmann, Y. M. Bunkov, E. Collin, and H. Godfrin, "Heat Capacity of Adsorbed Helium-3 at Ultra-Low Temperatures", Journal of Low Temperature Physics **148**, 749–753 (2007).

[118]A. F. Borghesani, *Electrons and Ions in Liquid Helium* (Oxford University Press, July 2007), 544 pp.

[119]P. Sharma and J. A. Sauls, "Magnetic Susceptibility of the Balian–Werthamer Phase of ^{3}He in Aerogel", Journal of Low Temeprature Physics **125**, 115–142 (2001).